WAVEFORM DESIGN FOR 5G AND BEYOND WIRELESS COMMUNICATION NETWORKS

A DISSERTATION SUBMITTED TO

THE GRADUATE SCHOOL OF

ENGINEERING AND NATURAL SCIENCES

OF ISTANBUL MEDIPOL UNIVERSITY

IN PARTIAL FULFILLMENT OF THE REQUIREMENTS FOR

THE DEGREE OF

DOCTOR OF PHILOSOPHY

IN

ELECTRICAL, ELECTRONICS ENGINEERING AND CYBER SYSTEMS

By

Salah Eddine ZEGRAR

January, 2024

WAVEFORM DESIGN FOR 5G AND BEYOND WIRELESS COMMUNICATION NETWORKS

By Salah Eddine ZEGRAR

05 January, 2024

We certify that we have read this dissertation and that in our opinion it is fully adequate, in scope and in quality, as a dissertation for the degree of Doctor of Philosophy.

_____

Prof. Dr. Hüseyin Arslan (Advisor)

_____

Prof. Dr. Zekai Şen

_____

Prof. Dr. Hakan Ali Çırpan

_____

Prof. Dr. Mehmet K. Özdemir

_____

Assoc. Prof. Dr. Ertuğrul Başar

Approved by the Graduate School of Engineering and Natural Sciences:

_____

Prof. Dr. Yasemin Yüksel Durmaz

Director of the Graduate School of Engineering and Natural Sciences

I hereby declare that all information in this document has been obtained and presented in accordance with academic rules and ethical conduct. I also declare that, as required by these rules and conduct, I have fully cited and referenced all material and results that are not original to this work.

Signature :

Name Surname: SALAH EDDINE ZEGRAR

ACKNOWLEDGEMENT

Praise be to Allah, by whose blessings righteous deeds are completed. Praise be to Allah, who has granted me success and guided me to the right path. Praise be to Allah, who has provided me with beneficial knowledge from His grace. O Allah, make me a radiant lamp that illuminates and enlightens. O Allah, grant me the ability to be a wellspring of knowledge that quenches the thirst of every seeker. O Allah may my knowledge be beneficial to the Islamic nation and all of humanity, and may it be an ongoing charity that brings light to my grave after death.

Secondly, I extend my gratitude to those who have stayed up and worked hard for my upbringing and education since my childhood. Thank you to those who have been the reason for my successful studies, without faltering or hesitation. I will never forget the look of pride in their eyes every time I excelled and received awards. It became the most beautiful sight I had ever seen, and I wished to witness it as long as I lived. O Allah, make me a source of happiness in their hearts, my dear parents, Laid and Megdouda.

Thirdly, to my brothers and sisters who have supported me whenever I felt tired and stressed, my siblings who put me before themselves and shaped me into the person I am today. Thank you, my brothers, and sisters. Fourthly, to my pillar of support and the love of my life, my fiancée, who has been a beacon of hope, support, and a source of positivity in my life, which has been filled with fatigue, challenges, and difficulties. Thank you for being a part of my life.

Then, to my teacher from whom I learned to be a student before becoming a scholar, to be patient before achieving success, and to be virtuous before being a role model. Thank you to whoever has been and will be a role model in my academic and practical life, my beloved Hocam Hüseyin Arslan.

Finally, to my friends and companions, both inside and outside the university, thank you for your support and patience with me. You have been the best companions, and I found solace in you whenever I needed it. Thank you all. Lastly, I would like to conclude with this prayer: "*O Allah, benefit me by that which You have taught me, and teach me that which will benefit me, and increase me in knowledge*", Ameen!

Salah Eddine Zegrar

January, 2024

CONTENTS

Page

ACKNOWLEDGEMENT ..... **iv**
CONTENTS ..... **v**
LIST OF FIGURES ..... **viii**
LIST OF TABLES ..... **xi**
LIST OF SYMBOLS ..... **xii**
ABBREVIATIONS ..... **xiii**
ÖZET ..... **xiv**
ABSTRACT ..... **xvi**
1. INTRODUCTION **1**
1.1. A Vision of 6G 1
1.2. What is the Approach Towards 6G PHY? 3
1.3. Aims & Objectives of The Thesis 5
1.4. Contributions of The Thesis 6
1.5. Layout of The Thesis 8
2. BACKGROUND: WIRELESS CHANNEL & WAVEFORM DESIGN **10**
2.1. Wireless Channel 10
2.1.1. Time-delay representation 10
2.1.2. Time-frequency representation 11
2.1.3. Delay-Doppler representation 12
2.1.4. Wireless channel and waveform design 12
2.2. What Is a Waveform? 14
2.2.1. What to transmit? 14
2.2.2. Where to transmit 14
2.2.3. How to transmit? 15
2.2.4. In what way to transmit? 15
2.3. 4G PHY Framework 15
2.3.1. Orthogonal frequency division multiplexing (OFDM) 15
2.4. 5G PHY Framework 16
2.4.1. 5G candidate waveforms 16
2.4.2. Multi-numerology OFDM 17
2.5. 6G Waveform Candidates 18
2.5.1. Orthogonal time-frequency space (OTFS) 19
2.5.2. Frequency modulated continuous wave (FMCW) 19
2.5.3. Orthogonal chirp division multiplexing (OCDM) 20
2.6. 6G PHY Framework 20
2.6.1. Data/Logical lattice 21
2.6.2. Physical resource grid (time-frequency (TF) Domain) 23
2.6.3. Transmission/Time domain 24
2.7. Key Takeaways 25
3. THEORETICAL PART: LITERATURE REVIEW **27**
3.1. Securing OFDM signaling via Physical Layer Security (PLS) 27
3.2. Channel Estimation in CCP-OFDM Systems 29
3.3. CP Configuration in OTFS Systems 30
3.4. Doubly-Dispersive Channel Estimation in OTFS Systems 31
3.5. Integrated Sensing and Communication via OTFS Signaling 34
3.6. Integrated Sensing and Communication (ISAC) via FMCW Signaling 38
3.7. Channel Estimation in OCDM Systems 41

4. EXPERIMENTAL PART: PROBLEMS AND PROPOSED SOLUTIONS... 44
4.1. Flexible Physical Layer Security for Joint Data and Pilots in OFDM Systems ... 44
4.1.1. System model and preliminaries ... 44
4.1.2. Proposed algorithm ... 46
4.1.3. Numerical analysis ... 52
4.2. Common CP-OFDM Transceiver Design for Low-Complexity Frequency Domain Equalization ... 57
4.2.1. Problem formulation ... 57
4.2.2. Proposed CCP-OFDM scheme ... 58
4.3. A Novel Cyclic Prefix Configuration for Enhanced Reliability and Spectral efficiency in OTFS Systems ... 64
4.3.1. System model ... 64
4.3.2. Proposed FCP-OTFS ... 67
4.4. Fractional Doubly-Dispersive Channel Estimation and Mitigation Framework in OTFS Systems ... 69
4.4.1. System model ... 69
4.4.2. Problem formulation ... 72
4.4.3. Preliminaries ... 72
4.4.4. Proposed channel estimation and equalization framework ... 80
4.5. OTFS-Based ISAC for Super-Resolution Range-Velocity Profile ... 86
4.5.1. Proposed system model ... 86
4.5.2. Properties of an OTFS carrier ... 92
4.5.3. Proposed OTFS-based ISAC framework ... 95
4.6. OTFS-FMCW Waveform Design for Low Complexity Joint Sensing and Communication ... 98
4.6.1. Preliminaries ... 98
4.6.2. The relationship between OTFS and chirp waveforms ... 104
4.6.3. Proposed OTFS-chirp JSAC waveform ... 107
4.6.4. JSAC signal processing ... 109
4.7. Delay-Doppler-Based Channel Estimation Method in Doubly-Dispersive OCDM Systems ... 114
4.7.1. OCDM in delay-Doppler domain ... 114
4.7.2. Proposed OCDM channel estimation ... 117
5. RESULTS AND DISCUSSION ... 120
5.1. Flexible Physical Layer Security for Joint Data and Pilots in OFDM Systems ... 120
5.2. Common CP-OFDM Transceiver Design for Low-Complexity Frequency Domain Equalization ... 124
5.3. A Novel Cyclic Prefix Configuration for Enhanced Reliability and Spectral Efficiency in OTFS Systems ... 127
5.4. Fractional Doubly-Dispersive Channel Estimation and Mitigation Framework in OTFS Systems ... 130
5.4.1. Cramer-Rao lower bound ... 130
5.4.2. Computational complexity analysis ... 132
5.4.3. Performance of the proposed channel estimation framework ... 133
5.5. OTFS-Based ISAC for Super-Resolution Range-Velocity Profile ... 136
5.5.1. Cramer-Rao lower bound ... 136
5.5.2. Computational complexity analysis ... 138
5.5.3. Communication and radar performance analysis ... 139

5.5.4. Experimental results 134
5.6. OTFS-FMCW Waveform Design for Low Complexity Joint Sensing and Communication 145
5.6.1. Computational complexity analysis 146
5.6.2. Sensing performance 146
5.6.3. Communication performance 148
5.6.4. Channel estimation 149
5.7. Delay-Doppler-Based Channel Estimation Method in Doubly-Dispersive OCDM Systems 152
6. CHALLENGES AND RESEARCH DIRECTIONS 154
7. CONCLUSION AND FUTURE WORK 156
BIBLIOGRAPHY 160
APPENDIX A 171
CURRICULUM VITAE 176

LIST OF FIGURES

Figure 1.1: Illustration of the envisioned 6G network including deployment scenarios/environments, selected use cases and requirements. The items in red indicate the require- ments not satisfied by fifth-generation (5G) physical (PHY). 3
Figure 2.1: Illustration of the relationship between the waveform and the TF lattice..... 15
Figure 2.2: Illustration of the 4G and 5G approaches to PHY design. 4G used a uni-form lattice with a single orthogonal frequency division multiplexing (OFDM) pulse. 5G candidates included multiple pulse shapes such as FBMC and multiple numerologies, i.e, non-uniform TF lattice. 18
Figure 2.3: PHY slices for different waveforms discussed in sixth generation (6G)..... 22
Figure 4.1: System model where Alice and Bob are communicating over rich scattering channel with the existence of Eve. 44
Figure 4.2: The zero-pole diagram of the minimum-phase all-pass decomposition of a wireless channel..... 47
Figure 4.3: The block diagram showing the main steps of the proposed joint data and pilot security algorithm. 51
Figure 4.4: The distribution of uncorrelated part of Eve's channel for $p_{ae} = 0.9$. 53
Figure 4.5: The channel correlation relationship between the conventional and proposed schemes. 55
Figure 4.6: The transceiver design for the proposed pilot-based channel estimation scheme. 58
Figure 4.7: The CP addition in full-CP (FCP)-OTFS systems in both delay-Doppler and time domains. 65
Figure 4.8: Proposed FCP OTFS frame. 66
Figure 4.9: Delay-Doppler domain OTFS waveform carrier (Pulsone). 67
Figure 4.10: Different prefix/suffix configurations in OTFS systems: (a) reduced-CP (RCP) (b) FCP (c) Equivalent discarded CP signal in FCP-OTFS. 73
Figure 4.11: Pilot and data symbols arrangement at the transmitter: (a) (i,i), (b) (i,f), (c) (f,i), (d) (f,f). 74
Figure 4.12: Pulsone properties. 78
Figure 4.13: Simple ISAC configuration with one target. 88
Figure 4.14: The pilot and data symbols structure at the transmitter. 89
Figure 4.15: Single OTFS carrier. 91
Figure 4.16: Single OTFS carrier's properties. 92
Figure 4.17: The time, time-frequency, and delay-Doppler representations of linear chirp with parameters: $L = 1$, $N = 32$, $M = 32$. 101
Figure 4.18: The time, time-frequency, and delay-Doppler representations of different OC signals with parameters: $L = 1$, $N = 32$, $M = 32$. 102
Figure 4.19: The time, time-frequency, and delay-Doppler representations of cascaded two linear chirps with parameters: $L = 2$, $N = 32$, $M = 32$. 103
Figure 4.20: Typical JSAC scenario for the proposed waveform. 108
Figure 4.21: The delay-Doppler representation of (a) transmitted signal, (b) received signal, (c) received filtered pilot signal from data interference, and (d) received pilot signal in case no data is transmitted (zero-interference). 112
Figure 4.22: The delay-Doppler representation of difference OCDM carriers with parameters: $L = 1$, $N_d = 32$, $M_d = 32$, $N = 1024$. 115
Figure 4.23: Pilot, guard, and data symbol arrangement. 117
Figure 4.24: The delay-Doppler representation of proposed pilot signal with parameters: $N_p = 8$, $N = 1024$, $l_p = 16$, and $l_{\max} = k_{\max} = 4$. 118

Figure 5.1: BER performance of the proposed data security algorithm vs channel shortening [141], AN [140] and conventional CP-OFDM [114]. 121
Figure 5.2: Performance comparison of the proposed algorithm (blue color) vs. LS [24] (red color) in terms of Eve's BER under correlated eavesdropping channels. The solid and dashed lines stand for the analytical and simulation results, respectively. 122
Figure 5.3: The CCDF of the PAPR for the proposed algorithm compared to channel shortening [141], AN [140], LS [24], and conventional CP-OFDM [3]. 123
Figure 5.4: The channel estimation's NMSE performance vs SNR at Bob and Eve com- pared to [19], [22], and [114]. 124
Figure 5.5: The normalized mean square error (NMSE) performance of proposed scheme compared to CP-OFDM using different channel estimators. 125
Figure 5.6: BER performance of the proposed CCP-OFDM and conventional CP-OFDM systems. 126
Figure 5.7: CCDF of the PAPR of the transmitted signal of CP-OFDM and proposed CCP-OFDM. 126
Figure 5.8: The BER performance of data in the CP portion. 128
Figure 5.9: Proposed pilot design for channel estimation in the case of: (a) inter delay-Doppler shifts, (b) fraction Doppler shifts. 128
Figure 5.10: OTFS system's capacity under integer and fractional Doppler channe. 129
Figure 5.11: Channel NMSE performance for different L taps. 130
Figure 5.12: NMSE vs α analysis. 133
Figure 5.13: NMSE vs SNR_p analysis. 134
Figure 5.14: BER vs SNR_p analysis. 135
Figure 5.15: Computational complexity analysis. 136
Figure 5.16: The delay-Doppler representation of the received pilot signal acquired using experimental setup for different α values. 137
Figure 5.17: Range-velocity map. 140
Figure 5.18: The RMSE performance of the estimated range and velocity vs SNR_p (N=M = 64, f_c = 77 GHz , B = 50 MHz). 141
Figure 5.19: The RMSE performance of the estimated range and velocity vs SNR$radar$ (N = M = 64, f_c = 77 GHz , B = 50 MHz). 142
Figure 5.20: The BER performance of the proposed ISAC scheme. 142
Figure 5.21: The experiment setup. 143
Figure 5.22: The relationship between E and performance (RMSE), complexity, and SNR_p. 144
Figure 5.23: Experimental results for $E_0 = E_{(f)} = 20$. 144
Figure 5.24: Complexity comparison between different sensing algorithms. 146
Figure 5.25: The range-velocity plot from the received: (a) single UT signal, (b)-(d) multi- UT signal. 147
Figure 5.26: The RMSE of the target range and velocity estimation vs SNR_r. 147
Figure 5.27: BER vs SNR_c analysis. 148
Figure 5.28: Communication rate vs SNR_c analysis. 148
Figure 5.29: Channel NMSE performance of the proposed chirp-based estimation vs em- bedded pilot threshold based channel estimation [29]. 149
Figure 5.30: Comparison of the CCDF of the PAPR of the transmitted signal in different systems. 150
Figure 5.31: Channel NMSE performance for different E_p/E_s values. 151
Figure 5.32: The BER performance for different E_p/E_s values. 152

LIST OF TABLES

Table 1.1: Comparison of the different PHY design approaches for 6G. 9
Table 2.1: OFDM from a waveform perspective. 16
Table 2.2: 5G candidate waveforms from a waveform perspective. 17
Table 2.3: Multi-numerology OFDM from a waveform perspective. 17
Table 2.4: 6G candidates from a waveform perspective. 21
Table 4.1: Complexity of the proposed security algorithm. 56
Table 5.1: Simulation parameters. 120
Table 5.2: Simulation parameters. 124
Table 5.3: Complexity comparison between different channel estimation algorithm. 125
Table 5.4: Simulation parameters. 127
Table 5.5: Computational complexity comparison. 139
Table 5.6: Simulation parameters. 140
Table 5.7: Simulation parameters. 145

LIST OF SYMBOLS

$(\cdot)^T$: Transpose
$(\cdot)^H$: Hermitian
$(\cdot)^{-1}$: Inverse
$\delta(\cdot)$: Dirac-delta function
j : Imaginary unit of complex numbers
$\mathcal{R}e\{c\}$: Real part of c
$\mathcal{I}m\{c\}$: Imaginary part of c
f_c : Carrier frequency
Δf : Subcarrier spacing
M : Number of delays and subcarriers
T : Symbol duration
N : Number of Dopplers and symbols
L : Number of channel taps
l : Integer delay index
ι : Fractional delay shift index
τ : Delay shift
r : Range
ΔR : Range resolution
ν : Doppler shift
v : Velocity
ΔV : Velocity spacing
k : Integer Doppler shift index
κ : Fractional Doppler shift index
h : Channel coefficient (time domain)
H : Channel coefficient (frequency domain)
$\boldsymbol{H}$: Channel Matrix
$\boldsymbol{H}_{\mathbf{eff}}$: Effective channel Matrix
$\mathrm{vec}(\cdot)$: Vectorization operator
$\mathrm{diag}(\cdot)$: Diagonal operator
$\mathbf{A}\otimes\mathbf{B}$: Kronecker product of $\mathbf{A}$ and $\mathbf{B}$
$\boldsymbol{F}$: DFT matrix
$\boldsymbol{I}$: Identity matrix
$\mathbb{C}^{M\times N}$: Space of $M \times N$ complex-valued matrices
μ : Mean
σ : Standard deviation
σ^2 : Variance
$\mathcal{N}(\cdot)$: Gaussian distribution
P : Signal power
C : Capacity
T_{cp} : Duration of the cyclic prefix (CP)
T_s : Sampling interval

$\boldsymbol{x}$: Transmitted signal (time domain)
$\boldsymbol{X}_{\mathbf{TF}}$: Transmitted signal (frequency domain)
$\boldsymbol{X}_{\mathbf{DD}}$: Transmitted signal (delay-Doppler domain)
$\boldsymbol{y}$: Received signal (time domain)
$\boldsymbol{Y}_{\mathbf{TF}}$: Received signal (frequency domain)
$\boldsymbol{Y}_{\mathbf{DD}}$: Received signal (delay-Doppler domain)

ABBREVIATIONS

1D	: One-dimensional
2D	: Two-dimensional
3D	: Three-dimensional
4G	: Fourth generation
5G	: Fifth generation
6G	: Sixth generation
AI	: Artificial intelligence
AN	: Artificial noise
AoA	: Angle of arrival
AWGN	: Additive white Gaussian noise
BER	: Bit error rate
BEP	: Bit error probability
BPSK	: Binary phase shift keying
BS	: Base station
CDF	: Cumulative distribution function
CCDF	: Complementary cumulative distribution function
CE	: Channel estimation
CFO	: Carrier frequency offset
CFR	: Channel frequency response
CIR	: Channel impulse response
CLT	: Central limit theorem
CP	: Cyclic prefix
CSI	: Channel state information
CRLB	: Cramer-Rao lower bound
DD	: Delay-Doppler
DFnT	: Discrete Fresnel transform
DFT	: Discrete Fourier transform
DFT-s-OTFS	: Discrete Fourier transform spread orthogonal time frequency space
DL	: Downlink
DNN	: Deep neural network
DZT	: Discrete Zak transform
eMBB	: Enhanced mobile broadband
eNB	: ENodeB
ELPC	: Extremely low-power communication
EM	: Electromagnetic
ERLLC	: Extremely reliable and low-latency communication
EVD	: Eigenvalue decomposition
FCP	: Full-CP
FDD	: Frequency-division duplexing
FeMBB	: Further-enhanced mobile broadband
FFT	: Fast Fourier transform
FIR	: Finite impulse response
FMCW	: Frequency modulated continuous wave

FSK : Frequency shift keying
FZS : Full-zero suffix
FZS : Full-zero suffix
fc : Carrier-frequency
ICI : Inter-carrier interference
IDeI : Inter-delay interference
IDFnT : Inverse discrete Fresnel transform
IDFT : Inverse discrete Fourier transform
IDZT : Inverse discrete Zak transform
i.i.d. : Independent and identically distributed
IFFT : Inverse fast Fourier transform
IDI : Inter-Doppler interference
IoT : Internet of things
ISAC : Integrated sensing and communication
ISFFT : Inverse symplectic Fourier transform
ISI : Inter-symbol interference
JSAC : Joint sensing and communication
LTE : Long-Term Evolution
LoS : Line-of-sight
MAC : Medium access control
MCC : Mission-critical communication
MEC : Mobile edge computing
MGF : Moment generating function
MIMO : Multiple-input multiple-output
MMSE : Minimum mean squared error
MP : Message passing
MPC : Multipath component
MRT : Maximum ratio transmission
MSE : Mean square error
mMIMO : Massive MIMO
mMTC : Massive machine type communication
mmWave : Millimeter wave
ML : Maximum likelihood
MRC : maximum-ratio combining
NLoS : Non-line-of-sight
NMSE : Normalized mean squared error
NOMA : Non-orthogonal multiple access
NTN : Non-terrestrial network
OC : Orthogonal chirp
OCDM : Orthogonal chirp division multiplexing
OFDM : Orthogonal frequency division multiplexing
OMA : Orthogonal multiple access
OMP : Orthogonal matching pursuit
OTFS : Orthogonal time-frequency space
PAPR : Peak-to-average power ratio
PDF : Probability distribution function

PHY : Physical
PLS : Physical layer security
PMI : Precoding matrix indicator
QAM : Quadrature amplitude modulation
QoS : Quality of service
QPSK : Quadrature Phase Shift Keying
REM : Radio environment map
RF : Radio frequency
RIS : Reconfigurable intelligent surface
RMSE : Root mean squared error
RSS : Received signal strength
RSSI : Received signal strength indicator
RV : Random variable
RCP : Reduced-CP
RZP : Reduced-zero padded
SBL : Sparse Bayesian learning
SER : Symbol error rate
SFFT : Symplectic finite Fourier transform
SIC : Successive interference cancellation
SINR : Signal-to-interference-plus-noise ratio
SISO : Single-input single-output
SNR : Signal-to-noise ratio
SOP : Secrecy outage probability
SVD : Singular value decomposition
TF : Time-frequency
TDD : Time-division duplexing
THz : Terahertz
UE : User equipment
UL : Uplink
umMTC : Ultra-massive machine-type communication
UP : User priority
uRLLC : Ultra-reliable low latency communication
UT : User terminal
V2I : Vehicle-to-infrastructure
V2N : Vehicle-to-network
V2V : Vehicle-to-vehicle
V2X : Vehicle-to-everything
VSA : Vector signal analyzer
VSG : Vector signal generator
WSN : wireless sensor network
XF : Explainable AI
XR : Extended reality
ZF : Zero-forcing
ZP : Zero padding
ZS : Zero suffix
ZSA : Zero suffix

5G VE ÖTESİ KABLOSUZ HABERLEŞME AĞLARI İÇİN DALGA FORMU TASARI

ÖZET

Salah Eddine ZEGRAR

Elektrik-Elektronik Mühendisliği ve Siber Sistemler, Doktora

Tez Danışmanı: Prof. Dr. Hüseyin Arslan

Ocak, 2024

Altıncı nesil (6G), güç, menzil, veri hızları, gecikme ve yayılma ortamı açısından çeşitli uygulamaların yanı sıra ağ varlıklarına da sahip olmayı vaat ediyor. Ağın genel heterojenliği, fiziksel (PHY) katman tasarımı açısından önemli zorluklar doğurmaktadır. Bu tez, PHY tasarımına yönelik olası yaklaşımları tartışmadan önce ilk olarak 5G çoklu-numerolojili ortogonal frekans bölmeli çoğullamanın (OFDM) yetersiz kaldığı bazı alanları tanımlamaktadır. Özellikle, zarif ve sürdürülebilir bir ağ gelişimini mümkün kılmak için yeni gereksinimler ortaya çıktıkça genişletilebilecek, geriye dönük olarak uyumlu, ileriye dönük ve genişletilebilir bir PHY katman çerçevesini tartışıyoruz. Ek olarak, Ortogonal Frekans Bölmeli Çoğullama (OFDM), Ortak Döngüsel Önek (CCP) OFDM, ortogonal zaman-frekans-uzay (OTFS), frekans modülasyonlu sürekli dalga (FMCW) ve ortogonal cıvıltı bölmeli çoğullama gibi 6G için çeşitli aday dalga biçimleri (OCDM) sunulmuş ve araştırılmıştır. Bu dalga formlarının kullanım durumlarına devam ederek, ilk olarak tez, MIMO sistemleri için ortogonal frekans bölmeli çoğullamaya (OFDM) dayalı yeni fiziksel katman güvenliği (PLS) şemaları önermektedir. Bu şemalar, meşru kullanıcıların performansından ödün vermeden güvenliği sağlamak için minimum aşamalı tüm geçişli kanal ayrıştırmasını kullanır. Ayrıca, CCP-OFDM için düşük karmaşıklıktaki frekans alanı kanal tahminini ve eşitlemesini mümkün kılan yeni bir alıcı-verici tasarımı tanıtılmıştır. Bu tasarım, karmaşık zaman alanı tahmin algoritmalarına olan ihtiyacı azaltır. Tez, sistem performansını artırmak için gecikme-Doppler alanındaki FCP yapısından yararlanarak ortogonal zaman-frekans-uzay (OTFS) modülasyonunda tam CP'nin (FCP) değiştirilmiş yapısını araştırıyor. Daha sonra, kesirli gecikmeyi ve düşük karmaşıklığa sahip kesirli Doppler kanalını tahmin etmek için pilot darbenin darbe-ton doğasını kullanan darbe bazlı bir kanal tahmin yöntemi önerilmektedir. Entegre algılama ve iletişim (ISAC) bağlamında, büyük bant genişliği iletimlerine veya uzun süreli çerçevelere ihtiyaç duymadan hassas aralık-hız profillerini mümkün kılan OTFS tabanlı bir sistem önerilmektedir. Bu yaklaşım, doğru algılama bilgisi sağlarken bant genişliği ve zaman üzerindeki kısıtlamaları hafifletir. ISAC ile ilgili zorlukların üstesinden gelmek için bu tezde yeni bir OTFS-FMCW dalga formu önerilmiştir. Dalga biçimi, OTFS ve FMCW'nin ortogonal çoğullamasını sağlamak için gecikme-Doppler alanındaki doğrusal cıvıltıların seyrekliğinden yararlanır ve eşzamanlı yüksek veri hızlı iletişimi ve düşük karmaşıklıkta doğru algılamayı kolaylaştırır. Ek olarak, aynı OTFS-FMCW dalga formu içinde birden fazla ortogonal cıvıltının (OC'ler) farklı kullanıcılara tahsis edildiği çok kullanıcılı bir ISAC şeması sunulmaktadır. Son olarak OCDM, potansiyel bir 6G dalga biçimi olarak araştırılıyor. Tez, OCDM dalga formlarının gecikme-

Doppler alanındaki temsilini araştırarak bunların seyrek doğasını ortaya koymaktadır. Bu gözlemden yararlanarak, Fresnel alanındaki pilotların tasarımını ve gecikme-Doppler alanındaki kanal tahminini içeren, düşük karmaşıklığa sahip bir kanal tahmin tekniği önerilmektedir.

Anahtar sözcükler: 5G, 6G, dalga biçimi, döngüsel önek (CP), ortogonal frekans bölmeli çoğullama (OFDM), ortogonal zaman-frekans alanı (OTFS), frekans modülasy- onlu sürekli dalga (FMCW) ve ortogonal cıvıltı bölmeli çoğullama (OCDM), fiziksel kat- man güvenliği (PLS), entegre algılama ve iletişim (ISAC), kanal tahmini.

WAVEFORM DESIGN FOR 5G AND BEYOND WIRELESS COMMUNICATION NETWORKS

ABSTRACT

Salah Eddine ZEGRAR

Ph.D. in Electrical, Electronics Engineering and Cyber Systems

Advisor: Prof. Dr. Hüseyin Arslan

January, 2020

A 6G promises to have a variety of applications, as well as network entities, in terms of power, range, data rates, latency, and propagation environment. The overall heterogeneity of the network poses significant challenges in terms of physical (PHY) layer design. This thesis first identifies some of the areas where the 5G multi-numerology orthogonal frequency division multiplexing (OFDM) falls short before discussing the possible approaches towards PHY design. In particular, it is discussed that a backward-compatible, forward- looking, and extendable PHY layer framework can be extended as new requirements arise to enable a graceful and sustainable network evolution. Additionally, several candidate waveforms for 6G, such as Orthogonal Frequency Division Multiplexing (OFDM), Common-Cyclic Prefix (CCP) OFDM, orthogonal time-frequency-space (OTFS), frequency modulated continuous wave (FMCW), and orthogonal chirp division multiplexing (OCDM) are presented and investigated. Continuing with the use cases of these waveforms, first, the thesis proposes novel physical layer security (PLS) schemes for MIMO systems based on orthogonal frequency division multiplexing (OFDM). These schemes utilize minimum-phase all-pass channel decomposition to ensure security without compromising the performance of legitimate users. Furthermore, a novel transceiver design for CCP-OFDM is introduced, enabling low-complexity frequency-domain channel estimation and equalization. This design mitigates the need for complex time-domain estimation algorithms. The thesis explores a modified structure of the full-CP (FCP) in orthogonal time-frequency-space (OTFS) modulation, leveraging the FCP structure in the delay-Doppler domain to enhance system performance. Then, an impulse-based channel estimation method is proposed, utilizing the pulse-tone nature of the pilot impulse to estimate fractional delay and fractional Doppler channel with low complexity. In the context of integrated sensing and communication (ISAC), an OTFS-based system is proposed, enabling precise range-velocity profiles without the need for large bandwidth transmissions or long-duration frames. This approach relaxes constraints on bandwidth and time while providing accurate sensing information. To address the challenges associated with ISAC, a novel OTFS-FMCW waveform is proposed in this thesis. The waveform leverages the sparsity of linear chirps in the delay-Doppler domain to enable orthogonal multiplexing of OTFS and FMCW, facilitating simultaneous high data rate communication and low-complexity accurate sensing. Additionally, a multi- user ISAC scheme is presented, where multiple orthogonal chirps (OCs) are allocated to different users within the same OTFS-FMCW waveform. Finally, OCDM is explored as a potential 6G waveform. The thesis investigates the representation of OCDM waveforms

in the delay-Doppler domain, revealing their sparse nature. Leveraging this observation, a low-complexity channel estimation technique is proposed, involving the design of pilots in the Fresnel domain and channel estimation in the delay-Doppler domain.

Keywords: 5G, 6G, waveform, cyclic prefix (CP), orthogonal frequency division multiplexing (OFDM), orthogonal time-frequency space (OTFS), frequency modulated continuous wave (FMCW), and orthogonal chirp division multiplexing (OCDM), physical layer security (PLS), integrated sensing and communication (ISAC), channel estimation.

CHAPTER 1

1. INTRODUCTION

1.1. A Vision Of 6G

The recent pandemic has reiterated the importance of wireless communication for mankind. The continuation of various facets of our lives including education, trading, banking, healthcare, transportation etc., over the last couple of years has largely been due to the reliable connectivity provided via cellular and WiFi networks. This is because of the paradigm shift promised by fifth-generation (5G), where the focus moved from merely high data rates to strict reliability, low latency, and massive connectivity. However, unlike previous generations, 5G did not introduce a completely new waveform or physical (PHY) layer design. Rather, the concept of numerology, i.e., different sets of values for PHY layer parameters, such as subcarrier spacing and cyclic prefix (CP) duration, was proposed. This was partially to ensure backward compatibility, and partially because none of the other proposed designs outperformed orthogonal frequency division multiplexing (OFDM) in all aspects.

Given that ,sixth-generation (6G) envisions a ubiquitous fabric of connectivity everywhere, at all times, and for everyone/everything, it is only logical to look at the compatibility of OFDM for beyond 5G applications. Some of these applications are extensions of the existing 5G services under the umbrellas of further-enhanced mobile broadband (FeMBB), extremely reliable and low-latency communication (ERLLC), long-distance and high-mobility communication (LDHMC), ultra-massive machine-type communication (umMTC), and extremely low-power communication (ELPC) that require high data rates, reliability, latency, mobility, power efficiency, and massive connectivity [7]. On

the other hand, there are new requirements such as integrated sensing and communication (ISAC), sustainability, security and privacy, and the need to support Artificial Intelligence (AI) throughout the network leading to a native-AI experience. The question then becomes, how do these requirements relate to the waveform and PHY design? And what are the instances, if any, where the existing 5G PHY layer fails to deliver?

OFDM is undoubtedly one of the most popular waveforms in wireless communication history (not only cellular but WiFi as well) due to its ability to combat multipath propagation and frequency-selective fading, simplified (frequency domain) equalization, enhanced spectral efficiency and multiple-input multiple-output (MIMO) support for improved data rates and reliability. However, despite its prolific success, it is unable to address some of the expected requirements of 6G mentioned above. Starting with sensing, even though the resolution of range and velocity depends on the total transmission bandwidth and duration, respectively, the processing required to extract the parameters is critical. While OFDM requires digital signal processing, analog processing is sufficient for waveforms like chirp. Moreover, OFDM systems suffer from large sidelobes in the frequency domain and high peak-to-average power ratio (PAPR). In terms of sensing, this causes target masking, especially in the presence of multiple targets [8]. While the effect of sidelobes can be suppressed using guards or other cancellation schemes, it ultimately leads to reduction in efficiency which is one of the main drivers behind OFDM. Furthermore, as OFDM packs the frequency domain carriers so close to each other, any frequency synchronization errors adversely affect the system. This manifests in high-mobility applications such as high-speed trains, vehicle-to-everything (V2X) communication, and low Earth orbit (LEO) satellites [9] where the mobility and resultant Doppler spread lead to loss of orthogonality. Similarly, grant-free initial/random access is critical in providing (sporadic) massive connectivity for Internet of things (IoT) and low-latency for extended reality (XR) applications, but OFDM's strict synchronization requirements become a hindrance here. In fact, this is one of the reasons why code division multiple access (CDMA)-like preambles are used in the uplink initial access of fourth generation (4G). The synchronization also lets OFDM down in multi-connectivity scenarios, which are necessary to provide ubiquitous connectivity at higher frequencies. Furthermore, while mini-slot and numerologies with larger subcarrier spacing were introduced to decrease latency, this approach is limited due to the symbol alignment constraints. Regarding security, even

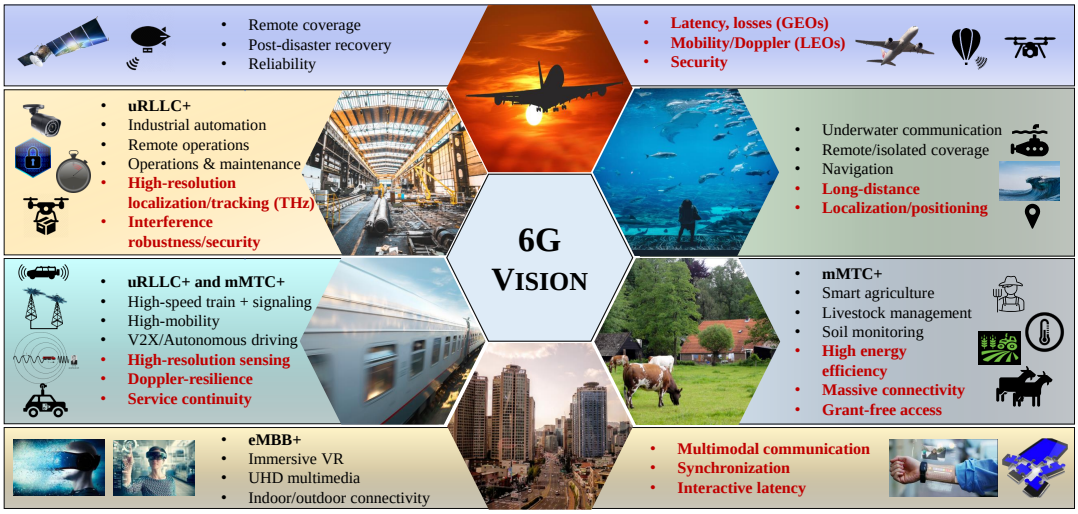


Figure 1.1: Illustration of the envisioned 6G network including deployment scenarios/environments, selected use cases and requirements. The items in red indicate the requirements not satisfied by 5G PHY.

though a plethora of OFDM-based physical layer security (PLS) literature exists, the inherent cyclostationarity due to use of CP can be exploited by malicious users.

Figure 1.1 illustrates a 6G network comprising different applications, environments, and deployment scenarios. The items indicated in red signal the requirements (discussed above) not met in their entirety by 5G multi-numerology PHY as defined in the 3rd Generation Partnership Project (3GPP) standardization.

Consequently, what 6G needs is a PHY design framework that provides the flexibility to adapt to different requirements and scenarios without causing an unbearable overhead in terms of implementation [10]. The following text first looks at potential approaches for 6G PHY, followed by a detailed description of the proposed framework. The authors argued that unlike 5G (and preceding generations), where the waveform and PHY design was limited to the time-frequency (T-F) resource plane, 6G needs additional flexibility by introducing (multiple) logical plane(s) where data can be populated. A case study based on multiple access is also presented to emphasize this point before highlighting associated research opportunities.

1.2. What Is The Approach Towards 6G PHY?

Each generation of cellular networks begins with identifying possible applications, use cases, and their requirements. These studies generally run concurrently with the last

release(s) of the previous generation, focusing on incremental improvements. Subsequent discussions usually cover various technological enablers, encompassing different waveform/PHY designs, hardware capabilities, spectrum ranges, deployment scenarios, and more. Ultimately, the standardization process commences, aiming to establish consensus among various stakeholders regarding different functionalities in PHY, medium access control (MAC), and higher network layers of the communication system.

Regarding PHY, it is possible to approach the problem in one of the following ways:

- Completely new PHY: This approach was the norm until 4G, where each cellular generation had its own PHY design. Generally, the new PHY was geared towards solving the biggest issues faced in the preceding one. The major advantage of this approach is being unhindered by any backward compatibility constraints. On the other hand, this approach requires the willingness of different stakeholders (users and operators) to replace the infrastructure and bear the associated cost.

- Extension of 5G multi-numerology OFDM: It can be argued that 5G was the first generation which did not focus on a single major requirement. Rather, it targeted spectral efficiency, high data rates, reduced latency, high reliability, massive connectivity, and energy efficiency simultaneously. Consequently, there was no unanimously approved PHY candidate, and multi-numerology OFDM was selected. A similar approach for 6G would ensure backward compatibility at the cost of increased inter-numerology interference (INI) [11]. Moreover, OFDM has been extensively studied for decades, and the possibility of finding any extensions that provide significant gains is rather remote [12].

- Coexistence of different waveforms: Another approach is to allow different PHY candidate waveforms to coexist with each other. The user chooses any of the possible ones depending on its requirement [13]. While this is reasonable for different frequency bands, using fundamentally different waveforms over the same frequencies means that the mutual relationships of the waveforms are not exploited. Moreover, the use of different PHY designs leads to a similar stumbling block as the first approach, i.e., increased cost of hardware replacement.

- Unified modular framework: A forward-looking yet backward-compatible framework is needed, containing not only different options of OFDM-like waveforms but also allowing the incorporation of new alternatives such as orthogonal time frequency space (OTFS), orthogonal time sequency multiplexing (OTSM), and orthogonal chirp division multiplexing (OCDM) [14]. This would enable a sustainable, gradual, and graceful network upgrade instead of necessitating instantaneous large-scale changes, which are highly undesirable for various stakeholders in the wireless communication industry [15]. This approach differs from the previous one as it brings different waveforms together under the same framework, allowing them to have different configurations for some constituent blocks without changing the overall structure. The following section takes a deeper dive into what constitutes such a unified framework.

Table 1.1 provides a comparison of the pros and cons of each of the aforementioned approaches.

1.3. Aims & Objectives Of The Thesis

The primary aim of this thesis is to contribute to the advancement of wireless communication systems, specifically focusing on the PHY design for 6G technology. The research aims to address the challenges and requirements posed by diverse applications and use cases envisioned for 6G, while considering the services, applications, and the technical requirements.

The objectives of this thesis are:

- To explore and analyze the existing literature on 6G technology, waveform design, and physical layer characteristics, in order to gain a comprehensive understanding of the research landscape.
- To develop a forward-looking and extendable physical layer framework for 6G, taking into account the diverse requirements of different applications and use cases.
- To propose novel waveform designs, including radar, communication, signal processing, and channel estimation algorithms, tailored specifically for 6G candidate waveforms.

- To address the challenges of backward compatibility in 6G and develop new low-complexity transceiver designs.
- To investigate the mutual relationships among different proposed waveforms and explore opportunities for leveraging their respective benefits more effectively.
- To provide recommendations and insights for future research directions in the field of 6G PHY design, considering emerging technologies and evolving communication requirements.
- By achieving these objectives, this thesis aims to contribute to the development of 6G wireless communication systems, enabling the realization of diverse applications and use cases while considering practical implementation constraints.

1.4. Contributions Of The Thesis

This section presents the contributions of this thesis towards the advancement and development of wireless communication systems, particularly in the context of 6G technology. Research endeavors have focused on addressing the challenges and requirements posed by the diverse range of applications and use cases envisioned for 6G, with a specific emphasis on the PHY design. Through a comprehensive exploration of various aspects, significant contributions are made that pave the way for the evolution and optimization of next-generation wireless networks. These contributions encompass novel approaches in PLS, waveform design, backward compatibility, forward-looking framework, and mutual relationships among different waveforms. By addressing the practical considerations and industry resistance, pragmatic solutions that balance innovation with the feasibility of implementation are provided. The following sections detail our contributions in tackling these key aspects, fostering the sustainable growth and transformative potential of 6G wireless communication systems. The contributions are summarized as follows:

- Developed a simultaneously backward-compatible and forward-looking physical layer (PHY) framework for 6G to address the diverse requirements of new use cases and applications while considering industry resistance to a complete redesign. This framework highlights the shared slices/blocks among different proposed waveforms, challenging the emphasis on their individuality. By recognizing the mutual

relationships between waveforms, new opportunities arise to leverage their respective benefits more effectively. The use of OFDM with a rectangular pulse shape and appropriate precoding is proposed as the optimal approach for next-generation wireless systems, providing a promising path forward.

- Proposed novel physical layer security (PLS) schemes for securing data and pilots in multiple-input multiple-output (MIMO) systems based on orthogonal frequency-division multiplexing (OFDM). Minimum-phase all-pass channel decomposition is utilized to enhance security without compromising the performance of legitimate users.

- Developed a novel transceiver design for common cyclic prefix-orthogonal frequency-division multiplexing (CCP-OFDM) systems, enabling low-complexity frequency-domain channel estimation and equalization. Overcame the challenges posed by slow time-variant channels and complex time-domain estimation algorithms.

- Introduced a novel orthogonal time-frequency-space (OTFS) structure, leveraging the full-CP (FCP) structure in OTFS modulation to enhance system performance. Instead of discarding the information in the CP block at the receiver, a method to decode it in the delay-Doppler domain is proposed.

- Proposed a low-complexity algorithm for impulse-based channel estimation, exploiting the unique properties of a pulsone (pulse tone) pilot impulse. Leveraged the pulse's ability to maintain its shape despite time delay and Doppler shift operations, along with its self-duality between time and frequency domains. Enabled accurate estimation of fractional delay and fractional Doppler channel.

- Proposed an orthogonal time-frequency space (OTFS)-based Integrated Sensing and Communication (ISAC) system for achieving highly accurate range-velocity profiles without the need for large bandwidth transmissions or long-duration frames. Leveraged a single OTFS carrier with rectangular pulse shaping as a pilot to estimate simultaneous accruing delay and Doppler, enabling precise sensing information beyond the resolution limitations set by time duration and bandwidth.

- Introduced a novel orthogonal time frequency space (OTFS)-chirp waveform for

joint sensing and communication (JSAC), addressing the coexistence challenge of both functionalities. Exploited the sparsity of linear chirps in the delay-Doppler domain to multiplex OTFS and chirp in an orthogonal manner. Proposed a multi-user JSAC scheme and a chirp-based channel estimation technique, reducing pilot guard overhead and peak-to-average power ratio (PAPR).

- Investigated the representation of Orthogonal Chirp Division Multiplexing (OCDM) waveforms in the delay-Doppler domain and revealed their sparse nature. Proposed a low-complexity channel estimation technique for OCDM systems, involving pilot design in the Fresnel domain and channel estimation in the delay-Doppler domain. Overcame the challenges of inseparable data symbols in high-mobility wireless channels.

1.5. Layout Of The Thesis

The layout of this thesis is organized as follows: **Chapter 2** provides a detailed discussion on waveform definition, including an examination of the wireless channel characteristics. Additionally, a general framework for 6G PHY is defined in this chapter. In **Chapter 3**, a comprehensive literature review is presented, focusing on the applications and use cases of the 6G candidate waveforms. **Chapter 4** introduces novel waveform designs, which encompass the development of radar, communication, signal processing, and channel estimation algorithms specifically tailored for selected 6G candidate waveforms. The simulation results are analyzed and discussed in **Chapter 5**, shedding light on the performance and efficacy of the proposed waveform designs. **Chapter 6** addresses the challenges encountered during the development of the 6G waveform, delving into the discussion of future work and potential areas for further research. Finally, the thesis is concluded in **Chapter 7**, where the key findings and contributions are summarized, and the implications of the research are discussed.

Table 1.1: Comparison of the different PHY design approaches for 6G.

Approach	Advantages	Disadvantages
Completely new PHY	1. No limitations regarding backward compatibility. We can explore fundamentally new domains such as wavelets as possible options.	1. A single waveform or PHY is unable to satisfy all (sensing and communication) requirements. 2. New signal processing hardware needed. 3. Requires complete infrastructure revamp. 4. Users also need to upgrade their devices.
Extension of 5G multi-numerology OFDM	1. Provides backward compatibility (for the existing numerologies). 2. The major issues of OFDM are well-investigated. 3. MIMO compatibility. 4. Low complexity. 5. Standardization would be relatively concentrated and straightforward.	1. The current numerology options are insufficient. 2. Addition of more numerologies would compound the INI problem. 3. The symbol alignment and synchronization issues limit the numerology options. 4. OFDM might not be best suited for some scenarios (mostly frequency-flat channels in NTNs) and higher frequency bands (THz).
Coexistence of different waveforms	1. Possible to choose the best option depending on the application and user requirements. 2. Can provide backward compatibility.	1. Since waveforms can be fundamentally different, guards would be needed to avoid interference. 2. Additional hardware would be required to support the other waveforms.
Proposed unified and modular framework	1. Provides backward compatibility. 2. Scalable to encompass more waveform options in future. 3. Exploits the relationships between different waveforms.	1. Standardization efforts would be complicated since they need to determine the different waveform options. 2. Overhead can be an issue if the number of options is large. 3. Resource allocation and multiple accessing would be challenging considering the different logical domains.

CHAPTER 2

2. BACKGROUND: WIRELESS CHANNEL & WAVEFORM DESIGN

2.1. Wireless Channel

Wireless communication has become an integral part of modern society, enabling seamless connectivity and data exchange across various devices and applications. To effectively analyze and understand wireless communication systems, it is crucial to employ suitable signal representations that capture the time, frequency, and spatial characteristics of the transmitted signals. In this section, we discuss three commonly used signal representations: Time-Delay Representation, Time-Frequency Representation, and Delay-Doppler Representation.

2.1.1. Time-delay representation

The Time-Delay Representation provides valuable insights into the temporal characteristics of wireless signals. It represents a received signal as a function of time delays, indicating the relative timing of the signal components. This representation is particularly useful for analyzing signals in multipath environments, where different signal paths experience various propagation delays due to reflections, diffractions, and scattering. By examining the time-delay profile of a received signal, it is possible to identify individual signal components and estimate the multipath channel impulse response.

Assume that a signal $s(t)$ is transmitted over an linear time varaint (LTV) channel. Then, with the noiseless assumption, the received signal $r(t)$ can be modelled by [16]

$$r(t) = \sum_{p=1}^{P} h_p s\left(t - \tau_p\right) e^{j2\pi\nu_p t}. \tag{2.1}$$

Equation **(2.1)** provides an interpretation of signal transmission over a wireless channel

involving P individual scatterers, each characterized by unique physical properties such as reflectivity (fading coefficient), time delay, and Doppler frequency. By examining (**2.1**), it becomes evident that the time-domain (TD) channel response of a LTV channel can be effectively represented by [16]

$$h_{\mathrm{TD}}(t,\tau) = \sum_{p=1}^{P} h_p e^{j2\pi\nu_p t}\delta\left(\tau-\tau_p\right), \tag{2.2}$$

and the input-output relationship between $s(t)$ and $r(t)$ is given by

$$r(t) = \int_{-\infty}^{\infty} s(t-\tau)h_{\mathrm{TD}}(t,\tau)\mathrm{d}\tau. \tag{2.3}$$

By examining (**2.2**), it becomes apparent that the TD channel representation exhibits a maximum of P separable responses along the delay domain. However, it encompasses responses for all time domain components in relation to the Doppler frequency.

2.1.2. Time-frequency representation

The Time-Frequency Representation allows the simultaneous analysis of the time and frequency domains of a signal. It provides a two-dimensional representation that reveals how the signal's spectral content evolves over time. Widely used time-frequency representations include the Short-Time Fourier Transform (STFT), Wigner-Ville Distribution (WVD), and Continuous Wavelet Transform (CWT). These representations are essential for analyzing signals with time-varying spectral characteristics, such as those encountered in frequency-selective fading channels and non-stationary communication scenarios. By employing time-frequency analysis, it is possible to identify signal components, detect modulation schemes, and mitigate interference effects.

The time-frequency (TF) domain channel can be obtained by performing the Fourier transform along the delay domain to (**2.2**), i.e.,

$$h_{\mathrm{TF}}(t,f) = \int_{-\infty}^{\infty} h_{\mathrm{TD}}(t,\tau)e^{-j2\pi f\tau}\mathrm{d}\tau = \sum_{p=1}^{P} h_p e^{j2\pi\nu_p t}e^{-j2\pi\tau_p f}. \tag{2.4}$$

The TF domain channel representation is widely recognized as the primary channel description in wireless communications, primarily due to the success of OFDM. In the upcoming chapter, we will delve into the fundamentals of OFDM and explore its connections with OTFS.

2.1.3. Delay-Doppler representation

The Delay-Doppler Representation combines the concepts of time delay and Doppler frequency shift to capture the joint time-frequency characteristics of wireless signals. It is particularly relevant for analyzing signals in radar systems, where both the time delay (related to target range) and Doppler frequency shift (related to target velocity) provide valuable information about the targets being detected. The Delay-Doppler Representation allows the identification of moving targets, estimation of target range and velocity, and clutter mitigation in radar applications. This representation plays a crucial role in radar signal processing and target detection algorithms.

The delay-Doppler (DD) domain channel response can be obtained by performing the Fourier transform along the time domain to (**2.2**), i.e.,

$$h_{\mathrm{DD}}(\tau,\nu)=\int_{-\infty}^{\infty}h_{\mathrm{TD}}(t,\tau)e^{-j2\pi t\nu}\mathrm{d}t=\sum_{p=1}^{P}h_p\delta\left(\tau-\tau_p\right)\delta\left(\nu-\nu_p\right). \tag{2.5}$$

Equivalently, the DD domain channel response can also be obtained via the so-called symplectic finite Fourier transform (SFFT) to the TF domain channel (**2.4**) [17], i.e.,

$$h_{\mathrm{DD}}(\tau,\nu)=\int_{-\infty}^{\infty}\int_{-\infty}^{\infty}h_{\mathrm{TF}}(t,f)e^{-j2\pi t\nu}e^{j2\pi f\tau}\mathrm{d}t\,\mathrm{d}f=\sum_{p=1}^{P}h_p\delta\left(\tau-\tau_p\right)\delta\left(\nu-\nu_p\right). \tag{2.6}$$

The SFFT is an important technique in wireless communication, which combines a Fourier transform in the time domain with an inverse Fourier transform in the frequency domain [17]. This transformation, as indicated by (**2.6**), leads to a transition from dense channel responses in the TF domain to sparse channel responses in the DD domain. In the DD domain, responses associated with different signal paths are separable, indicating the absence of interference between them. Additionally, the DD domain channel response is compact due to the constraints of maximum delay and Doppler, limiting the responses to a defined region within the time delay and Doppler frequency ranges.

2.1.4. Wireless channel and waveform design

The design of the waveform in wireless communication is crucial to effectively combat the impairments introduced by the wireless propagation channel, such as fading, noise, interference, and the Doppler effect. It is no longer limited to equalizing the channel at the

receiver side; there is a growing need to fulfill new requirements and perform additional tasks, which can all be achieved through the waveform design.

The influence of the wireless channel on the optimal waveform selection can be seen in various scenarios:

2.1.4.1. Channel estimation

The distribution of pilots within the waveform and the method of channel estimation are directly related to achieving reliable and simplified channel estimation.

2.1.4.2. Channel representation (sparsity)

In certain cases, the channel needs to be estimated with minimal parameters, requiring a sparse representation. Conversely, a more spread representation may be necessary to mitigate the effects of fractional shifts in time or frequency.

2.1.4.3. Sensing

Future technologies aim to radio map the surrounding environment, necessitating the selection of a waveform that interacts with physical targets to extract relevant information.

2.1.4.4. Low-complexity sensing

The bandwidth and time duration of the frame impact the extraction of sensing information from the received signal, while the complexity of signal processing is influenced by the chosen waveform at the transmitter.

2.1.4.5. Channel equalization complexity

When channel effects result in data interference, equalization complexity depends on the effective channel impact on the waveform, assuming perfect channel estimation.

2.1.4.6. Interference

In the presence of narrow-band or narrow-time interference, waveforms that are spread in both time and frequency are preferred due to their robustness against this type of interference.

2.1.4.7. High mobility

High mobility introduces Doppler spread, which can lead to inter-carrier interference (ICI). Waveforms with wider bandwidths are preferred in such scenarios, as they are more resilient to the Doppler effect, which diminishes with increasing bandwidth.

2.2. What Is A Waveform?

A waveform or physical (PHY) design dictates how a wireless signal is transmitted over the physical resources, i.e., time and frequency. This encompasses design questions such as *what*, *where*, *how*, and *in what way* to transmit. Technically, a waveform defines the structure of the lattice where the data/symbols are placed, the pulse shape used to represent the data at these points, and the multiple accessing that allows resource sharing among different users. Mathematically, it is represented as

$$s(t) = \sum_{n \in N} \sum_{m \in M} \underbrace{\mathcal{T}\{\mathrm{X}(M_1, M_2, \ldots, M_D)\}(n,m)}_{\text{What?}} \overbrace{g_{tx}}^{\text{How?}} \underbrace{(t - \mu_t nT)\, e^{j2\pi \overbrace{\mu_f}^{\text{What way?}} \Delta f nm}}_{\text{Where?}}. \quad \textbf{(2.7)}$$

Figure 2.1 depicts of the relationship between the waveform and the TF lattice. Note that the space dimension can be added to the waveform equation; however, since TF and space are independent, the space dimension is ignored in **(2.7)**.

2.2.1. What to transmit?

The data bits are modulated over complex symbols $\mathrm{x} \in \mathbb{C}$, these symbols are obtained using different modulation techniques such as: M-QAM and M-PSK, which eventually would impact the transmitted signal.

2.2.2. Where to transmit

The complex data symbols are then mapped into a D hyper-dimensional space $\mathrm{X} \in \mathbb{C}^{M_1 \times M_2 \times \cdots \times M_D}$ where $N = M_1 \times M_2 \times \cdots \times M_D$. This hyperspace is logical domain that should not necessarily have a physical meaning. Examples: delay, Doppler, code, time, frequency. To transmit the data, these are transformed to real physical resources i.e.,

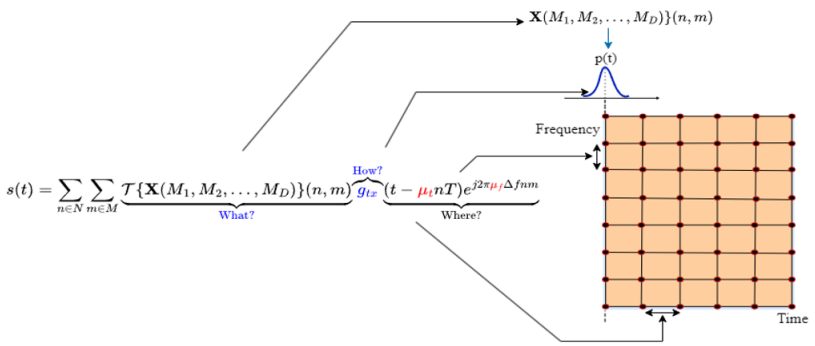


Figure 2.1: Illustration of the relationship between the waveform and the TF lattice.

time and frequency via the transform $\mathcal{T}\{\mathrm{X}(M_1, M_2, \ldots, M_D)\}$.

2.2.3. How to transmit?

The how to transmit defines each complex coefficient of the domain using pulse shaping filters $g_{tx}(t)$. The shape of these filters plays a vital role in determining the spread of energy over the time and frequency domains, which ultimately affects the signal characteristics.

2.2.4. In what way to transmit?

The way of transmission is denoted by the distribution of the vertices in the time-frequency axes. For instance, they can be perpendicular and equispaced, perpendicular and non-uniformly spaced, non-perpendicular and equispaced, and non-perpendicular and non-uniformly spaced.

2.3. 4G PHY Framework

2.3.1. Orthogonal frequency division multiplexing (OFDM)

OFDM is a widely used modulation technique in wireless communications. It is particularly advantageous in scenarios with frequency-selective channels, where different frequency components of a transmitted signal experience varying levels of attenuation and delay. In OFDM, the information to be transmitted is divided into multiple parallel substreams, each of which is modulated onto a separate subcarrier. These subcarriers are carefully chosen to be orthogonal to each other, meaning that they do not interfere with

4G adopted rectangular pulse shape with fixed subcarrier spacing.	
What to transmit?	Symbols/Data
How to transmit?	Rectangular pulses
Where to transmit?	Frequency domain
In what way?	Perpendicular uniform (orthogonal) lattice.

Table 2.1: OFDM from a waveform perspective.

one another. This orthogonality allows for efficient frequency utilization and simplifies the equalization process at the receiver.

Mathematically, let's consider an OFDM system with N subcarriers. The transmitted signal can be represented as a sum of modulated subcarriers:

$$s_{4G}(n) = \sum_{m=-\infty}^{+\infty} \sum_{k=0}^{N-1} X(m,k)\text{rect}(t - mT) \cdot e^{j2\pi k\Delta f t}, \tag{2.8}$$

where $X(m,k)$ represents the modulated symbol on the k-th subcarrier and m-th time slot, Δf is the subcarrier spacing, and rect(t) is the rectangular pulse shape. **Table 2.1** describes OFDM from a waveform perspective.

2.4. 5G PHY Framework

2.4.1. 5G candidate waveforms

One proposal for 5G involved utilizing alternative waveforms such as Filter Bank Multicarrier (FBMC). However, this introduced additional complexity due to the filtering required for these pulse shapes. Moreover, the advantages associated with using FFTs were no longer applicable. As a result, all candidates that attempted to modify the rectangular pulse shaping faced challenges. **Table 2.2** provides a description of the various 5G candidates from a waveform perspective. Mathematically, let's consider a 5G waveform system; the transmitted signal can be represented as:

$$s_{\text{5G candidate}}(n) = \sum_{m=-\infty}^{+\infty} \sum_{k=0}^{N-1} X(m,k) g_{\text{tx}}(t - mT) \cdot e^{j2\pi k\Delta f t}, \tag{2.9}$$

where $g_{\text{tx}}(t)$ is the pulse shape such as Gaussian or RRC.

5G candidate waveforms attempted to alter the rectangular pulse shape.	
What to transmit?	Symbols/Data
How to transmit?	Gaussian, RRC,...
Where to transmit?	Frequency domain
In what way?	Perpendicular uniform lattice.

Table 2.2: 5G candidate waveforms from a waveform perspective.

2.4.2. Multi-numerology OFDM

As a result of the challenges faced by the 5G candidate waveforms, the decision was made to adopt OFDM with multiple numerologies, which introduced a non-uniform lattice structure. It is important to highlight that while the non-uniform structure increased the flexibility of OFDM, it also led to the emergence of non-orthogonal characteristics and inter-numerology interference. Consequently, it is fair to say that the 5G generation cannot be considered highly successful due to these limitations. **Table 2.3** provides a description of the multi-numerology OFDM from a waveform perspective. Mathematically, let's consider a multi-numerology OFDM system with N subcarriers. The transmitted signal can be represented as a sum of modulated subcarriers:

$$s_{5G}(n) = \sum_{m=-\infty}^{+\infty} \sum_{k=0}^{N-1} X(m,k)\text{rect}(t - mT) \cdot e^{j2\pi k\mu\Delta f t}, \tag{2.10}$$

where μ represents the numerology and determines the subcarrier spacing.

5G adopted rectangular pulse shape with adaptive subcarrier spacing.	
What to transmit?	Symbols/Data
How to transmit?	Rectangular pulses
Where to transmit?	Frequency domain
In what way?	Perpendicular non-uniform lattice.

Table 2.3: Multi-numerology OFDM from a waveform perspective.

Figure 2.2 illustrates the primary distinction between Long-Term Evolution (LTE) and 5G in terms of waveform characteristics. LTE employed a uniform lattice with the same pulse shape, namely, OFDM.

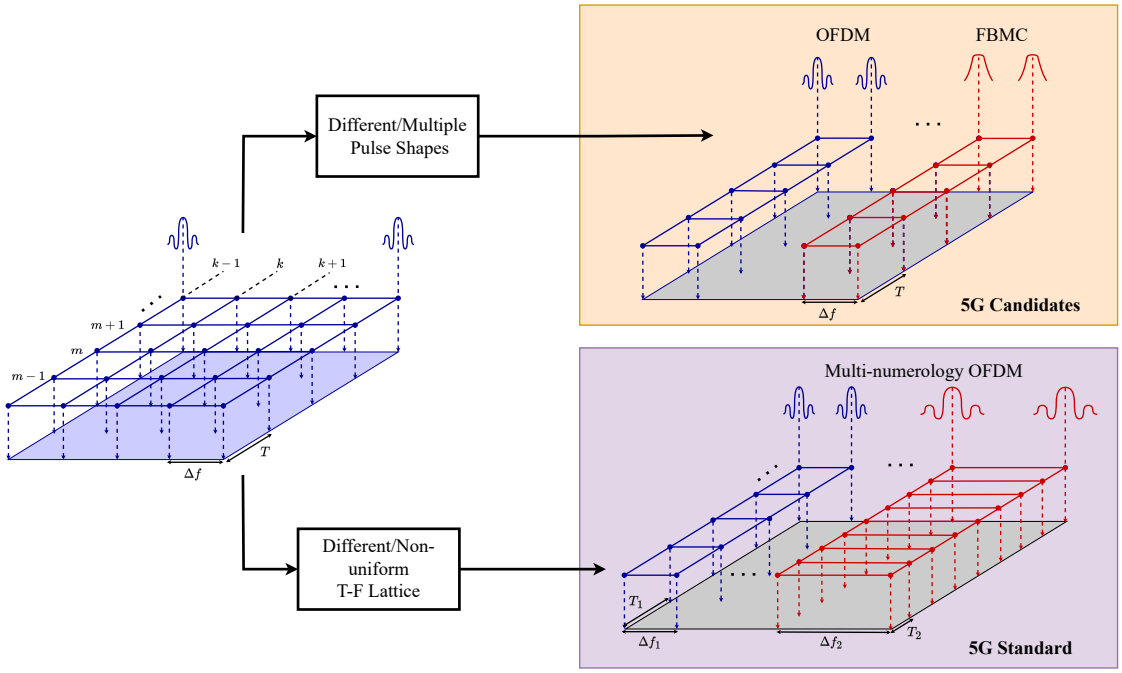


Figure 2.2: Illustration of the 4G and 5G approaches to PHY design. 4G used a uniform lattice with a single orthogonal frequency division multiplexing (OFDM) pulse. 5G candidates included multiple pulse shapes such as FBMC and multiple numerologies, i.e, non-uniform TF lattice.

2.5. 6G Waveform Candidates

In the pursuit of advanced waveforms for 6G wireless communication systems, several candidates have emerged. orthogonal time-frequency space (OTFS) presents a novel approach by operating in a joint time-frequency domain, offering enhanced performance in dynamic channels, improved spectral efficiency, and increased interference resilience. Frequency modulated continuous wave (FMCW) waveform, known for its application in radar systems, has gained attention due to its potential for high-resolution range and velocity measurements, as well as its capability to support simultaneous communication and sensing functionalities. orthogonal chirp division multiplexing (OCDM) combines the benefits of OFDM and chirp signals, offering improved spectral efficiency and robustness against multipath fading. These waveform candidates hold significant promise for the future of 6G networks, addressing the evolving demands of higher data rates, ultra-low latency, massive connectivity, and diverse applications.

2.5.1. Orthogonal time-frequency space (OTFS)

Consider a wireless communication system where $M \times N$ data symbols are modulated using OTFS over a total bandwidth B operating at the carrier frequency f_c. Firstly, the OTFS modulator distributes these symbols $\{X_{\mathrm{DD}}(k,l),\ k = 0,\ldots,N-1,\ l = 0,\ldots,M-1\}$ in the two-dimensional delay-Doppler grid. Then, the samples $X_{\mathrm{DD}}(k,l)$ are converted to the time–frequency domain grid $\{X_{\mathrm{TF}}(n,m),\ n = 0,\ldots,N-1,\ m = 0,\ldots,M-1\}$ using the inverse symplectic finite Fourier transform (ISFFT) as follows [18]

$$X_{\mathrm{TF}}(n,m) = \frac{1}{\sqrt{MN}} \sum_{l=0}^{M-1} \sum_{k=0}^{N-1} X_{\mathrm{DD}}(k,l) e^{j2\pi\left(\frac{nk}{N} - \frac{ml}{M}\right)}. \tag{2.11}$$

The time-frequency signal $\mathrm{X_{TF}}$ in **(2.11)** needs to be converted to time domain before transmission. For this purpose, practical OFDM systems which are based on the inverse discrete Fourier transform (IDFT) are used. Hence, the discrete output of an OFDM modulator is

$$x(m+nM) = \frac{1}{\sqrt{M}} \sum_{m=0}^{M-1} X_{\mathrm{TF}}(n,m) e^{j2\pi\frac{m}{M}n}. \tag{2.12}$$

Note that the total length of the discrete sequences representing the frame is $M \times N$. Substituting **(2.11)** in **(2.12)** and using $(1/M)\sum_{m=0}^{M-1} e^{j2\pi m/M(l-l')} = \delta(l-l')$, we obtain

$$x(l+nM) = \frac{1}{\sqrt{N}} \sum_{k=0}^{N-1} X_{\mathrm{DD}}(k,l) e^{j2\pi\frac{k}{N}n}. \tag{2.13}$$

2.5.2. Frequency modulated continuous wave (FMCW)

Consider a linear FMCW signal, $x_c(t)$, sweeping linearly across B bandwidth during the time interval T. The time-domain representation of $x_c(t)$ is given by [19]

$$x_c(t) = e^{j\pi\eta t^2} e^{j2\pi f_c t}, \quad 0 \le t < T, \tag{2.14}$$

where $\eta = B/T$ is the chirp rate, T is the chirp time duration, B is the chirp bandwidth, and BT is the time-bandwidth product, and $\eta,\ T$, and $B \in \mathbb{R}$. Sampling **(2.14)** at times $t = p\frac{T}{K},\ 0 \le p < K$, produces the discrete chirp

$$x_c(p) = e^{j\pi\frac{\eta p^2 T^2}{K^2}} e^{j2\pi\frac{f_c p T}{K}}, \quad 0 \le p < K. \tag{2.15}$$

2.5.3. Orthogonal chirp division multiplexing (OCDM)

Supposing that there are K chirp waveforms, these chirps can be obtained from the kernel of Fresnel transform which is given by [20]

$$\varphi_{\omega}(t) = e^{-j\frac{\pi}{4}} e^{j\frac{\pi}{\omega}t^2}, \tag{2.16}$$

where $\omega = T^2/K$. By substituting ω in **(2.16)**, the 'root' chirp is given as

$$\begin{aligned} \psi_0(t) &= \Pi_T(t)\varphi^*_{\omega}(t)\big|_{\omega=\frac{T^2}{K}} \\ &= e^{j\frac{\pi}{4}} e^{-j\pi\frac{N}{T^2}t^2}, \quad 0 \le t < T, \end{aligned} \tag{2.17}$$

where $\Pi_T(t)$ is the rectangular function expressed as

$$\Pi_T(t) = \begin{cases} 1 & 0 \le t < T \\ 0 & \text{otherwise} \end{cases}. \tag{2.18}$$

It is possible to get a set of K orthogonal chirp (OC)s using the root chirp in **(2.17)**, the i-th, $i = 0, 1, \ldots, K-1$, OC is given as

$$\begin{aligned} \psi_i(t) &= \Pi_T(t)\varphi^*_{\frac{T^2}{K}}(t - i(T/K)) \\ &= e^{j\frac{\pi}{4}} e^{-j\pi\frac{K}{T^2}\left(t - i\frac{T}{K}\right)^2}, 0 \le t < T. \end{aligned} \tag{2.19}$$

Note that the chirp waveforms $\psi_i(t)$ in **(2.19)** are mutually orthogonal, i.e.,

$$\begin{aligned} \int \psi^*_m(t)\psi_i(t)dt &= \int_0^T e^{j\pi\frac{N}{T^2}\left(t - m\frac{T}{N}\right)^2} e^{-j\pi\frac{N}{T^2}\left(t - i\frac{T}{N}\right)^2} \\ &= \delta(m-i). \end{aligned} \tag{2.20}$$

Sampling **(4.243)** at times $t = p\frac{T}{K}$, gives the i-th discrete OC

$$\psi_i(p) = e^{j\frac{\pi}{4}} e^{-j\pi\frac{(p-i)^2}{K}}, 0 \le p < K. \tag{2.21}$$

2.6. 6G PHY Framework

The remainder of this section aims to answer the question above by providing a generalized, modular, backward-compatible, and forward-looking PHY framework for sixth generation (6G) networks. From **Section 2.5**, it is noted that 6G candidate waveforms focuses on changing the "*where to transmit*" part as shown in **Table 2.4**.

As illustrated in **Figure 2.3**, this framework is divided into three major segments: the

6G candidate waveforms focuses on changing the “where to transmit” part.	
What to transmit?	Symbols/Data
How to transmit?	Rectangular pulses
Where to transmit?	delay, Doppler, code, chirp, ...
In what way?	Perpendicular uniform/non-uniform lattice.

Table 2.4: 6G candidates from a waveform perspective.

logical (data) lattice, defining what to transmit; the PHY resource grid, specifying where to transmit; and the transmission domain, determining how to transmit. **Figure 2.3** also demonstrates that the primary difference between the candidate waveforms lies in the design and population of the data lattice. Moreover, the decoupling of the data lattice and resource grid grants an additional degree of freedom in using whichever lattice (with certain rules) is suitable for a given instance. The following text describes each of the segments and their constituent slices, accompanied by selected examples.

2.6.1. Data/Logical lattice

The data lattice is a mathematical construct that enables data symbols to be distributed and transmitted in a multidimensional space. Beyond time and frequency dimensions, the data lattice can use a range of logical dimensions to distribute the data symbols in their raw form, such as quadrature amplitude modulation (QAM) or phase-shift keying (PSK). These dimensions can include delay, Doppler, code, user, angle, or any other logical domains that can improve the system’s performance. The flexibility and versatility of the dimensions used in the data lattice allows systems to serve different goals, such as combating delay and Doppler spread, secure communications, sensing the environment, sparse channel representation, and more. For example, using the delay and Doppler dimensions, wireless communication systems can combat the effects of doubly selective channels. Secure communication systems can use dimensions that are difficult to jam, eavesdrop, or intercept, such as code domain. In sensing, using physical parameters like range, velocity, and location as data lattice dimensions can be useful. Channel characterization can select lattice dimensions to provide the sparsest wireless channel representation, reducing channel estimation and equalization complexity. The data lattice is composed of two main slices, i.e., reshaping and precoding/spreading.

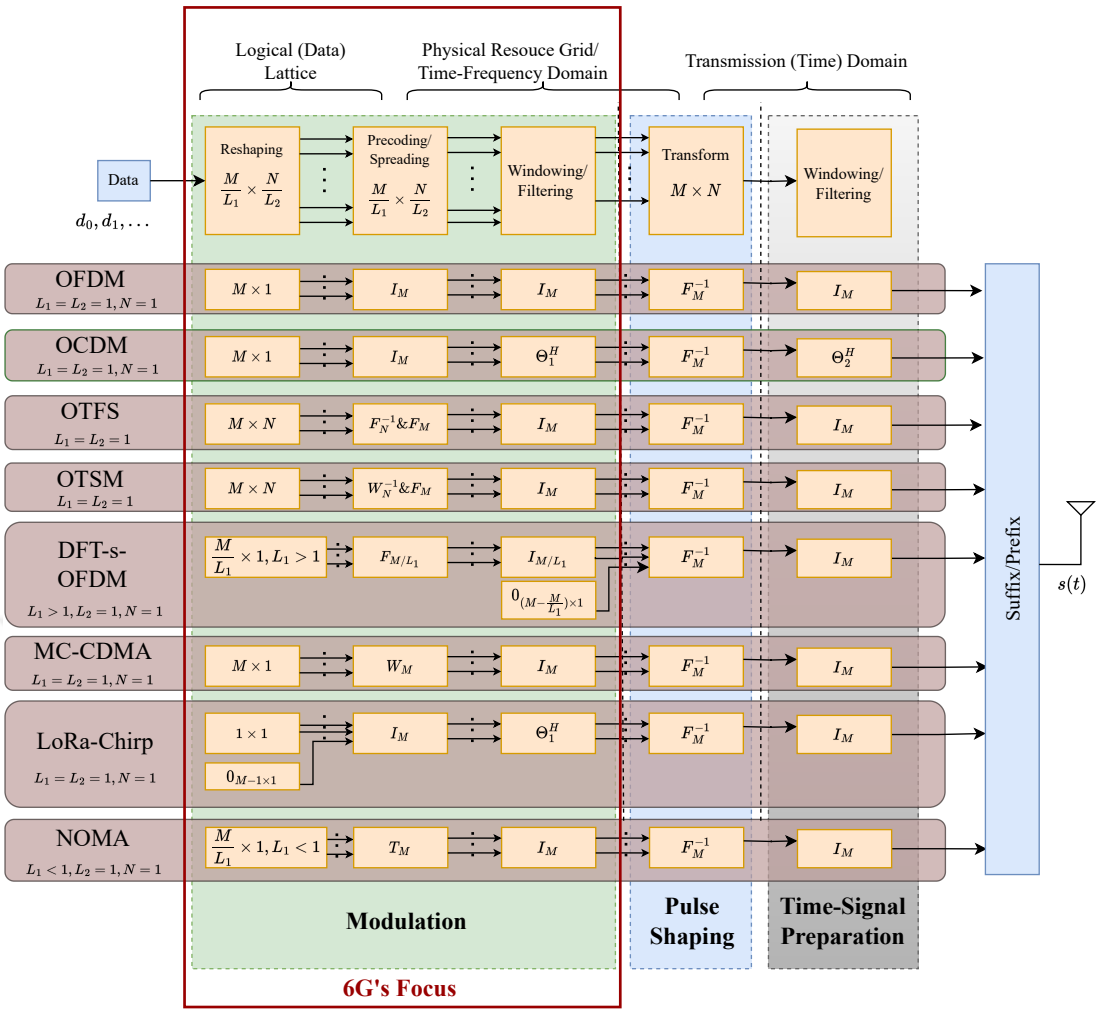


Figure 2.3: PHY slices for different waveforms discussed in 6G.

2.6.1.1. Reshaping slice

The *reshaping* slice determines the number of data dimensions used, mapping symbols from a one-dimensional input stream into a multidimensional logical lattice by assigning each data symbol to a specific lattice point. Logical lattice dimensions are chosen for optimal transmission and reception. Reshaping parameters also determine the mapping type: one-to-one, one-to-many (orthogonal), or many-to-one (non-orthogonal). For example, OTFS maps MN data symbols to MN TF points, while discrete Fourier transform-spread-OFDM (DFT-s-OFDM) maps M/L_1, (where $L_1 > 1$) data symbols to M TF points. On the contrary, in code domain non-orthogonal multiple access (NOMA), M/L_1, (where $L_1 < 1$) data symbols map to M resources. These parameters significantly shape the intended transmitted waveform.

2.6.1.2. Precoding/Spreading slice

Data symbols mapped onto the multidimensional logical lattice must be converted to the PHY resources represented by the two-dimensional TF grid. The *precoding/spreading* slice achieves this, transforming and/or combining data localized at different lattice points, resulting in a signal spread across time, frequency, or both.

The choice of spreading technique depends on system requirements. fast Fourier transform (FFT) spreading is commonly used to combat the effects of dispersion. For instance, in OTFS systems, the two-dimensional FFT spreads the data symbols over the whole TF grid to combat doubly dispersive channel by providing diversity [21]. This can also help mitigate the effects of narrowband interference or jamming as in code division multiple access (CDMA) systems, where the Walsh-Hadamard transform spreads the data symbols over a wider frequency band using codes to distinguish between different users. Spreading the signal over the TF grid is also beneficial for sensing applications where fine range-velocity resolution is needed.

2.6.2. Physical resource grid (TF Domain)

The resources of a system are represented by PHY quantities such as time and frequency. The TF domain is characterized by three primary parameters: 1) the minimum spacing in frequency, Δf, which determines the symbols duration $T = \frac{1}{\Delta f}$, 2) the minimum sampling rate, T_s, which determines the total bandwidth according to $B = \frac{1}{T_s}$, and 3) the maximum time duration of the frame $T_{\text{frame}} = NT$ containing N symbols being transmitted with the minimum frequency spacing. Note that the resolution of the data lattice varies depending on the PHY resources used. For instance, a finer Doppler resolution in OTFS requires larger transmission duration of the signal, T_{frame}. While LTE and fifth generation (5G) have generally provided orthogonal distribution of TF resources, it is possible to have multiple data lattices or different users over the same lattice occupying overlapping TF resources (more on this in the next section).

After precoding, spreading, and reducing the multi-dimensional data block to two-dimensional TF signal, windowing/filtering alters the temporal and spectral characteristics of this signal as follows:

2.6.2.1. Windowing slice

Windowing is a critical signal processing technique, determining the TF mask of the signal. It involves multiplying the signal by a window function, leading to signal scaling or rotation, selected based on specific applications or requirements. For instance, in the TF domain, windowing has demonstrated an ability to increase the sparsity of delay-Doppler channels in OTFS systems, thereby reducing the error floor for channel estimation [22]. Moreover, windowing with rotation can be employed before transmission to rotate the TF representation of the signal, as seen in OCDM or chirp systems. Here, the TF signal undergoes a $\pi/4$ phase shift, giving it the characteristic sloped TF representation.

Before transmission, the TF domain signal requires conversion into its one-dimensional time domain equivalent. The sample locations in the TF domain define the filter coordinates, determining where and when the signal is transmitted. This conversion is facilitated by a T-F2T transform block.

2.6.2.2. T-F2T transform

The T-F2T transform defines each complex coefficient of the domain using pulse shaping filters. The filter shapes crucially determine energy spread over time and frequency domains[1]. Consequently, the pulse shaping filters used at the transmitter and receiver jointly determine transferred power and the correlation between the points in the lattice. A well-localized pulse in time or frequency increases selectivity, while a wider one is more susceptible to interference. Balancing spectral efficiency and signal quality often involves choosing a pulse shape well-localized in both time and frequency. Common examples include Gaussian and rectangular pulse shapes.

2.6.3. Transmission/Time domain

To counteract channel effects and prevent leakage between adjacent channels due to imperfect pulse shaping, the time domain signal undergoes the following processes:

[1]The sequence of the windowing and suffix/prefix blocks depends on the modulation. For instance, OCDM performs windowing before adding the prefix/suffix while it is the opposite for OFDM.

2.6.3.1. Prefix/Suffix addition

Signals often experience multipath propagation. The use of prefix/suffix allows one to combat the challenges posed by multipath-induced frequency-selective fading, and inter-symbol interference (ISI), leading to improved data transmission reliability and robustness in wireless communication. Additionally, this simplifies the process of channel equalization at the receiver.

2.6.3.2. Windowing/Filtering

Before transmission, the time domain signal undergoes windowing operation to reduce the spectral leakage and manage interference, ultimately improving demodulation performance. A notable example is the use of (root) raised cosine filters in OFDM systems. This window helps mitigate ISI and minimize out-of-band emission (OOBE), ensuring reliable communication. It is important to note that the window does not need to be uniform throughout the grid. Rather, adaptive windowing can be leveraged to improve system's performance.

2.7. Key Takeaways

Considering the discussed PHY layer framework, several conclusions emerge:

- The potential waveform candidates for 6G, such as OTFS, OCDM, chirp, and DFT-s-OFDM, mainly differ in their modulation or time-signal processing, while the pulse shape is chosen independently. This enables the generation of various waveform variants, such as using different pulse shapes for OTFS, including rectangular, Gaussian, raised cosine, or root raised cosine.
- In 5G, the different candidate waveforms focused on changing the pulse shape itself, i.e, using different pulses instead of the rectangular one used in LTE. However, altering the pulse shape introduces additional implementation and computational complexity, and destroys backward compatibility with legacy devices.
- Rectangular pulse shapes, such as those used in OFDM, are highly convenient to implement because they are based on FFT/IFFT transforms. Moreover, they have

been extensively studied and proven to work well up to a certain extent. Therefore, switching entirely to a new waveform may be costly and inefficient.

Based on these observations, the use of the same general waveform framework is proposed, as depicted in **Figure 2.3**, where "rectangular pulse" shaping is adopted at the transform slice. This can be represented by rewriting **(2.7)** as

$$s(t) = \sum_{n \in N} \sum_{m \in M} \underbrace{f(X_{n,m})}_{\text{Precoding}} \overbrace{\text{rect}\left(\frac{t - nT}{T}\right)}^{\text{Uniform Pulse Shaping}} e^{j2\pi\Delta f nm}, \qquad \textbf{(2.22)}$$

where the time domain signal may go under additional windowing operation.

CHAPTER 3

3. THEORETICAL PART: LITERATURE REVIEW

3.1. Securing OFDM Signaling Via Physical Layer Security (PLS)

Due to the wireless channel decorrelation property, the attacker cannot decode the data even if it knows the algorithm and tries to apply it based on its channel. However, the work in [23] claimed that under certain assumptions the attacker can acquire the channel state information (CSI) between the legitimate nodes, which puts channel-based physical layer security (PLS) techniques at high risk of failure. For instance, the attacker can reverse engineer the beamforming matrix to acquire the CSI between legitimate nodes. The beamforming matrix can be estimated under the assumption that the attacker possesses the CSI between the legitimate transmitter and itself, and that it is equipped with the same number of antennas as that of a legitimate transmitter. After estimating CSI corresponding to legitimate nodes, it can compromise channel-dependent PLS techniques like artificial noise (AN) as well as key generation-based techniques [24]. The security can still be ensured in such cases by enforcing poor channel estimation quality at the attacker for the CSI between the legitimate transmitter and the attacker, which motivates the need for pilot security. Securing the pilots protects the propagation environment properties from being extracted at the attacker side. Additionally, pilot security plays a critical role in physical layer authentication techniques.

From the pilot security perspective, few techniques are proposed in the literature. In [5], the phases of pilots subcarriers are rotated based on the previously estimated CSI. However, the channel is assumed to be known at both communicating nodes before the start of the algorithm. Moreover, the phase is manipulated for a single value which makes it easy to attack such a technique. In [25], [26], the security of downlink pilots is provided based on CSI at the transmitter via uplink training. Particularly, AN is added in the null

space of the channel to degrade the channel estimation capability at the attacker, though it may increase the peak to average power ratio (PAPR) of the signal. On top of that, power allocation between pilot and noise signal needs to be done intelligently in order to enhance security performance. Similarly, in [6], anti-eavesdropping pilots are designed such that the channel can be estimated at legitimate nodes only. However, the proposed algorithm requires full-duplex communication. In [27], the legitimate parties employ secret pilots for channel estimation. In the first step, the first node transmits the secret pilot to another node. Afterwards, the receiving node sends the received signal to the transmitting node using amplify and forward strategy. The second node follows the same procedure as that of the first node. This approach requires extra overhead to share feedback. Although authors in [4] exploit the uniqueness of channel responses between different nodes in order to degrade the channel estimation at the attacker node and showed the effect in terms of bit error rate (BER), they did not consider the sign ambiguity issue when taking the square root of the channel, which in the practical case leads to huge BER due to the erroneous channel estimation.

In order to address the above-mentioned challenges, we propose novel schemes that can provide security for data, pilots, or joint data and pilots. The design of the proposed schemes is based on the all-pass and minimum-phase decomposition of the channel and exploiting the property of the decomposed components to provide security. The proposed schemes are the first work that enables flexible adaptive security based on security needs. Specifically, the security of data, pilot, or both can be adaptively selected based on the security requirements of the applications. Additionally, the proposed novel security scheme is robust against spatially correlated eavesdroppers located near legitimate nodes. The main contributions of the proposed work are as follows:

- We propose two novel minimum-phase all-pass channel decomposition-based PLS schemes for multiple-input multiple-output (MIMO)-OFDM system in rich scattering environments, where the first method secures the data and the latter secures the pilots. The proposed data security algorithm ensures strong security compared to conventional schemes without compromising on or degrading the communication performance of the legitimate user. On top of that, the proposed pilot security algorithm degrades the ability of the eavesdropper in estimating its channel; thus, protecting CSI, sensing, and radio environment mapping information.

- Our novel security methods, focusing on both data and pilot security, exploit the all-pass component of the channel which has unit power property. Therefore, we provide security without any power constraint, particularly PAPR. Whereas, the conventional PLS techniques such as AN, zero forcing, and channel shortening provide security at the cost of changing the power distribution of the transmitted signal. These changes create high power peaks in time (i.e., PAPR) and frequency (exceeding spectrum mask limits).

- The secrecy of the proposed data security algorithm is evaluated under correlated and uncorrelated eavesdropping channels via closed-form expressions for achievable BER. Whereas for pilot security, we analyzed the normalized mean square error (NMSE) performance of the estimated channel. The simulations agree with the analytical formulas emphasizing the effectiveness of the proposed algorithms.

3.2. Channel Estimation In CCP-OFDM Systems

Flexibility is one of the main features of next generation communication systems, where the parameters of the network are no longer fixed. For instance, The fifth-generation (5G) has introduced the numerology concept where the OFDM waveform is flexibly configured in time-frequency lattice to satisfy the varying requirements of the users [28]. To further enhance the multi-numerology systems for the ,sixth-generation (6G), a flexible and adaptive cyclic prefix (CP) was proposed in [29].

One configuration of the flexible CP waveforms is called common cyclic prefix-orthogonal frequency division multiplexing (CCP-OFDM) which is also known as multi-symbol encapsulated OFDM [30]. CCP-OFDM groups several OFDM symbols and uses one CP to protect them when the channel is slow time-variant [31], thus reducing the redundancy caused by the CP. CCP-OFDM waveform has been widely used as a solution to mitigate the inter-numerology interference (INI) in multi-numerology OFDM systems [32], where it provides perfect alignment of the symbols with different numerologies since they are encapsulated with one CP [33].

In CCP-OFDM systems, inter-symbol interference (ISI) between the OFDM symbols occurs due to the fact that one CP is added for the whole frame [34]. Due to this unique frame structure, channel estimation for CCP-OFDM is unlike the conventional OFDM systems,

where the channel frequency response (CFR) is estimated and tracked in the frequency domain using known symbols (pilots) multiplexed with the data. Hence, the conventional OFDM channel estimation process is not applicable to these systems. As a result, complex time-domain equalizers are used for CCP-OFDM. For instance, [35] proposes iterative ISI estimation and cancellation techniques for the CCP-OFDM system; however, this algorithm is computationally complex and achieves low performance compared to CP-OFDM. Some other studies [34], [36], [37] consider the maximum likelihood (ML) estimator, which is extremely computationally expensive compared to other estimators such as link-signature (LS) that is used in CP-OFDM.

In this section, a novel CCP-OFDM transceiver design is proposed, where two cascaded DFT processes are applied at the transmitter and the receiver sides. Unlike conventional CCP-OFDM schemes, the developed system enables channel estimation and equalization in the frequency domain allowing the use of low-complexity estimators such as LS estimator, while achieving the same performance as conventional CP-OFDM systems. The computational complexity is investigated for the proposed channel estimation algorithm. Besides, the superiority of the proposed design is emphasized throughout performance measures in terms of estimated channel NMSE and BER.

3.3. CP Configuration In OTFS Systems

OTFS modulation has been recently introduced to parameterize the effect of the time-varying channels for any waveform by representing the channel in delay-Doppler domain where the real objects/reflectors in the propagation environment are seen, and thus, for a relatively short time frame the channel can be considered invariant [17]. Similar to OFDM, OTFS exploits CP to combat the channel effects and ensure circularity. Therefore, based on the prefix type there are different ways of realizing OTFS systems. For instance, in reduced-CP (RCP)-OTFS systems, only one CP is added to the beginning of the OTFS frame with a duration larger than the channel's maximum delay spread [38]–[40]. On the other hand, in full-CP (FCP)-OTFS systems, a CP is inserted into each OTFS subsymbol [41], [42]. FCP-OTFS has the advantage of being able to guarantee that there will be no inter-carrier interference (ICI) as well as ISI between neighboring OTFS subsymbols,

but it necessitates a significantly increased signaling overhead [43]. In contrast to FCP-OTFS, The RCP technique does not ensure ISI-free transmission after removing the CP at the receiver side, making the receiver more complex. However, RCP-OTFS is taken into account for better utilization of the time-frequency resources [44].

Even though the CP configuration in FCP-OTFS systems is similar to the one in OFDM systems implementation-wise, it differs in terms of the information carried withing the prefix. The CPs in OFDM are added only for the sake of removing the channel effects and they contain meaningless information, which is the reason why they are discarded at the receiver [45]. On the other hand, as depicted in **Figure 4.7**, appending one CP before each OTFS subsymbol in time-domain is equivalent to repeating the data in delay-Doppler domain. Therefore, the CPs used in FCP-OTFS contain relevant information that needs to be extracted instead of being discarded as in OFDM system.

Motivated by the above problem, in this section, we propose a novel CP structure for OTFS signal, where a reduced-CP is appended to the FCP-OTFS frame. While the full-CP ensures no ISI between the OTFS subsymbols, the added reduced-CP guarantees that the CP block can be decodable as well instead of being discarded at the receiver side, unlike the CP block in OFDM signal. Based on the proposed FCP-OTFS structure, we present a simple combiner scheme that makes use of the CP block and its corresponding repeated data to enhance BER performance for reliable communication. Also, we introduce a spectrally efficient pilot allocation scheme for channel estimation.

3.4. Doubly-Dispersive Channel Estimation In OTFS Systems

OTFS modulation has been proposed as a robust waveform suitable for doubly-dispersive channels as in high mobility scenarios [46]. For any waveform, OTFS modulation parameterizes the effect of the time-varying channels by representing the channel in the delay-Doppler domain, where the reflectors distributed in the propagation environment correspond to the channel seen at the receiver, and thus, for a relatively short time frame the channel can be considered invariant [47].

One of the most critical challenges pertaining to the OTFS waveform is channel estimation, which is necessary to equalize the signal and demodulate the data. For instance,

impulse-based channel estimation is used in [41], [48] to estimate the OTFS MIMO channel. In particular, in [41] delay-Doppler impulses are adopted as pilots for channel estimation, while message passing algorithm is used for symbol detection. OTFS exhibits delay-Doppler-angle 3D sparsity in massive MIMO (mMIMO) systems, and accordingly, 3D structured orthogonal matching pursuit (3D-SOMP) based channel estimation technique is used with low pilot overhead. The authors in [48] used the expectation maximization-based variational Bayesian (EM-VB) method in order to obtain Doppler shift, delays, angles, and channel gains in the uplink channel. Then, reciprocity is exploited to estimate the downlink channel parameters at the base station. In order to increase the spectral efficiency, [49] used superimposed pilots with a data-aided channel estimation algorithm, where the guard band is not used anymore and the pilot-data interference is mitigated with iterative data detection. Moreover, compressed sensing-based delay-Doppler channel estimation is proposed for OTFS multiple access systems in [50]. In [51], a 2D structured turbo compressed sensing-based channel estimation method is proposed for the high mobility scenarios. Additionally, a sparse Bayesian learning-based channel estimation method is studied in [52] with a new pilot pattern without a guard. This new pattern converts the channel estimation problem into a sparse signal recovery problem.

These studies [41], [48]–[52], however, only consider integer delay-Doppler scenarios, which are impractical in real-world implementations where fractional delay and Doppler shifts are always present. Therefore, the authors in [53] proposed a low-complexity message-passing algorithm which mitigates the highest inter-Doppler interference (IDI) components for OTFS channel estimation. This work was followed by [54], where delay-Doppler embedded pilot symbols are adopted for channel estimation using the threshold method. Furthermore, in [55], Raviteja *et al.* arranged the pilot, guard, and data such that interference is avoided. Delay-Doppler domain embedded pilot-based time domain channel estimation method is proposed in [56] considering carrier frequency offset, residual frame timing offset, and fractional Doppler shifts, which are further used to construct channel estimation and equalization methods. Shi *et al.* investigated MIMO OTFS systems and proposed a modified sensing matrix-based channel estimation with a deterministic pilot design for a downlink CSI acquiring scheme [57]. In [58], the OTFS channel is estimated using pilots in the delay-Doppler domain with a cross-correlation-based algorithm. This method has lower computational complexity than the traditional channel

estimation methods with pseudo sequences. In [59], two superimposed pilot-aided channel estimation methods are proposed. The first method considers data as interference and estimates the channel. However, it degrades the signal-to-noise ratio (SNR). The second method reduces the degradation of SNR by exploiting the iterations between data detection and channel estimation. The authors in [60] adopted Bayesian learning, which formulates the problem as sparse signal recovery. Then, the channel gains along with the fractional Doppler shifts are estimated rather than estimating the delay-Doppler domain channel directly. The authors in [61] adopted sparse Bayesian learning for off-grid actual delay-Doppler domain channel response estimation rather than effective channel response, which is investigated in the literature. The OTFS channel estimation is formulated as sparse signal recovery where both delays and Doppler shifts are estimated separately; however, this suffers from high computational complexity, especially in the case of having doubly-spreading channels.

However, in these works [54]–[60], only fractional Doppler shifts were of concern, even though fractional delays occur with the same likelihood in OTFS systems as fractional Doppler shifts. Moreover, considering only wideband signals for OTFS system to provide sufficient delay resolution limits the potential of this waveform. OTFS should be flexible enough to freely tune the bandwidth ($M\Delta f$) and the time duration (NT) of the signal based on the application and user requirement instead of delay and Doppler resolution. Moreover, [61] suffer from high computational complexity which also limit the use of this method.

In this section, we propose a framework that can be adopted to estimate fractional Doppler and fractional delay channels using impulse-based channel estimation. The pilot, being an impulse, can be seen as a single OTFS subcarrier or pulsone (pulse-tone), which has two main properties: 1) it holds its shape under the operations of time delay and Doppler shift, as well as 2) being self-dual between time and frequency. Exploiting these two features, a low-complexity algorithm is proposed where we raise the received pilot pulsone to higher powers in both time and frequency domains to estimate fractional Doppler and delay shifts, respectively. By raising the received time-pulsone/frequency-pulsone to the α-power, we can tune the Doppler shifts or delay shifts until we find an option ($\alpha = \alpha_{\mathrm{opt}}$) that converts both fractional delay and Doppler shifts to integer ones. These fractional shifts are then calculated using α_{opt}.

The contributions of this section are summarized as follows:

- We propose a general channel estimation and equalization framework that can be applied to estimate and equalize both fractional delays and Doppler shifts. A complete wireless communication OTFS system model is considered, assuming the multi-tap channel to be doubly-dispersive in both time and frequency domains, including residual delays and Doppler shifts. This framework is based on the fact that an impulse-pilot is shape-invariant under the operations of time delay and Doppler shift, as well as being self-dual between time and frequency.

- The proposed method achieves fine-resolution estimation of the fractional delay and Doppler shifts. On top of that, We show that the proposed framework provides the flexibility to adapt the computational complexity according to the required delay and Doppler resolution. This makes it implementable in low-cost, limited-power devices such as internet of things (IoT) devices.

- Unlike the recent proposed methods, our solution achieves the lowest possible mean squared error among all unbiased methods where it achieves the Cramer-Rao lower bound (CRLB) performance. This means that the proposed estimator gives a lower estimate for the variance than an unbiased estimator; thus, it is *efficient estimator*.

- We derive the tensor form of the input-output relationship between the transmitted and received signals in the case of fractional delay channels by introducing the up-sampled channel matrix. Then, the minimum mean squared error (MMSE) detector is derived to equalize the effect of the fractional delay channel.

- Finally, the proposed method's practicality and efficiency are confirmed by testing and evaluating it in a real-time experiment using the Keysight Agilent Technologies EXA signal analyzer N9010A.

3.5. Integrated Sensing And Communication Via OTFS Signaling

Past decade has seen remarkable advancements in wireless communication technology, and the forthcoming 6G of wireless communication is anticipated to deliver much more than just rapid mobile internet connectivity. Among the visionary claims about 6G is the

notion that sensing will play an even more substantial role than in previous generations. This is due to the evolution of radio sensing and communication, which drives the development of new technologies, such as higher frequencies and MIMO systems, that can be supported by similar hardware architectures. This has spurred researchers to integrate these technologies into a new research theme known as integrated sensing and communication (ISAC).

Automotive radar is an important application area for ISAC systems, as autonomous vehicles rely on detecting objects, obstacles, and their respective positions and speeds in complex environments to enable safe and coherent self-driving [62]. Although various techniques have been proposed to sense the environment, including cameras, global positioning systems, laser-based sensors, and radar transceivers, radar has been found to be the most robust in diverse conditions [63]. In addition to environment sensing, automotive radars are expected to communicate with nearby communication systems such as vehicle-to-vehicle (V2V), vehicle-to-network (V2N), and vehicle-to-everything (V2X) [64]. Therefore, a ISAC system can be advantageous for autonomous vehicles, as it can exploit both sensing and communication while minimizing size and power consumption.

At the start of automotive radar, FMCW was selected as the proper modulation due to its analog downconversion of the chirp, which allows the sampling in large bandwidths using simple components [65]. In [66], a phase-coded FMCW system is proposed where a group-delay filter and a linear-frequency-modulated continuous waveform are used to mitigate interference. Being generated in the analog domain, FMCW suffers from a critical drawback where it is hard to distinguish between similar waveforms. To overcome this limitation and gain a high angle of arrival (AoA) resolution, an integration of MIMO and FMCW is a subject of investigation in [67] and [68]. Moreover, with the increasing number of autonomous vehicles, more interference is expected, leading to the need for complex interference mitigation for FMCW systems. Additionally, despite its main advantage of simple component use, FMCW cannot provide high-data-rate communication.

Another waveform that has gained attention for its potential use in automotive radar and ISAC applications is OFDM, as it is already utilized in the fourth-generation (4G) and 5G and offers compatibility with MIMO systems. The use of OFDM pilot carriers to estimate the channel was introduced in [69] by investigating the pilot and data allocations for

optimized communication and sensing. The work was followed by [70] where a multi-target ranging system was investigated using dynamic pilot allocation. Recently, authors in [71] used the OFDM waveform deployed in 5G new radio to obtain target parameter estimation. They built their work on the multi-beam design and optimal sub-pattern assignment. However, all the extensive work on OFDM as a ISAC waveform suffers from a huge degradation in communication performance due to the loss of orthogonality caused by Doppler spread [72].

In recent years, a novel modulation scheme called OTFS has emerged as a promising candidate for communication in high-mobility scenarios, including automotive radar applications [73]. Unlike traditional time-frequency (TF) domain modulation schemes, OTFS modulates information in the delay-Doppler (DD) domain, enabling full diversity utilization and robustness against doubly-dispersive channels [46], [74]. OTFS has several advantages in high-mobility scenarios, as reported in [75], [76]. The effectiveness of OTFS for automotive radar was demonstrated in [77], where a ML parameter estimation scheme based on matched filtering is proposed to estimate sensing parameters from received echoes, and the CRLB bound for range and velocity is derived. In [78], the authors presented a beam-space MIMO system using OTFS and a multi-target likelihood ratio detector for target discovery and an ML-based scheme for fractional radar parameter estimation during tracking. Furthermore, a Bayesian learning scheme exploiting the structural sparsity of the channel in the DD-domain is proposed in [79]. Moreover, [80] presented a framework based on a guard space-free symbol placement scheme that uses road side units (RSUs) units to estimate and pre-equalize channel effects and predict the motion parameters of vehicles based on reflected echoes. Finally, the authors in [81] propose a ISAC transmission framework based on spatially spread OTFS (SS-OTFS) in which they exploit the angular domain discretization enabled by spatial spreading and de-spreading in order to develop an effective model for both radar sensing and communication.

However, despite the promising results achieved by the works [69], [70], [77]–[81], the methods used for estimating the radar parameters of targets are complex and add to the receiver's overall complexity. Moreover, the high range resolution requirements of automotive radars, which typically demand the use of a very wide transmission bandwidth, can result in higher sampling frequencies that require high power and processing capabilities. This makes the implementation complex and expensive, leading to limited utility in

practical scenarios, especially when using low-complexity devices [62].

This section presents a novel approach to designing a low-complexity automotive radar system by proposing a narrowband ISAC OTFS system that can achieve high-resolution range-velocity profiles through impulse channel estimation. To address the limitations of traditional wideband signals, the proposed approach uses a single OTFS carrier as a pilot to estimate both fractional delay and Doppler shifts, leveraging the self-duality property of its Fourier transform and its ability to maintain shape under time delays and Doppler shifts. We introduce an algorithm that allows for estimating the range and velocity of radar targets beyond the resolution limitations set by the transmitted signal's time duration and bandwidth. This is achieved by modulating the received OTFS pilot signal in both time and frequency domains with fractional tones until the fractional shifts become integers in the DD domain. The main contributions of this section are given as follows:

- A novel OTFS-Based ISAC scheme for automotive radar applications is proposed that can achieve high-resolution range-velocity profiles based on using a single OTFS carrier as a pilot signal to estimate both range and velocity without requiring long-duration wideband signals. The proposed method can be also used to achieve accurate channel estimation improving the reliability of the communication system.

- The proposed method achieves high-range resolution in automotive radar systems while using smaller bandwidths. This approach reduces the cost and power consumption associated with implementing such systems, which conventionally require high-speed analog-to-digital converters (ADCs) and digital-to-analog converters (DACs) due to the wide bandwidth transmission requirements.

- The proposed estimator gives the lowest variance estimate of an unbiased estimator, and it achieves the lowest possible root mean squared error (RMSE) among all unbiased methods, where it almost converges to the CRLB performance, thus, it is near-optimum.

- Finally, the proposed ISAC scheme is evaluated through simulation analysis in terms of the RMSE of the estimated range and velocity as well as the BER. The theoretical models and simulation results were validated by testing and evaluating

the proposed method in a real-time experiment using the Keysight Agilent Technologies EXA signal analyzer N9010A. The observed results align well with the expected outcomes from theoretical models.

3.6. Integrated Sensing And Communication (ISAC) Via FMCW Signaling

The diversity of applications and use cases for wireless networks is increasing exponentially. In order to provide optimum services, sixth generation (6G) networks need to be aware, flexible, and intelligent [10]. In case of wireless communication systems, the awareness is usually acquired through radio signals, and the process is referred to as sensing [82]. Since both communication and sensing processes share a lot of common elements including transceiver architecture, processing, spectrum, etc., it is only intuitive to integrate them, as is the case in joint sensing and communication (JSAC) paradigm, which has garnered significant attention in recent years [83]. Apart from improving utilization of the pricey and heavily populated spectrum [84], JSAC can also improve the accuracy and reliability of the network by allowing nodes to pool their information and make more informed decisions where both sensing and communication functions are executed on a single hardware platform. Therefore, JSAC decreases system size and cost while increasing resource efficiency. These benefits turn JSAC into one of the most promising technologies for contemporary applications in both military and civilian applications, such as flying wireless mesh networks, airborne systems, ground-based systems [85], augmented reality, digital twins, and unmanned aerial vehicles (UAVs) [86].

However, as 6G networks are expected to enable a massive increase in the number of connected devices, interference from multiple users can occur when multiple systems are trying to access the same resources at the same time. This can cause conflicts and degrade the performance of the system, as both sensing and communication networks may not be able to operate in a correct manner leading to serious problems in some scenarios. Consequently, a new robust waveform is needed to handle the co-existence between sensing and communication of multiple users [87].

One of the candidate waveforms to efficiently support high mobility communication scenarios is OTFS waveform, which modulates data in the delay-Doppler domain and provides extended channel coherence time [47]. Motivated by the slow time-varying property

of the delay-Doppler domain channel, the authors in [88] proposed a method to predict channel parameters utilizing the geometrical relationship of the vehicles, which is determined by the sensing parameters. Moreover, OTFS has been exploited to provide better range and velocity estimation for sensing. For instance, in [89] the authors proposed a machine learning (ML)-based iterative optimization method to solve the sensing problem while minimizing the interference. In [90], a matrix-inversion based algorithm is presented to better estimate the target's radar parameters by canceling the modulation symbols from the received echoes. The authors in [91] introduced a novel matched filtering algorithm at the receiver side to well estimate the object's range and velocity. In addition to its range and velocity, the study in [92], used MIMO radar approach in the beam-space domain to estimate the angular position of a target. In [80], a JSAC-assisted OTFS transmission scheme was proposed for vehicle-to-infrastructure (V2I) scenarios. The scheme considers both uplink and downlink transmissions and utilizes the OTFS-JSAC signals to obtain estimates of delays, Dopplers, and angles associated with vehicles in the communication range. These estimates can be used to construct the dynamic topology of the vehicular network. However, these methods [80], [88]–[92] are computationally expensive and require matrix-inversions and complex algorithms such as maximum-likelihood, which makes them infeasible for IoT devices with restricted power and computational abilities. Even though the work in [93] attempted to reduce the complexity of the OTFS-based sensing using waveform pre-processing, the resulting complexity is still relatively high for IoT devices. While most of the literature related to JSAC considers a single communication and sensing user/transmission each, it is imperative to consider scenarios where multiple users are present and require JSAC capabilities. In such cases, the situation is further exacerbated due to the difference is processing/storage capabilities of the devices involved.

While OTFS presents an example of a communication-centric waveform which has the added capability of sensing, FMCW represents the opposite case where the strength of the waveform lies in its pulse compression, large bandwidth and simple processing capabilities for sensing [94]. Since, JSAC systems also require communication, various approaches have been developed to embed data on FMCW signals for communication. Modulating the frequency of the carrier is one method for encoding binary information into the chirp. The linear frequency sweep from low to high or "up-chirp" is represented

as bit '1'. Alternatively, the frequency sweep from high to low or "down-chirp" is encoded as '0' [95], [96]. In chirp spread spectrum (CSS) systems, a large bandwidth is used to modulate information thereby sacrificing spectral efficiency for chirp's ability to provide high multipath resolution. Moreover, the use of multiple chirps for a given bandwidth and time duration leads to interference issues, rendering chirp suitable only for low data rate and highly reliable communication systems [20]. In [97], frequency shift keying (FSK) modulation scheme is used to embed information over a chirp signal by altering the starting frequency of each chirp. Additionally, authors in [98] used fractional Fourier transform to embed data on chirp subcarriers with varying time frequency signatures. However, the achieved throughput in [20], [95]–[98] is the limiting factor for current JSAC applications compared to other waveforms. Consequently, throughput needs to be enhanced for the use cases offered by 5G and beyond wireless systems.

In this section, we investigate the prerequisites for the generation of sparse linear frequency modulated chirp and orthogonal chirps (OCs) in the delay-Doppler domain. Then, we propose a novel hybrid waveform that couples linear chirp signal that suffers from low communication data rates with OTFS waveform that suffers from high radar processing complexity. Thus, we achieve a joint OTFS-Chirp waveform that is easily implemented in the existing IoT devices for sensing, and yet provides higher data rates for communication. Then, we propose a channel estimation method for OTFS transmission that exploits the chirp signal designed for sensing. This approach eliminates the need for a guard band, which leads to improved spectral efficiency. Additionally, because the chirp signal is spread in the delay-Doppler domain, it results in a lower PAPR compared to embedded-pilot channel estimation methods that use high-power signal pilots for estimation. The main contributions of our work are summarized as follows:

- We derive the representation of the chirp/OCs in the Zak-space, showing that linear chirp signals have a sparse nature in delay-Doppler lattice which implies that chirp is a pre-processed sparse OTFS signal. This sparse representation allows us to distribute data symbols orthogonal to chirp (i.e., the chirp equivalent signal in delay-Doppler domain), while OTFS transform ensures that both chirp and data symbols are transmitted simultaneously.
- Then, we propose a joint OTFS-Chirp waveform providing a solution that can be

simultaneously used by low-end devices like IoT terminals and more sophisticated devices to fulfill their requirements. This is accomplished by combining OTFS and Chirp waveforms to achieve high data rates exploiting the robustness of OTFS against doubly-selective channels while achieving low complexity radar receiver for sensing due to the chirp sampling features, that can be simply incorporated in existing IoT devices with limited power and processing capabilities.

- This is the first thesis presenting a waveform that enables multi-user JSAC system while satisfying both data rate and radar computational complexity constraints. This is achieved by allocating OCs for different users in uplink transmission, such that these chirps are sparse and superimposed in delay-Doppler domain.

- We propose a novel power and spectrally efficient chirp-based channel estimation method for OTFS systems that exploits the sparse nature of the chirps in both delay Doppler and Fresnel (chirp) domain. This approach eliminates the need for a pilot guard band in the delay-Doppler domain, which significantly improves the power and spectral efficiency of the system.

- The performed simulations validate the proposed JSAC waveform design by computing the computational complexity of the proposed OTFS-Chirp sensing and comparing it to existing schemes. Then, we show that the proposed scheme exhibits the same chirp performance while preserving high data rates.

3.7. Channel Estimation In OCDM Systems

Recently OCDM has emerged as a promising alternative waveform to conventional multicarrier modulation schemes. Unlike OFDM which modulates the data over complex sinusoidals, OCDM utilizes the discrete Fresnel transform (DFnT) to modulate data onto orthogonal complex linear chirps in the time domain, which have the ability to combat challenges associated with wireless channels [99]. For instance, by spreading data over the entire time and bandwidth of the signal, OCDM exhibits increased robustness against

multipath propagation [100], and narrowband interference [101]. This is particularly beneficial for achieving reliable communication in complex and frequency-selective environments. Moreover, by leveraging the close relationship between the DFnT and the discrete Fourier transform (DFT), the compatibility of OCDM systems with OFDM can be achieved, enabling seamless integration of OCDM into existing OFDM-based communication systems and satisfying the crucial condition of backward compatibility [102].

The reliability of communications with OCDM highly depends on the accuracy of channel estimation, particularly in the presence of delay and Doppler spread. Yet, most existing works only consider the static channels to estimate in OCDM systems without considering mobility [103]–[105] where pilots are embedded in the time or frequency domain. In [106], only a single frequency offset is considered when doing estimation in the Fresnel domain. On the other hand, for doubly selective channels, a basis expansion model (BEM) is adopted to characterize doubly selective channels in [107] using pilot chirp assisted (PCA)-OCDM systems. A method is developed to minimize the MMSE of the channel estimator. However, the complexity of the matrix inversion required in MMSE is $O(N^3)$, which is highly complex and prohibitive for channels with long delays. Additionally, MMSE requires prior knowledge of channel statistics.

This thesis derives the representation of the OCDM in the delay-Doppler domain, showing that each OCDM carrier has a sparse nature in the delay-Doppler lattice. Then, exploiting the sparse nature of the orthogonal chirps in both domains, this thesis proposes a novel low-complexity channel estimation scheme for OCDM systems by designing the pilots in the chirp domain and estimating the channel in the delay-Doppler domain. The main contributions are summarized as follows:

- We derive the mathematical representation of OCDM carriers in the Zak-space and demonstrate that linear orthogonal chirps possess a sparse nature in the delay-Doppler lattice. Additionally, we establish that OCDM can be seen as a pre-processed delay-Doppler modulation and introduce a relationship between OCDM and the OTFS modulation.

- We propose a novel low-complexity pilot-based channel estimation method for

OCDM systems that exploits the sparse nature of the OCDM carriers in both delay-Doppler and Fresnel (chirp) domain. The proposed method offers enhanced flexibility by allowing the utilization of any channel estimation scheme developed for the delay-Doppler domain, depending on the capabilities and requirements of the users or transceivers.

- We assess the performance of the proposed channel estimation method by analyzing two metrics: NMSE and BER for OCDM systems. The simulations highlight the effectiveness of the proposed algorithm in achieving accurate channel estimation with low-complexity.

CHAPTER 4

4. EXPERIMENTAL PART: PROBLEMS AND PROPOSED SOLUTIONS

4.1. Flexible Physical Layer Security For Joint Data And Pilots In OFDM Systems

4.1.1. System model and preliminaries

As demonstrated in **Figure 4.1**, a multiple-input multiple-output (MIMO)-orthogonal frequency division multiplexing (OFDM) system is considered that consists of a legitimate transmitter (Alice, {a}), legitimate receiver (Bob, {b}), and passive eavesdropper (Eve, {e}) that is trying to intercept the transmission between Alice and Bob, where each node is equipped with M_a, N_b, and N_e antennas, respectively.

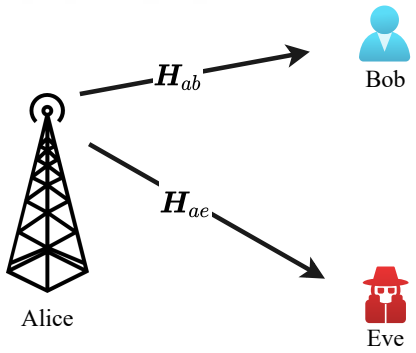


Figure 4.1: System model where Alice and Bob are communicating over rich scattering channel with the existence of Eve.

OFDM system is adopted for the communication, where during the i-th OFDM symbol N complex data symbols in frequency domain $\underline{X}_i = \left[X_i(0) \quad X_i(1) \quad \dots \quad X_i(N-1)\right]^{\mathrm{T}}$ are converted to time-domain $\underline{x}_i = \left[x_i(0) \quad x_i(1) \quad \dots \quad x_i(N-1)\right]^{\mathrm{T}}$ using inverse fast Fourier transform (IFFT) to form one OFDM symbol as

$$x_i(v) = \frac{1}{\sqrt{N}} \sum_{k=0}^{N-1} X_i(k) e^{j2\pi vk/N}. \qquad \textbf{(4.1)}$$

To combat the inter-symbol interference (ISI), a cyclic prefix (CP) is appended to $\underline{\mathrm{x}}_i$ before transmission. Finally, the signal is transmitted through the wireless channel and reaches the Bob and Eve.

For the n-th receive antenna, the channel impulse response (CIR) $\underline{\mathrm{h}}_i^{(n,m)}$ associated with the m-th transmit antenna (where $m = 1, \ldots, M_a$, and $n = 1, \ldots, N_b$) can be denoted by [108]

$$\underline{\mathrm{h}}_i^{(n,m)}(t,\tau) = \sum_{l=0}^{L-1} h_{i,l}^{(n,m)}(t)\delta(\tau - \tau_l), \tag{4.2}$$

where $h_{i,l}^{(n,m)}(t)$ and τ_l are the complex channel gain and the delay of the l-th path at time t, respectively. $h_{i,l}^{(n,m)}(t)$ is assumed to have Gaussian distribution with zero-mean. L is the maximum number of effective channel taps and $\delta(\cdot)$ is the Kronecker delta function. The channel frequency response (CFR) is then expressed as

$$H_i^{(n,m)}(t,f) = \int_{-\infty}^{+\infty} h_i^{(n,m)}(t,\tau)e^{-j2\pi f\tau}d\tau. \tag{4.3}$$

Assuming that the channel is time-invariant during one OFDM symbol period T_s, and that the frequency spacing is Δf_c, the CIR and the CFR can be respectively represented as [109]

$$h_i^{(n,m)}(\nu) = h_i^{(n,m)}(\nu T_s, \tau),\ H_i^{(n,m)}(k) = H_i^{(n,m)}(\nu T_s, k\Delta f_c). \tag{4.4}$$

Given the system description above, we can represent the MIMO-OFDM channel in another form such as

$$\mathrm{G}(\nu) = \sum_{l=0}^{L-1} \mathrm{G}_l\delta(\nu - l) \tag{4.5}$$

where G is the MIMO CIR, and G_l is a complex matrix describing the MIMO channel coefficients at delay l. Then, the $N_b \times M_a$ MIMO channel seen at the k-th subcarrier is given by [110]

$$\mathrm{H}(k) = \frac{1}{\sqrt{N}} \sum_{l=0}^{L-1} \mathrm{G}_l e^{(-j\frac{2\pi kl}{N})}. \tag{4.6}$$

At the receiver, the CP is discarded first, and then the fast Fourier transform (FFT) process is applied. The received signal $Y_i(k)$ on the k-th subcarrier is found as

$$Y_i^{(n)}(k) = H_i(k)X_i^{(n)}(k) + W_i^{(n)}(k), \tag{4.7}$$

where $W_i^{(n)}(k)$ is the zero-mean additive white Gaussian noise (AWGN) vector with variance σ^2 at the k-th subcarrier. It is assumed that the sampling rate satisfies the Nyquist criteria.

As the time-frequency information in every OFDM symbol will be exploited by every transmit-receive antenna pairs adopting the identical processing, the transmit-receive antenna indices will be omitted from now on. Furthermore, the channels observed at Alice $\underline{\mathrm{h}}_{ba} \in \mathbb{C}^{L\times 1} \sim \mathcal{CN}(0, \sigma_b)$, Bob $\underline{\mathrm{h}}_{ab} \in \mathbb{C}^{L\times 1} \sim \mathcal{CN}(0, \sigma_a)$, and Eve $\underline{\mathrm{h}}_{ae} \in \mathbb{C}^{L\times 1} \sim \mathcal{CN}(0, \sigma_e)$ are considered as multi-path slowly varying channels following complex Gaussian distribution. Moreover, due to the channel reciprocity assumption, the channel between Alice-Bob $\underline{\mathrm{h}}_{ab}$ can be estimated from the channel between Bob-Alice $\underline{\mathrm{h}}_{ba}$, where $\underline{\mathrm{h}}_{ab} = \underline{\mathrm{h}}_{ba}^T$ [111]. In addition, due to rich scattering environment with enough distance separation between the nodes, the channel experienced by Bob and Eve is assumed to be independent unless stated otherwise. Furthermore, it is also assumed that Alice has no information about the channel of Eve because of its passive operation.

4.1.2. Proposed algorithm

The increase in the number of wireless communication-based applications with varying requirements motivates the need for adaptive and flexible security designs [112]. Inspired by that, in this section, we firstly present the channel decomposition concept, and then we propose novel algorithms that are capable of providing adaptive and flexible security. Particularly, we start by providing a data security mechanism followed by a method for securing the pilots. Afterwards, the high security case is considered where both data and pilots need to be secured.

4.1.2.1. Minimum-phase all-pass channel decomposition

Wireless channel systems are causal because they are real-time systems, where the samples belong only to the present or past. Additionally, the CIR of a wireless channel can be represented by a finite impulse response (FIR) filter, and thus it is stable [113]. Consequently, a stable and causal system with system function $H_\Lambda(z)$ would have all poles at the origin inside its unit circle where $\Lambda = \{ab, ae\}$; however, the zeros are free to wander outside. Let $H_\Lambda^1(z)$ be the system function with all zeros and poles inside the unit circle, and let the zeros outside be at $1/p_k$. This implies that we can decompose such a system

a) **b)** **c)**

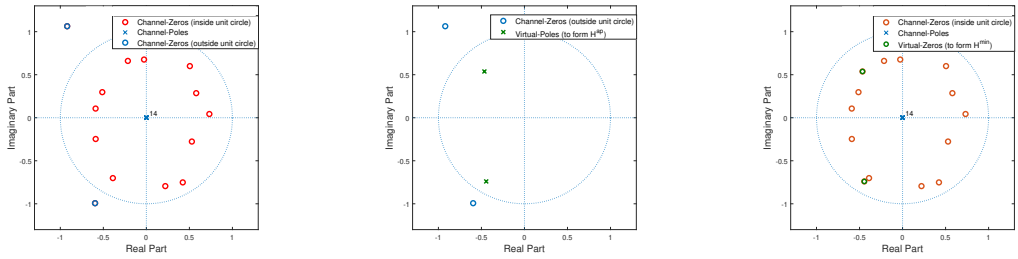


Figure 4.2: The zero-pole diagram of the minimum-phase all-pass decomposition of a wireless channel: **a**) overall Channel, **b**) all-pass channel, **c**) minimum-phase channel.

into two components as

$$H_{\Lambda}(z) = \underbrace{\left(H_{\Lambda}^{1}(z)\prod_{k=1}^{q}\left(1-p_{k}^{*}z^{-1}\right)\right)}_{H_{\Lambda}^{\min}(z)}\overbrace{\prod_{k=1}^{q}\left(\frac{z^{-1}-p_{k}}{1-p_{k}^{*}z^{-1}}\right)}^{H_{\Lambda}^{\mathrm{ap}}(z)}, \tag{4.8}$$

where $H_{\Lambda}^{\min}(z)$ and $H_{\Lambda}^{\mathrm{ap}}(z)$ are defined as the minimum-phase and all-pass components of $H_{\Lambda}(z)$, respectively. For instance, **Figure 4.2** illustrates the zero-pole diagram of the minimum-phase all-pass decomposition of a random channel. As seen in **Figure 4.2a**, the overall channel contains zeros inside and outside the unit circle where the poles are centered at the origin. As shown in **Figure 4.2b**, for the all-pass channel only the zeros outside the unit circle are considered along with virtual poles added at the inverse of the zeros' location to cancel out the attenuation effect, thus passing all frequencies as the name stands. To compensate the effect of these virtual poles, zeros are added on top of them having a system with all zeros inside the unit circle (i.e., minimum-phase system) as illustrated in **Figure 4.2c**.

The resulting components have various properties; for instance, in terms of the magnitude response $|H(e^{j\omega})|$, the factorization in **(4.8)** implies that $|H_{\min}(e^{j\omega})| = |H(e^{j\omega})|$ and $|H_{ap}(e^{j\omega})| = 1$. These properties of the decomposed channel will be exploited to provide security for both data and pilots.

4.1.2.2. Proposed precoder/combiner design

The designed algorithm is based on a novel precoder that exploits the components of the channel separately, instead of using the full channel as in conventional security algorithms [114]. The proposed method uses only the all-pass component of the channel for precoding as explained in **Subsection 4.1.2.1**; therefore, the peak to average power ratio (PAPR) will not be affected [115]. Additionally, it provides an effective solution to ensure secure communication against eavesdropping. **Algorithm 4.1** summarizes the precoder/combiner design.

Algorithm 4.1 The proposed precoder design.

Input: H_{ba}

Output: Q_D and Q_P

1-Bob sends orthogonal pilot signals P to Alice to estimate the MIMO channel $\mathrm{H}_{ba} \in \mathbb{C}^{N_b \times M_a \times N}$ [116], where due to channel reciprocity we assume that uplink and downlink channel state information (CSI) are available at Alice.

2-Alice decomposes the CFR $\underline{\mathrm{H}}_{ba}$ into all-pass $\underline{\mathrm{H}}_{ab}^{\mathrm{ap}}$ and minimum-phase $\underline{\mathrm{H}}_{ab}^{\mathrm{min}}$ components for each (n, m) antenna pair, as explained in **Subsection 4.1.2.1**.

3-Alice reconstructs the MIMO all-pass and minimum-phase channels $\mathrm{H}_{ab}^{\mathrm{ap}} \in \mathbb{C}^{N_b \times M_a \times N}$ and $\mathrm{H}_{ab}^{\mathrm{min}} \in \mathbb{C}^{N_b \times M_a \times N}$, respectively, where $\mathrm{H}_{ab} = \mathrm{H}_{ab}^{\mathrm{min}} \circ \mathrm{H}_{ab}^{\mathrm{ap}}$, and $\circ$ denotes the element-wise product.

4-Alice designs the precoder $\mathrm{Q}_D(k) \in \mathbb{C}^{M_a \times M_a}$ and $\mathrm{Q}_P(k) \in \mathbb{C}^{M_a \times M_a}$ for data and pilots security for each subcarrier k, respectively, as follows

$$\mathrm{Q}_D(k) = \mathrm{diag}\left(\frac{1}{M_a \times N_b} \sum_{l=m}^{M_a} \sum_{n=1}^{N_b} H_{ab}^{\mathrm{ap}}(k, n, m) \right)^H, \tag{4.9}$$

and

$$\mathrm{Q}_P(k) = \mathrm{diag}\left(H_{ab}^{\mathrm{ap}}(k, n', m') \right), \tag{4.10}$$

where $H_{ab}^{\mathrm{ap}}(k, n', m')$ is the (n', m')-th element of $H_{ab}^{\mathrm{ap}}(k)$ which can be set by default to $(n', m') = (1, 1)$.

Note that $|\mathrm{H}_{ab}(k)\mathrm{Q}_D(k)| = |\mathrm{H}_{ab}(k)\mathrm{Q}_P(k)| = |\mathrm{H}_{ab}(k)|$, thus the proposed precoder indeed does not affect the PAPR.

4.1.2.3. Proposed data security method

This subsection presents the details of the proposed algorithm for providing data security. The proposed algorithm exploits a component of channel for precoding that is capable of providing security without degrading the BER performance. The basic steps are described in **Algorithm 4.2**.

Algorithm 4.2 The proposed data security scheme.

1- Alice precodes the data subcarriers $\underline{\mathrm{X}}(k_d)$ at indices k_d with $\mathrm{Q}_D(k)$, while the pilots $\underline{\mathrm{X}}(k_p)$ at k_p indices are intact. Then, the transmitted signal by Alice can be expressed as

$$\underline{\mathrm{X}}(k) = \begin{cases} \mathrm{Q}_D(k)\underline{\mathrm{D}}(k) & k \in k_d \\ \underline{\mathrm{P}}(k) & k \in k_p. \end{cases} \tag{4.11}$$

2- The received signal at Bob can be given as:

$$\underline{\mathrm{Y}}_{ab}(k) = \begin{cases} \mathrm{H}_{ab}(k)\mathrm{Q}_D(k)\underline{\mathrm{D}}(k) + \underline{\mathrm{W}}_{ab}(k) & k \in k_d \\ \mathrm{H}_{ab}(k)\underline{\mathrm{P}}(k) + \underline{\mathrm{W}}_{ab}(k) & k \in k_p. \end{cases} \tag{4.12}$$

Using the pilots $\underline{\mathrm{P}}(k)$ at k_p, the CFR $\tilde{\mathrm{H}}_{ab}$ is estimated.

3- Applying channel decomposition to the estimated channel as in **Subsection 4.1.2.1**, Bob obtains $\tilde{\mathrm{H}}_{ab}^{\min}(k)$ and $\tilde{\mathrm{H}}_{ab}^{\mathrm{ap}}(k)$ which will be exploited to design the combiner as in (**4.9**). The combined data of the received signal by Bob is given as

$$\begin{aligned} \underline{\mathrm{Y}}_{ab}(k) &= \tilde{\mathrm{Q}}_D^H(k)\mathrm{H}_{ab}(k)\mathrm{Q}_D(k)\underline{\mathrm{D}}(k) + \tilde{\mathrm{Q}}_D^H(k)\underline{\mathrm{W}}_{ab}(k) \\ &= \mathrm{H}_{ab}(k)\underline{\mathrm{D}}(k) + \mathrm{Q}_D^H(k)\underline{\mathrm{W}}_{ab}(k)\ k \in k_d, \end{aligned} \tag{4.13}$$

wherein case of perfect channel estimation $\tilde{\mathrm{Q}}_D(k) = \mathrm{Q}_D(k)$.

4- Using the results of step 3, Bob equalizes H_{ab} using zero-forcing [3] to decode the data as

$$\begin{aligned} \hat{\underline{\mathrm{X}}}_{Bob}(k) &= \mathrm{Q}_{ZF}(k)\underline{\mathrm{Y}}_{ab}(k) \\ &= \underline{\mathrm{D}}(k) + \tilde{\underline{\mathrm{W}}}_{ab}(k)\ k \in k_d, \end{aligned} \tag{4.14}$$

where $\mathrm{Q}_{ZF}(k) = \left(\mathrm{H}_{ab}^H(k)\mathrm{H}_{ab}(k)\right)^{-1}\mathrm{H}_{ab}^H(k)$, $\tilde{\underline{\mathrm{W}}}_{ab}(k) = \mathrm{Q}_{ZF}(k)\mathrm{Q}_D^H(k)\underline{\mathrm{W}}_{ab}(k)$.

On the other hand, the received signal at Eve can be given by

$$\underline{\mathrm{Y}}_{ae}(k) = \begin{cases} \mathrm{H}_{ae}(k)\mathrm{Q}_D(k)\underline{\mathrm{D}}(k) + \underline{\mathrm{W}}_{ae}(k) & k \in k_d \\ \mathrm{H}_{ae}(k)\underline{\mathrm{P}}(k) + \underline{\mathrm{W}}_{ae}(k) & k \in k_p. \end{cases} \tag{4.15}$$

Applying zero-forcing at Eve, the processed signal at Eve can be given as

$$\hat{\underline{\mathrm{X}}}_{Eve}(k) = \mathrm{Q}_D(k)\underline{\mathrm{D}}(k) + \tilde{\underline{\mathrm{W}}}_{ae}(k)\ k \in k_d, \tag{4.19}$$

where $\tilde{\underline{\mathrm{W}}}_{ae}(k) = \mathrm{Q}_{ZF}(k)\underline{\mathrm{W}}_{ae}(k)$, $\mathrm{Q}_{ZF}(k) = \left(\mathrm{H}_{ae}^H(k)\mathrm{H}_{ae}(k)\right)^{-1}\mathrm{H}_{ae}^H(k)$.

As seen from (**4.19**), Eve will not be able to decode the data even if it perfectly estimates its channel. This is due to the unknown randomness caused by the term $\mathrm{Q}_D(k)$ which is uncorrelated with its channel.[2]

[2]Note that due to channel decorrelation in rich scattering environment between H_{ab} and H_{ae}, Eve will not be able to estimate and remove the effect of Q_D.

Algorithm 4.3 The proposed pilot security scheme.

1- Alice precodes the pilots subcarriers $\underline{\mathrm{X}}(k_p)$ at indices k_p with $\mathrm{Q}_P(k)$, while the data subcarriers $\underline{\mathrm{X}}(k_d)$ at k_d indices are intact. Then, the transmitted signal by Alice can be expressed as

$$\underline{\mathrm{X}}(k) = \begin{cases} \underline{\mathrm{D}}(k) & k \in k_d \\ \mathrm{Q}_P(k)\underline{\mathrm{P}}(k) & k \in k_p. \end{cases} \tag{4.16}$$

2- The received signal at Bob can be given as

$$\underline{\mathrm{Y}}_{ab}(k) = \begin{cases} \mathrm{H}_{ab}(k)\underline{\mathrm{D}}(k) + \underline{\mathrm{W}}_{ab}(k) & k \in k_d \\ \mathrm{H}_{ab}(k)\mathrm{Q}_P(k)\underline{\mathrm{P}}(k) + \underline{\mathrm{W}}_{ab}(k) & k \in k_p. \end{cases} \tag{4.17}$$

Using the pilots, the precoded CFR corresponding to the (n', m')-th antenna pair $\underline{\tilde{\mathrm{H}}}_{ab}^{(n',m')} = \underline{\mathrm{H}}_{ab}^{(n',m')} \circ \underline{\mathrm{H}}_{ab}^{\mathrm{ap}}(n', m')$ is estimated.

3- In order to find $\underline{\mathrm{H}}_{ab}^{\mathrm{ap}}(n', m')$ from the estimated $\underline{\tilde{\mathrm{H}}}_{ab}^{(n',m')}$, channel decomposition is applied to the estimated precoded channel as explained in **Subsection 4.1.2.1** as follows: $\underline{\tilde{\mathrm{H}}}_{ab}^{(n',m')} = \underline{\tilde{\mathrm{H}}}_{ab}^{\min}(n', m') \circ \left(\underline{\tilde{\mathrm{H}}}_{ab}^{\mathrm{ap}}(n', m')\right)^2$, where $\underline{\tilde{\mathrm{H}}}_{ab}^{\min}(n', m')$ is minimum-phase component while $\left(\underline{\tilde{\mathrm{H}}}_{ab}^{\mathrm{ap}}(n', m')\right)^2$ is all-pass component of $\underline{\tilde{\mathrm{H}}}_{ab}^{(n',m')}$.

4- The estimated combiner at Bob can be calculated as: $\tilde{\mathrm{Q}}_P(k) = \mathrm{diag}\left(\sqrt{\underline{\tilde{\mathrm{H}}}_{ab}^{\mathrm{ap}}(n', m')^2}\right)$. The combined pilots of the received signal by Bob is given as

$$\begin{aligned} \underline{\mathrm{Y}}_{ab}(k) &= \tilde{\mathrm{Q}}_P^H(k)\mathrm{H}_{ab}(k)\mathrm{Q}_P(k)\underline{\mathrm{P}}(k) + \tilde{\mathrm{Q}}_P^H(k)\underline{\mathrm{W}}_{ab}(k) \\ &= \mathrm{H}_{ab}(k)\underline{\mathrm{P}}(k) + \mathrm{Q}_P^H(k)\underline{\mathrm{W}}_{ab}(k) k \in k_p. \end{aligned} \tag{4.18}$$

where in case of perfect channel estimation $\tilde{\mathrm{Q}}_P(k) = \mathrm{Q}_P(k)$. Therefore the channel can be securely estimated and equalized.

4.1.2.4. Proposed pilot security method

This subsection presents the details of the proposed algorithm for providing pilot security. Similar to data security, the proposed pilot security algorithm exploits the components of the channel separately. It ensures that only a legitimate receiver will be able to estimate the channel while Eve will not be able to learn the channel or environment without affecting PAPR as in [25]. Additionally, the proposed algorithm is also suitable for the security of feedbacks, hardware impairments, and hardware-based authentication. Furthermore, the eavesdropper will not be able to extract information of precoder corresponding to the channel of legitimate nodes from the received signal and thus will not be able to launch attacks to learn CSI corresponding to legitimate node [23]. The basic steps are described in **Algorithm 4.3**.

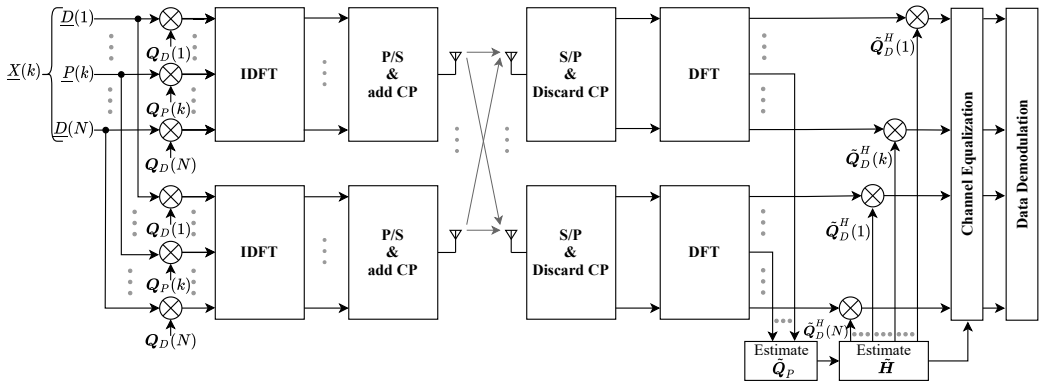


Figure 4.3: The block diagram showing the main steps of the proposed joint data and pilot security algorithm.

Whereas, at Eve's side, the received signal is given by

$$\underline{\mathrm{Y}}_{ae}(k) = \begin{cases} \mathrm{H}_{ae}(k)\underline{\mathrm{D}}(k) + \underline{\mathrm{W}}_{ae}(k) & k \in k_d \\ \mathrm{H}_{ae}(k)\mathrm{Q}_P(k)\underline{\mathrm{P}}(k) + \underline{\mathrm{W}}_{ae}(k) & k \in k_p. \end{cases} \tag{4.20}$$

As seen from **(4.20)**, eavesdropper will not be able to correctly estimate the channel because of the randomness caused by all-pass component $\mathrm{Q}_P(k)$ of the legitimate channel in **(4.20)**. Hence, it can neither estimate the channel nor learn the environment.

4.1.2.5. Joint pilot and data security

This subsection presents the details of the proposed algorithm for providing joint data and pilot security. Particularly, in case of a very high-security risk, there is a need of securing both pilot and data to provide a very high level of security. Thus, the attacker will not able to learn the channel, environment, and data. Here, the idea is to exploit the proposed algorithm presented in Subsections **Subsection 4.1.2.3** and **Subsection 4.1.2.4** to ensure both pilot and data security. The transmitted signal by Alice after applying both data and pilot security can be expressed as

$$\underline{\mathrm{X}}(k) = \begin{cases} \mathrm{Q}_D(k)\underline{\mathrm{D}}(k) & k \in k_d \\ \mathrm{Q}_P(k)\underline{\mathrm{P}}(k) & k \in k_p. \end{cases} \tag{4.21}$$

In this case, Bob will first estimate the channel using the pilots as described in **Subsection 4.1.2.4**, and then he will use the estimated channel to extract the data as shown in **Subsection 4.1.2.3**. **Figure 4.3** illustrates the block diagram of the proposed joint data and pilot security algorithm in MIMO-OFDM systems. On the other hand, the received

signal at Eve can be given as:

$$\underline{\mathrm{Y}}_{ae}(k) = \begin{cases} \mathrm{H}_{ae}(k)\mathrm{Q}_D(k)\underline{\mathrm{D}}(k) + \underline{\mathrm{W}}_{ae}(k) & k \in k_d \\ \mathrm{H}_{ae}(k)\mathrm{Q}_P(k)\underline{\mathrm{P}}(k) + \underline{\mathrm{W}}_{ae}(k) & k \in k_p. \end{cases} \quad \textbf{(4.22)}$$

It should be noted from **(4.22)** that Eve will neither be able to estimate its channel nor the data due to the randomness caused by $\mathrm{Q}_P(k)\underline{\mathrm{P}}(k)$ and $\mathrm{Q}_D(k)\underline{\mathrm{D}}(k)$, respectively. Thus, providing two-level security that is suitable for critical applications.

4.1.3. Numerical analysis

In this section, we provide the theoretical analysis for both data and pilot security for the proposed methods. For the former, we analyze the bit error rate (BER) performance for Bob and Eve under correlated and uncorrelated eavesdropping channels. For the latter, we derive the minimum mean squared error minimum mean squared error (MMSE) of the estimated channel.

4.1.3.1. Data security: BER-based secrecy gap

In this subsection, we analyze the bit error probability (BEP) under correlated and uncorrelated eavesdropping channels and use it to compare the BER performance gap between Bob and Eve.

4.1.3.1.1 Uncorrelated Bob-Eve channel

One elaborate method to suppress the effect of $\underline{\mathrm{W}}(k)$ when estimating the channel is the MMSE estimation [117]. After estimating the channel $\tilde{\mathrm{H}}_{ab}$, the received signal at the data subcarriers k_d is given in **(4.12)** and expressed by

$$\underline{\mathrm{Y}}_{ab}(k) = \mathrm{H}_{ab}(k)\mathrm{Q}_D(k)\underline{\mathrm{D}}(k) + \underline{\mathrm{W}}_{ab}(k)\ k \in k_d. \quad \textbf{(4.23)}$$

The receiver applies zero-forcing equalization. In case of perfect channel estimation, $\mathrm{E}[|\mathrm{H}_{ab} - \tilde{\mathrm{H}}_{ab}|^2] = 0$, and the correlation coefficients between the actual and the estimated channel responses are respectively found as $\rho_{ab}^1 = 1$ and $\rho_{ab}^2 = 0$. The BEP performance

a) **b)**

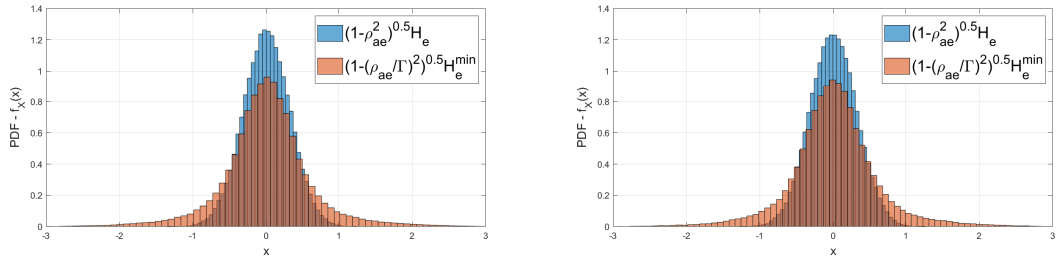


Figure 4.4: The distribution of uncorrelated part of Eve's channel for $\rho_{ae} = 0.9$: **a**) real part, **b**) imaginary part.

will become the lower bound performance of **(A1.5)**, and it is given as

$$P_{ab}\mathbf{e} = \frac{1}{N_b}\sum_{n=1}^{N_b}\frac{1}{2}\left[1 - \frac{1}{\sqrt{1+\frac{1}{\gamma_{ab}^{(n)}}}}\right]. \tag{4.24}$$

where $\gamma_{ab}^{(n)}$ denotes the signal-to-noise ratio (SNR) of the received signal at the k-th sub-carrier and n-th receive antenna. Please refer to **Appendix A.1**.

4.1.3.1.2 Correlated Bob-Eve channel

To further evaluate the performance of the proposed scheme and emphasize its reliability, we consider the effects of the Eve location with respect to the Bob. For that, we consider a correlated eavesdropping channel scenario, where it is assumed that Eve is located near Bob. For a fair comparison with [4], we assume single-input single-output (SISO) system where $\mathrm{Q}_D(k) = (\underline{\mathrm{H}}_{ab}^{\mathrm{ap}}(k))^H$. Note that the results can be extended to MIMO as we did in **Subsection 4.1.3.2**. We model the correlation between channel coefficients [118] as

$$\underline{\mathrm{H}}_{ae} = \rho_{ae}\underline{\mathrm{H}}_{ab} + \sqrt{1-\rho_{ae}^2}\underline{\mathrm{H}}_{e}, \tag{4.25}$$

where $\underline{\mathrm{H}}_e$ is i.i.d. $\sim \mathcal{CN}(0, \sigma_a)$ and ρ_{ae} is the correlation function of the legitimate channel gain with the eavesdropping channel given as

$$\rho_{ae} = \frac{\mathrm{Cov}[\underline{\mathrm{H}}_{ab}, \underline{\mathrm{H}}_{ae}^H]}{\sqrt{\mathrm{var}(\underline{\mathrm{H}}_{ab})\,\mathrm{var}(\underline{\mathrm{H}}_{ae}^H)}} = \frac{\mathrm{E}[\underline{\mathrm{H}}_{ab}\underline{\mathrm{H}}_{ae}^H]}{\sigma_a\sigma_e}. \tag{4.26}$$

Please refer to **Appendix A.2**.

In the proposed algorithm, the overall channel is not used, and instead, only one component (i.e., all-pass channel) is exploited. Therefore, even if Eve estimates the channel with high correlation, still it will suffer from the error raised due to the decomposition of its channel. This leads to lower eavesdropping channel correlation and enhanced security performance. **Figure 4.4** shows the distribution of the real and imaginary parts of the uncorrelated part of the channel $\underline{\mathrm{H}}_e$. It is clearly seen that the variance of the uncorrelated term, given blue color, increases after performing the channel decomposition as shown by the orange distribution in **Figure 4.4**. Assuming the same channel model as in **(4.25)** we have

$$\underline{\mathrm{H}}_{ae} = \rho_{ae}\underline{\mathrm{H}}_{ab}^{\min}\underline{\mathrm{H}}_{ab}^{\mathrm{ap}} + \sqrt{1-\rho_{ae}^2}\underline{\mathrm{H}}_e. \tag{4.27}$$

For the channel equalization, only the minimum-phase component of the channel is needed. So, after performing the channel decomposition and normalization, Eve finds

$$\begin{aligned}\underline{\mathrm{H}}_{ae}^{\min} &= \rho_{ae}^{\min}\underline{\mathrm{H}}_{ab}^{\min} + \sqrt{1-\left(\rho_{ae}^{\min}\right)^2}\underline{\mathrm{H}}_e^{\min} \\ &= \frac{\rho_{ae}}{\Gamma}\underline{\mathrm{H}}_{ab}^{\min} + \sqrt{1-\left(\frac{\rho_{ae}}{\Gamma}\right)^2}\underline{\mathrm{H}}_e^{\min},\end{aligned} \tag{4.28}$$

where Γ is the correlation attenuation factor. Note that Γ satisfies the following constraints

$$\Gamma \sim \sqrt{1-\rho_{ae}^2} \tag{4.29a}$$

$$\Gamma \geq 1 \ \forall \rho_{ae} \tag{4.29b}$$

$$\Gamma = 1, \text{ for } \rho_{ae} = 1 \tag{4.29c}$$

$$0 \leq \frac{\rho_{ae}}{\Gamma} \leq 1, \ \forall \rho_{ae}, \tag{4.29d}$$

where the symbol ~ denotes the proportionality. Taking all the constraints given in **(5.56)**, we find that

$$\Gamma = 1 + \sqrt{1-\rho_{ae}^2}. \tag{4.30}$$

Please refer to **Appendix A.3**.

Figure 4.5 shows the relationship between the correlation of the overall channel of Eve and Alice and the correlation of the minimum-phase component of their channels. As observed from **Figure 4.5**, the correlation factor decreases after performing the channel decomposition causing degradation in the data decoding capability at Eve.

Therefore, the correlation function becomes $\rho_{ae}^{\min} = \rho_{ae}/(1+\sqrt{1-\rho_{ae}^2}) < \rho_{ae}$. This result

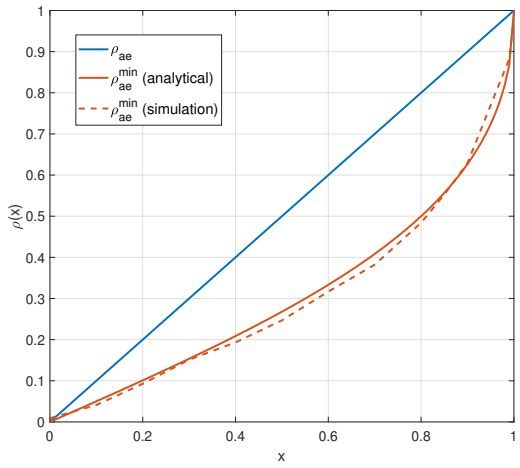


Figure 4.5: The channel correlation relationship between the conventional and proposed schemes.

shows another advantage of using the proposed scheme in case of correlated eavesdropping channels. Please refer to **Appendix A.4**.

To evaluate the results above, the BER performance is analyzed. we adopt the same BER expression given by **(4.24)** by including the spatial correlation factor ρ [4]. Then, the BER at both Bob and Eve can be found using **(A1.5)** as

$$P_{\Lambda}\mathbf{e} = \frac{1}{2N_b}\sum_{n=1}^{N_b}\left[1 - \frac{\rho_{\Lambda}}{\sqrt{1+\frac{1}{\gamma_{ab}^{(n)}}}}\right], \tag{4.31}$$

and $\Lambda = \{ab, ae\}$.

4.1.3.2. Pilot security: channel NMSE

For the MIMO-OFDM channel estimation, frequency domain estimation is used by transmitting orthogonal pilots, which converts the channel estimation in MIMO systems to that in SISO systems. By using the pilot scheme as adopted in **Subsection 4.1.2.4**, the MMSE channel estimation for the MIMO-OFDM system between the m'-th transmitter and n'-th receiver can be obtained as [117]

$$\tilde{\mathrm{H}}_{ab}^{\mathrm{MMSE}(n',m')} = \mathrm{FR}_{h_{ab}Y_{ab}}\mathrm{R}_{Y_{ab}Y_{ab}}^{-1}\mathrm{Y}_{ab}^{(n')}, \tag{4.32}$$

Table 4.1: Complexity of the proposed security algorithm.

	Complexity (MIMO)
Z-transform	$O(M_a N_b L \log L \log(bL))$
$H^{\min}(z)$ estimation	$O(M_a N_b N)$
$H^{\mathrm{ap}}(z)$ estimation	$O(M_a N_b 2NL)$
Precoding/Combining	$O(M_a N_b N)$
Total transmitter	$O\left(M_a N_b \left(2N(L+1) + L \log L \log(bL)\right)\right)$
Total receiver	$O\left(M_a N_b \left(2N(L+1) + L \log L \log(bL)\right)\right)$
Total complexity	$O\left(2M_a N_b \left(2N(L+1) + L \log L \log(bL)\right)\right)$

where

$$\begin{aligned} \mathrm{R}_{h_{ab}Y_{ab}} &= \mathrm{R}^{(n',m')}_{h_{ab}h_{ab}} \mathrm{F}^H (\mathrm{P}^{(n')})^H \\ \mathrm{R}_{Y_{ab}Y_{ab}} &= \mathrm{P}^{(n')} \mathrm{F} \mathrm{R}^{(n',m')}_{h_{ab}h_{ab}} \mathrm{F}^H (\mathrm{P}^{(n')})^H + \sigma^2 \mathrm{I}_N, \end{aligned} \tag{4.33}$$

where $\mathrm{R}_{h_{ab}h_{ab}}$ is the channel autocorrelation matrix, F is the discrete Fourier transform (DFT) matrix, and I_N is the identity matrix. Substituting **(4.33)** in **(4.32)** we find

$$\begin{aligned} \tilde{\mathrm{H}}_{ab}\mathrm{MMSE}(n',m') = \mathrm{F}\mathrm{R}^{(n',m')}_{h_{ab}h_{ab}} \mathrm{F}^H (\mathrm{P}^{(n')})^H \times \\ \left(\mathrm{P}^{(n')} \mathrm{F} \mathrm{R}^{(n',m')}_{h_{ab}h_{ab}} \mathrm{F}^H (\mathrm{P}^{(n')})^H + \sigma^2 \mathrm{I}_N\right)^{-1} \mathrm{Y}^{(n')}_{ab}. \end{aligned} \tag{4.34}$$

Decomposing the estimated channel $\tilde{\mathrm{H}}^{\mathrm{MMSE}(n',m')}_{ab}$ would result in

$$\underline{\tilde{\mathrm{H}}}^{\mathrm{MMSE}}_{ab} = \underline{\tilde{\mathrm{H}}}^{\min}_{ab} \left(\underline{\tilde{\mathrm{H}}}^{\mathrm{ap}}_{ab}\right)^2. \tag{4.35}$$

4.1.3.3. Computational complexity analysis

The total system design of the proposed security method includes Z-transform, $H^{\min}(z)$ estimation, $H^{\mathrm{ap}}(z)$ estimation, and precoding at both transmitter and receiver. Accordingly, the computational complexity is calculated considering the number of multiplications. For instance, the Z-transform converts a discrete-time signal, which is a sequence of real or complex numbers, into a complex frequency-domain representation as follows

$$H(z) = \sum_{\nu=-\infty}^{\infty} h(\nu) z^{-\nu}, \tag{4.36}$$

where n is an integer and z is, in general, a complex number. The wireless channel is a causal finite system with maximum L taps, therefore

$$H(z) = \sum_{\nu=0}^{L-1} h(\nu) z^{-\nu}. \tag{4.37}$$

After obtaining the Z-transform of the wireless channel, the zeros of the resultant polynomial are computed to calculate the minimum-phase component of the channel. Furthermore, the arithmetic complexity of approximating to all the zeros of a polynomial $H(z)$ is $O(L \log L \log(bL))$ [119], where b is the bit size. After, computing the zeros of $H(z)$, the zeros outside the unit circle with value $1/p_k$ are selected; then, the all-pass part is computed as follows

$$H^{\mathrm{ap}}(e^{j\omega}) = \prod_{k=1}^{q} \left(\frac{e^{-j\omega} - p_k}{1 - p_k^* e^{-j\omega}} \right), \tag{4.38}$$

where $1 \leq q \leq L$. The maximum complexity of computing **(4.38)** is $O(2NL)$. The minimum-phase part is found straight forward by using element-wise division as $H^{\min}(e^{j\omega}) = H(e^{j\omega})/H^{\mathrm{ap}}(e^{j\omega})$, which has complexity of $O(N)$. The precoder applies element-wise multiplication for each subcarrier, thus its complexity is of order $O(N)$. Then, for single antenna pair (n, m) the total computational complexity is of order $O\left(2N(L+1) + L \log L \log(bL)\right)$. Considering the total MIMO system the total complexity becomes $O\left(2M_a N_b \left(2N(L+1) + L \log L \log(bL)\right)\right)$. **Table 4.1** summarizes the computational complexity of each component.

4.2. Common CP-OFDM Transceiver Design For Low-Complexity Frequency Domain Equalization

4.2.1. Problem formulation

In conventional CCP-OFDM, At the tth symbol time, the CCP-OFDM transmitter converts M OFDM symbols $\underline{\mathrm{S}}_m(k),\ k = 1, \ldots, N,\ m = 1, \ldots, M$ comprising N orthogonal subcarriers from frequency-domain to $\underline{\mathrm{x}}_m(n),\ n = 1, \ldots, N$ in time-domain using the inverse discrete Fourier transform (IDFT). To combat ISI, one CP is appended to the modulated signal $\underline{\mathrm{x}} = [\underline{\mathrm{x}}_1^T, \ldots, \underline{\mathrm{x}}_M^T]^T$ and then it is transmitted [34]. At the receiver side, after discarding the CP, the received signal can be expressed as

$$\underline{\mathrm{y}} = \mathrm{H}_c(\mathrm{I}_M \otimes \mathrm{F}_N^{-1})\underline{\mathrm{x}}, \tag{4.39}$$

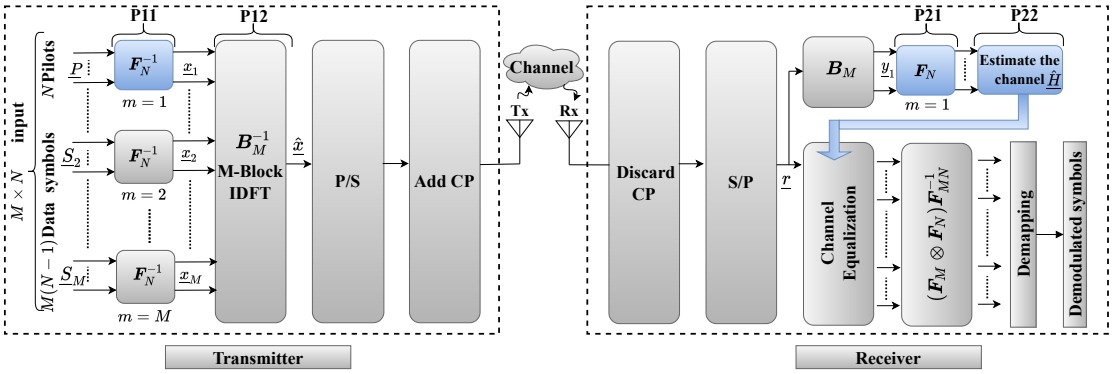


Figure 4.6: The transceiver design for the proposed pilot-based channel estimation scheme.

where $\mathrm{H}_c \in \mathbb{C}^{MN\times MN}$ denotes the circulant channel matrix, $\mathrm{F}_N \in \mathbb{C}^{N\times N}$ is the unitary DFT matrix, and I_M represents the $M \times M$ identity matrix. If an inverse operation is applied at the transmitter, as in CP-OFDM, we find

$$\underline{\mathrm{Y}} = (\mathrm{I}_M \otimes \mathrm{F}_N)\mathrm{H}_c(\mathrm{I}_M \otimes \mathrm{F}_N^{-1})\underline{\mathrm{x}}, \tag{4.40}$$

Note that although $\underline{\mathrm{Y}}$ is sufficient statistics for channel estimation, $(\mathrm{I}_N \otimes \mathrm{F}_M)\mathrm{H}_c(\mathrm{I}_N \otimes \mathrm{F}_M^{-1})$ is not a diagonal matrix; thus, the estimation of CFR as in conventional OFDM is not straightforward in the frequency domain. As a result, complex time-domain equalizers are used for CCP-OFDM.

4.2.2. Proposed CCP-OFDM scheme

4.2.2.1. Proposed transmitter design

Differently from the conventional CCP-OFDM transceiver, in the proposed design, we introduce two successive processes (i.e., process P11 and process P12) at both transmitter and receiver sides, as depicted in **Figure 4.6**, in order to ensure the diagonality of the effective channel matrix, as follows

- In process P11, for each mth OFDM symbol an IDFT is applied for modulation as follows

$$\underline{\mathrm{x}}_m = \mathrm{F}_N^{-1}\underline{\mathrm{S}}_m, \tag{4.41}$$

- Process P12 performs a $M \times M$ block-IDFT process on the output of process P11

denoted by the block-DFT operator B_M, which is a DFT process that takes complex vectors as an input instead of complex values. It can be explicitly represented as $\mathrm{B}_M = \mathrm{F}_M \otimes \mathrm{I}_N$. Then, the transmitted signal is found as

$$\begin{aligned} \underline{\hat{\mathrm{x}}} &= \left(\mathrm{F}_M^{-1} \otimes \mathrm{I}_N\right) \times \left(\mathrm{I}_M \otimes \mathrm{F}_N^{-1}\right) \underline{\mathrm{S}} \\ &= \left(\mathrm{F}_M^{-1} \otimes \mathrm{F}_N^{-1}\right) \underline{\mathrm{S}}, \end{aligned} \tag{4.42}$$

where $\underline{\mathrm{S}} = [\underline{\mathrm{S}}_1^T, \underline{\mathrm{S}}_2^T, \ldots, \underline{\mathrm{S}}_M^T]^T$.

4.2.2.2. Proposed pilot design

In the proposed CCP-OFDM system, N known pilots $\underline{\mathrm{P}} \in \mathbb{C}^{N\times 1}$ are used for channel estimation, where the rest symbols $\underline{\mathrm{S}}_m$, $m = 2, \ldots, M$ are used for data transmission. These pilots occupy the first OFDM symbol out of the M symbols. Thus, the unmodulated transmitted signal becomes $\underline{\mathrm{S}} = [\underline{\mathrm{P}}^T, \underline{\mathrm{S}}_2^T, \ldots, \underline{\mathrm{S}}_M^T]^T$.

4.2.2.3. The wireless channel

The wireless channel is assumed to be slow time-varying, i.e., CIR is invariant for each CCP-OFDM symbol, with N_{tap} path components [34]. Also, the number of pilots is assumed to be $N \geq N_{tap}$. Then, the received signal after discarding the CP is expressed as

$$\begin{aligned} \underline{\mathrm{r}} &= \underline{\mathrm{h}} \circledast \underline{\hat{\mathrm{x}}} + \underline{\mathrm{z}} \\ &= \mathrm{H}_c \underline{\hat{\mathrm{x}}} + \underline{\mathrm{z}}, \end{aligned} \tag{4.43}$$

where $\underline{\mathrm{z}}$ denotes the zero-mean AWGN vector with variance σ^2, and $\underline{\mathrm{h}} = [h_1, \ldots, h_{N_{tap}}]^T$ represents the CIR. H_c is given as

$$\mathrm{H}_c = \begin{bmatrix} h_1 & 0 & 0 & \cdots & h_{N_{tap}} & h_{N_{tap}-1} \cdots & h_2 \\ h_2 & h_1 & 0 & \cdots & 0 & h_{N_{tap}-1} \cdots & h_3 \\ \vdots & & & \ddots & & & \vdots \\ 0 & \cdots & 0 & h_{N_{tap}} & h_{N_{tap}-1} & \cdots & h_1 \end{bmatrix}. \tag{4.44}$$

The channel matrix H_c is a block circulant matrix with M blocks, each of size $N \times N$;

therefore, H_c can be rewritten as

$$H_c = \begin{bmatrix} H_1 & O & O & \cdots & H_2 \\ H_2 & H_1 & O & \cdots & O \\ \vdots & & \ddots & & \vdots \\ O & \cdots & O & H_2 & H_1 \end{bmatrix}, \tag{4.45}$$

where $O \in \mathbb{C}^{N\times N}$ denotes the zeros matrix, and $H_1 \in \mathbb{C}^{N\times N}$ and $H_2 \in \mathbb{C}^{N\times N}$ are given by

$$H_1 = \begin{bmatrix} h_1 & 0\ 0 & \cdots 0 \\ \vdots & \ddots & \vdots \\ h_{N_{tap}} & \cdots & h_1 \cdots 0 \\ \vdots & \ddots & \vdots \\ 0 \cdots & h_{N_{tap}} & \cdots h_1 \end{bmatrix}, H_2 = \begin{bmatrix} 0 \cdots 0 & h_{N_{tap}} \cdots & h_2 \\ \vdots & \ddots & \vdots \\ 0 \cdots 0 & \cdots & 0 \end{bmatrix}. \tag{4.46}$$

It should be noticed that $\mathfrak{H} = H_1 + H_2$ is also a circulant matrix and it is a sufficient statistic for estimating H_c. Therefore, in order to estimate the CFR estimating $\mathfrak{H}$ is sufficient.

4.2.2.4. Proposed receiver design

As shown in **Figure 4.6** at the receiver side, there are two DFT processes (i.e., process P21 and P22) after discarding the CP. Let $\underline{y}$ be the output of the block DFT process, then

$$\begin{aligned} \underline{y} &= B_M \underline{r} = B_M H_c B_M^{-1} \underline{x} + B_M \underline{z} \\ &= H_D \underline{x} + B_M \underline{z}. \end{aligned} \tag{4.47}$$

The added DFTs are block-based DFTs i.e., each submatrix in H_c is treated as one single element and the block DFT matrix B_M serves to block-diagonalize H_c. therefore, H_D is a block diagonal matrix given by

$$H_D = \begin{bmatrix} H_{D_1} & O & O & \cdots & O \\ O & H_{D_2} & O & \cdots & O \\ \vdots & & \ddots & & \vdots \\ O & \cdots & O & O & H_{D_N} \end{bmatrix}, \tag{4.48}$$

where $H_{D_1} = \mathfrak{H}$.

Algorithm 4.4 Proposed channel estimation algorithm.

Input: Received noisy signal $\underline{y}$ in **(4.43)** with pilot design shown in **Figure 4.6**.
Output: Estimated channel $\hat{\underline{H}}$.
1- Reshape $\underline{r}$ into M signals.
2- Perform M block DFT on $\underline{r} \rightarrow \underline{y} = [\underline{y}_1^T, \ldots, \underline{y}_M^T]^T$.
3- Perform N DFT on the first N samples of $\underline{y}_1 \rightarrow \hat{\underline{y}}_1$.
4- Estimate the channel using **(4.51)**.

4.2.2.5. Channel estimation scheme

In order to estimate the channel, only the first N samples of $\underline{y}$ denoted by $\underline{y}_1 = [y(1), \ldots, y(N)]^T$ are considered for the channel estimation. Then, the output of the second process P22 is given by

$$\begin{aligned} \hat{\underline{y}}_1 &= \mathrm{F}_N \underline{y}_1 = \mathrm{F}_N \mathbf{\mathfrak{H}} \mathrm{F}_N^{-1} \underline{\mathrm{P}} + \mathrm{F}_N \underline{z}_1 \\ &= \mathrm{P} \underline{\mathrm{H}}_N + \mathrm{F}_N \underline{z}_1, \end{aligned} \tag{4.49}$$

where $\underline{z}_1$ contains the first N samples of $\mathrm{B}_M \underline{z}$, $\mathrm{P} = \mathrm{diag}(\underline{\mathrm{P}})$, and $\underline{\mathrm{H}}_N$ is the N point CFR of the wireless channel given by

$$\underline{\mathrm{H}}_N = \mathrm{F}_N \underline{\mathrm{h}}. \tag{4.50}$$

After acquiring **(4.256)**, conventional OFDM channel estimation algorithms can be applied, such as MMSE and link-signature (LS) estimators [120]. Since one of main contributions of this work is enabling linear low-complexity frequency domain channel estimation, in this thesis, the LS estimator is used for the estimation of the CFR due to its simple structure.

Let $\underline{\mathrm{H}} = [H(1), \ldots, H(MN)]^T$ be the CFR vector, then the estimated channel $\hat{\underline{\mathrm{H}}}$ is readily found as

$$\begin{aligned} \hat{\underline{\mathrm{H}}} &= \mathrm{F}_{MN} \mathrm{Z}_{MN} \mathrm{F}_N^{-1} \mathrm{P}^{-1} \hat{\underline{y}}_1 \\ &= \underline{\mathrm{H}} + \tilde{\underline{z}}_1, \end{aligned} \tag{4.51}$$

where Z_{MN} denotes the zero-padding matrix and $\tilde{\underline{z}}_1 = \mathrm{F}_{MN} \mathrm{Z}_{MN} \mathrm{F}_N^{-1} \mathrm{P}^{-1} \mathrm{F}_N \underline{z}_1$. The channel estimation algorithm for the proposed system is summarized in **Algorithm 4.4**.

4.2.2.6. Data detection

For data demodulation of each OFDM symbol the same steps as in conventional CCP-OFDM demodulation are followed. First, the whole received frame is equalized in frequency domain to get rid of the channel effect. Then, it is converted back to time domain, and finally N point DFT demodulation for each M OFDM symbols is performed [34].

Specifically, the received signal in **(4.42)** can be written as

$$\underline{\mathrm{r}} = \mathrm{H}_c \mathrm{F}_{MN}^{-1} \mathrm{F}_{MN} \hat{\underline{\mathrm{x}}} + \underline{\mathrm{z}}. \tag{4.52}$$

Then, a $MN \times MN$ DFT is applied on **(4.52)** and we find

$$\mathrm{F}_{MN} \underline{\mathrm{r}} = \mathrm{diag}(\underline{\mathrm{H}}) \mathrm{F}_{MN} \hat{\underline{\mathrm{x}}} + \mathrm{F}_{MN} \underline{\mathrm{z}}. \tag{4.53}$$

Next, single tap per-subcarrier equalization is used to mitigate the channel effect, the equalized signal is then

$$\underline{\mathrm{r}}_{eq} = \mathrm{F}_{MN} \hat{\underline{\mathrm{x}}} + \mathrm{diag}(\underline{\mathrm{H}})^{-1} \mathrm{F}_{MN} \underline{\mathrm{z}}. \tag{4.54}$$

Finally, the transmitted data is estimated by inverting the operations performed at the transmitter and receiver as follows

$$\hat{\underline{\mathrm{S}}} = (\mathrm{F}_M \otimes \mathrm{F}_N)\, \mathrm{F}_{MN}^{-1} \underline{\mathrm{r}}_{eq}. \tag{4.55}$$

4.2.2.7. Computational complexity analysis

To analyze the complexity of the proposed scheme, transmitter, receiver, and channel estimation's computational complexities are considered. For a fair comparison, we assume MN data symbols to be transmitted for CP-OFDM, conventional CCP-OFDM, and the proposed CCP-OFDM which use MMSE, maximum likelihood (ML), and LS estimators, respectively. The proposed CCP-OFDM implements M(N-DFT) + N(M-DFT)+MN-DFT at both transmitter and receiver. Conventional CCP-OFDM implements MN-DFT and MN-DFT+ MN-DFT at the transmitter and receiver, respectively. Finally, conventional OFDM implements MN-DFT at both transmitter and receiver. The complexity of α-DFT is calculated for each α as in [121].

Additionally, three channel estimators are used, namely, MMSE, LS, and ML estimators [34], [122]. To determine the computational complexity only the number of multiplications is considered. $O\left(h_{\mathrm{MMSE}}\right)$, $O\left(h_{\mathrm{LS}}\right)$ and $O\left(h_{\mathrm{ML}}\right)$ denote the complexity of

MMSE, LS and ML, respectively. As given in [122], $O\left(h_{\mathrm{MMSE}}\right)$ is the summation of the computational complexity of six operations, and is readily given by

$$O\left(h_{\mathrm{MMSE}}\right) = 2MN\log_2(MN) + (5(MN)^2 + 1)(MN + 1). \tag{4.56}$$

$O\left(h_{\mathrm{LS}}\right)$ is expressed as

$$O\left(h_{\mathrm{LS}}\right) = MN + (MN)^2 = MN(1 + MN). \tag{4.57}$$

The computational complexity of ML is given readily as in [34] by

$$\begin{aligned} O\left(h_{\mathrm{ML}}\right) = {} & 2N^2 + N^3 + 2MN\left\lfloor \log_2 P \right\rfloor - 2MN - 4P \\ & + 4 + \frac{2MNP}{2^{\lfloor \log_2 P \rfloor}}, \end{aligned} \tag{4.58}$$

where the function $\lfloor \cdot \rfloor$ returns the integer part of an argument and P denotes the CP length. Note that the term $2N^2 + N^3$ arises from double multiplication and the inverse operations of $N \times N$ matrices.

4.2.2.8. Peak to average power ratio analysis

Each sample of the discrete time representation of the transmitted signal $\underline{r}$ given by

$$r(n + qN) = \frac{1}{\sqrt{MN}} \sum_{m=0}^{M-1} \sum_{k=0}^{N-1} S_m(k) e^{j\frac{2\pi nk}{N}} e^{j\frac{2\pi qm}{M}}. \tag{4.59}$$

where $n = 0, 1, \ldots, N-1$ and $q = 0, 1, \cdots, M-1$. From **(4.59)**, it can be seen that the time domain samples of the proposed transmitted signal is nothing but the N and M-point IDFT values of the symbols in the time-frequency domain. Hence, if N and M are large, then by central limit theorem, the transmitted samples can be approximated to have complex Gaussian distribution with zero mean.

Assuming the transmitted samples to be mutually uncorrelated, the probability that the PAPR of the transmit CCP-OFDM signal in a frame does not exceed γ_0 is given by $P\left(\mathrm{PAPR} \le \gamma_0\right) \approx \prod_{i=0}^{NM-1}\left(1 - e^{-\gamma_0}\right) = \left(1 - e^{-\gamma_0}\right)^{MN}$. This can be written as [123]

$$P\left(\text{ PAPR } > \gamma_0\right) \approx 1 - \left(1 - e^{-\gamma_0}\right)^{MN} \tag{4.60}$$

On the other hand, the probability that the PAPR is below some threshold level for an

OFDM signal with $M \times N$ subcarriers can be written as [123]

$$P(\mathrm{PAPR} > \gamma_0) = 1 - (1 - e^{-\gamma_0})^{MN} . \quad \textbf{(4.61)}$$

From **(4.60)** and **(4.61)** we conclude that the PAPR of the proposed scheme is the same as of the conventional CP-OFDM if if N and M are large.

4.3. A Novel Cyclic Prefix Configuration For Enhanced Reliability And Spectral Efficiency In OTFS Systems

4.3.1. System model

4.3.1.1. Transmitter

Consider a wireless communication system where $M \times N$ data symbols are modulated using OTFS transform. The OTFS modulator distributes these symbols $\{X_{\mathrm{DD}}(l,k), l = 0,\ldots,M-1\ ,\ k = 0,\ldots,N-1\}$ in the 2D delay-Doppler grid which is discretized into M delays and N Dopplers. Then, the samples $X_{\mathrm{DD}}(l,k)$ are converted to the time–frequency domain grid $\{X_{\mathrm{TF}}(n,m),\ n = 0,\ldots,N-1,\ m = 0,\ldots,M-1\}$ using the inverse symplectic finite Fourier transform (ISFFT) as follows

$$X_{\mathrm{TF}}(n,m) = \frac{1}{\sqrt{MN}} \sum_{l=0}^{M-1} \sum_{k=0}^{N-1} X_{\mathrm{DD}}(l,k) e^{j2\pi\left(\frac{nk}{N} - \frac{ml}{M}\right)}. \quad \textbf{(4.62)}$$

To cast **(4.189)** from serial to matrix-vector form, we define F_N to be an $N \times N$ unitary DFT matrix; therefore, **(4.189)** is rewritten as

$$\mathrm{X_{TF}} = \mathrm{F}_M \mathrm{X_{DD}} \mathrm{F}_N^H. \quad \textbf{(4.63)}$$

Next, $\mathrm{X_{TF}}$ is converted to time domain signal s by applying the Heisenberg transform as follows

$$\mathrm{s} = \mathrm{vec}\,(\mathrm{S}) = (\mathrm{F}_N^H \otimes \mathrm{I}_M)\mathrm{x}, \quad \textbf{(4.64)}$$

where $\mathrm{S} = \mathrm{X_{DD}} \mathrm{F}_N^H$, $\mathrm{x} = \mathrm{vec}\,(\mathrm{X_{DD}})$, and I_M denotes the $M \times M$ identity matrix. Then, s is transmitted over the channel.

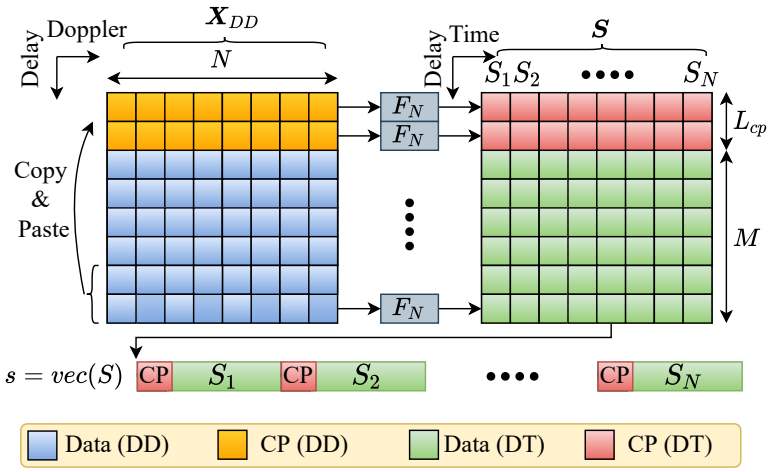


Figure 4.7: The CP addition in full-CP (FCP)-OTFS systems in both delay-Doppler and time domains.

4.3.1.2. Channel

Consider the L-tap doubly-selective CIR, modeling L propagation paths in the dynamic environment as follows

$$h(\tau, \nu) = \sum_{i=0}^{L-1} h_i \delta(\tau - \tau_i)\delta(\nu - \nu_i), \tag{4.65}$$

where h_i, $\tau_i = \frac{l_i}{M\Delta f}$ and $\nu_i = \frac{k_i}{NT}$ denote the complex channel gain, delay, and Doppler shift corresponding to the i-th path, respectively.

4.3.1.3. Receiver

The received time-frequency signal $Y_{\mathrm{TF}}(n, m)$ is converted back to delay-Doppler domain via symplectic finite Fourier transform (SFFT), as follows

$$Y_{\mathrm{DD}}(l, k) = \sum_{n=0}^{N-1} \sum_{m=0}^{M-1} Y(n, m) e^{-j2\pi\left(\frac{nk}{N} - \frac{ml}{M}\right)}. \tag{4.66}$$

The input-output relation can be derived as

$$\begin{aligned} \mathrm{y} &= \mathrm{H}_{\mathrm{eff}}\mathrm{x} + \mathrm{w} \\ &= (\mathrm{F}_N \otimes \mathrm{I}_M)\mathrm{H}(\mathrm{F}_N^H \otimes \mathrm{I}_M)\mathrm{x} + \mathrm{w}, \end{aligned} \tag{4.67}$$

where $\mathrm{y} = \mathrm{vec}(\mathrm{Y}_{\mathrm{DD}})$, $\mathrm{H}_{\mathrm{eff}} \in \mathbb{C}^{MN \times MN}$ denotes the delay-Doppler effective channel matrix, and $\mathrm{H} \in \mathbb{C}^{MN \times MN}$ represents the time equivalent channel matrix.

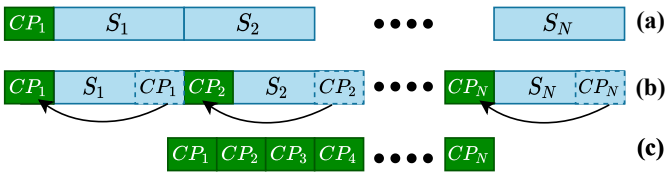


Figure 4.8: Different prefix/suffix configurations in OTFS systems: (a) RCP (b) FCP (c) Equivalent discarded CP signal in FCP-OTFS.

4.3.1.3.1 Reduced-CP (RCP)-OTFS case

In RCP OTFS systems, only one CP is appended to the whole orthogonal time-frequency space (OTFS) frame (see **Figure 4.8a**); therefore, $\mathrm{H}^{\mathrm{R_{cp}}}$ is expressed as

$$\mathrm{H}^{\mathrm{R_{cp}}} = \sum_{i=0}^{L-1} h_i \mathbf{\Pi}_{MN}^{l_i} \mathbf{\Delta}_{MN}^{k_i}, \tag{4.68}$$

where $\mathbf{\Pi}_{MN}^{l_i}$ is the $MN \times MN$ permutation matrix with $\Pi_{MN}^{l_i}(l,k) = \delta([l-k]_N - l_i)$, and $\mathbf{\Delta}_{MN}$ represents the $MN \times MN$ diagonal matrix

$$\mathbf{\Delta}_{MN}^{k_i} = \mathrm{diag}\left[z_i^0, z_i^1, \ldots, z_i^{(MN-1)}\right], \tag{4.69}$$

with $z_i = e^{\frac{j2\pi k_i}{MN}}$. Then, the effective channel can be found as

$$\mathrm{H}_{\mathrm{eff}}^{\mathrm{R_{cp}}} = (\mathrm{F}_N \otimes \mathrm{I}_M)\mathrm{H}^{\mathrm{R_{cp}}}(\mathrm{F}_N^H \otimes \mathrm{I}_M), \tag{4.70}$$

Next, the input-output relationship for each received sample $Y_{\mathrm{DD}}^{\mathrm{R_{cp}}}(l,k)$ can be found as [124, eq.(30)]

$$\begin{aligned} Y_{\mathrm{DD}}^{\mathrm{R_{cp}}}(l,k) = \sum_{i=0}^{L-1} & h_i e^{j2\pi \frac{k_i}{N}\frac{l-l_i}{M}} \Lambda_i(l,k) \\ & \times X_{\mathrm{DD}}\left([l-l_i]_M, [k-k_i]_N\right), \end{aligned} \tag{4.71}$$

where

$$\Lambda_i(l,k) = \begin{cases} 1 & l_i \le l < M \\ e^{-j2\pi \frac{k}{N}} & 0 \le l < l_i \end{cases}. \tag{4.72}$$

4.3.1.3.2 FCP-OTFS case

In FCP OTFS systems, N CPs of length $L_{\mathrm{cp}} \ge L$ are used to protect each OTFS subsymbol as in OFDM modulation (see **Figure 4.8b**). Particularly, the $(M + L_{\mathrm{cp}})N \times (M + L_{\mathrm{cp}})N$

channel matrix in this case can be given as

$$\hat{\mathrm{H}}^{\mathrm{F_{cp}}} = \sum_{i=0}^{L-1} h_i \boldsymbol{\Pi}^{l_i}_{(M+L_{\mathrm{cp}})N} \boldsymbol{\Delta}^{k_i}_{(M+L_{\mathrm{cp}})N}. \tag{4.73}$$

After discarding the CPs, the channel matrix $\hat{\mathrm{H}}^{\mathrm{F_{cp}}}$ becomes a block diagonal matrix with N blocks, each of size $M \times M$ given as

$$\mathrm{H}^{\mathrm{F_{cp}}} = \mathrm{diag}\left(\mathrm{H}_0^{\mathrm{F_{cp}}}, \ldots, \mathrm{H}_{N-1}^{\mathrm{F_{cp}}}\right), \tag{4.74}$$

where $\mathrm{H}_n^{\mathrm{F_{cp}}} = \sum_{i=0}^{L-1} h_i \boldsymbol{\Pi}_M^{l_i} \boldsymbol{\Delta}_M^{k_i,n}$, and

$$\boldsymbol{\Delta}_M^{k_i,n} = \mathrm{diag}\left[z_i^{n(M+L_{\mathrm{cp}})+L_{\mathrm{cp}}}, \ldots, z_i^{((n+1)(M+L_{\mathrm{cp}})-1)}\right]. \tag{4.75}$$

The input-output relationship for each received sample $Y_{\mathrm{DD}}^{\mathrm{F_{cp}}}(l,k)$ for the FCP structure can be derived as [125, eq.(14)]

$$Y_{\mathrm{DD}}^{\mathrm{F_{cp}}}(l,k) = \sum_{i=0}^{L-1} h_i e^{\frac{j2\pi k_i (L_{\mathrm{cp}}+l-l_i)}{(M+L_{\mathrm{cp}})N}} X_{\mathrm{DD}}\left([l-l_i]_M, [k-k_i]_N\right). \tag{4.76}$$

4.3.2. Proposed FCP-OTFS

In this section, CP addition in OFDM and FCP-OTFS systems are compared. Then, the relationship between the CP block in time and delay-Doppler in OTFS system is presented. Finally, a novel OTFS CP structure is proposed.

4.3.2.1. CP addition in OFDM

Consider $\mathrm{P}^{\mathrm{F_{cp}}} \in \mathbb{C}^{(M+L_{\mathrm{cp}})\times M}$ the CP addition matrix [126], the 2D transmit OFDM signal $\mathrm{S}_{\mathrm{OFDM}}^{\mathrm{F_{cp}}} \in \mathbb{C}^{(M+L_{\mathrm{cp}})\times N}$ can be given as follows

$$\begin{aligned} \mathrm{S}_{\mathrm{OFDM}}^{\mathrm{F_{cp}}} &= \mathrm{P}^{\mathrm{F_{cp}}} \mathrm{S}_{\mathrm{OFDM}} = \mathrm{P}^{\mathrm{F_{cp}}} \mathrm{F}_M^H \mathrm{X}_{\mathrm{OFDM}} \\ &= \mathrm{F}_M^{\mathrm{F_{cp}}} \mathrm{X}_{\mathrm{OFDM}}, \end{aligned} \tag{4.77}$$

where $\mathrm{F}_M^{\mathrm{F_{cp}}} = \mathrm{P}^{\mathrm{F_{cp}}} \mathrm{F}_M^H$ represents the $(M+L_{\mathrm{cp}})\times M$ cyclic extended inverse-DFT matrix, and both $\mathrm{S}_{\mathrm{OFDM}}$ and $\mathrm{X}_{\mathrm{OFDM}}$ are of size $M \times N$. Then, the CP block (which is illustrated in **Figure 4.7** by the red block in delay-time domain) can be written as

$$\mathrm{S}_{\mathrm{OFDM}}^{\mathrm{cp}} = \mathcal{F}_M^H \mathrm{X}_{\mathrm{OFDM}}, \tag{4.78}$$

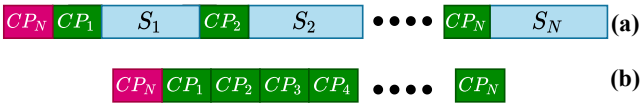


Figure 4.9: Proposed FCP OTFS frame.

where $\mathcal{F}_M^H \in \mathbb{C}^{(L_{\text{cp}})\times M}$ denotes the last L_{cp} rows of F_M^H. It is clearly seen that **(4.78)** is a linear equation system with infinite solutions since the number of unknowns is larger than the number of equations i.e., $M \times N > L_{\text{cp}} \times N$. This is the reason why the CP block is discarded in OFDM systems.

4.3.2.2. CP addition in FCP-OTFS

Consider the 2D transmitted delay-Doppler FCP-OTFS signal $\text{S}^{\text{F}_{\text{cp}}} \in \mathbb{C}^{(M+L_{\text{cp}})\times N}$ as follows

$$\begin{aligned}\text{S}^{\text{F}_{\text{cp}}} &= \text{P}^{\text{F}_{\text{cp}}}\text{S} = \text{P}^{\text{F}_{\text{cp}}}\text{X}_{\text{DD}}\text{F}_N^H \\ &= \text{X}_{\text{DD}}^{\text{F}_{\text{cp}}}\text{F}_N^H,\end{aligned} \tag{4.79}$$

where $\text{X}_{\text{DD}}^{\text{F}_{\text{cp}}} = \text{P}^{\text{F}_{\text{cp}}}\text{X}_{\text{DD}}$ represents the $(M+L_{\text{cp}})\times N$ extended OTFS frame in the delay-Doppler domain. Therefore, adding FCP is equivalent to extending the delay-Doppler grid to $(M+L_{\text{cp}})\times N$ by repeating the last L_{cp} rows of X_{DD}. **Figure 4.7** graphically illustrates the relationship between adding the CP in delay-Doppler and time domains in FCP OTFS system.

The CP block in FCP-OTFS can be written as

$$\text{S}^{\text{cp}} = \mathcal{X}_{\text{DD}}\text{F}_N^H, \tag{4.80}$$

where $\mathcal{X}_{\text{DD}} \in \mathbb{C}^{(L_{\text{cp}})\times N}$ denotes the last L_{cp} rows of X_{DD}. It is clearly seen that **(4.80)** is a solvable linear equation system with number of unknowns equals to the number of equations i.e., $L_{\text{cp}} \times N = L_{\text{cp}} \times N$. Therefore, the CP block in FCP-OTFS is interpretable and conveys data that can be extracted and decoded. **Figure 4.8c** depicts the equivalent transmitted signal of the FCP-OTFS CP block.

4.3.2.3. Proposed FCP OTFS

In this subsection, a novel OTFS CP configuration is proposed in which one RCP is appended to the FCP OTFS frame as depicted in **Figure 4.9a**. We call this type of mixed

CP configuration proposed FCP-OTFS. By doing so, we ensure that both the symbols in the data block ($M \times N$ symbols) and symbols in the CP block ($N \times L_{\text{cp}}$ symbols) can be decoded. Specifically, at the receiver side, only the added reduced-CP is discarded, then the received samples are reshaped and converted to delay-Doppler domain as follows

$$Y_{\text{DD}}(l,k) = \begin{cases} Y_{\text{cp}}^{R_{\text{cp}}}(l,k), & \text{if } l \leq l_{\text{cp}} \\ Y_{\text{cp}}^{F_{\text{cp}}}(l,k), & \text{if } l > l_{\text{cp}} \end{cases}. \tag{4.81}$$

From (**4.81**), it is observed that the received delay-Doppler data signal $Y_{\text{cp}}^{F_{\text{cp}}}(l,k)$ is ISI-free and follows the model of FCP-OTFS as given in (**4.76**). On the contrary, the repeated data $Y_{\text{cp}}^{R_{\text{cp}}}(l,k)$ in the CP block follows the model of RCP-OTFS as seen in (**4.71**) which is illustrated in **Figure 4.9b**. The proposed scheme can also be viewed as transmitting data in the form of a FCP-OTFS signal in the delay-Doppler domain, where the final portion of the data along the delay axis is repeated and overlaid on top of the 2D data frame. Then, prior to transmission, a RCP is added in the time domain.

The proposed FCP-OTFS configuration allows the exploitation of the information contained in the CPs, unlike in OFDM systems as explained in **Subsection 4.3.2.2**. For instance, the repeated data in the proposed FCP can be used to provide diversity between the transmitted data symbols. A user with high-reliability requirements can be allocated the last rows of the delay-Doppler data matrix, which will be repeated in the CP block. At the receiver side, the user decodes the data block and the CP block together and gets two copies of his transmitted data. Also, proposed FCP-OTFS can be used to reduce the guard interval dedicated for pilot to half by locating the pilot at the end part of the delay-Doppler grid.[3]

4.4. Fractional Doubly-Dispersive Channel Estimation And Mitigation Framework In OTFS Systems

4.4.1. System model

In this section, the OTFS system model, comprising transmitter, channel, and receiver, is introduced. Then, the input-output relationship of the received signal is investigated for various doubly-dispersive channel scenarios.

[3]Note that these two use examples are only one of many possible use cases of proposed FCP-OTFS.

4.4.1.1. Transmitter

Consider $M \times N$ information symbols $\{X(l,k),\ l = 0,\ldots,M-1;\ k = 0,\ldots,N-1\}$ distributed over the two-dimensional (2D) delay-Doppler grid. These symbols are modulated and mapped onto 2D time-frequency domain $\{\mathcal{X}[m,n],\ m = 0,\ldots,M-1;\ n = 0,\ldots,N-1\}$ using OTFS modulation. M and N refer to total delay and Doppler bins, respectively. The delay-Doppler symbols are converted to the time-frequency grid $X[n,m]$ via the ISFFT as follows

$$\mathcal{X}[m,n] = \frac{1}{\sqrt{MN}} \sum_{l=0}^{M-1} \sum_{k=0}^{N-1} X(l,k) e^{j2\pi\left(\frac{nk}{N} - \frac{ml}{M}\right)}. \tag{4.82}$$

The time-frequency grid sampling intervals can be defined by T symbol duration and $\Delta f = 1/T$ subcarrier spacing. Therefore, total symbol duration and bandwidth are represented as NT and $M\Delta f$, respectively. This implies a spacing of $\frac{1}{M\Delta f}$ and $\frac{1}{NT}$ between adjacent delay and Doppler bins, respectively.

Using Heisenberg transform, $\mathcal{X}[m,n]$ can be transformed to one-dimensional time domain signal $s(t)$ as follows

$$s(t) = \sum_{n=0}^{N-1} \sum_{m=0}^{M-1} \mathcal{X}[m,n] e^{j2\pi m\Delta f(t-nT)} g_{\mathrm{tx}}(t-nT), \tag{4.83}$$

where g_{tx} is the transmitted pulse shape. Considering that rectangular pulse shapes are used at both transmitter and receiver, the transmitted signal can be expressed as

$$s(t) = \sum_{n=0}^{N-1} \sum_{m=0}^{M-1} \mathrm{rect}\left(\frac{t-nT}{T}\right) \mathcal{X}[m,n] e^{j2\pi m\Delta f(t-nT)} \tag{4.84}$$

where rect (t) is the rectangular pulse function. Finally, in order to combat the channel effect and provide circularity, we append a CP of length M_{cp} as given in [18]. To cast **(4.189)** from serial to matrix-vector form, we define F_N to be the $N \times N$ unitary DFT matrix; therefore, **(4.189)** is rewritten as

$$\mathrm{X}_{\mathrm{TF}} = \mathrm{F}_M \mathrm{X}_{\mathrm{DD}} \mathrm{F}_N^H. \tag{4.85}$$

Next, X_{TF} is converted to time signal s by applying the Heisenberg transform. Then, s is transmitted over the doubly-dispersive channel as follows

$$\mathrm{s} = \mathrm{vec}\,(\mathrm{S}) = (\mathrm{F}_N^H \otimes \mathrm{I}_M)\mathrm{x}, \tag{4.86}$$

where $\mathrm{S} = \mathrm{X}_{\mathrm{DD}}\mathrm{F}_N^H$, $\mathrm{x} = \mathrm{vec}\,(\mathrm{X}_{\mathrm{DD}})$, and I_M denotes the $M \times M$ identity matrix.

4.4.1.2. Wireless channel

Consider the doubly-dispersive channel with L-taps modeling L reflectors in the propagation environment as follows

$$h(\tau, \nu) = \sum_{i=0}^{L-1} h_i \delta(\tau - \tau_i)\delta(\nu - \nu_i), \tag{4.87}$$

where h_i and L denote the complex channel gain and number of propagation paths, respectively. The delay and Doppler shifts corresponding the i-th reflector with l_i and k_i integer delay and Doppler indices are respectively given by $\tau_i = \frac{l_i + \iota_i}{M\Delta f}$ and $\nu_i = \frac{k_i + \kappa_i}{NT}$ where ι_i and $\kappa_i \in [-0.5, 0.5]$ represent the fractional delay and Doppler indices of the i-th path of the channel.

For channel estimation, in this thesis, the impulse-based channel estimation is adopted [55], where one pilot X_p having $\mathrm{SNR}_p = |X_p|^2/\sigma^2$ is placed in the delay-Doppler grid surrounded by guard symbols (σ^2 denotes the noise variance). The guard is inserted to insure that no interference occurs between the data symbols and the pilot after passing through the channel. Therefore, the guard and pilot arrangement differs depending on the channel scenarios.

4.4.1.3. Receiver

The transmit signal passes through the L-tap doubly-dispersive fading channel given in (**4.254**). Then, the received signal $r(t)$ can be represented as

$$r(t) = \sum_{i=0}^{L-1} h_i e^{j2\pi\nu_i(t-\tau_i)} s(t - \tau_i). \tag{4.88}$$

At the receiver side, matched filtering applied with receiver pulse shape $g_{\mathrm{rx}}(t)$. This filtering operation is defined by cross-ambiguity function $A_{g_{\mathrm{rx}},r}(\tau, \nu)$ and can be expressed as

$$A_{g_{\mathrm{rx}},r}(\tau, \nu) \triangleq \int e^{-j2\pi\nu(t-\tau)} g_{\mathrm{rx}}^*(t - \tau) r(t) dt. \tag{4.89}$$

Sampling the cross-ambiguity function at the given points, the time-frequency domain

symbols $\mathcal{Y}[n,m]$ obtained as

$$\mathcal{Y}[n,m] = A_{g_{\mathrm{rx}},r}(\tau,\nu)\big|_{\tau=nT,\nu=m\Delta f}\,. \tag{4.90}$$

This transformation is also known as the Wigner transform, which is the inverse of the Heisenberg transform.

The received time-frequency signal $\mathcal{Y}(n,m)$ is converted back to delay-Doppler domain via SFFT as follows

$$Y(l,k) = \sum_{n=0}^{N-1}\sum_{m=0}^{M-1} \mathcal{Y}(n,m)e^{-j2\pi\left(\frac{nk}{N}-\frac{ml}{M}\right)}. \tag{4.91}$$

4.4.2. Problem formulation

Most of the recent studies assume only fractional Doppler shifts in OTFS systems, where they assume wideband OTFS transmitted signals in order to provide enough delay resolution, thus integer delay shifts. However, this assumption limits the potential of this waveform and forces OTFS signals to have a fixed time-frequency distribution which is undesired in the next wireless generations. OTFS should be flexible enough to freely tune the bandwidth ($M\Delta f$) and the time duration ($NT = \frac{N}{\Delta f}$) of the signal based on the application and user requirement instead of delay and Doppler resolution. In this case, fractional delays occur with the same likelihood in OTFS systems as fractional Doppler shifts.

Moreover, the large bandwidth condition is not sufficient to ensure resolvable integer delays. In fact, the propagation environment also decides if the communication system have fractional delays or not. As a result, a generic paradigm for estimating and equalizing fractional delays and Doppler shifts is proposed in this thesis.

4.4.2.1. Integer delay & integer Doppler

When the OTFS signal occupies large time and frequency resources the wireless channel exhibits both integer delay and Doppler shifts, and the input-output relationship is derived as

$$\begin{aligned} \mathrm{y} &= \mathrm{H}_{\mathrm{eff}}^{(i,i)}\mathrm{x} + \mathrm{w} \\ &= (\mathrm{F}_N \otimes \mathrm{I}_M)\mathrm{H}^{(i,i)}(\mathrm{F}_N^H \otimes \mathrm{I}_M)\mathrm{x} + \mathrm{w}, \end{aligned} \tag{4.92}$$

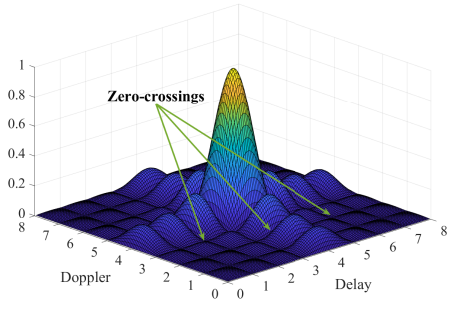


Figure 4.10: Delay-Doppler domain OTFS waveform carrier (Pulsone).

where w, $\mathrm{H}_{\mathrm{eff}}^{(i,i)} \in \mathbb{C}^{MN\times MN}$, and $\mathrm{H}^{(i,i)} \in \mathbb{C}^{MN\times MN}$ denote the AWGN vector with variance σ^2, the delay-Doppler, and the time equivalent channel matrices, respectively[4]. From [18], it is shown that the received signal has a common form given as

$$Y^{(i,i)}(l,k) = \sum_{i=0}^{L-1} h_i \Gamma^{(i)}(l,k) X_{\mathrm{DD}}\left([l-l_i]_M, [k-k_i]_N\right) + W(l,k), \tag{4.93}$$

where $\Gamma^{(i)}$ is a known phase term that denotes the type of prefix/suffix used and $W(l,k)$ represents the (l,k)-th element of noise matrix in delay-Doppler domain. The value of $\Gamma^i(l,k)$ depends on the prefix/suffix used [18]. In this thesis, full-CP OTFS configuration is used, therefore $\Gamma^i(l,k)$ is found as

$$\Gamma^i(l,k) = e^{j2\pi \frac{k_i}{N}\frac{l-l_i}{M}}. \tag{4.94}$$

Figure 4.10 shows the two-dimensional carrier in the delay-Doppler domain. The main lobe of the carrier/pulse is located on top of the integer indices of the grid, while the side-lobes are spread over the entire delay-Doppler grid. However, these side-lobes have zero-crossings with the integer indices preserving the orthogonality between the neighboring data carriers as seen from **(4.93)**.

Moreover, $\mathrm{H}^{(i,i)}$ in **(4.238)** can be expressed as

$$\mathrm{H}^{(i,i)} = \sum_{i=0}^{L-1} h_i \mathbf{\Pi}_{MN}^{l_i} \mathbf{\Delta}_{MN}^{k_i}, \tag{4.95}$$

where $\mathbf{\Pi}_a^b$ is the $a \times a$ permutation matrix with $\Pi_a^b(l,k) = \delta([l-k]_a - b)$, and $\mathbf{\Delta}_a^c$ is the

[4]The channel matrix superscript denotes the type of delay and Doppler shifts, for instance, (i,i), (i,f), (f,i), and (f,f) stand for integer-integer, integer-fractional, fractional-integer, and fractional-fractional delay and Doppler shifts, respectively.

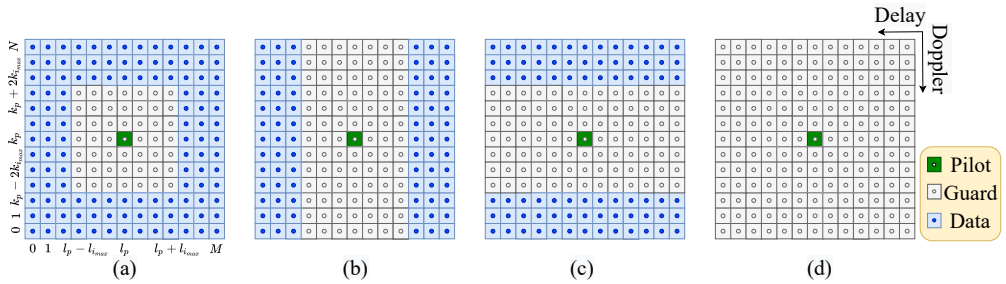


Figure 4.11: Pilot and data symbols arrangement at the transmitter: **(a)** (i,i), **(b)** (i,f), **(c)** (f,i), **(d)** (f,f).

$a \times a$ diagonal matrix given as

$$\mathbf{\Delta}_a^c = \text{diag}\left[z_i^0, z_i^1, \ldots, z_i^{(a-1)}\right], \text{ for } z_i = e^{\frac{j2\pi c}{a}}. \tag{4.96}$$

Then, in order to estimate the channel and based on (**4.93**), the pilot X_p is arbitrarily placed in the (l_p, k_p) location where the guard is chosen so that the spectral efficiency is maximized as seen in **Figure 4.14a**.

At the receiver side, the received symbols $Y_p^{(i,i)}(l,k)$ are used for channel estimation where

$$Y_p^{(i,i)}(l,k) = \begin{cases} Y^{(i,i)}(l,k), & l_p \le l \le l_p + l_{i_{max}} \\ & k_p - k_{i_{max}} \le k \le k_p + k_{i_{max}}, \\ 0, & \text{otherwise} \end{cases} \tag{4.97}$$

where $l_{i_{max}}$ and $k_{i_{max}}$ denote the maximum delay and Doppler spread, respectively.

4.4.2.2. Integer delay & fractional Doppler

In case of OTFS signal occupying large bandwidth with a small time duration integer delays and fractional Doppler shifts occur in the channel. Then, the channel matrix becomes

$$\mathrm{H}^{(i,f)} = \sum_{i=0}^{L-1} h_i \mathbf{\Pi}_{MN}^{l_i} \mathbf{\Delta}_{MN}^{(k_i+\kappa_i)}, \tag{4.98}$$

with $z_i = e^{\frac{j2\pi(k_i+\kappa_i)}{MN}}$. Consequently, the received signal becomes [127]

$$\begin{aligned} Y^{(i,f)}(l,k) = \sum_{i=0}^{L-1} \sum_{q'=0}^{N-1} h_i \Gamma^{(i)}(l,k) \left(\frac{e^{-j2\pi(-q'-\kappa_i)} - 1}{N e^{-j\frac{2\pi}{N}(-q'-\kappa_i)} - N} \right) \\ X\left([l-l_i]_M, [k-k_i+q']_N\right) + W(l,k). \end{aligned} \tag{4.99}$$

The new appearing term $\left(\frac{e^{-j2\pi(-q'-\kappa_i)}-1}{Ne^{-j\frac{2\pi}{N}(-q'-\kappa_i)}-N}\right)$ in (**4.99)** is due to fractional shifts of the two dimensional sinc pulse (shown in **Figure 4.10**) in Doppler dimension of the delay-Doppler grid causing inter-Doppler interference (IDI) since sampling is no more at zero-crossings.

As seen from (**4.99)**, the range of motion of the Doppler bins is the whole Doppler dimension as demonstrated by $q' = 0, 1, \ldots, N-1$. Therefore, the channel spreads throughout the Doppler dimension. Since the delay propagation is still integer, it would be sufficient to put guard as $l_p - l_i \leq l_p \leq l_p + l_i$ around the pilot in the delay dimension as depicted in **Figure 4.14b**.

At the receiver side, the received symbols $Y_p^{(i,f)}(l,k)$ are used for channel estimation where

$$Y_p^{(i,f)}(l,k) = \begin{cases} Y^{(i,f)}(l,k), & l_p \leq l \leq l_p + l_{i_{max}} \\ & 0 \leq k \leq N-1 \\ 0, & \text{otherwise} \end{cases} . \tag{4.100}$$

4.4.2.3. Fractional delay & integer Doppler

Having fractional delays and integer Doppler shifts in the system is equivalent to having an integer delays channel but downsampled at the receiver side. So, the fractional delay channel matrix is a downsampled version of a larger matrix with integer delays. Specifically, the L tap fractional delay time-domain channel matrix can be given as

$$\mathrm{H}_{up}^{(f,i)} = \sum_{i=0}^{L-1} h_i \mathbf{\Pi}_{\Omega MN}^{l_i} \mathbf{\Delta}_{\Omega MN}^{k_i}, \tag{4.101}$$

where Ω is the upsampling factor such that all the delay shifts are integers. Therefore, the upsampled received time-domain signal can be found as

$$\begin{aligned} \mathrm{r}_{up} &= \mathrm{H}_{up}^{(i,i)} \mathrm{F}_{\Omega MN}^{-1} \mathrm{A}(\mathrm{F}_{MN}\mathrm{s}) + \tilde{\mathrm{w}}_{up} \\ &= \underbrace{\mathrm{H}_{up}^{(i,i)} \mathrm{F}_{\Omega MN}^{-1} \mathrm{B}}_{\mathrm{G}^{(f,i)}}(\mathrm{As}) + \tilde{\mathrm{w}}_{up}, \end{aligned} \tag{4.102}$$

where $\tilde{\mathrm{w}}_{up}$ is the oversampled time-domain AWGN noise vector, A is the $\Omega MN \times MN$ zero padding matrix, and $\mathrm{B} = \mathrm{BlkDiag}(\mathrm{F}_{MN}, 0_{MN}, \ldots, 0_{MN})$ and 0_{MN} is the $MN \times MN$ zeros matrix. Therefore, the time domain received signal can be computed from (**4.102)**

as follows

$$\mathrm{r} = \mathrm{H}^{(f,i)}\mathrm{s} + \tilde{\mathrm{w}}, \tag{4.103}$$

where $\mathrm{H}^{(f,i)}(n', m') = \mathrm{G}^{(f,i)}(n'\Omega, m')$ for $n' = 0, \ldots, MN-1$ and $m' = 0, \ldots, MN-1$. Then, the received signal in delay-Doppler domain is found as [127]

$$\begin{aligned} Y^{(f,i)}(l,k) = \sum_{i=0}^{L-1}\sum_{q=0}^{M-1} h_i \Gamma^{(i)}(l,k) \left(\frac{e^{j2\pi(-q-\iota_i)}-1}{Me^{j\frac{2\pi}{M}(-q-\iota_i)}-M}\right) \\ X\left([l-l_i+q]_M, [k-k_i]_N\right) + W(l,k). \end{aligned} \tag{4.104}$$

The new appearing term $\left(\frac{e^{j2\pi(-q-\iota_i)}-1}{Me^{j\frac{2\pi}{M}(-q-\iota_i)}-M}\right)$ in (**4.104**) is due to fractional shifts of the two dimensional sinc pulse in delay-Doppler domain in the delay directional causing inter-delay interference (IDeI) since these sinc pulses are no more sampled at their zero-crossings.

As indicated in (**4.104**), the fractional delay shifts induce spreading of all the symbols in delay dimension. Thus, to avoid the IDeI the pilot arrangement is chosen to be as shown in **Figure 4.14c**.

At the receiver side, the received symbols $Y_p^{(f,i)}(l,k)$ are used for channel estimation where

$$Y_p^{(f,i)}(l,k) = \begin{cases} Y^{(f,i)}(l,k), & 0 \le l \le M-1 \\ & k_p - k_{i_{max}} \le k \le k_p + k_{i_{max}} \\ 0, & \text{otherwise} \end{cases}. \tag{4.105}$$

4.4.2.4. Fractional delay & fractional Doppler

In the case of fractional delay and Doppler, time domain channel matrix $\mathrm{H}^{(f,f)}$ can be found by combining (22), (26) and (27). Then, we find $\mathrm{H}^{(f,f)}(n', m') = \mathrm{G}^{(f,f)}(n'\Omega, m')$ for $n' = 0, \ldots, MN-1$ and $m' = 0, \ldots, MN-1$ where

$$\mathrm{G}^{(f,f)} = \sum_{i=0}^{L-1} h_i \Pi_{\Omega MN}^{l_i} \Delta_{\Omega MN}^{(k_i+\kappa_i)} \mathrm{F}_{\Omega MN}^{-1} \mathrm{B}. \tag{4.106}$$

The received signal in delay-Doppler domain can be found as

$$Y^{(f,f)}(l,k) = \sum_{i=0}^{L-1} \sum_{q=0}^{M-1} \sum_{q'=0}^{N-1} h_i \Gamma^{(i)}(l,k) \left(\frac{e^{j2\pi(-q-\iota_i)} - 1}{M e^{j\frac{2\pi}{M}(-q-\iota_i)} - M} \right) \left(\frac{e^{-j2\pi(-q'-\kappa_i)} - 1}{N e^{-j\frac{2\pi}{N}(-q'-\kappa_i)} - N} \right) X\left([l - l_i + q]_M , [k - k_i + q']_N \right) + W. \quad \textbf{(4.107)}$$

Note that (31) combines both fractional shift effects by having two extra terms introducing inter-delay and IDI in the delay and Doppler directions. The 2D sinc pulse depicted in 1 is slightly shifted in both the delay and Doppler directions thus causing interference all over the delay-Doppler grid. Therefore, the guard symbols are chosen as whole delay-Doppler grid except pilot location ($0 \le l_p \le M-1, 0 \le k_p \le N-1$) as depicted in 2(d). At the receiver side, the received symbols $Y_p^{(f,f)}(l,k)$ are used for channel estimation where

$$Y_p^{(f,f)}(l,k) = \begin{cases} Y^{(f,f)}(l,k), & 0 \le k \le N-1 \\ 0, & 0 \le l \le M-1 \\ 0 \text{ otherwise} \end{cases} . \quad \textbf{(4.108)}$$

The received symbols of the whole received frame $Y_p^{(f,f)}(l,k) = Y^{(f,f)}(l,k)$ is used for channel estimation.

4.4.3. Preliminaries

First, we introduce the lemma on the self-duality of the pulsone between time and frequency domains. Then, we introduce the lemma on the pulsone being shape-invariant to delay and Doppler shifts.

Lemma 1: A pulsone is self-dual between time and frequency, such that applying Fourier transform to a pulsone results in a pulsone as well. The time domain pulsone can be seen as a frequency modulated pulse train, thus it is expressed as

$$s_p(n) = \sum_{k'=0}^{N-1} \delta\left(n - (l_p + k'M)\right) e^{j2\pi \frac{k_p n}{MN}}. \quad \textbf{(4.109)}$$

The frequency representation of the pulsone can be found by applying DFT operation to **(4.162)** as follows

$$S_p(f) = \mathcal{F}\{\mathrm{s}_p\} = \sum_{n=0}^{MN-1} s_p(n) e^{\frac{-j2\pi fn}{MN}}. \quad \textbf{(4.110)}$$

The frequency shifting property states that the Fourier transform of the modulated signal

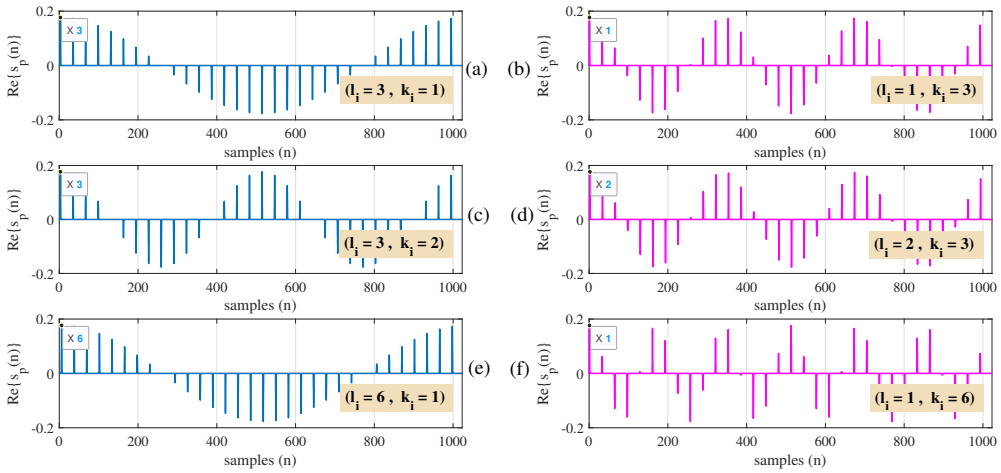


Figure 4.12: Pulsone properties: **a)** $s_p(t)$; **b)** $S_p(f) = \mathcal{F}\{s_p(t)\}$; **c)** $[s_p(t)]^2$; **d)** $\mathcal{F}\{[s_p(t)]^2\}$; **e)** $[S_p(f)]^2$; **f)** $\mathcal{F}^{-1}\{[S_p(f)]^2\}$.

in time is the shifted version of its Fourier transforms in frequency [128]. Then, we find

$$\begin{aligned} S_p(f) &= \sum_{k'=0}^{N-1} \mathcal{F}\{\delta\left(n-(l_p+k'M)\right)\} * \delta(f-k_p) \\ &= \sum_{k'=0}^{N-1} e^{\frac{-j2\pi(f-k_p)(l_p+k'M)}{MN}} = e^{\frac{-j2\pi l_p(f-k_p)}{MN}} \sum_{k'=0}^{N-1} e^{\frac{-j2\pi k'(f-k_p)}{N}}. \end{aligned} \tag{4.111}$$

The second term in **(4.164)** is periodic over $f \in [0, MN-1]$, with period N as follows

$$\sum_{k'=0}^{N-1} e^{\frac{-j2\pi k'(f-k_p)}{N}} = \sum_{k'=0}^{N-1} e^{\frac{-j2\pi k'([f]_N-k_p)}{N}}. \tag{4.112}$$

Also, for $f \in [0, N-1]$ the summation in **(4.165)** becomes equivalent to the DFT which results in

$$\sum_{k'=0}^{N-1} e^{\frac{-j2\pi k'(f-k_p)}{N}} = \delta\left(f-k_p\right). \tag{4.113}$$

Then, the frequency representation of a pulsone in **(4.164)** becomes

$$S_p(f) = \sum_{l'=0}^{M-1} \delta\left(f-(k_p+l'N)\right) e^{\frac{-j2\pi l_p(f-k_p)}{MN}}. \tag{4.114}$$

As seen from **(4.167)**, the frequency representation of a pulsone is indeed a pulsone where k_p becomes the amount of the shift of the pulse train and l_p becomes the frequency of the modulator tone in frequency domain, so, τ and ν are interchangeable between time and frequency domains.[5]

[5]The pilot-pulsone location in delay-Doppler domain does not affect the performance of the channel estimation. Then, for simplicity it is assumed that $l_p = 0$ and $k_p = 0$ for the rest of this thesis.

Lemma 2: The OTFS waveform carrier or pulsone holds its shape under the operations of time delay and Doppler shifts, where it extends quasi-periodically in the delay-Doppler grid. Here, the cases of integer-delay fractional-Doppler and fractional-delay integer-Doppler are considered as follows

Case 1: In the case of integer-delay ($\iota_i = 0$) fractional-Doppler channel and if $M > l_i$, after passing through a doubly-dispersive channel, the received signal can be found according to (**4.152)** as

$$r_p^{(i,f)}(n) = \sum_{k'=0}^{N-1} \sum_{i=0}^{L-1} h_i \delta\left(n - (l_i + k'M)\right) e^{j2\pi k' \frac{(k_i+\kappa_i)}{N}}. \tag{4.115}$$

Consider the α-th power of $r_p^{(i,f)}(n)$ given by

$$[r_p^{(i,f)}(n)]^{\alpha} = \left[\sum_{k'=0}^{N-1} \sum_{i=0}^{L-1} h_i \delta\left(n - (l_i + k'M)\right) e^{j2\pi k' \frac{(k_i+\kappa_i)}{N}}\right]^{\alpha}. \tag{4.116}$$

Lemma 2 states that for $M > l_i$, there is no inter-symbol interference between $r_p(n)^{(i,f)}$ samples. Thus, powers of $[r_p^{(i,f)}(n)]^{\alpha}$ can be found by taking the power of each element ignoring the double summation in (**4.116)**. Therefore, we find

$$[r_p^{(i,f)}(n)]^{\alpha} = \sum_{k'=0}^{N-1} \sum_{i=0}^{L-1} \left[h_i \delta\left(n - (l_i + k'M)\right) e^{j2\pi k' \frac{(k_i+\kappa_i)}{N}}\right]^{\alpha}. \tag{4.117}$$

Case 2: In the case of fractional-delay integer-Doppler ($\kappa_i = 0$) channel and if $M > l_i$, after passing through a doubly-dispersive channel, the received time domain signal $r_p^{(f,i)}(n)$ can be found as follows

$$r_p^{(f,i)}(n) = \sum_{k'=0}^{N-1} \sum_{i=0}^{L-1} h_i \delta\left(n - (l_i + \iota_i + k'M)\right) e^{\frac{j2\pi k' k_i}{N}}. \tag{4.118}$$

Using *Lemma 1*, it is found that the transmitted pilot impulse is self-dual between time and frequency, such that applying Fourier transform to it results in another OTFS carrier. However, the only change is that the delay and Doppler shifts will exchange places as shown in (**4.164)**. Therefore, the frequency representation $R_p(f) = \mathcal{F}\{r_p(n)\}$ of the whole received time pilot signal in (**4.118)** can be found based on (**4.167)** as

$$R_p^{(f,i)}(f) = \sum_{l'=0}^{M-1} \sum_{i=0}^{L-1} h_i \delta\left(f - k_i - l'N\right) e^{\frac{-j2\pi(l_i+\iota_i)f}{MN}}. \tag{4.119}$$

Consider the α-th power of $R_p^{(f,i)}(f)$ given by

$$[R_p^{(f,i)}(f)]^{\alpha} = \left[\sum_{l'=0}^{M-1}\sum_{i=0}^{L-1} h_i \delta\left(f - k_i - l'N\right) e^{\frac{-j2\pi\alpha(l_i+\iota_i)f}{MN}}\right]^{\alpha}. \qquad \textbf{(4.120)}$$

Lemma 2 states that for $M > l_i$, there is no inter-symbol interference between $R_p(f)^{(f,i)}$ samples. Thus, powers of $[R_p^{(f,i)}(f)]^{\alpha}$ can be found by taking the power of each element ignoring the double summation in **(4.134)**. Therefore, we find

$$[R_p^{(f,i)}(f)]^{\alpha} = \sum_{l'=0}^{M-1}\sum_{i=0}^{L-1}\left[h_i \delta\left(f - k_i - l'N\right) e^{\frac{-j2\pi\alpha(l_i+\iota_i)f}{MN}}\right]^{\alpha}. \qquad \textbf{(4.121)}$$

Figure 4.12 summarizes both *Lemma 1* and *Lemma 2*. For instance, **Figure 4.12a** depicts a time-domain pulsone $s_p(t)$ while **Figure 4.12b** illustrates its frequency representation $S_p(f)$. It is clearly seen that the frequency representation of a pulsone is indeed another pulsone and that the delay and Doppler shifts are interchanged between time and frequency domains as stated in *Lemma 1*. This is also the case between **Figure 4.12c**-**Figure 4.12d** and **Figure 4.12e**-**Figure 4.12f**. On the other hand, raising the pulsone to power $\alpha = 2$, results in another pulsone $[s_p(t)]^2$ having the same delay shift l_i and αk_i Doppler shift as shown in **Figure 4.12c**. Additionally, raising the frequency domain pulsone to power $\alpha = 2$, as shown in **Figure 4.12f**, results in pulsone $\mathcal{F}^{-1}\{[S_p(f)]^2\}$ having the same Doppler shift k_i and αl_i delay shift as shown in **Figure 4.12e**, thus proving *Lemma 2*.

4.4.4. Proposed channel estimation and equalization framework

In this section, we provide a paradigm for estimating and equalizing fractional doubly-dispersive channels. The analysis is divided into two parts. Specifically, in the first part we show that for a chosen α_{opt} fractional delay and Doppler shifts can be changed to integers ones in delay Doppler domain. Based on these findings, in the second part, we propose a framework to estimate the fractional delay and Doppler shifts without the need of finding α_{opt}. Note that the main scope of this thesis is estimating the fractional delay and Doppler shifts. Then, the estimation of the complex gain of each channel tap is not covered since it is studied in [54]–[61], [129].

4.4.4.1. Fractional Doppler Shift Estimation

For simplicity, the proposed method is explained first considering a single-tap fractional Doppler channel. Then, it is generalized for any doubly-dispersive channel.

4.4.4.1.1 One-tap channel

To estimate fractional Doppler shifts in the channel, the received $Y_p^{(i,f)}(l,k)$ signal in (**4.100**) is exploited. In fact, $Y_p^{(i,f)}(l,k)$ is delay-Doppler representation of a pulsone that passed through a one-tap doubly-dispersive channel which is given by (**4.169**). *Lemma 2* states that the powers of $[r_p^{(i,f)}(n)]^\alpha$ can be found as

$$[r_p^{(i,f)}(n)]^\alpha = \sum_{k'=0}^{N-1} h_i^\alpha \delta\left(n-(l_i+k'M)\right) e^{j2\pi k' \frac{\alpha(k_i+\kappa_i)}{N}}. \tag{4.122}$$

Note that the term h_i^α in (**4.170**) will cause the term to vanish for $\alpha >> 1$, such that

$$\lim_{\alpha\to\infty}(h_i^\alpha) = 0; \quad \text{for } |h_i| < 1. \tag{4.123}$$

Therefore, instead of taking the powers of $r_p^{(i,f)}(n)$, we consider the powers of the phase of the received signal $\angle r_p^{(i,f)}(n)$ since it is the one containing the Doppler shift information. Then, we find

$$\begin{aligned}[r_p^{(i,f)}(n)]^\alpha &= |r_p^{(i,f)}(n)| \cdot [\angle r_p^{(i,f)}(n)]^\alpha \\ &= \sum_{k'=0}^{N-1} |h_i| e^{\alpha\theta_i} \delta\left(n-(l_i+k'M)\right) e^{j2\pi k' \frac{\alpha(k_i+\kappa_i)}{N}},\end{aligned} \tag{4.124}$$

where $\theta_i = \angle h_i$. Consequently, the delay-Doppler representation of $[r_p^{(i,f)}(n)]^\alpha$ is found as

$$\begin{aligned}Y_{p,\alpha}^{(i,f)}(l,k) = \sum_{q'=0}^{N-1} |h_i| e^{\alpha\theta_i} \Gamma^{(i)}(l,k) \left(\frac{e^{-j2\pi(-q'-\alpha\kappa_i)}-1}{N e^{-j\frac{2\pi}{N}(-q'-\alpha\kappa_i)}-N}\right) \\ \delta\left([l-l_i]_M, [k-\alpha k_i+q']_N\right).\end{aligned} \tag{4.125}$$

As seen from (**4.170**) and (**4.125**), it is possible to convert the fractional Doppler shift into integer just by ensuring the following condition

$$\alpha_{\text{opt}}\kappa_i \in \mathbb{Z}; \quad \alpha = 1, 2, \ldots, \alpha_{\max}. \tag{4.126}$$

Algorithm 4.5 The proposed fractional Doppler channel estimation framework

Input: $\mathrm{Y}^{(i,f)}$
Output: $k_i + \kappa_i$ for $i \in [0, L-1]$.
Extract $\mathrm{Y}_p^{(i,f)}$ from $\mathrm{Y}^{(i,f)}$ as in **(4.100)**.
Convert $\mathrm{Y}_p^{(i,f)}$ from delay-Doppler to time domain $r_p^{(i,f)}(n)$ **(4.169)**.
Estimate the integer and fractional Doppler shift induced by the channel.
for $i = 0, 1, \ldots, L-1$ **do**
  while $\alpha \leq \alpha_{max}$ **do**
    Compute $[r_p^{(i,f)}(n)]^{\alpha}$ as in **(4.124)**.
    Convert $[r_p^{(i,f)}(n)]^{\alpha}$ to delay-Doppler domain $Y_{p,\alpha}^{(i,f)}(l,k)$ **(4.175)**.
    $\mathcal{K}_{i,\alpha} = \arg\max_k(|Y_{p,\alpha}^{(i,f)}(l_i,k)|)$.
    $\mathcal{D}_{i,\alpha} = \mathcal{K}_{i,\alpha} - \mathcal{K}_{i,\alpha-1}$.
  end while$k_i + \kappa_i = \mathrm{E}_{\alpha}\{\mathcal{D}_{i,\alpha}\}$.
end for

Then, we have

$$\begin{aligned} Y_{p,\alpha}^{(i,f)}(l,k) &= |h_i| e^{\alpha\theta_i} \Gamma^{(i)}(l,k)\delta(q' + \alpha\kappa_i) s\delta\left([l-l_i]_M, [k - \alpha k_i + q']_N\right) \\ &= |h_i| e^{\alpha\theta_i} \Gamma^{(i)}(l,k)\delta\left([l-l_i]_M, [k - \alpha(k_i+\kappa_i)]_N\right). \end{aligned} \tag{4.127}$$

From **(4.175)**, it is concluded that trying different α values until the condition in **(4.126)** is satisfied, can give us the exact integer and fractional Doppler shifts as follows

$$[\alpha_{\mathrm{opt}}(k_i + \kappa_i)]_M = \gamma \in \mathbb{Z}. \tag{4.128}$$

4.4.4.1.2 Multi-tap channel

In the case of multi-tap doubly-dispersive channels with fractional Doppler shifts, the same process in the one-tap case can be followed. The only difference is that all Doppler bins are monitored in parallel for each value of α. For instance, the first tap can turn to integer for $\alpha_{\mathrm{opt}} = 2$, where the second tap becomes integer at $\alpha_{\mathrm{opt}} = 5$. The delay-Doppler representation of the received pilot signal is given by

$$Y_{p,\alpha}^{(i,f)}(l,k) = \sum_{i=1}^{L} |h_i| e^{\alpha\theta_i} \Gamma^{(i)}(l,k)\delta\left([l-l_i]_M, [k - \alpha(k_i+\kappa_i)]_N\right). \tag{4.129}$$

4.4.4.2. Fractional Doppler channel estimation framework

In the method proposed in **Subsection 4.4.4.1** finding α_{opt} is a requirement. To overcome this constraint, we propose an enhanced algorithm to find all integer and fractional Doppler

shifts at once. Initially, $Y_{p,\alpha}^{(i,f)}(l,k)$ is computed for $\alpha = 1, \ldots, \alpha_{max}$. Then, for each α and delay l_i values, the Doppler grid index of the highest bin (in terms of power) is found as follows

$$\mathcal{K}_{i,\alpha} = \arg\max_{k}(|Y_{p,\alpha}^{(i,f)}(l_i,k)|). \tag{4.130}$$

After that, the difference between each successive $\mathcal{K}_{i,\alpha}$ is calculated as follows

$$\mathcal{D}_{i,\alpha} = \mathcal{K}_{i,\alpha} - \mathcal{K}_{i,\alpha-1}. \tag{4.131}$$

Finally, the integer and fractional Doppler shifts are found by taking the mean of the differences as follows

$$k_i + \kappa_i = \mathrm{E}_{\alpha}\{\mathcal{D}_{i,\alpha}\}. \tag{4.132}$$

Algorithm 1 summarizes the proposed fractional Doppler channel estimation framework.

4.4.4.3. Fractional delay shift estimation

For simplicity, we first explain the proposed method considering a single tap with fractional delay shift, and then, the proposed method is generalized for any doubly-dispersive channel. To estimate fractional delay shifts in the channel, the received $Y_p^{(f,i)}(l,k)$ signal in (**4.105**) is exploited. Using *Lemma 1*, the frequency representation of the whole received time pilot signal can be found based on (**4.167**) as

$$R_p^{(f,i)}(f) = \sum_{l'=0}^{M-1} h_i \delta\left(f - k_i - l'N\right) e^{\frac{-j2\pi(l_i+\iota_i)f}{MN}}. \tag{4.133}$$

4.4.4.3.1 One-tap channel

In the method proposed in **Subsection 4.4.4.1** finding α_{opt} is a requirement. To overcome this constraint, To estimate fractional delay shifts in the channel, the same steps applied in **Subsection 4.4.4.1** can be followed here but on the frequency representation of the received pilot signal. Assuming a single tap channel, the α-th power of $R_p^{(f,i)}(f)$ given by

$$[R_p^{(f,i)}(f)]^{\alpha} = \sum_{l'=0}^{M-1} |h_i| e^{\alpha\theta_i} \delta\left(f - k_i - l'N\right) e^{\frac{-j2\pi\alpha(l_i+\iota_i)f}{MN}}. \tag{4.134}$$

Algorithm 4.6 The proposed fractional delay shift estimation framework

Input: $\mathrm{Y}^{(f,i)}$

Output: $l_i + \iota_i$ for $i \in [0, L-1]$.

Extract $\mathrm{Y}_p^{(f,i)}$ from $\mathrm{Y}^{(f,i)}$ as in **(4.105)**.
Convert $\mathrm{Y}_p^{(f,i)}$ from delay-Doppler to time domain $r_p^{(f,i)}(n)$ **(4.118)**.
Convert $r_p^{(f,i)}(n)$ from time to frequency domain $R_p^{(f,i)}(f)$ **(4.133)**.
Estimate the integer and fractional delay shift induced by the channel
for $i = 0, 1, \ldots, L-1$ **do**
  while $\alpha \leq \alpha_{max}$ **do**
    Compute $[R_p^{(f,i)}(f)]^{\alpha}$ as in **(4.134)**.
    Convert $[R_p^{(f,i)}(f)]^{\alpha}$ to time domain $r_{p,\alpha}^{(f,i)}(n) = \mathcal{F}^{-1}\left\{R_p^{(f,i)}(f)\right\}$ **(4.135)**.
    Convert $r_{p,\alpha}^{(f,i)}(n)$ to delay-Doppler domain $Y_{p,\alpha}^{(f,i)}(l,k)$ **(4.138)**.
    $\mathcal{L}_{i,\alpha} = \arg\max_{l}(|Y_{p,\alpha}^{(f,i)}(l,k_i)|)$.
    $\mathcal{D}_{i,\alpha} = \mathcal{L}_{i,\alpha} - \mathcal{L}_{i,\alpha-1}$.
  end while$l_i + \iota_i = \mathrm{E}_{\alpha}\{\mathcal{D}_{i,\alpha}\}$.
end for

Consequently, the time-domain single of $[R_p^{(f,i)}(f)]^{\alpha}$ can be found by taking the inverse DFT of **(4.134)** as follows

$$\begin{aligned} r_{p,\alpha}^{(f,i)}(n) &= \mathcal{F}^{-1}\left\{R_p^{(f,i)}(f)\right\} \\ &= \sum_{k'=0}^{N-1} |h_i| \delta\left(n - (\alpha(l_i+\iota_i) + k'M)\right) e^{\frac{j2\pi k' k_i}{N}}. \end{aligned} \tag{4.135}$$

Furthermore, the delay-Doppler representation of $r_{p,\alpha}^{(f,i)}(n)$ is found as

$$\begin{aligned} Y_{p,\alpha}^{(f,i)}(l,k) = \sum_{q=0}^{N-1} |h_i| e^{\alpha\theta_i} \Gamma^{(i)}(l,k) \left(\frac{e^{j2\pi(-q-\alpha\iota_i)} - 1}{M e^{j\frac{2\pi}{M}(-q-\alpha\iota_i)} - M}\right) \\ \delta\left([l - \alpha l_i + q]_M, [k - k_i]_N\right). \end{aligned} \tag{4.136}$$

As seen from **(4.135)** and **(4.136)**, it is possible to convert the fractional delay shift into an integer just by ensuring the following condition

$$\alpha_{\mathrm{opt}} \iota_i \in \mathbb{Z}. \tag{4.137}$$

Then, we have

$$\begin{aligned} Y_{p,\alpha}^{(f,i)}(l,k) &= |h_i| e^{\alpha\theta_i} \Gamma^{(i)}(l,k) \delta(q + \alpha\iota_i) \delta\left([l - \alpha l_i + q]_M, [k - k_i]_N\right) \\ &= |h_i| e^{\alpha\theta_i} \Gamma^{(i)}(l,k) \delta\left([l - \alpha(l_i + \iota_i)]_M, [k - k_i]_N\right). \end{aligned} \tag{4.138}$$

It is concluded from **(4.138)** that trying different α until the condition in **(4.174)** fulfilled

can give us the exact integer and fractional delay shift.

4.4.4.3.2 Multi-tap channel

In the case of multi-tap channels with fractional delay shifts, all Doppler bins are processed in parallel for each value of α. The delay-Doppler representation of the received pilot signal is given by

$$Y_{p,\alpha}^{(f,i)}(l,k) = \sum_{i=1}^{L} |h_i| e^{\alpha\theta_i} \Gamma^{(i)}(l,k) \delta\left([l-\alpha(l_i+\iota_i)]_M, [k-k_i]_N\right). \tag{4.139}$$

4.4.4.4. Fractional delay channel estimation framework

Similar to estimating fractional Doppler shifts, in the approach proposed in **Subsection 4.4.4.3** finding α_{opt} is a needed. Thus, to overcome this constraint we propose an enhanced algorithm to find all integer and fractional delay shifts at once. Initially, $Y_{p,\alpha}^{(f,i)}(l,k)$ is computed for $\alpha = 1, \ldots, \alpha_{max}$. Then, for each α and Doppler shift k_i values, the Doppler index of the max power bin is found as

$$\mathcal{L}_{i,\alpha} = \arg\max_{l}(|Y_{p,\alpha}^{(f,i)}(l,k_i)|). \tag{4.140}$$

After that, the difference between each successive $\mathcal{L}_{i,\alpha}$ is calculated as follows

$$\mathcal{D}_{i,\alpha} = \mathcal{L}_{i,\alpha} - \mathcal{L}_{i,\alpha-1}. \tag{4.141}$$

Finally, the integer and fractional Doppler shifts are found by taking the mean of the differences as follows

$$l_i + \iota_i = \mathrm{E}_{\alpha}\{\mathcal{D}_{i,\alpha}\}. \tag{4.142}$$

Algorithm 2 summarizes the proposed fractional delay channel estimation framework.

4.4.4.5. Joint fractional delay and Doppler channel estimation framework

Since delays and Doppler shifts are uncoupled, they can be estimated separately by compiling both Algorithms 1 and 2, which do not need to neither determine α_{opt} nor verify the condition $(\alpha\kappa_j, \alpha\iota_j) \in \mathbb{Z}$. In the proposed algorithm, the only design parameter is $\alpha_{\max}$ (not α_{opt}) as shown by 5, which will be investigated in detail in the simulation section. 5 helps to determine $\alpha_{\max}$ based on the SNR of the pilot transmitted. Specifically, the

design parameter $\alpha_{\max}$ is selected based on three criteria:

- **Pilot power ($\mathbf{SNR}_p$)**: based on the transmitted pilot power, the upper limit of α is found. For instance, as depicted in 5(a), for $\mathrm{SNR}_p = 30$ dB the upper limit of α before the performance decreases is $\alpha_{opt} = 22$.
- **Performance**: in case that high accuracy estimation is needed, then $\alpha_{\max}$ is set up to be $\alpha_{\max} = \alpha_{opt}$. However, this will be computationally expensive to execute.
- **Computational complexity**: in the case of computationally limited devices or low-latency communication where very high accuracy is not needed, then $\alpha_{\max}$ can be set from 8 based on the required computational complexity.

Here is a simple example to illustrate how the algorithm works. Consider a single tap channel with $l_0 = 0$ and $k_0 + \kappa_0 = 1.12$. Ignoring the received noiseless pilot is given as

$$Y_{p,\alpha}(l,k) = |h_0| e^{\alpha\theta_0} \Gamma^{(0)}(l,k) \delta\left([l]_M, [k - 1.12\alpha]_N\right). \qquad \textbf{(4.143)}$$

Assuming that $\mathrm{SNR}_p = 35$ dB, which is practical, the upper limit is given in 5(a) as $\alpha_{opt} = 38$.

In the event that high accuracy estimation (performance) is needed, then:

1. Choose $\alpha_{\max} = \alpha_{opt} = 38$.
2. Compute $Y_{p,\alpha}$ for each $\alpha = 1, 2, \ldots, 36$.
3. Find the Doppler bin index of the peak of the tap for each α. Then put the result in a vector $\mathcal{K}_0 = [1, 2, 3, 4, 15, 0, 8, 9, 10, \ldots, 35, 36, 37, 38, 39, 40]$. Note that the fifth and sixth elements of $\mathcal{K}_0$ are erroneous (should be 6 and 7 instead of 15 and 0, respectively), we did that to show the noise effect.
4. Compute the difference vector as follows
   $\mathcal{D}_0 = \mathcal{K}_0(l+1) - \mathcal{K}_0(l) = [1, 1, 1, 11, -15, 1, 1, \ldots, 1, 1, 1, 1]$.
5. Estimate the Doppler shift $\hat{k}_0 + \hat{\kappa}_0 = \mathrm{E}\{\mathcal{D}_0\} = 1.114$.

The MSE of the estimator is: $\mathrm{MSE}(\hat{k}_0 + \hat{\kappa}_0) = 3.25 \cdot 10^{-5}$. In cases of low computational

$$\frac{\partial U_z^{(i,f)}}{\partial \kappa_i} = \sum_{q'=0}^{N-1} h_i \Gamma^{(i)}(l,k) \Bigg[\frac{j2\pi(l-l_i)}{MN} \frac{e^{-j2\pi(-q'-\kappa_i)} - 1}{Ne^{-j\frac{2\pi}{N}(-q'-\kappa_i)} - N} + 2j\pi \frac{e^{-j2\pi(-q'-\kappa_i)} \left(Ne^{-j\frac{2\pi}{N}(-q'-\kappa_i)} - N \right) - e^{-j\frac{2\pi}{N}(-q'-\kappa_i)} \left(e^{-j2\pi(-q'-\kappa_i)} - 1 \right)}{\left(Ne^{-j\frac{2\pi}{N}(-q'-\kappa_i)} - N \right)^2} \Bigg] \cdot X\left([l-l_i]_M, [k-k_i+q']_N \right), \tag{4.144}$$

$$\frac{\partial U_z^{(f,i)}}{\partial \iota_i} = \sum_{q=0}^{M-1} h_i \Gamma^{(i)}(l,k) \Bigg[\frac{-j2\pi k_i}{MN} \frac{e^{j2\pi(-q-\iota_i)} - 1}{Me^{j\frac{2\pi}{M}(-q-\iota_i)} - M} - 2j\pi \frac{e^{j2\pi(-q-\iota_i)} \left(Me^{j\frac{2\pi}{M}(-q-\iota_i)} - M \right) - e^{j\frac{2\pi}{M}(-q-\iota_i)} \left(e^{-j\frac{2\pi}{N}(-q-\iota_i)} - 1 \right)}{\left(Me^{j\frac{2\pi}{M}(-q-\iota_i)} - M \right)^2} \Bigg] \cdot X\left([l-l_i+q]_M, [k-k_i]_N \right). \tag{4.145}$$

complexity requirements, $\alpha_{\max}$ could be set to a lower value, giving up some of the performance. For instance, for $\alpha_{\max} = 20$ the MSE of the estimator is: $\text{MSE}(\hat{k}_0 + \hat{\kappa}_0) = 2.16 \cdot 10^{-4}$.

4.5. OTFS-Based ISAC For Super-Resolution Range-Velocity Profile

4.5.1. Proposed system model

This section examines an OTFS-ISAC system, analyzing the transmitter, wireless channel, and receiver. Accordingly, the input-output relationship of the received signal in a doubly-dispersive channel is investigated.

4.5.1.1. Transmitter side

Consider a wireless communication system where $M \times N$ data symbols are modulated using OTFS over a total bandwidth B operating at the carrier frequency f_c. Firstly, the OTFS modulator distributes these symbols $\{X(k,l),\ k = 0, \ldots, N-1,\ l = 0, \ldots, M-1\}$ in the two-dimensional delay-Doppler grid where the bandwidth of each of the M subcarriers is defined as $\Delta f = B/M$, the time duration of one symbol is $T = 1/\Delta f$, and the OTFS frame

duration is NT. This imposes $1/M\Delta f$ and $1/NT$ delay and Doppler spacing, respectively. The delay-Doppler domain (i.e., Zak space) is an intermediate space between the direct signal space "time" and the Fourier space "frequency". Assuming rectangular pulse shaping, the time sequence x corresponding to X can be generated via the inverse discrete Zak transform (IDZT) by the formula [130]

$$s(k+nM) = \frac{1}{\sqrt{N}} \sum_{l=0}^{N-1} X(k,l) e^{-j2\pi \frac{l}{N} n}, \quad \text{for } 0 \leq k < M, 0 \leq n < N. \tag{4.146}$$

Computing $x(k+nM)$ requires obtaining M DFT operations of size N of the data sets s. To cast **(4.246)** from serial to matrix-vector form, we define F_N to be the $N \times N$ unitary DFT matrix; then, **(4.246)** is rewritten as

$$\mathrm{s} = (\mathrm{F}_N^H \otimes \mathrm{I}_M)\mathrm{x}, \tag{4.147}$$

where $\mathrm{x} = \mathrm{vec}\,(\mathrm{X})$ and s is the time domain signal.

Finally, to combat the channel effect and provide circularity, we append a reduced-CP of length M_{cp} as given in [18].

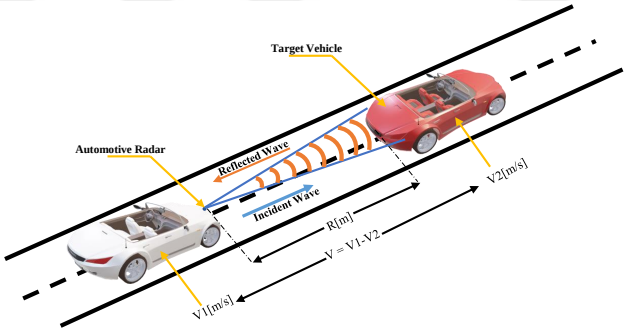


Figure 4.13: Simple ISAC configuration with one target.

4.5.1.2. Doubly-dispersive channel

For the narrow band short duration signal model, the multiple scatterers near a target are neither resolved in range nor in velocity. Therefore, it is appropriate to consider the point target assumption to model the response of the targets. The setup assumes a doubly-dispersive channel with L targets moving toward or away from the radar receiver as shown

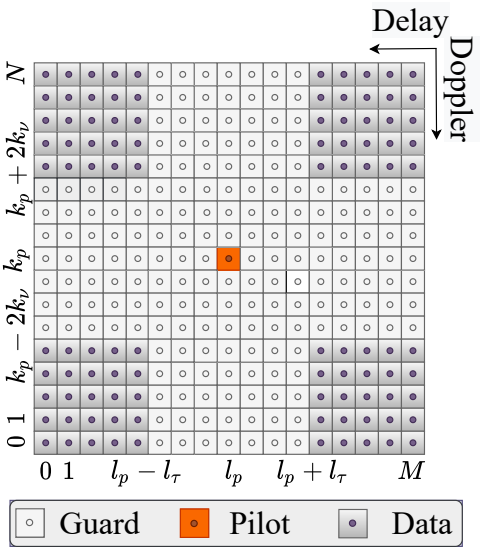


Figure 4.14: The pilot and data symbols structure at the transmitter.

in **Figure 4.13**. The channel can be modeled as follows

$$h(\tau, \nu) = \sum_{i=0}^{L-1} h_i \delta(\tau - \tau_i)\delta(\nu - \nu_i), \tag{4.148}$$

where h_i is the channel fading coefficient and follows a uniform power delay and power Doppler profiles, which is independent of delay and Doppler indices [81]. τ_i and ν_i represent the round-trip delay and Doppler shifts of the i-th path respectively, and they are given as

$$\tau_i = \frac{2R_i}{c} = \frac{l_i + \iota_i}{M\Delta f}, \tag{4.149}$$

and

$$\nu_i = \frac{2V_i f_c}{c} = \frac{k_i + \kappa_i}{NT}, \tag{4.150}$$

where R_i, V_i, l_i, and k_i denote the range, velocity, integer delay, and integer Doppler indices corresponding to the i-th reflector, respectively, and $c = 3 \times 10^8 m/s$ is the speed of light. ι_i and $\kappa_i \in [-0.5, 0.5]$ represent the fractional delay and Doppler of the i-th reflector of the channel.

Based on the channel model in **(4.254)**, the impulse-based channel estimation is adopted [55]. Specifically, one pilot is placed on the delay-Doppler grid surrounded by guard symbols to prevent interference between pilot and data symbols when passing through the channel, as depicted in **Figure 4.14**. The SNR of the pilot is assumed to be $\text{SNR}_p =$

$|X_p|^2/\sigma^2$, where σ^2 denotes noise variance. Then, the delay-Doppler grid at the transmitter is populated as follows:

$$X(k,l) = \begin{cases} X_p, & l = l_p, k = k_p \\ 0, & l_p - l_\tau \le l \le l_p + l_\tau \\ & \text{or } \; k_p - 2k_\nu \le k \le k_p + 2k_\nu \\ X_d(l,k), & \text{otherwise} \end{cases}, \tag{4.151}$$

where X_d and X_p are the data and pilot symbols, respectively. l_p, k_p, l_τ, and k_ν denote the pilot delay index, Doppler shift index, maximum delay, and Doppler shift, respectively. Note that l_τ and k_ν values depend on the amount of leakage between the delay-Doppler carriers, where in extreme channel cases, l_τ and k_ν can be set to be M and N, respectively. In this case, channel estimation and data transmission are done within different OTFS frames.

4.5.1.3. Receiver

After the transmitted signal goes through L-tap doubly-dispersive channel given in **(4.254)**, the receiver captures a received signal $y(t)$ which is given as follow [131]

$$y(t) = \sum_{i=0}^{L-1} h_i e^{j2\pi\nu_i(t-\tau_i)} s(t-\tau_i) + w(t), \tag{4.152}$$

where $w(t)$ is the AWGN with zero mean and variance σ^2.

Sampling **(4.152)** at times $t = \frac{mT}{M}$, $0 \le m < MN$, produces the discrete received OTFS signal which is expressed by

$$\begin{aligned} y(m) &= y(t)|_{t=\frac{mT}{M}} \\ &= \sum_{i=0}^{L-1} h_i e^{j2\pi(k_i+\kappa_i)\frac{m-(l_i+\iota_i)}{MN}} s\left(m-(l_i+\iota_i)\right) + w(m). \end{aligned} \tag{4.153}$$

To convert back the data to the delay-Doppler domain we set $m = k + nM$.

Then, the discrete Zak transform (DZT), Y, of $\boldsymbol{y}$ is an isometry $\mathbb{C}^K \rightarrow \mathbb{C}^{N\times M}$, given by [130]

$$\begin{aligned} Y(k,l) =& \frac{1}{\sqrt{N}} \sum_{n=0}^{N-1} y(k+nM) e^{j2\pi\frac{l}{N}n}, \\ & \text{for } 0 \le l < M, 0 \le k < N. \end{aligned} \tag{4.154}$$

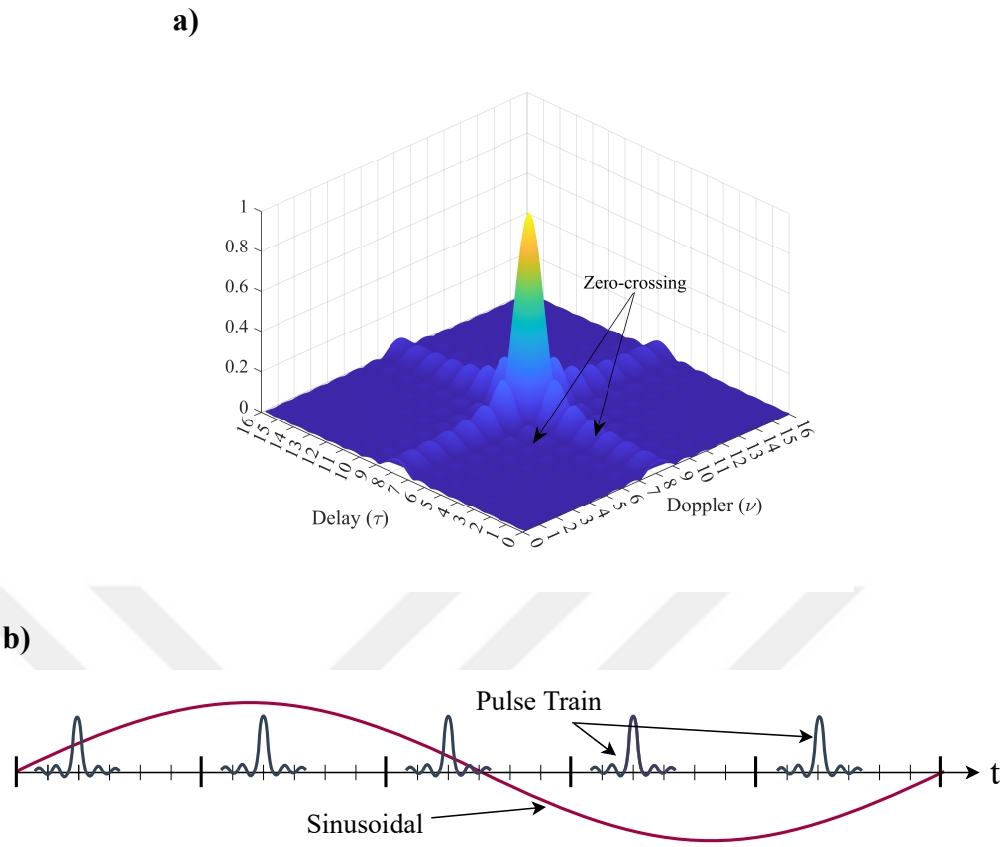


Figure 4.15: Single OTFS carrier: **a**) Delay-Doppler domain visualization, **b**) Time domain visualization.

Hence, the noiseless delay-Doppler domain received signal is given by [127]

$$Y(k,l) = \sum_{i=0}^{L-1} \sum_{q'=0}^{N-1} \sum_{q=0}^{M-1} h_i \Gamma^{(i)}(k,l) \left(\frac{e^{-j2\pi(-q'-\kappa_i)} - 1}{N e^{-j\frac{2\pi}{N}(-q'-\kappa_i)} - N} \right) \left(\frac{e^{j2\pi(-q-\iota_i)} - 1}{M e^{j\frac{2\pi}{M}(-q-\iota_i)} - M} \right) X\left([l - l_i + q]_M , [k - k_i + q']_N \right), \tag{4.155}$$

where Γ^i is a known phase term which, for reduced-CP structure, is given by

$$\Gamma^i(k,l) = \begin{cases} e^{j2\pi\frac{k_i}{N}\frac{l-l_i}{M}} & l_i \leq l < M \\ e^{-j2\pi\frac{k}{N}} e^{j2\pi\frac{k_i}{N}\frac{l-l_i}{M}} & 0 \leq l < l_i \end{cases}. \tag{4.156}$$

The fractional shift of the two-dimensional sinc pulse in both delay and Doppler dimensions causes the appearance of the two terms $\left(\frac{e^{-j2\pi(-q'-\kappa_i)}-1}{N e^{-j\frac{2\pi}{N}(-q'-\kappa_i)}-N} \right)$ and $\left(\frac{e^{j2\pi(-q-\iota_i)}-1}{M e^{j\frac{2\pi}{M}(-q-\iota_i)}-M} \right)$ in (**4.155**), which denote the inter-Doppler interference and inter-delay interference, respectively, as illustrated in **Figure 4.15a**.

The received signal which is used for channel estimation is given by

$$Y(k,l) = \begin{cases} Y_p(k,l), & l_p - l_\tau \le l \le l_p + l_\tau \\ & \text{or } k_p - 2k_\nu \le k \le k_p + 2k_\nu \\ Y_d(k,l), & \text{otherwise} \end{cases}, \tag{4.157}$$

where Y_p is the received signal due to pilot which is used for channel estimation, and Y_d is the received signal containing data along with the channel effects.

The tensor form derivation of the input-output relationship of the received signal is given by

$$\mathrm{y} = \mathrm{H}_{\text{eff}}\mathrm{x} + \mathrm{w} = (\mathrm{F}_N \otimes \mathrm{I}_M)\mathrm{H}(\mathrm{F}_N^H \otimes \mathrm{I}_M)\mathrm{x} + \mathrm{w}, \tag{4.158}$$

where w is the AWGN vector, $\mathrm{H}_{\text{eff}} \in \mathbb{C}^{MN\times MN}$ and $\mathrm{H} \in \mathbb{C}^{MN\times MN}$ denote the delay-Doppler and time equivalent channel matrices, respectively.

The fractional delay channel matrix can be considered as a down-sampled version of a larger channel matrix with integer delays H_{int}. Specifically, the L tap fractional time-domain channel matrix H can be found as

$$\begin{gathered} \mathrm{H}(k',l') = \mathrm{H}_{\text{int}}(Kk',l'), \\ \text{for } 0 \le l' < MN, 0 \le k' < MN. \end{gathered} \tag{4.159}$$

where

$$\mathrm{H}_{\text{int}} = \sum_{i=0}^{L-1} h_i \mathbf{\Pi}_{KMN}^{l_i} \mathbf{\Delta}_{KMN}^{k_i+\kappa_i} \mathrm{F}_{KMN}^{-1} \mathrm{A}\mathrm{F}_{MN}, \tag{4.160}$$

and K is the down-sampling factor. A is the $KMN \times KMN$ zero padding matrix. $\mathbf{\Pi}_a^b$ is the $a \times a$ permutation matrix with $\Pi_a^b(l,k) = \delta([l-k]_a - b)$, and $\mathbf{\Delta}_a$ is the $a \times a$ diagonal matrix

$$\mathbf{\Delta}_a^c = \mathrm{diag}\left[z_i^0, z_i^1, \ldots, z_i^{(a-1)}\right], \text{ for } z_i = e^{\frac{j2\pi c}{a}}. \tag{4.161}$$

4.5.2. Properties of an OTFS carrier

In this section, the OTFS carrier is introduced, and then its three main properties are discussed namely [132], 1) self-duality between time and frequency domains [133], 2) shape-invariance under time delay and Doppler shifts, and 3) tunable delay and Doppler shifts.

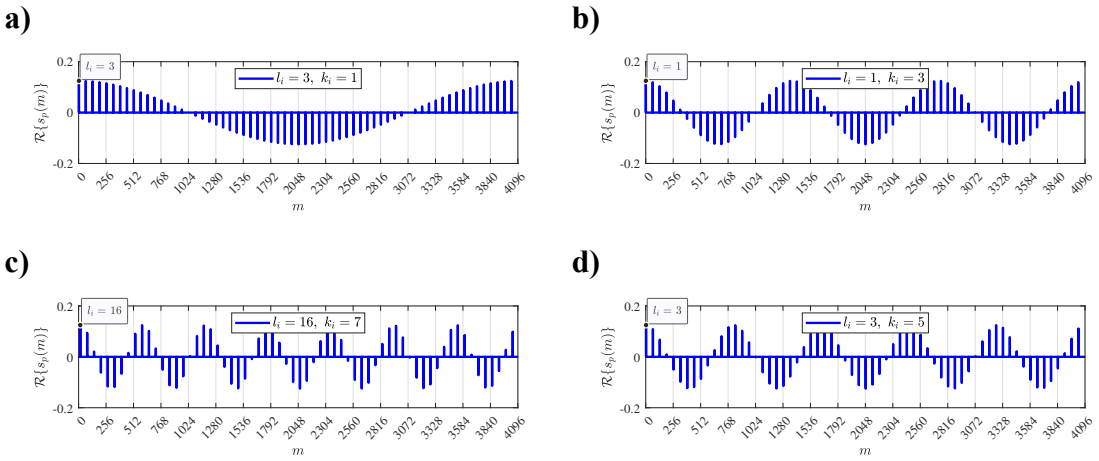


Figure 4.16: Single OTFS carrier's properties: **a)** $s_p(m)$, **b)** $\mathcal{F}\{s_p(m)\}$, **c)** $s_p(m) * (\delta(m-13)e^{j2\pi\frac{6m}{4096}})$, **d)** $s_p(m)e^{j2\pi 4m}$.

4.5.2.1. *Property 1*: Self-duality between time and frequency domains

The time domain OTFS carrier can be seen as a frequency-modulated pulse train as depicted in **Figure 4.15b**, and it is expressed as

$$s_p(m) = \sum_{\alpha=0}^{N-1} \delta\left(m - (l_p + \alpha M)\right) e^{j2\pi\frac{k_p m}{MN}}. \tag{4.162}$$

To get the frequency representation of the OTFS carrier in the frequency domain, DFT operation is applied to **(4.162)** as follows

$$S_p(r) = \mathcal{F}\{\mathrm{s}_p\} = \sum_{m=0}^{MN-1} s_p(m) e^{-j2\pi\frac{rm}{MN}}. \tag{4.163}$$

Modulating a signal in time domain with an exponential tone is equivalent to shifting its Fourier transform in frequency domain [128]. Accordingly, we find

$$\begin{aligned} S_p(r) &= \sum_{j=0}^{N-1} \mathcal{F}\{\delta\left(m - (l_p + \alpha M)\right)\} * \delta(r - k_p) \\ &= \sum_{\alpha=0}^{N-1} e^{-j2\pi\frac{(r-k_p)(l_p+\alpha M)}{MN}} \\ &= e^{-j2\pi\frac{l_p(r-k_p)}{MN}} \underbrace{\sum_{\alpha=0}^{N-1} e^{-j2\pi\frac{\alpha(r-k_p)}{N}}}_{A}. \end{aligned} \tag{4.164}$$

$$Y_p^{(\theta,\varphi)}(k,l) = \sum_{i=0}^{L-1}\sum_{q'=0}^{N-1}\sum_{q=0}^{M-1} h_i X_p \Gamma^{(i)}(k,l)\left(\frac{e^{-j2\pi(-q'-\kappa_i-\varphi)}-1}{Ne^{-j\frac{2\pi}{N}(-q'-\kappa_i-\varphi)}-N}\right)\left(\frac{e^{j2\pi(-q-\iota_i-\theta)}-1}{Me^{j\frac{2\pi}{M}(-q-\iota_i-\theta)}-M}\right)$$
$$\delta\left([l-l_i+q]_M, [k-k_i+q']_N\right). \tag{4.168}$$

Note that the term A in **(4.164)** is periodic with period N as follows

$$\begin{aligned} A(r) &= \sum_{\alpha=0}^{N-1} e^{\frac{-j2\pi\alpha([r]_N-k_p)}{N}} \\ &= A([r]_N), \quad \text{for } r \in [0, MN-1]. \end{aligned} \tag{4.165}$$

Therefore, for $r \in [0, N-1]$, the summation in **(4.165)** becomes equivalent to the DFT, resulting in

$$A([r]_N) = \mathcal{F}\{e^{\frac{j2\pi\alpha k_p}{N}}\text{rect}([r]_N)\} = \delta\left([r]_N - k_p\right), \tag{4.166}$$

where rect(m) denotes the rectangular pulse shape. Then, the frequency representation of an OTFS carrier in **(4.164)** becomes

$$\begin{aligned} S_p(r) &= \delta\left([r]_N - k_p\right) e^{\frac{-j2\pi l_p(r-k_p)}{MN}} \\ &= \sum_{\beta=0}^{M-1} \delta\left(r-(k_p+\beta N)\right) e^{\frac{-j2\pi l_p(r-k_p)}{MN}}. \end{aligned} \tag{4.167}$$

As seen from **(4.167)**, the frequency representation of an OTFS carrier is indeed an OTFS carrier where l_p becomes the frequency of the modulator tone in the frequency domain and k_p becomes the amount of the shift of the pulse train, so, τ and ν are interchangeable between time and frequency domains. This can be also concluded from **Figure 4.16a** that illustrates an OTFS carrier with $(l_p = 3, k_p = 1)$ and its frequency representation depicted in **Figure 4.16b**. Note that in **Figure 4.16b**, the OTFS carrier parameters are switched to be $(l_p = 1, k_p = 3)$.

4.5.2.2. *Property 2*: Shape-invariance under time delay and Doppler shifts

The OTFS carrier of maintains its shape under the operations of time delay and Doppler shifts, where it extends quasi-periodically in the delay-Doppler grid. Considering the i-th moving target in the propagation environment reflecting the transmitted OTFS carrier in

(**4.162**). Then, the received signal can found as

$$y_p(m) = \sum_{\alpha=0}^{N-1} h_i \delta\left(m - (l_i + l_p + \alpha M)\right) e^{j2\pi \frac{(k_i+k_p)m}{MN}}. \tag{4.169}$$

As seen in (**4.169**), $y_p(m)$ is an OTFS carrier with a shifted delay (i.e., $l_i + l_p$), shifted Doppler (i.e., $k_i + k_p$), and with new gain (i.e., h_i). The same conclusion can be extracted from **Figure 4.16c**, where after $s_p(m)$ passed through the channel $h_i = \delta(m-13)e^{j2\pi \frac{6m}{4096}}$, the received signal held its shape overall, however, with new parameters ($l = l_p + l_i = 13 + 3 = 16,\ k = k_p + k_i = 1 + 6 = 7$).

4.5.2.3. *Property* 3: Tunable delay and Doppler shifts

Using *Property 1* and *Property 2*, it can be deduced that we can tune the delay and Doppler shift parameters by modulating the OTFS carrier with a tone in frequency and time domains, respectively. Specifically, shifting the OTFS carrier in (**4.162**) by l_i delays and k_i Doppler shifts can be achieved as follows

$$\begin{aligned} s_p^{(l_i,k_i)}(m) &= \mathcal{F}^{-1}\{S_p(r)e^{j2\pi \frac{l_i r}{MN}}\}e^{j2\pi \frac{k_i m}{MN}} \\ &= \sum_{\alpha=0}^{N-1} \delta\left(m - (l_i + l_p + \alpha M)\right) e^{j2\pi\alpha \frac{(k_i+k_p)}{N}}. \end{aligned} \tag{4.170}$$

Figure 4.16d shows that modulating the OTFS carrier in time and frequency domains with a tone results indeed in another OTFS carrier with shifted delay and Doppler. Note that the impulse pilot's location in the delay-Doppler domain neither affects *Property 1, 2*, and *3* nor the channel estimation. Therefore, for simplicity, it is assumed that $l_p = 0$ and $k_p = 0$ for the rest of this thesis.

4.5.3. Proposed OTFS-based ISAC framework

Consider integrated sensing and communication (ISAC) parameter estimation over a channel bandwidth B and a carrier frequency f_c. The transmitter is attached to a mono-static radar, where a message is sent to the target for communication purposes while the estimation of radar parameters is done using the reflected back-scattered echoes. In this section, we propose a framework to jointly communicate with efficiency and sense with high-resolution range-velocity profile.

After receiving (**4.155**), only the bins corresponding to the pilot are selected to get $Y_p(k,l)$

as in **(4.157)**. Hence, $Y_p(k,l)$ is converted to time signal as follows

$$\begin{aligned} y_p(m) &= \sum_{i=0}^{L-1} h_i e^{j2\pi(k_i+\kappa_i)\frac{m-(l_i+\iota_i)}{MN}} s_p\left(m-(l_i+\iota_i)\right) + w(m) \\ &= \sum_{i=0}^{L-1} \hat{h}_i \sum_{\alpha=0}^{N-1} e^{j2\pi\frac{m(k_i+\kappa_i)}{MN}} \delta\left(m-(l_i+\iota_i+\alpha M)\right) + w(m), \end{aligned} \tag{4.171}$$

where $\hat{h}_i = h_i e^{-j2\pi\frac{(k_i+\kappa_i)(l_i+\iota_i)}{MN}}$.

Applying *Property 3* to **(4.171)**, we find

$$\begin{aligned} y_p^{(\theta,\varphi)}(m) &= \mathcal{F}^{-1}\{Y_p(r)e^{j2\pi\frac{\theta r}{MN}}\}e^{j2\pi\frac{\varphi m}{MN}} \\ &= \sum_{i=0}^{L-1} \hat{h}_i \sum_{\alpha=0}^{N-1} \delta\left(m-(l_i+\iota_i+\theta+\alpha M)\right) e^{j2\pi\alpha\frac{(k_i+\kappa_i+\varphi)}{N}} \\ &+ \hat{w}(m), \end{aligned} \tag{4.172}$$

where $\hat{w}(m) = \mathcal{F}^{-1}\{W(r)e^{j2\pi\frac{\theta r}{MN}}\}e^{j2\pi\varphi m}$ and $Y_p(r) = \mathcal{F}\{y_p(m)\}$. Note that $\hat{w}(m)$ has the same statistics as $w(m)$ (i.e., $\hat{w}(m) \sim \mathcal{CN}(0,\sigma^2)$). Consequently, the delay-Doppler representation of **(4.172)** is found as given in **(4.168)**.

According to **(4.168)** and for each reflecting object in the environment, if the following two constraints are ensured

$$\theta + \iota_i \in \mathbb{Z}; \quad \text{for } \theta \in (0,1), \tag{4.173}$$

and

$$\varphi + \kappa_i \in \mathbb{Z}; \quad \text{for } \varphi \in (0,1), \tag{4.174}$$

the fractional delay and fractional Doppler shifts can be converted into integers.

So, for the i-th object the noiseless **(4.168)** can be rewritten as

$$\begin{aligned} Y_{p,i}^{(\theta,\varphi)}(k,l) &= X_p h_i \Gamma^i(l,k)\delta(q'+\kappa_i+\varphi)\delta(q+\iota_i+\theta) \\ &\quad \times \delta\left([l-l_i+q]_M, [k-k_i+q']_N\right) \\ &= X_p h_i \Gamma^i(l,k)\delta\left(\left[l-\hat{l}_i\right], \left[k-\hat{k}_i\right]\right), \end{aligned} \tag{4.175}$$

where $\hat{l}_i = l_i + \iota_i + \theta \in \mathbb{Z}$ and $\hat{k}_i = k_i + \kappa_i + \varphi \in \mathbb{Z}$ are the new equivalent integer delay and Doppler shifts, respectively.

4.5.3.1. Fractional delay and Doppler shifts Estimation

In the case of multi-tap doubly-dispersive channels with fractional delay and Doppler shifts, all channel bins are monitored in parallel in delay-Doppler domain for each value of θ and φ. Once the conditions in (**4.173)** and (**4.174)** are satisfied, then the fractional delay and Doppler shifts are found as

$$l_i + \iota_i = \hat{l}_i - \theta, \tag{4.176}$$

and

$$k_i + \kappa_i = \hat{k}_i - \varphi. \tag{4.177}$$

4.5.3.2. High resolution range-velocity Estimation

Let's set $\theta \in [\frac{0}{\epsilon_\theta}, \frac{1}{\epsilon_\theta}, \ldots, 1]$ and $\varphi \in [\frac{0}{\epsilon_\varphi}, \frac{1}{\epsilon_\varphi}, \ldots, 1]$, where $\frac{1}{\epsilon}$ is discretization step size. The range and the velocity can be, respectively, estimated from (**4.176)** and (**4.177)** as follows

$$R_i = \frac{(l_i + \iota_i)c}{2M\Delta f} = \frac{\tilde{l}_i c}{2\frac{M\Delta f}{\epsilon_\theta}}, \tag{4.178}$$

and

$$V_i = \frac{(k_i + \kappa_i)c}{2f_c NT} = \frac{\tilde{k}_i c}{2f_c \frac{NT}{\epsilon_\varphi}}, \tag{4.179}$$

where $\tilde{l}_i = (l_i + \iota_i)\epsilon_\theta \in \mathbb{Z}$ and $\tilde{k}_i = (k_i + \kappa_i)\epsilon_\varphi \in \mathbb{Z}$.

Note that (**4.178)** and (**4.179)** imply that the range and velocity resolution are both dependent on the number of discretization step ϵ. This implies that as ϵ value gets small, the resolution of both range and velocity estimation increase, achieving *high-resolution range-velocity profile*. The new resolutions of range and velocity are respectively given as

$$\Delta_R^{\text{proposed}} = \frac{c}{2\frac{M\Delta f}{\epsilon}} = \frac{\Delta_R}{\epsilon_\theta}, \tag{4.180}$$

and

$$\Delta_V^{\text{proposed}} = \frac{c}{2f_c \frac{NT}{\epsilon}} = \frac{\Delta_V}{\epsilon_\varphi}. \tag{4.181}$$

Note that in order to achieve high-resolution range-velocity profile for multi-target scenario, the objects are assumed to have $V_i - V_j \leq \Delta_V$ or $R_i - R_j \leq \Delta_R$. However, this constraint can be easily addressed by deploying beamforming.

$$\frac{\partial U_z}{\partial V_i} = \sum_{q'=0}^{N-1}\sum_{q=0}^{M-1} h_i \Gamma^{(i)}(l,k)\left(\frac{e^{j2\pi(-q-(\gamma R_i - l_i))}-1}{M e^{j\frac{2\pi}{M}(-q-(\gamma R_i - l_i))}-M}\right)\cdot X\left([l-l_i+q]_M, [k-k_i+q']_N\right)$$
$$\left[\frac{j2\pi\beta(l-\gamma R_i)}{MN}\left(\frac{e^{-j2\pi(-q'-(\beta V_i - k_i))}-1}{N e^{-j\frac{2\pi}{N}(-q'-(\beta V_i - k_i))}-N}\right) + \frac{j2\pi\beta}{N}\frac{\left(e^{-j2\pi(-q'-(\beta V_i - k_i))}\left(e^{-j\frac{2\pi}{N}(-q'-(\beta V_i - k_i))}-1\right) - e^{-j\frac{2\pi}{N}(-q'-(\beta V_i - k_i))}\left(e^{-j2\pi(-q'-(\beta V_i - k_i))}-1\right)\right)}{\left(e^{-j\frac{2\pi}{N}(-q'-(\beta V_i - k_i))}-1\right)^2}\right] \quad \textbf{(4.185)}$$

4.5.3.3. Enhanced range-velocity estimation algorithm

We propose a single algorithm to find all ranges and velocities corresponding to all targets at once. Initially, $Y_p^{(\theta,\varphi)}(k,l)$ is computed for $\theta \in [\frac{0}{\epsilon_\theta}, \ldots, 1]$. Then, for each i-th target and θ value, the delay index of the max power bin is found as

$$\mathcal{M}_{i,\epsilon_\theta} = \arg\max_l(|Y_p^{(\theta,\varphi)}(k_i,l)|). \quad \textbf{(4.182)}$$

After that, the integer and fractional delay shifts are found by taking the mean of **(4.182)** for all θ values as follows

$$l_i + \iota_i = \mathrm{E}_{\epsilon_\theta}\{\mathcal{M}_{i,\epsilon_\theta}\}. \quad \textbf{(4.183)}$$

Finally, the range of each target is found by computing **(4.178)**. Similar steps can be followed to estimate the velocities. The summary of the enhanced range-velocity estimation scheme is shown in **Algorithm 1**.

4.5.3.4. Channel equalization

The estimated fractional delay and Doppler shifts are used to generate the effective channel based on the channel matrix in **(4.159)**. After that, to recover the transmitted symbols, a MMSE equalizer is used to equalize the effects of the channel and get the estimated data $\hat{\mathrm{X}}$ symbols as follows [134]

$$\hat{\mathrm{X}} = \mathrm{H}_{\mathrm{eff}}^H\left(\mathrm{H}_{\mathrm{eff}}\mathrm{H}_{\mathrm{eff}}^H + \sigma^2\mathrm{I}_{\mathrm{MN}}\right)^{-1}\mathrm{Y}. \quad \textbf{(4.184)}$$

$$\frac{\partial U_z}{\partial R_i} = \sum_{q'=0}^{N-1}\sum_{q=0}^{M-1} h_i \Gamma^{(i)}(l,k)\left(\frac{e^{-j2\pi(-q'-(\beta V_i - k_i))}-1}{Ne^{j\frac{2\pi}{N}(-q'-(\beta V_i-k_i))}-N}\right)\cdot X\left([l-l_i+q]_M, [k-k_i+q']_M\right)$$
$$\left[-\frac{j2\pi\beta V_i\gamma}{MN}\left(\frac{e^{j2\pi(-q-(\gamma R_i-l_i))}-1}{Me^{j\frac{2\pi}{M}(-q-(\gamma R_i-l_i))}-M}\right)-\frac{j2\pi\gamma}{M}\frac{\left(e^{j2\pi(-q-(\gamma R_i-l_i))}\left(e^{j\frac{2\pi}{M}(-q-(\gamma R_i-l_i))}-1\right)-e^{j\frac{2\pi}{M}(-q-(\gamma R_i-l_i))}\left(e^{j2\pi(-q-(\gamma R_i-l_i))}-1\right)\right)}{\left(Me^{j\frac{2\pi}{M}(-q-(\gamma R_i-l_i))}-M\right)^2}\right] \quad \textbf{(4.186)}$$

4.6. OTFS-FMCW Waveform Design For Low Complexity Joint Sensing And Communication

4.6.1. Preliminaries

In this section, the DZT transform is presented first followed by the description of OTFS, chirp, and orthogonal chirp (OC) signals.

4.6.1.1. Discrete Zak transform

The delay-Doppler domain (i.e., Zak space) is an intermediate space between the direct signal space "time" and the Fourier space "frequency". Assume that the delay-Doppler grid is discretized into N delays and M Dopplers, and consider an arbitrary discrete K-point sequence $\boldsymbol{x}$, where $K = LN^2$, $M = LN$ and $N, M \in \mathbb{N}$. The DZT, $\mathrm{X_{DD}}$, of $\boldsymbol{x}$ is an isometry $\mathbb{C}^K \rightarrow \mathbb{C}^{N\times M}$, given by [130]

$$X_{\mathrm{DD}}(k,l) = \frac{1}{\sqrt{N}}\sum_{n=0}^{N-1} x(l+nM)e^{-j2\pi\frac{k}{N}n}, \quad \text{for } 0 \le l < M, 0 \le k < N. \quad \textbf{(4.187)}$$

Computing $X_{\mathrm{DD}}(k,l)$ requires obtaining M DFT operations of size N of the data sets $x(l), x(l+M), \ldots, x(l+(N-1)M)$, $0 \le l < M$. The sequence $\boldsymbol{x}$ can be recovered from its DZT by the formula

$$x(l+nM) = \frac{1}{\sqrt{N}}\sum_{k=0}^{N-1} X_{\mathrm{DD}}(k,l)e^{j2\pi\frac{k}{N}n} \quad \text{for } 0 \le l < M, 0 \le n < N. \quad \textbf{(4.188)}$$

Algorithm 4.7 The proposed high-resolution range-velocity estimation framework

Input: Y

Output: $l_i + \iota_i$, $k_i + \kappa_i$, R_i, and V_i.

Extract Y_p from Y as in (**4.157**).
Convert Y_p from delay-Doppler to time domain $y_p(m)$.
Estimate the range-velocity profile of the radar channel.
for $i = 0, 1, \ldots, L-1$ **do**
  Estimate the Doppler shift/velocity induced by the radar channel
  for $j = 0, 1, \ldots, \epsilon_\varphi$ **do**
    Compute $y_p^{(\theta=0,\varphi(j))}(m)$.
    Convert $y_p^{(\theta=0,\varphi(j))}(m)$ to delay-Doppler domain.
    $\mathcal{M}_{i,\epsilon_\varphi} = \arg\max_l(|Y_p^{(\theta=0,\varphi(j))}(k_i, l)|)$.
  end for
  Estimate the delay shift/range induced by the radar channel
  for $j = 0, 1, \ldots, \epsilon_\theta$ **do**
    Compute $\mathcal{F}\{y_p^{(\theta(j),\varphi=0)}(m)\}$.
    convert $\mathcal{F}\{y_p^{(\theta(j),\varphi=0)}(m)\}$ to time domain.
    Convert $y_p^{(\theta(j),\varphi=0)}(m)$ to delay-Doppler domain.
    $\mathcal{M}_{i,\epsilon_\theta} = \arg\max_l(|Y_p^{(\theta(j),\varphi=0)}(k_i, l)|)$.
  end for
  $l_i + \iota_i = \mathrm{E}_{\epsilon_\theta}\{\mathcal{M}_{i,\epsilon_\theta}\}$.
  $k_i + \kappa_i = \mathrm{E}_{\epsilon_\varphi}\{\mathcal{M}_{i,\epsilon_\varphi}\}$.
  $R_i = \frac{(l_i+\iota_i)c}{2M\Delta f}$.
  $V_i = \frac{(k_i+\kappa_i)c}{2f_cNT}$.
end for
$(\mathrm{l}, \boldsymbol{\iota}) = [(l_0, \iota_0), (l_1, \iota_1), \ldots, (l_{L-1}, \iota_{L-1})]$.
$(\mathrm{k}, \boldsymbol{\kappa}) = [(k_0, \kappa_0), (k_1, \kappa_1), \ldots, (k_{L-1}, \kappa_{L-1})]$.
$\boldsymbol{r} = [R_0, R_1, \ldots, R_{L-1}]$.
$\boldsymbol{v} = [V_0, V_1, \ldots, V_{L-1}]$.

4.6.1.2. OTFS signal model

Consider a wireless communication system where $M \times N$ data symbols are modulated using OTFS over a total bandwidth B operating at the carrier frequency f_c. Firstly, the OTFS modulator distributes these symbols $\{X_{\mathrm{DD}}(k,l),\ k = 0, \ldots, N-1,\ l = 0, \ldots, M-1\}$ in the two-dimensional delay-Doppler grid. Denoting the bandwidth of each of the M subcarriers as $\Delta f = B/M$, then the time duration of one symbol is $T = 1/\Delta f$, and the OTFS frame duration is NT. This imposes $1/M\Delta f$ and $1/NT$ delay and Doppler spacing, respectively. Then, the samples $X_{\mathrm{DD}}(k,l)$ are converted to the time–frequency domain

grid $\{X_{\mathrm{TF}}(n,m),\ n=0,\ldots,N-1,\ m=0,\ldots,M-1\}$ using the ISFFT as follows [18]

$$X_{\mathrm{TF}}(n,m)=\frac{1}{\sqrt{MN}}\sum_{l=0}^{M-1}\sum_{k=0}^{N-1}X_{\mathrm{DD}}(k,l)e^{j2\pi\left(\frac{nk}{N}-\frac{ml}{M}\right)}. \tag{4.189}$$

The time-frequency signal $\mathrm{X_{TF}}$ in **(4.189)** needs to be converted to time domain before transmission. For this purpose, practical OFDM systems which are based on the IDFT are used. Hence, the discrete output of an OFDM modulator is

$$x(m+nM)=\frac{1}{\sqrt{M}}\sum_{m=0}^{M-1}X_{\mathrm{TF}}(n,m)e^{j2\pi\frac{m}{M}n}. \tag{4.190}$$

Note that the total length of the discrete sequences representing the frame is $M\times N$. Substituting **(4.189)** in **(4.190)** and using $(1/M)\sum_{m=0}^{M-1}e^{j2\pi m/M(l-l')}=\delta\,(l-l')$, we obtain

$$x(l+nM)=\frac{1}{\sqrt{N}}\sum_{k=0}^{N-1}X_{\mathrm{DD}}(k,l)e^{j2\pi\frac{k}{N}n}, \tag{4.191}$$

which precisely corresponds to the IDZT described in **(4.246)**. As a result, the DFT-based cascaded ISFFT and OFDM modulation have a similar structure to the IDZT. In order to obtain the discrete sequence without employing the ISFFT, one can use the IDZT. Similar outcomes can be attained for the receiver when the DZT-based OFDM demodulation is coupled with the SFFT, which yields the DZT.

4.6.1.3. Chirp signal model

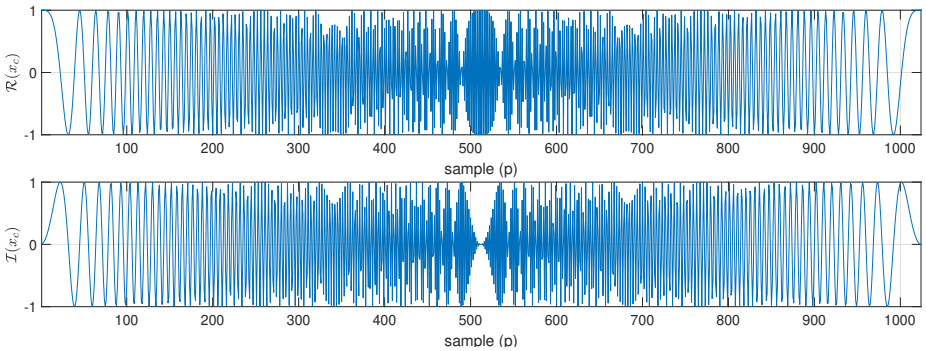
Consider a linear frequency modulated continuous wave (FMCW) signal, $x_c(t)$, sweeping linearly across B bandwidth during the time interval T. The time-domain representation of $x_c(t)$ is given by [19]

$$x_c(t)=e^{j\pi\eta t^2}e^{j2\pi f_c t},\quad 0\le t<T, \tag{4.192}$$

where $\eta=B/T$ is the chirp rate, T is the chirp time duration, B is the chirp bandwidth, and BT is the time-bandwidth product, and $\eta,\ T$, and $B\in\mathbb{R}$. Sampling **(4.192)** at times $t=p\frac{T}{K},\ 0\le p<K$, produces the discrete chirp

$$x_c(p)=e^{j\pi\frac{\eta p^2T^2}{K^2}}e^{j2\pi\frac{f_cpT}{K}},\quad 0\le p<K. \tag{4.193}$$

a)



b) **c)** **d)** **e)**

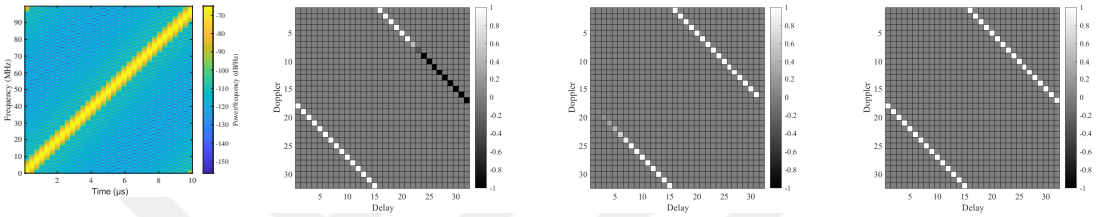


Figure 4.17: The time, time-frequency, and delay-Doppler representations of linear chirp with parameters $L = 1$, $N = 32$, $M = 32$: **a**) the real and imaginary parts of the chirp signal x_c, **b**) spectrogram, **c**) $\mathcal{R}e\{X^c_{\mathrm{DD}}\}$, **d**) $\mathcal{I}m\{X^c_{\mathrm{DD}}\}$, **e**) $|X^c_{\mathrm{DD}}|$.

Choosing a factorization $K = LN^2, N, M = LN \in \mathbb{N}$ gives the following[6]

$$\begin{aligned} x_c(p) &= e^{j\pi \frac{\eta p^2 T^2}{M^2 N^2}} e^{j2\pi \frac{f_c p T}{MN}} \\ &= e^{j\pi \frac{ap^2}{N^2}} e^{j2\pi \frac{bp}{N}}, \quad 0 \le p < K, \end{aligned} \tag{4.194}$$

where $a = \eta \left(\frac{T}{M}\right)^2 = \eta \left(\frac{T}{LN}\right)^2$ is the discrete chirp rate, $b = f_c \frac{T}{M} = f_c \frac{T}{LN}$ is the discrete carrier frequency, and aM^2 is the discrete time-bandwidth product, where $a, b \in \mathbb{R}$. **Figure 4.17a** shows the real and imaginary parts of $x_c(p)$, while **Figure 4.17b** depicts the time-frequency representation of linear chirp.

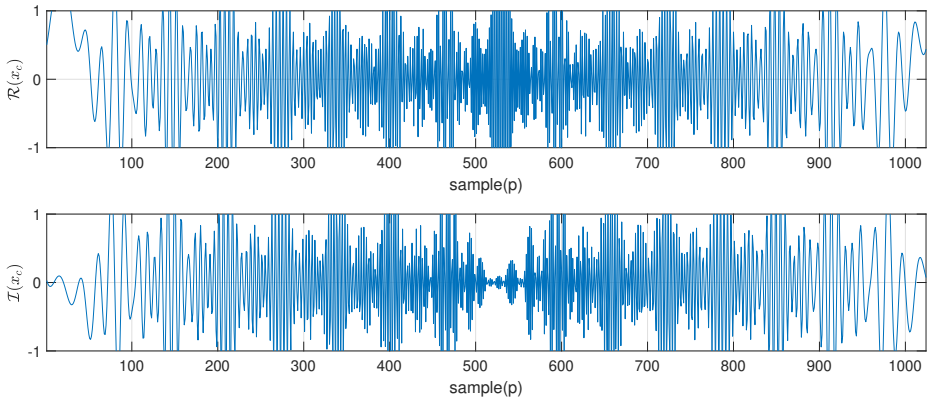
4.6.1.4. Orthogonal chirp signals' model

Supposing that there are K chirp waveforms, these chirps can be obtained from the kernel of Fresnel transform which is given by [20]

$$\varphi_\omega(t) = e^{-j\frac{\pi}{4}} e^{j\frac{\pi}{\omega}t^2}, \tag{4.195}$$

[6]Note that this factorization is useful when computing the DZT of a chirp, as will be explained in **Subsection 4.6.2.1**.

a)



b) **c)** **d)** **e)**

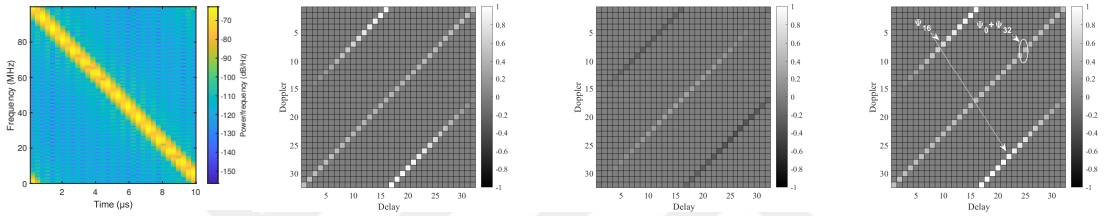


Figure 4.18: The time, time-frequency, and delay-Doppler representations of different OC signals with parameters $L = 1$, $N = 32$, $M = 32$: **a**) the real and imaginary parts of the chirp signal $\sum_{i=0,16,32} \psi_i$, **b**) spectrogram, **c**) $\mathcal{R}e\{\sum_{i=0,16,32} \psi_i\}$, **d**) $\mathcal{I}m\{\sum_{i=0,16,32} \psi_i\}$, **e**) $|\sum_{i=0,16,32} \psi_i|$.

where $\omega = T^2/K$. By substituting ω in **(4.195)**, the 'root' chirp is given as

$$\begin{aligned} \psi_0(t) &= \Pi_T(t)\varphi^*_{\omega}(t)\Big|_{\omega=\frac{T^2}{K}} \\ &= e^{j\frac{\pi}{4}} e^{-j\pi\frac{N}{T^2}t^2}, \quad 0 \le t < T, \end{aligned} \tag{4.196}$$

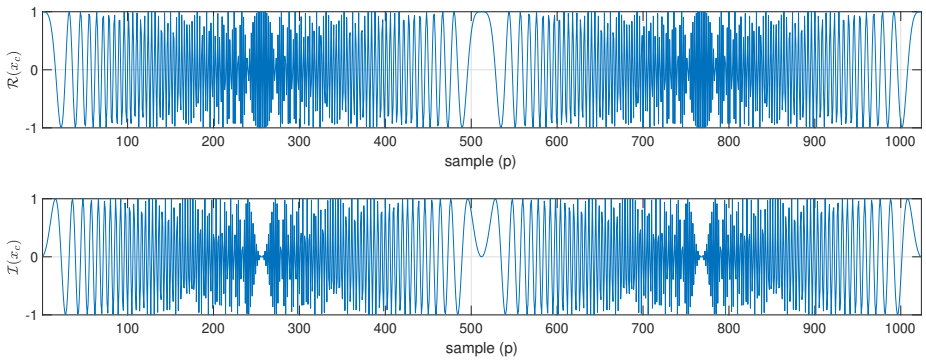
where $\Pi_T(t)$ is the rectangular function expressed as

$$\Pi_T(t) = \begin{cases} 1 & 0 \le t < T \\ 0 & \text{otherwise} \end{cases}. \tag{4.197}$$

It is possible to get a set of K OCs using the root chirp in **(4.196)**, the i-th, $i = 0, 1, \ldots, K-1$, OC is given as

$$\begin{aligned} \psi_i(t) &= \Pi_T(t)\varphi^*_{\frac{T^2}{K}}\,(t - i(T/K)) \\ &= e^{j\frac{\pi}{4}} e^{-j\pi\frac{K}{T^2}\left(t - i\frac{T}{K}\right)^2}, 0 \le t < T. \end{aligned} \tag{4.198}$$

a)



b) **c)** **d)** **e)**

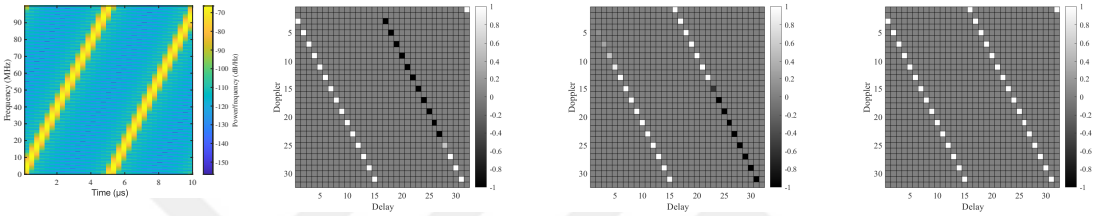


Figure 4.19: The time, time-frequency, and delay-Doppler representations of cascaded two linear chirps with parameters $L = 2$, $N = 32$, $M = 32$: **a**) the real and imaginary parts of the chirp signal x_c, **b**) spectrogram, **c**) $\mathcal{R}e\{X_{\mathrm{DD}}^c\}$, **d**) $\mathcal{I}m\{X_{\mathrm{DD}}^c\}$, **e**) $|X_{\mathrm{DD}}^c|$.

Note that the chirp waveforms $\psi_i(t)$ in **(4.243)** are mutually orthogonal, i.e.,

$$\int \psi_m^*(t)\psi_i(t)dt = \int_0^T e^{j\pi\frac{N}{T^2}\left(t-m\frac{T}{N}\right)^2} e^{-j\pi\frac{N}{T^2}\left(t-i\frac{T}{N}\right)^2} = \delta(m-i). \tag{4.199}$$

Sampling **(4.243)** at times $t = p\frac{T}{K}$, gives the i-th discrete OC

$$\psi_i(p) = e^{j\frac{\pi}{4}} e^{-j\pi\frac{(p-i)^2}{K}}, 0 \le p < K. \tag{4.200}$$

The real and imaginary parts of the sum of three OCs (i.e., $\sum_{i=0,16,32}\psi_i$) are depicted in **Figure 4.22a**. **Figure 4.22b** illustrates the time-frequency representation of these three OCs where they linearly sweep a band B over time duration T.

4.6.2. The relationship between OTFS and chirp waveforms

In this section, we first compute the DZT of linear chirp and OC signals, then prove that chirp signals have a sparse representation in delay-Doppler domain.

4.6.2.1. DZT of linear chirp

Taking $p = l + nM,\ 0 \le l < M, 0 \le n < N$, the chirp in **(4.194)** can be expressed as

$$\begin{aligned} x_c(l+nM) &= e^{j\pi a(l+nM)^2/N^2} e^{j2\pi b(l+nM)/N} \\ &= e^{j2\pi \frac{\frac{aLl^2}{2}+alnL^2N+blNL}{K}} e^{j2\pi\left(\frac{an^2L^2}{2}+bnL\right)}. \end{aligned} \tag{4.201}$$

Setting $W_K(k) := e^{j2\pi l/K}$, the chirp in **(4.201)** can be expressed as

$$\begin{aligned} x_c(l+nM) &= W_K\left(\frac{aLl^2}{2} + alL^2Nn + blNL\right) \\ &\quad \times W_1\left(\frac{aL^2n^2}{2} + bLn\right) \\ &= W_N\left(aNL^2n^2 + (alL + bNL)n + \frac{aNl^2}{2} + bl\right). \end{aligned} \tag{4.202}$$

The DZT of $\boldsymbol{x}_c$ in **(4.202)** can be written as

$$\begin{aligned} X^c_{\mathrm{DD}}(k,l) &= \frac{1}{\sqrt{N}} \sum_{n=0}^{N-1} x_c(l+nM) W_N(nk) \\ &= \frac{x_k}{\sqrt{N}} \sum_{n=0}^{N-1} W_N\left(\alpha n^2 + \beta n\right), \end{aligned} \tag{4.203}$$

where $x_k := W_K\left(\frac{al^2L}{2} + bLNl\right)$, $\alpha = \frac{aNL^2}{2}$, and $\beta = alL + k + bNL$.

To check the sparsity of the chirp in delay-Doppler domain, we will show that X^c_{DD} is nonzero only at M points in the Zak space. First,

$$W_N\left(\alpha n^2\right) = e^{2j\pi \frac{2aNL^2}{N} n^2} = e^{j\pi aL^2n^2}. \tag{4.204}$$

Since

$$e^{j\pi n} = \begin{cases} 1, & n \text{ is even} \\ -1, & n \text{ is odd} \end{cases}, \tag{4.205}$$

and

$$n^2 = \begin{cases} \text{even}, & n \text{ is even} \\ \text{odd}, & n \text{ is odd} \end{cases}, \tag{4.206}$$

then, provided that $aL \in \mathbb{Z}, aL^2 \in \mathbb{Z}$, we find

$$W_N\left(\alpha n^2\right) = (-1)^{aL^2n^2} = (-1)^{aL^2n}. \tag{4.207}$$

Therefore, the DZT of chirp signal can be written as

$$X_{\mathrm{DD}}^{c}(k,l) = \frac{x_k}{\sqrt{N}} \sum_{n=0}^{N-1} W_N((\alpha+\beta)n). \tag{4.208}$$

This means that only if $(\alpha+\beta) \bmod N = 0$, $X_{\mathrm{DD}}^{c}(k,l)$ is nonzero. It follows that $X_{\mathrm{DD}}^{c}(k,l)$ is sparse, i.e.,

$$X_{\mathrm{DD}}^{c}(k,l) = \begin{cases} \sqrt{N}x_k, & (\alpha+\beta) \bmod N = 0 \\ 0, & \text{otherwise} \end{cases}, \tag{4.209}$$

provided $\alpha+\beta \in \mathbb{Z}$, or equivalently $aL \in \mathbb{Z}, aL^2 \in \mathbb{Z}$, and $\frac{aL^2N}{2} + bLN \in \mathbb{Z}$. Note that the condition

$$(\alpha+\beta) \bmod N = (Lk+l) = 0, \tag{4.210}$$

has a single solution for each $l = 0, \ldots, M-1$, thus the chirp is indeed sparse and represented by only M nonzero points in the delay-Doppler domain. Figures **Figure 4.17c-e** show example of chirp with a sparse representation in the delay-Doppler domain. Also, as long as the conditions above are satisfied, multiple chirps can be generated from only M-points in delay-Doppler, an example of which is depicted in **Figure 4.19**. This can be exploited to adaptively control the maximum observable range-velocity of linear chirps by adjusting the total number of transmitted chirps, which corresponds to changing the slope of the chirp waveform within a single OTFS symbol.

This characteristic of linear chirps can be effectively utilized to dynamically control the maximum observable range-velocity in wireless communication systems. By adjusting the total number of transmitted chirps, which corresponds to changing the slope of the chirp waveform within a single OTFS (Orthogonal Time Frequency Space) frame, the maximum observable range-velocity can be adaptively controlled.

4.6.2.2. DZT of OCs

The i-th OC in **(4.244)** can be expressed as

$$\psi_i(l+nM) = e^{-j\frac{\pi}{4}} W_K \left(-\frac{1}{2}(l+nM-i)^2 \right). \tag{4.211}$$

Then, the DZT of ψ_i in **(4.247)** can be expressed as

$$\begin{aligned}\Psi_{i,\mathrm{DD}}(k,l) &= \frac{1}{\sqrt{N}}\sum_{n=0}^{N-1}\psi_i(l+nM)W_N\,(nk)\\ &= \frac{\Omega_i}{\sqrt{N}}\sum_{n=0}^{N-1}W_N\left(\hat{\alpha}n^2+\hat{\beta}_i n\right),\end{aligned} \tag{4.212}$$

where $\Omega_i := e^{-j\frac{\pi}{4}}W_K\left((l-i)^2/2\right)$, $\hat{\alpha} := -LN/2$, and $\hat{\beta}_i := k+i-l$.

To check the sparsity of the chirp signal in delay-Doppler domain, similar to what we have done in **Subsection 4.7.1.1**, we show that if $\hat{\alpha}+\hat{\beta}_i \in \mathbb{Z}$, $\Psi_{i,\mathrm{DD}}$ is nonzero at only M points in delay-Doppler domain. Observe that since

$$W_N\left(\hat{\alpha}n^2\right) = (-1)^{Ln^2} = (-1)^{Ln} = W_N(\hat{\alpha}n), \tag{4.213}$$

then, we can write

$$\Psi_{i,\mathrm{DD}}(k,l) = \frac{\Omega_i}{\sqrt{N}}\sum_{n=0}^{N-1}W_N((\hat{\alpha}+\hat{\beta}_i)n), \tag{4.214}$$

provided $L \in \mathbb{Z}$. It follows that $\Psi_{i,\mathrm{DD}}(k,l)$ is sparse, i.e.,

$$\Psi_{i,\mathrm{DD}}(k,l) = \begin{cases}\sqrt{N}\Omega_i, & (\hat{\alpha}+\hat{\beta}_i) \bmod N = 0\\ 0, & \text{otherwise}\end{cases}, \tag{4.215}$$

provided $\hat{\alpha}+\hat{\beta}_i \in \mathbb{Z}$, or equivalently $L \in \mathbb{Z}$. **Figure 4.22c-e** show example of three OCs with a sparse representation in the delay-Doppler domain where it is seen that two OC carriers can be orthogonal by occupying different delay and Doppler resources (i.e., Ψ_0 and Ψ_{16}). Also, **Figure 4.22c-e** show that if two OC carriers having indices satisfying $\hat{i} = [i]_N$, they can be overlapping in delay-Doppler yet orthogonal by having different real and complex coefficients (i.e., Ψ_0 and Ψ_{32}). As a conclusion, an MN OCs in delay-Doppler domain consists of M non-overlapping orthogonal signals (shifted in delay Doppler) each having N overlapping orthogonal signals.

4.6.2.3. Linear chirp/OC signals as precoded-OTFS

As demonstrated in Subsections **Subsection 4.6.2.1** and **Subsection 4.7.1.1**, we conclude that linear chirp signals can be presented as a *precoded sparse OTFS signal* given by

$$X_{\mathrm{DD}}^{c}(k,l)=\begin{cases}\sqrt{N}x_k, & (\alpha+\beta)\bmod N=0\\ 0, & \text{otherwise}\end{cases}, \tag{4.216}$$

for FMCW, or by

$$\Psi_{i,\mathrm{DD}}(k,l)=\begin{cases}\sqrt{N}\Omega_i, & (\hat{\alpha}+\hat{\beta}_i)\bmod N=0\\ 0, & \text{otherwise}\end{cases}, \tag{4.217}$$

for linear OCs. Also, note that we can fully populate an $M\times N$ delay-Doppler grid with $M\times N$ OCs as follows

$$X_{\mathrm{DD}}^{\mathrm{ocdm}}(k,l)=\sum_{i=0}^{MN-1}\Psi_{i,\mathrm{DD}}(k,l). \tag{4.218}$$

$\mathrm{X}_{\mathrm{DD}}^{\mathrm{ocdm}}$ in **(4.252)** is equivalent to the orthogonal chirp division multiplexing (OCDM) signal [20], thus OCDM can be seen as a pre-processed OTFS modulation as well. This feature is exploited in the following section where both data and chirp signal are orthogonally distributed in the delay-Doppler.

4.6.3. Proposed OTFS-chirp JSAC waveform

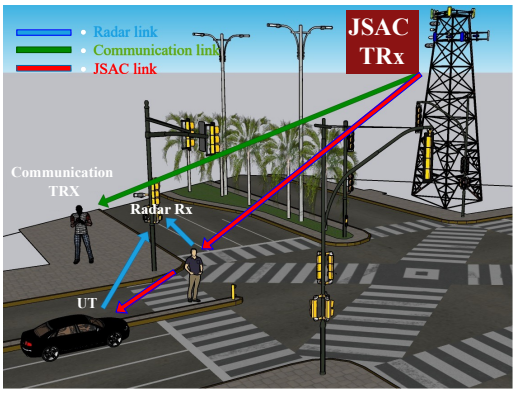
In this section, the proposed OTFS-Chirp waveform is presented, where the sparse representation of chirps is exploited to orthogonally multiplex chirp and data in delay-Doppler domain to realize the two JSAC scenarios shown in **Figure 4.20**.

4.6.3.1. Single-user OTFS-Chirp JSAC waveform

As presented in **Subsection 4.6.2.1**, a chirp only occupies M points of the delay-Doppler grid. Therefore, in the proposed OTFS-Chirp waveform, $(N-1)M$ data symbols $\mathrm{X}_{\mathrm{DD}}^{d}$ are distributed orthogonally with the chirp signal in the delay-Doppler domain as follows

$$X_{\mathrm{DD}}(k,l)=\begin{cases}\sqrt{P_c N}x_k, & (\alpha+\beta)\bmod N=0\\ X_{\mathrm{DD}}^{d}(k,l), & \text{otherwise}\end{cases}, \tag{4.219}$$

a)



b)

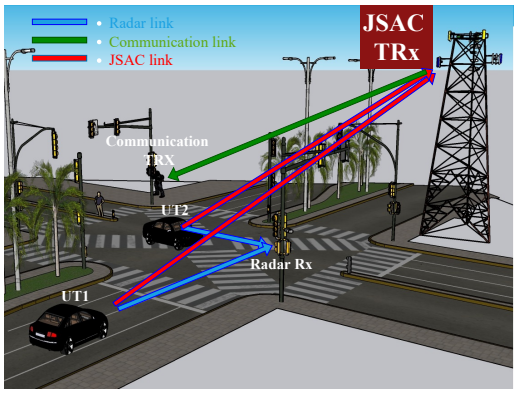


Figure 4.20: Typical JSAC scenario for the proposed waveform: **a**) single UT (downlink), **b**) multi-UT (Uplink).

where P_c is the power of the transmitted chirp.[7] The transmitted time-domain signal is found using **(4.191)** as follows

$$x(p) = x_d(p) + x_c(p), \tag{4.220}$$

where $x_d(l + nM) = 1/\sqrt{N} \sum_{k=0}^{N-1} X_{\mathrm{DD}}^{d}(k,l) e^{j2\pi \frac{k}{N} n}$. Hence, the transmitted signal $x(t)$ is intended for two purposes, namely, *communication* which is served via the term $x_d(t)$ and *sensing* that is done by $x_c(t)$. A typical JSAC scenario for the proposed OTFS-Chirp waveform is provided in **Figure 4.20a**, where a communication link is set between the JSAC transceiver (TRx) and user terminal (UT), while IoT devices embedded in a traffic light exploits the same transmitted signal for sensing and mapping the surrounding environment to adaptively control traffic. On the other hand, automotive car on the road is jointly communicating and learning the targets around to facilitate the driving and avoid accidents.

4.6.3.2. Multi-user OTFS-Chirp JSAC waveform

A typical multi-UT JSAC scenario is depicted in **Figure 4.20b**, where the JSAC transceiver (TRx) base station/radar needs to communicate and sense the channels seen by multi-UT simultaneously in uplink. In the uplink transmission of OTFS systems, each UT is allocated a non-overlapping delay-Doppler resource block protected by guard

[7] Note that **(4.259)** should not necessarily include both sensing and communication signals. For instance, in case of sensing only, the data term can be set to zero (i.e., $\mathrm{X}_{\mathrm{DD}}^{d} = 0$). On the other hand, in case of communication only, the chirp term can be set to zero (i.e., $\mathrm{X}_{\mathrm{DD}}^{c} = 0$).

bands [135]. In the proposed multi-user JSAC OTFS-Chirp waveform, I UTs are transmitting simultaneously in the uplink transmission. $(N-1)M/I$ data symbols $\mathrm{X}^{d}_{i,\mathrm{DD}}$, corresponding to the i-th UT, are distributed along with the i-th OC signal in the delay-Doppler domain as follows

$$X_{i,\mathrm{DD}}(k,l) = \begin{cases} \sqrt{P_c N}\Omega_i, & (\hat{\alpha}+\hat{\beta}_i) \bmod N = 0 \\ X^{d}_{i,\mathrm{DD}}(k,l), & \text{otherwise} \end{cases}. \tag{4.221}$$

The transmitted time-domain signal can be found using **(4.191)** as

$$x(p) = x^{i}_{d}(p) + \psi_i(p), \tag{4.222}$$

where $x^{i}_{d}(l+nM) = 1/\sqrt{N}\sum_{k=0}^{N-1} X^{d}_{i,\mathrm{DD}}(k,l)e^{j2\pi\frac{k}{N}n}$. Since the transmitted chirps are orthogonal, the base station can differentiate the radar information corresponding to each UT. The succeeding section demonstrates the process of extracting and processing radar information for sensing purposes, as well as the proposed technique for channel estimation and equalization to decode the data for communication.

4.6.4. JSAC signal processing

JSAC systems encompass a variety of applications that involves communication, sensing, or a combination of both. Depending on the specific application requirements, the nodes within the system execute distinct processing tasks at the receiver side. These tasks can be tailored to suit the specific needs of each application, ensuring optimal performance and functionality as follows

- Communication Receiver: When a communication UT receives the OTFS-Chirp signal, it processes it as an OTFS signal with known redundant symbols (chirp carriers) embedded in it.
- Low-Complexity Radar Receiver: In the case of a low-end device intended solely for sensing, a chirp receiver is employed. This receiver is easily implemented in existing IoT devices due to the sampling properties of FMCW signals where the intermediate frequency (IF) signal is sampled instead of the received RF signal. This approach enables the analog-to-digital converter (ADC) to sample a signal of only a few MHz. This is advantageous for IoT devices that have low-sampling frequency ADCs.

- JSAC receiver: UTs interested in both sensing and communication do not have limited computational power or sampling constraints. Therefore, they process the OTFS frame for communication purposes, while digitally process the chirp signal for sensing information.

In this section, echo processing for sensing, data decoding, and channel estimation for communication are explained.

4.6.4.1. Radar echo (chirp) processing

For the scenario given in **Figure 4.20**, consider an R-tap doubly-selective radar channel modeling R targets in the environment with r_r range and v_r velocity as follows

$$h(\tau, \nu) = \sum_{r=0}^{R-1} h_r \delta(t - \tau_r) e^{j2\pi\nu_r(\tau-\tau_r)}, \tag{4.223}$$

where h_r denotes the complex channel gain corresponding to the r-th path, $\tau_r = 2r_r/c$ and $\nu_r = 2v_r f_c/c$ denote the round-trip delay and Doppler, respectively; and $c = 3 \times 10^8 m/s$ is the speed of light. Therefore, the output of the radar channel can be given as

$$y(t) = \sum_{r=0}^{R-1} h_r x(t - \tau_r) e^{j2\pi\nu_r(t-\tau_r)}. \tag{4.224}$$

The signal reflected from this channel is conjugately mixed with the transmitted chirp signal $x_c^*(t)$ in case of single UT (or $\psi_i^*(t)$ in case of multi-UT) JSAC to produce low-frequency beat signal. For a stationary target, this beat frequency depends only on time delay and frequency changing rate of the waveform. However, in the case of mobile target, Doppler shift is also added to the beat frequency along with the delay [136]. Therefore, the beat frequency f_b can be equated as

$$f_b = \frac{2r_r B}{cT} + \nu_r, \tag{4.225}$$

where ν_r is the Doppler shift that occurs due to the difference in velocities between the host radar and a target. FFT is applied to the beat frequencies to get the range of the targets. The number of beat frequencies corresponds to the number of targets. In **(4.225)**, range r_r and velocity v_r of the targets are coupled. Therefore, to separate these two quantities, multiple chirp sweeps should be transmitted [137]. In this case, 2D-FFT is applied to the beat frequencies to get the range-velocity map. The distance and velocity separability/resolution

of the targets are respectively given by

$$\Delta r = \frac{c}{2B}, \quad \Delta v = \frac{\lambda}{2T}. \tag{4.226}$$

4.6.4.2. Proposed delay-Doppler channel estimation

The conventional embedded channel estimation techniques, as in [138], typically arranges pilot, guard, and data symbols in the delay-Doppler grid to avoid interference between pilot and data symbols at the receiver. However, this approach reduces the spectral efficiency of the communication due to the large guard and increases the PAPR of the transmitted signal [138].

To address these concerns, we propose a novel FMCW-based channel estimation technique for OTFS systems, where the linear FMCW is used as a pilot signal in delay-Doppler domain. Since the linear chirp occupies M points in delay-Doppler domain, the power of the pilot spreads over these points leading to less PAPR. Moreover, the sparse representation of the chirp in Fresnel domain is exploited to get rid of the interference due to data symbols without the need of using any guard which enhances the communication rate.

For that, we assume the same signal model in **(4.221)** where as an example the first OC (0-th OC) is used as a pilot signal in the delay-Doppler domain, as shown in **Figure 5.9a**, as follows

$$X_{\mathrm{DD}} = \begin{cases} X^{p}_{\mathrm{DD}}(k,l) = \sqrt{P_c N}\Omega_0, & (\hat{\alpha} + \hat{\beta}_0) \bmod N = 0 \\ X^{d}_{\mathrm{DD}}(k,l), & \text{otherwise} \end{cases}. \tag{4.227}$$

First, let's rewrite the received signal as follows:

$$y(p) = y_c(p) + y_d(p), \tag{4.228}$$

where $y_c(p)$ and $y_d(p)$ denote the chirp and data symbols contributions, respectively.

1. At the receiver side, in order to eliminate the interference between the data and the pilot symbols, shown in **Figure 5.9b**, the received signal is initially converted to the Fresnel domain as follows

$$\begin{aligned} y_F(m) &= \mathcal{FR}\{y(p)\} \\ &= \mathcal{FR}\{y_c(p)\} + \mathcal{FR}\{y_d(p)\}. \end{aligned} \tag{4.229}$$

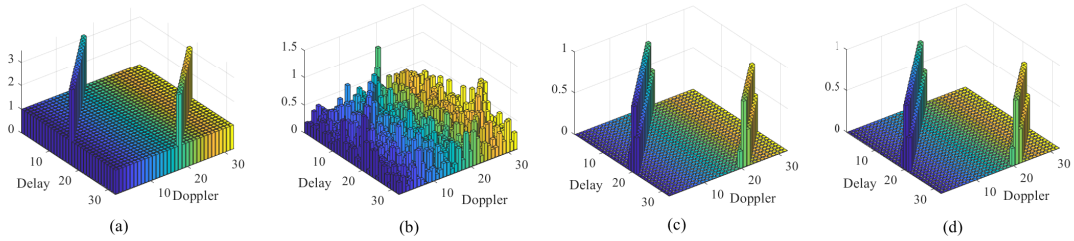


Figure 4.21: The delay-Doppler representation of **a**) transmitted signal, **b**) received signal, **c**) received filtered pilot signal from data interference, and **d**) received pilot signal in case no data is transmitted (zero-interference).

2. The Fresnel domain signal is then weighted to get rid of the interference as follows

$$\tilde{y}_F(m) = G(m) \cdot y_F(m), \tag{4.230}$$

where $G(m)$ is the weighting vector defined as

$$G(m) = \begin{cases} 1, & m \leq (l_{max} + k_{max}) \\ 0, & \text{otherwise} \end{cases}, \tag{4.231}$$

with l_{max} and k_{max} denoting the maximum delay and Doppler spread, respectively. Since

$$\mathcal{FR}\{y_c\}(m) = \begin{cases} \mathcal{FR}\{y_c\}(m), & m \leq (l_{max} + k_{max}) \\ 0, & \text{otherwise} \end{cases}, \tag{4.232}$$

then,

$$\tilde{y}_F(m) = \mathcal{FR}\{y_c(p)\} + G(m) \cdot \mathcal{FR}\{y_d(p)\}. \tag{4.233}$$

3. Then, the signal $\tilde{y}_F(m)$ is converted back to time domain

$$\begin{aligned} \tilde{y}(p) &= \mathcal{FR}^{-1}\{\tilde{y}_F(m)\} \\ &= y_c(p) + \mathcal{FR}^{-1}\{G(m) \cdot \mathcal{FR}\{y_d(p)\}\}. \end{aligned} \tag{4.234}$$

Note that for $\frac{MN}{l_{max}+k_{max}} >> 1$ (which is always the case), we have

$$\mathrm{E}\{|\mathcal{FR}^{-1}\{G(m) \cdot \mathcal{FR}\{y_d(p)\}\}|^2\} << 1, \quad \text{for } \frac{MN}{l_{max} + k_{max}} >> 1. \tag{4.235}$$

Therefore,

$$\begin{aligned} \tilde{y}(p) &\approx y_c(p) \\ &\approx \sum_{r=0}^{R-1} h_r \psi_0(p - l_r) e^{j2\pi \frac{k_r(p-l_r)}{MN}}. \end{aligned} \tag{4.236}$$

where $l_r = \frac{\tau_r}{M\Delta f}$ and $k_r = \frac{\nu_r}{NT}$.

4. The interference free received discretized time pilot signal $\tilde{y}(p)$ is converted back to delay-Doppler domain via DZT, as follows

$$\tilde{Y}_{\mathrm{DD}}(k,l) = \frac{1}{\sqrt{N}} \sum_{n=0}^{N-1} \tilde{y}(l+nM) e^{j2\pi \frac{k}{N} n}. \tag{4.237}$$

It is clearly seen from **Figure 5.9c** that totally agrees with the perfectly received pilot signal illustrated by **Figure 5.9d**.

5. The tensor form of **(4.236)** can be written as [18]

$$\tilde{\mathrm{y}} = \mathrm{H}\boldsymbol{\psi}_0 + \mathrm{w}, \tag{4.238}$$

where w denotes the AWGN vector and $\mathrm{H} \in \mathbb{C}^{K\times K}$ represents the time equivalent channel matrix which is expressed as

$$\mathrm{H} = \sum_{r=0}^{R-1} h_r \boldsymbol{\Pi}_K^{l_r} \boldsymbol{\Delta}_K^{k_r}, \tag{4.239}$$

with $\boldsymbol{\Pi}$ being the permutation matrix, and $\boldsymbol{\Delta}_K$ being the $K \times K$ diagonal matrix given as

$$\boldsymbol{\Delta}_K^{k_r} = \mathrm{diag}\left\{W_K(0\cdot k_r), W_K(1\cdot k_r), \ldots, W_K((K-1)\cdot k_r)\right\}. \tag{4.240}$$

6. The radar information estimated from the chirp part of the signal can be exploited to estimate the delay-Doppler channel impulse response. Specifically, after estimating the parameters (τ_r, ν_r) for all R paths as explained in **Subsection 4.6.4.1**, we find $l_r = \frac{\tau_r}{M\Delta f}$ and $k_r = \frac{\nu_r}{NT}$. The only unknowns left to be estimated are the channel's complex coefficient. For that, **(4.238)** is rewritten as follows

$$\tilde{\mathrm{y}} = \boldsymbol{\Psi}_0 \mathrm{h} + \mathrm{w}, \tag{4.241}$$

where $\boldsymbol{\Psi}_0$ is a $K \times R$ matrix with r-th column expressed by $\boldsymbol{\Psi}_0(:,r) = \boldsymbol{\Pi}_K^{l_r} \boldsymbol{\Delta}_K^{k_r} \boldsymbol{\psi}_0$ and $\mathrm{h} = [h_0, \ldots, h_{R-1}]^T$.

7. we use the maximum-likelihood estimator to determine the channel complex gain corresponding to each one of them. Since the received signal $\tilde{\mathrm{y}}$ can be expressed by the linear model in **(4.241)** where $\boldsymbol{\Psi}_0$ is a known $K \times R$ matrix with $K > R$ and of rank R, h is a $p \times 1$ parameter vector to be estimated, and w is a noise vector with probability density function (PDF) $\mathcal{N}(0, \mathrm{C})$, then the maximum-likelihood

estimator of h is [139]

$$\hat{\mathrm{h}} = \left(\boldsymbol{\Psi}_0^H \mathrm{C}^{-1} \boldsymbol{\Psi}_0\right)^{-1} \boldsymbol{\Psi}_0^H \mathrm{C}^{-1} \tilde{\mathrm{y}}. \tag{4.242}$$

4.7. Delay-Doppler-Based Channel Estimation Method In Doubly-Dispersive OCDM Systems

4.7.1. OCDM in delay-Doppler domain

In this work, we consider an OCDM transmission spanning a bandwidth B and time duration T, where a set of N orthogonal chirps are used to modulate N data symbols x using the inverse discrete Fresnel transform (IDFnT). These N orthogonal chirp waveforms exhibit a linear frequency sweep over time and possess orthogonal properties, enabling them to be transmitted simultaneously without interference. The i-th ($i = 0, 1, \ldots, N-1$) OCDM carrier can be given as [99]

$$\psi_i(t) = e^{j\frac{\pi}{4}} e^{-j\pi\frac{N}{T^2}\left(t - i\frac{T}{N}\right)^2}, 0 \leq t < T. \tag{4.243}$$

To facilitate practical implementation, the OCDM carriers in (**4.243**) are discretized by sampling them at times $t = m\frac{T}{N}$. This yields the discrete i-th OCDM carrier $\psi_i(m)$ given as

$$\psi_i(m) = e^{j\frac{\pi}{4}} e^{-j\pi\frac{(m-i)^2}{N}}, 0 \leq m < N. \tag{4.244}$$

4.7.1.1. OCDM representation in delay-Doppler domain

The delay-Doppler domain serves as an intermediate representation between the time domain and the frequency domain. Let's suppose that the delay-Doppler grid is discretized into N_d delays and M_d Dopplers. Now, consider an arbitrary discrete sequence $\boldsymbol{x}$ with a length of N points, where $N = M_d \times N_d = LN_d^2$, $M_d = LN_d$ and $L, N_d, M_d \in \mathbb{N}$. The DZT, $\mathrm{X_{DD}}$, of $\boldsymbol{x}$ is given by [130]

$$\begin{aligned} X_{\mathrm{DD}}(k,l) =& \frac{1}{\sqrt{N_d}} \sum_{n=0}^{N_d-1} x(k + nM_d) e^{-j2\pi\frac{l}{N_d}n}, \\ & \text{for } 0 \leq k < M_d, 0 \leq l < N_d. \end{aligned} \tag{4.245}$$

Computing $X_{\mathrm{DD}}(k,l)$ requires obtaining M_d DFT operations of size N_d of the data sets $x(k), x(k+M_d), \ldots, x(k+(N_d-1)M_d)$ for $0 \leq k < M_d$. The sequence $\boldsymbol{x}$ can be recovered

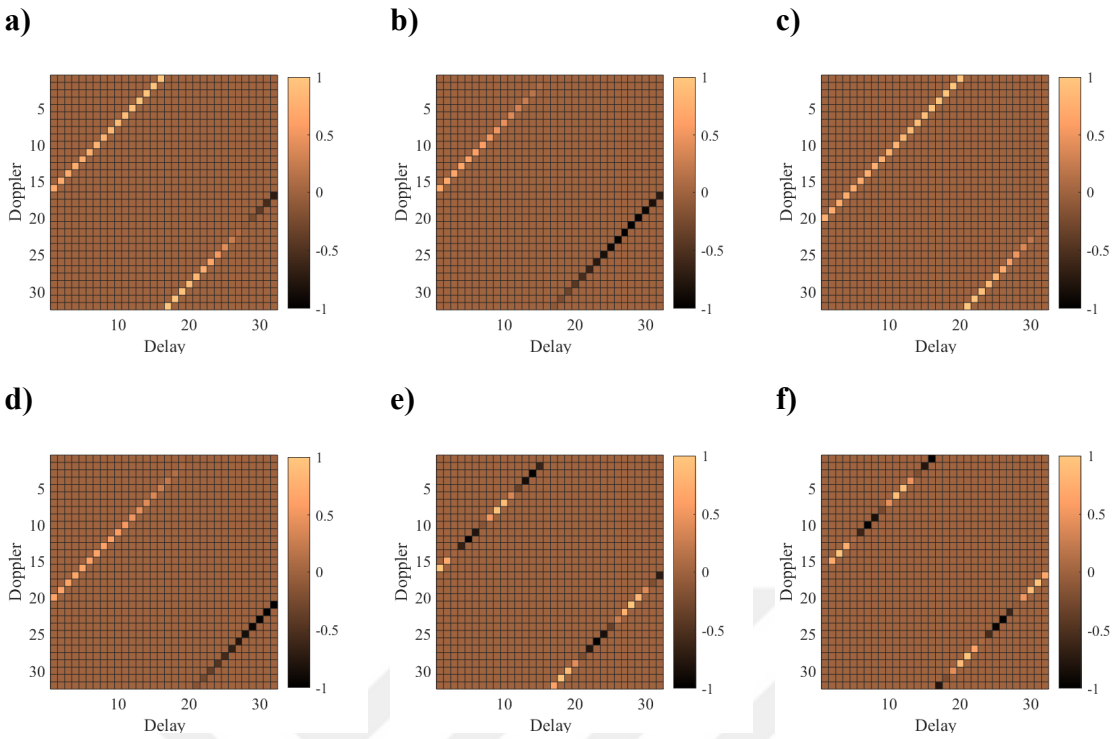


Figure 4.22: The delay-Doppler representation of difference OCDM carriers with parameters $L = 1$, $N_d = 32$, $M_d = 32$, $N = 1024$: **a)** $\mathcal{R}e\{\Psi_{0,\mathrm{DD}}\}$, **b)** $\mathcal{I}m\{\Psi_{0,\mathrm{DD}}\}$, **c)** $\mathcal{R}e\{\Psi_{4,\mathrm{DD}}\}$, **d)** $\mathcal{I}m\{\Psi_{4,\mathrm{DD}}\}$, **e)** $\mathcal{R}e\{\Psi_{128,\mathrm{DD}}\}$, **f)** $\mathcal{I}m\{\Psi_{128,\mathrm{DD}}\}$.

from its DZT by the formula

$$x(k+nM_d) = \frac{1}{\sqrt{N_d}} \sum_{l=0}^{N_d-1} X_{\mathrm{DD}}(k,l) e^{j2\pi \frac{l}{N_d} n} \qquad \text{for } 0 \le k < M_d, 0 \le n < N_d. \tag{4.246}$$

The i-th OCDM carrier in **(4.244)** can be expressed as

$$\psi_i(k+nM_d) = e^{j\frac{\pi}{4}} W_N \left(-\frac{1}{2}(k+nM_d-i)^2 \right), \tag{4.247}$$

where $W_K(k) := e^{j2\pi k/K}$. Then, the DZT of ψ_i in **(4.247)** can be expressed as

$$\begin{aligned} \Psi_{i,\mathrm{DD}}(k,l) &= \frac{1}{\sqrt{N_d}} \sum_{n=0}^{N_d-1} \psi_i(k+nM_d) W_{N_d}(nl) \\ &= \frac{\Omega_i}{\sqrt{N_d}} \sum_{n=0}^{N_d-1} W_{N_d}\left(\alpha n^2 + \beta_i n\right), \end{aligned} \tag{4.248}$$

where $\Omega_i := e^{j\frac{\pi}{4}} W_N\left(-(k-i)^2/2\right)$, $\alpha := -LN_d/2$, and $\beta_i := l + i - k$.

In order to assess the sparsity of OCDM carriers in the delay-Doppler domain, we show that if $\alpha + \beta_i \in \mathbb{Z}$, $\Psi_{i,\mathrm{DD}}$ is only non-zero at M_d specific points within the delay-Doppler

domain. Observe that since

$$W_{N_d}\left(\alpha n^2\right) = (-1)^{Ln^2} = (-1)^{Ln} = W_{N_d}(\alpha n), \tag{4.249}$$

then, we can write

$$\Psi_{i,\mathrm{DD}}(k,l) = \frac{\Omega_i}{\sqrt{N_d}} \sum_{n=0}^{N_d-1} W_{N_d}((\alpha+\beta_i)n), \tag{4.250}$$

provided $L \in \mathbb{Z}$. It follows that $\Psi_{i,\mathrm{DD}}(k,l)$ is sparse, i.e.,

$$\Psi_{i,\mathrm{DD}}(k,l) = \begin{cases} \sqrt{N_d}\Omega_i, & [\alpha+\beta_i]_{N_d} = 0 \\ 0, & \text{otherwise} \end{cases}. \tag{4.251}$$

Figure 4.22 provides an illustrative example of OCDM carriers exhibiting a sparse representation in the delay-Doppler domain. Specifically, **Figure 4.22a-f** showcases the real and imaginary parts of the 0-th, 4-th, and 128-th OCDM carriers, respectively. **Figure 4.22a-b** demonstrate that the root (i.e., 0-th) OCDM carrier of length $N = N_d \cdot M_d$ can be represented by N_d points in the delay-Doppler domain. Furthermore, **Figure 4.22c-d** reveal that the 4-th OCDM carrier is essentially a shifted version of the 0-th carrier in the delay-Doppler domain. It is important to note that the OCDM carriers having index greater than N_d are the same with the root OCDM carrier shifted by $[i]_{N_d}$ changing its complex coefficient values. This is clearly depicted in **Figure 4.22e-f**, where $\hat{i} = [128]_{32} = 0$. Therefore, an OCDM in delay-Doppler domain consists of M_d non-overlapping orthogonal signals (shifted in delay and Doppler) each having N_d overlapping orthogonal signals.

4.7.1.2. OCDM as precoded-OTFS

As demonstrated in Subsections **Subsection 4.7.1.1**, we conclude that each OCDM carrier can be presented as a precoded sparse delay-Doppler signal as given in **(4.251)**. Therefore, OCDM will fully populate an $M_d \times N_d$ delay-Doppler grid with $M_d \times N_d$ OCDM carriers as follows

$$X_{\mathrm{DD}}^{\mathrm{OCDM}}(k,l) = \sum_{i=0}^{M_d N_d - 1} \Psi_{i,\mathrm{DD}}(k,l). \tag{4.252}$$

Then, OCDM can be seen as a pre-processed OTFS modulation [74]. This feature is exploited in the following section to design a novel channel estimation method for the OCDM signal where channel estimation pilots are designed in the chirp domain and the estimation is performed in the delay-Doppler domain.

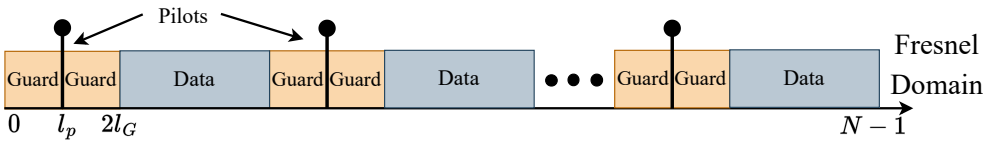


Figure 4.23: Pilot, guard, and data symbol arrangement.

4.7.2. Proposed OCDM channel estimation

The discrete time-domain OCDM signal is given as [99]

$$s(n) = e^{j\frac{\pi}{4}} \frac{1}{\sqrt{N}} \sum_{m=0}^{N-1} x(m) e^{-j\frac{\pi}{N}(m-n)^2} \tag{4.253}$$

Let $h(n)$ be a doubly-dispersive channel with the following time response

$$h(n) = \sum_{i=0}^{P-1} h_i \delta(n - l_i) e^{\frac{j2\pi k_i}{N}(n-l_i)}, \tag{4.254}$$

where P, h_i, l_i, and k_i denote the number of propagation paths, the channel gain, the integer delay, and Doppler shift of the i-th reflector, respectively. After the transmitted signal passes through the wireless channel, the received signal is found as

$$r(n) = \sum_{i=0}^{P-1} h_i s(n - l_i) e^{\frac{j2\pi k_i}{N}(n-l_i)} + w(n), \tag{4.255}$$

where $w(n)$ represents the AWGN with variance σ^2. By applying the discrete Fresnel transform (DFnT) we get the received signal in the Fresnel Domain as follows

$$\begin{aligned} y(m) &= e^{-j\frac{\pi}{4}} \sqrt{N} \sum_{n=0}^{N-1} r(n) e^{j\frac{\pi}{N}(m-n)^2} + w(m) \\ &= \sum_{i=0}^{P-1} h_i e^{j\frac{\pi}{N}\left(m^2 - ([m-l_i-k_i]_N)^2\right)} e^{-j\frac{2\pi}{N}\left(\frac{l_i^2}{2} + l_i[m-l_i-k_i]_N + k_i l_i\right)} \\ &\quad \times x\left([m - l_i - k_i]_N\right) + w(m). \end{aligned} \tag{4.256}$$

By simplifying (**4.256**), we find

$$y(m) = \sum_{i=0}^{P-1} \hbar_i e^{j\frac{2\pi}{N} k_i (m - [l_i + k_i])} x\left([m - l_i - k_i]_N\right) + w(m), \tag{4.257}$$

where $\hbar_i = h_i e^{j\pi\frac{k_i^2}{N}}$.

We propose a novel pilot design-based channel estimation in which N_p pilot symbols are distributed in the Fresnel domain such that they are overlapping orthogonally in delay-Doppler domain (i.e., $\hat{i} = [i]_{N_d}$ as depicted in **Figure 4.22**). In order to be able to estimate

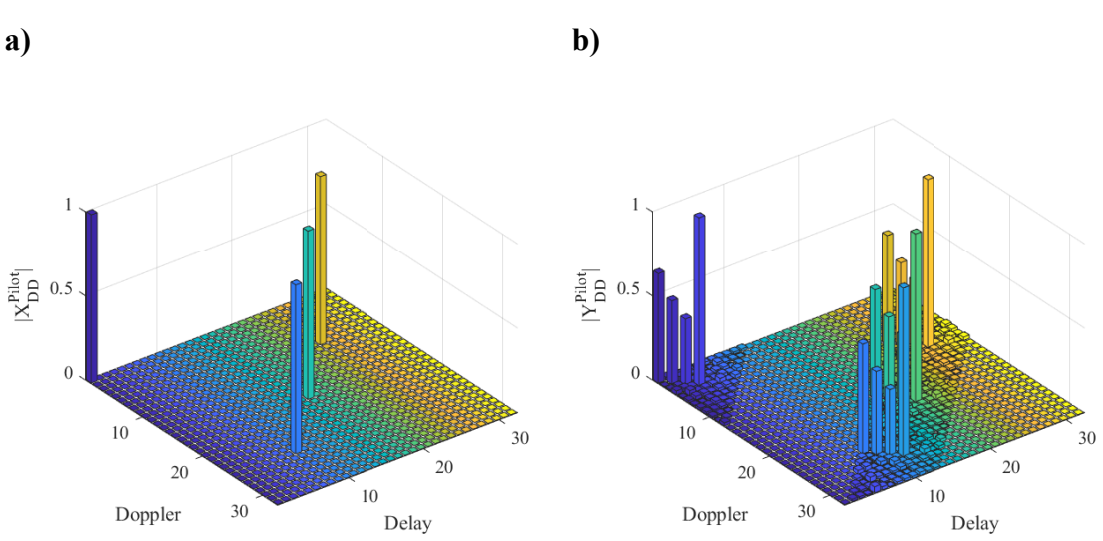


Figure 4.24: The delay-Doppler representation of proposed pilot signal with parameters $N_p = 8$, $N = 1024$, $l_p = 16$, and $l_{\max} = k_{\max} = 4$: **a**) transmitter side, **b**) receiver side.

the channel, the combination of these N_p pilots in delay-Doppler domain must be sparser and their spacing must be larger than the maximum delay $l_{\max}$ and Doppler spreads $k_{\max}$, respectively. Therefore, the number of pilots should be $N_p \geq \max(l_{\max}, k_{\max})$. Using the previous results, consider N_p pilots $x_p(m_p) = \sqrt{E_p}\delta(m-m_p)$ where E_p and m_p denote the power and location of the pilots, respectively. The pilots are transmitted within the data frame, and guards are added to eliminate interference from the data after passing through the wireless channel, as depicted in **Figure 4.23**. The proposed OCDM frame along with the pilot, guard, and data symbol arrangements in the Fresnel domain is given as

$$x(m) = \begin{cases} x_p, & [m]_{\frac{N}{N_p}} = 0 \;\&\; m_p = l_p + \lfloor \frac{mN_p}{N} \rfloor \\ 0, & [m]_{\frac{N}{N_p}} = 0 \;\&\; m_p - l_G \leq m \leq m_p + l_G \\ \sqrt{E_s}x_d, & \text{otherwise} \end{cases}, \tag{4.258}$$

where $l_p \in [0, \frac{N}{N_p} - 1]$, $l_G = 2k_{\max} + l_{\max}$ gives the guard length, respectively. E_s denotes the average data symbol energy. Thus, the equivalent pilot symbols in delay-Doppler domain can be given as

$$X_{\mathrm{DD}}^{\mathrm{Pilot}}(k,l) = \sum_{i=0}^{N_p-1} \Psi_{l_p+i\frac{N}{N_p},\mathrm{DD}}(k,l). \tag{4.259}$$

Figure 4.24 illustrates the pilot signal in the delay-Doppler domain before and after passing through the channel. To estimate the channel accurately in the delay-Doppler domain,

we can employ any channel estimation technique designed for OTFS systems. In this study, we adopt a threshold-based estimation approach inspired by the work conducted in [140]. The channel estimation framework is summarized in Algorithm 1.

Algorithm 4.8 The proposed channel estimation

Input: Received signal $y(m)$

Output: l_i, k_i, and h_i.

Extract the pilot signal y_p from y in Fresnel domain as follows: $y_p(m) = y(m)$ for $m_p \leq m \leq m_p + l_G \forall m_p$.

Transform y_p to time domain and then to delay-Doppler domain and get Y_{DD}^{Pilot} as in **Figure 4.24b**.

Apply threshold-based pilot detection to the received pilot signal as in [140].

Estimate the channel parameters l_i, k_i, and h_i using threshold detection.

CHAPTER 5

5. RESULTS AND DISCUSSION

5.1. Flexible Physical Layer Security For Joint Data And Pilots In OFDM Systems

In this section, we demonstrate the performance of channel decomposition-based physical layer security (PLS) algorithms proposed for MIMO-orthogonal frequency division multiplexing (OFDM) systems. To do so, the bit error rate (BER)-based secrecy gap and normalized mean square error (NMSE)-based secrecy gap metrics are used to evaluate the security of data and pilots, respectively. The BER-based secrecy gap will quantify the amount of information leakage to the Eve, evaluate the secrecy, and also shows the effect of the proposed algorithm on the reliability with respect to legitimate nodes [141]. On the other hand, NMSE-based secrecy gap shows the difference between the quality of estimated channel at the legitimate node and illegitimate node. Moreover, the effect of the proposed algorithm on the peak to average power ratio (PAPR) is also presented along with the comparison to the conventional algorithms. The simulated MIMO-OFDM system parameters are described in **Table 5.1**.

Table 5.1: Simulation parameters

Parameters	Specifications
FFT Size N	256
Pilot Rate	$1/4$
(M_a, N_b, N_e)	$(4, 4, 4)$
Guard Interval (CP)	64
Signal Constellation	QPSK
Channel Model	IEEE 802.11 channel model PDP [3]
Max channel taps L	11

Figure 5.1 shows the BER performance versus signal-to-noise ratio (SNR) of the proposed

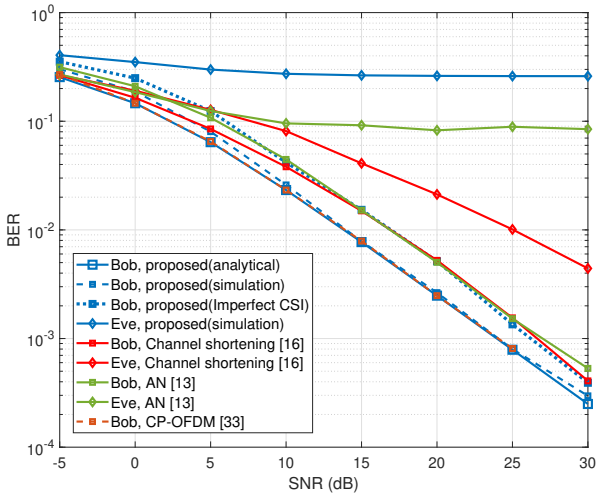


Figure 5.1: BER performance of the proposed data security algorithm vs channel shortening [1], AN [2] and conventional CP-OFDM [3].

data security algorithm when $M_a = N_b = N_e = 4$, along with the comparison to the conventional algorithms such as artificial noise (AN)-based [2], channel shortening [1], and conventional CP-OFDM [3]. In [2], the transmitted signal is added to a properly designed AN in such a way that AN gets accumulated over the cyclic prefix (CP) part of the signal at Bob only while degrading the performance of attacker, where equal power is allocated to data and noise. In [1], a channel shortening filter is designed based on the channel of the legitimate user (Bob) in such a way that the length of the effective channel is made equal to or less than the CP at Bob only, while the length of the effective channel at the illegitimate receiver (Eve) is greater than CP. Firstly, it is observed from **Figure 5.1** that the derived analytical results match well with the simulations except at low SNR regime where a small mismatch is noted. Because, when deriving the BER formula, it is assumed that the channel frequency response is normally distributed. This is because of the assumption in theoretical analysis that channel frequency response (CFR) is normally distributed. However, at very low SNR, after performing the minimum-phase all-pass decomposition to channel, the distribution of the $H^{\min}$ and H^{ap} becomes different from the normal distribution due to the effect of noise decomposition. This effect gets smaller as the SNR increases and the BER finally converges to the derived formula. Also, note that under perfect channel estimation the proposed scheme performs exactly as the CP-OFDM [3], while Eve suffers from high error rates. This implies that the proposed data scheme does not degrade the performance of the legitimate user. Moreover, our novel design

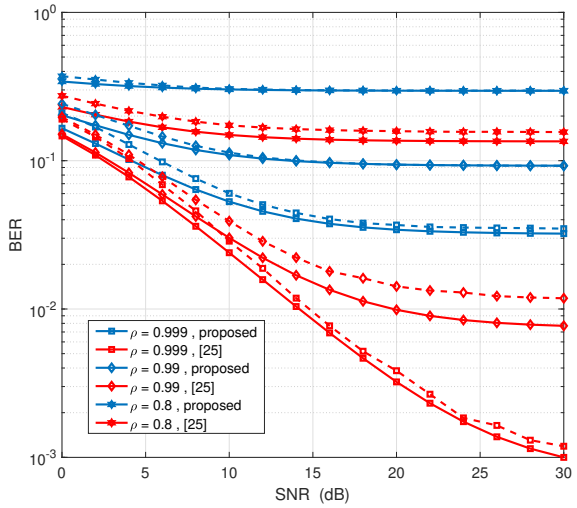


Figure 5.2: Performance comparison of the proposed algorithm (blue color) vs. LS [4] (red color) in terms of Eve's BER under correlated eavesdropping channels. The solid and dashed lines stand for the analytical and simulation results, respectively.

exhibits a significant BER gap performance compared to AN and channel shortening by ensuring the lowest BER values at Bob and the highest error rate at Eve. This result emphasizes the effectiveness of the data security algorithm in maintaining high secrecy levels while preserving the performance of the legitimate user. **Figure 5.1** also shows the BER performance of Bob under imperfect channel estimation. It is seen that at low SNR values, Bob has almost the same performance as AN while at high SNR values larger than 20 dB it performed slightly better.

Figure 5.2 illustrates the analytical as well as the simulated results of Eve's BER performance of the proposed algorithm and link-signature (LS) based algorithm in [4] for the case when Eve's channel is correlated with Bob's. The analytical results agree well with the simulations confirming the model developed in **Subsection 4.1.3.1**. The BER performance is evaluated for the correlation values of $\rho = \{0.999, 0.99, 0.8\}$. It is observed that the performance of Eve improves as the correlation values increase. However, for the same correlation value, we notice a large BER performance gap between the proposed algorithm and LS, where the proposed algorithm clearly outperforms LS method. For instance, when $\rho = 0.999$ the error floor of the proposed scheme settles at 0.03; while if LS is used, the error falls below 0.001. This is due to the fact that the proposed algorithm is using one component of the channel instead of the overall channel, which provides resilience against eavesdroppers near the legitimate nodes as explained in **Subsection 4.1.3.1**.

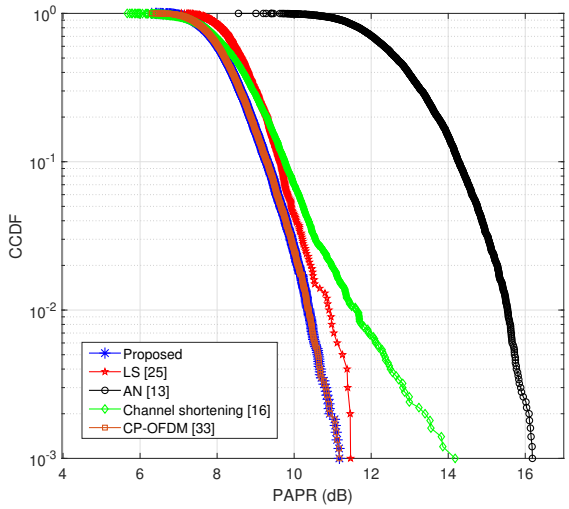


Figure 5.3: The CCDF of the PAPR for the proposed algorithm compared to channel shortening [1], AN [2], LS [4], and conventional CP-OFDM [3].

Thanks to the unit power property of the all-pass channel as explained in **Subsection 4.1.2.1**, the proposed precoding would not cause any power issues since it only changes the phase of each OFDM subcarriers. **Figure 5.3** depicts the complementary cumulative distribution function (CCDF) performance of the PAPR of the proposed algorithm compared to CP-OFDM, AN, LS, and channel shortening methods. It is observed that the PAPR performance of the proposed algorithm is similar to that of conventional OFDM while the application of other security schemes causes an increase in PAPR. This result makes the usage of the proposed precoding technique independent of any power constraint.

Figure 5.4 shows the NMSE versus SNR performance of the estimated channel at the legitimate node and Eve when $M_a = N_b = N_e = 4$. The proposed algorithm is compared to [5], [6], and CP-OFDM [3]. It is observed that there is a significant estimation error gap between Bob and Eve at the cost of some degradation in the estimation quality at very low SNR values compared to conventional channel estimation [3]. This ensures that Eve will neither be able to estimate its channel nor acquire the sensing information from the surrounding environment. It is also observed that the estimation error slightly increases when estimating the minimum-phase or the all-pass channels compared to the effective channel, which justifies the BER performance degradation in **Figure 5.1**. The plots also show that the proposed algorithm outperforms the schemes in [5] and [6] especially at high SNR values.

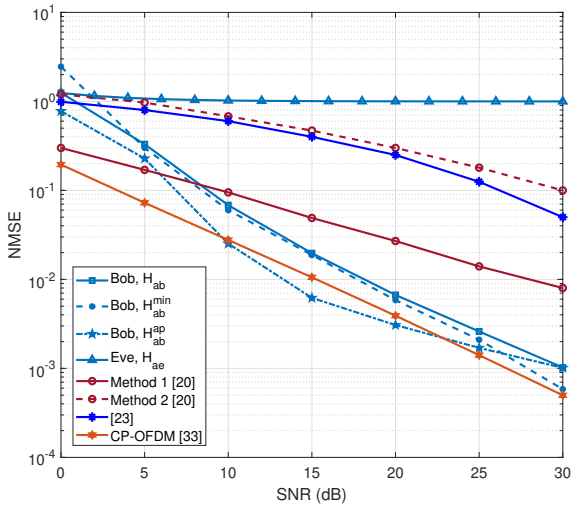


Figure 5.4: The channel estimation's NMSE performance vs SNR at Bob and Eve compared to [5], [6], and [3].

5.2. Common CP-OFDM Transceiver Design For Low-Complexity Frequency Domain Equalization

Table 5.2: Simulation parameters

Parameters	**Specifications**
FFT size	1024
Pilot ratio	1/8, 1/16, 1/32
Guard interval (CP)	128
Signal constellation	4 QAM, 16 QAM, 64 QAM, 256 QAM
Channel model	IEEE 802.11 channel model PDP [3]
N_{tap}	32

In this section, we demonstrate the performance of the proposed pilot-aided channel estimation algorithm for the designed CCP-OFDM system. First, the complexity and the NMSE performance of the channel estimation are computed and compared. Then, the impact of the proposed scheme on the BER performance and the PAPR is investigated to emphasize the robustness of the designed transceiver. The simulated CCP-OFDM system parameters are described in **Table 5.2**.

Table 5.3 includes the evaluation of the computational complexities of the transmitter, receiver, and the channel estimation in the proposed CCP-OFDM, conventional CCP-OFDM, and traditional CP-OFDM schemes in terms of the number of real multiplication

Table 5.3: Complexity comparison between different channel estimation algorithms.

	Tx	Estimation	Rx	Total
LS (Proposed)	4640	16512	4640	25808
ML (CCP-OFDM)	4128	2143748	11300	2159176
MMSE (CP-OFDM)	7172	10569601	7172	10583945

for $M = 8$, $N = 128$ and $MN = 1024$. The complexity of complex discrete Fourier transform (DFT) is computed using the Split-Radix algorithm as in [121], where the channel estimators' complexities are computed as shown in Subsection II-D.

Overall, it is observed that the proposed scheme is almost 100 and 400 times less complex than minimum mean squared error (MMSE) and maximum likelihood (ML) estimators, respectively. These results clearly show the importance of enabling channel estimation and equalization in the frequency domain, thus making low-complexity estimators implementable at the receiver unlike in conventional CCP-OFDM. In addition, it is seen that the total complexity of the transmitter and the receiver is also small compared to the conventional MSE and CP-OFDM systems. This emphasizes the superiority of the proposed scheme.

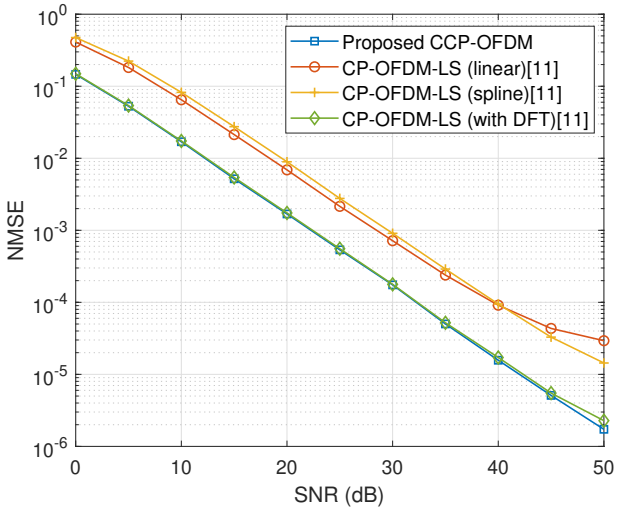


Figure 5.5: The NMSE performance of proposed scheme compared to CP-OFDM using different channel estimators.

Figure 5.5 presents the NMSE performance of the proposed algorithm versus classical CP-OFDM using LS estimator. The figure shows the reliability of the estimated channel in the proposed scheme under time-invariant channel of $N_{tap} = 32$ taps. **Figure 5.5** also depicts that the proposed channel estimation outperforms the channel NMSE performance

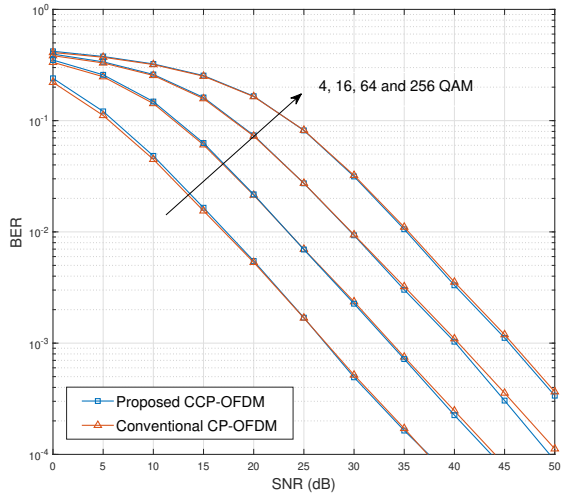


Figure 5.6: BER performance of the proposed CCP-OFDM and conventional CP-OFDM systems.

when LS estimator is used for CP-OFDM (with linear or spline interpolation). This is because only N samples are used to recover the channel frequency response (CFR) instead of using MN samples in the proposed scheme, which eliminates the effect of noise outside the maximum channel delay. This is emphasized when the proposed method's NMSE performance is compared to CP-OFDM with DFT which ignores the channel impulse response (CIR)'s coefficients that contain noise only.

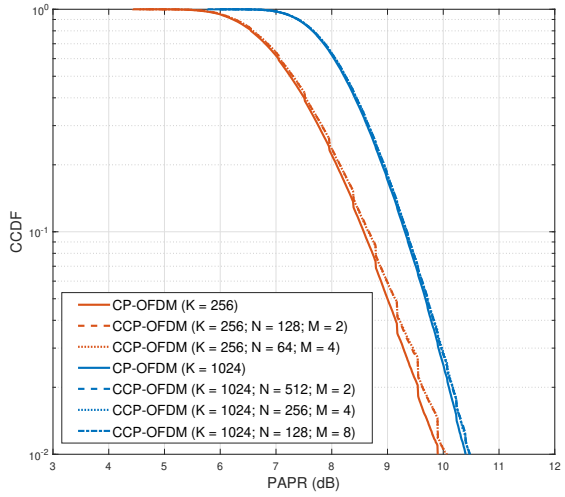


Figure 5.7: CCDF of the PAPR of the transmitted signal of CP-OFDM and proposed CCP-OFDM.

Figure 5.6 illustrates the BER results for $M = 8$ and $MN = 1024$ for the proposed CCP-OFDM and the conventional CP-OFDM. It is observed from **Figure 5.6** that the developed

scheme achieves the same BER performance as the CP-OFDM for all simulated quadrature amplitude modulation (QAM) parameters in **Table 5.2**. However, in the proposed CCP-OFDM system, only one CP is used for all M OFDM symbols and thus providing higher spectral efficiency and data rates.

One of the main problems of OFDM is the high PAPR value, which is caused after the DFT process at the transmitter. In the proposed scheme, cascaded DFT processes are used, **Figure 5.7** compares the CCDF of the PAPR of the transmitted signal of CP-OFDM and the proposed CCP-OFDM. It is shown that a cascaded DFT process of $N \times N$ and $M \times M$ sizes have similar PAPR behavior as of one DFT process of size $MN \times MN$ for large N and M values, showing that the proposed scheme does not cause any further artifact to the OFDM system.

5.3. A Novel Cyclic Prefix Configuration For Enhanced Reliability And Spectral Efficiency In OTFS Systems

Table 5.4: Simulation parameters

Parameters	**Specifications**
Delay-Doppler grid size	$M = 64,\ N = 64$
Signal constellation	BPSK
Channel model	Extended Vehicular A model (EVA) [142]
Channel taps (L)	4
maximum delay spread $l_{\max}$	$M/8$
maximum Doppler spread $k_{\max}$	$N/8$

In this section, we present and analyze the performance of the two use cases of proposed FCP-OTFS mentioned above. The first one is a simple combiner scheme that makes use of the CP block and its corresponding repeated data to enhance BER performance for reliable communication. The second is a spectrally efficient pilot allocation scheme for channel estimation. The system parameters used for simulation are summarized in **Table 5.4**.

One use of the proposed FCP-OTFS is enhancing the SNR of the repeated data in the proposed FCP block. To do so, a simple equal-weight combiner is used after equalizing the channel effects, where the noise signal gets averaged. Let S be a data symbol falling within the repeated block of the proposed FCP-OTFS. Then, at the receiver side and after

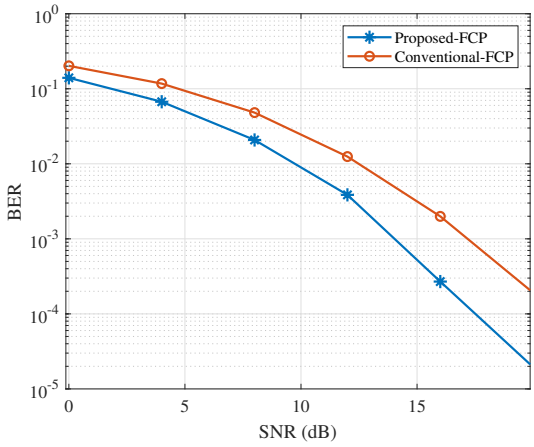


Figure 5.8: The BER performance of data in the CP portion.

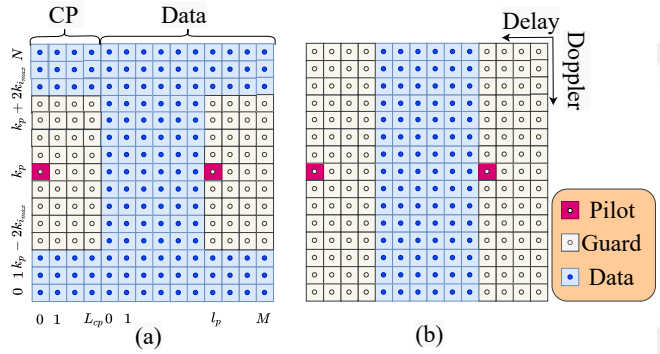


Figure 5.9: Proposed pilot design for channel estimation in the case of: **a**) inter delay-Doppler shifts, **b**) fraction Doppler shifts.

channel equalization, the symbol corresponding to S is found as

$$\begin{cases} R_d = S + n_1, & \text{in data block} \\ R_{\text{cp}} = S + n_2, & \text{in CP block,} \end{cases} \tag{5.1}$$

where $n1$ and $n2$ denote the additive white Gaussian noise (AWGN) with zero mean and variance σ^2 i.e., $n_1, n_2 \sim \mathcal{CN}(0, \sigma^2)$. A simple equal-weight combiner is given as

$$\hat{S} = \frac{1}{2}(R_d + R_{\text{cp}}) = S + n, \tag{5.2}$$

where $n = \frac{n_1+n_2}{2}$ which is also normally distributed with $n \sim \mathcal{CN}(0, \frac{\sigma^2}{2})$. This implies that the noise power is reduced to half which is equivalent to almost 3 dB SNR enhancement. This SNR improvement is clearly observed in **Figure 5.8**, where the performance of the BER of data repeated in the CP block in our proposed structure is 3 dB better than the conventional FCP-OTFS. Therefore, proposed FCP-OTFS is suitable for the ultra-reliable communication.

a) **b)**

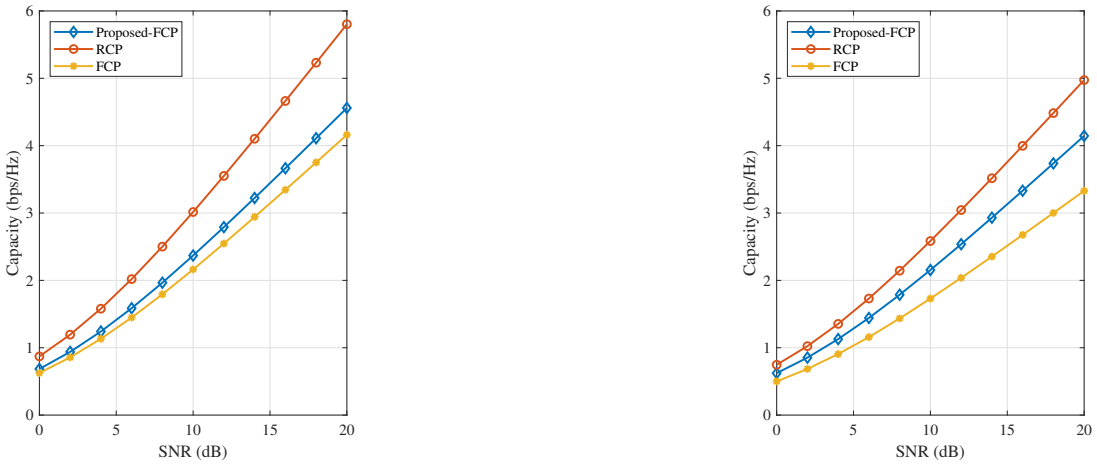


Figure 5.10: OTFS system's capacity under integer and fractional Doppler channel: **a**) integer Doppler channel, **b**) fractional Doppler channel.

The delay-Doppler guard band adopted in embedded pilot channel estimation [140] reduces the spectral efficiency of the OTFS system. Therefore, the proposed FCP configuration can be used to minimize the guard size into half as shown in **Figure 5.9**, where the pilot is embedded within the data portion that is copied for CP. **Figure 5.9a** shows the proposed pilot design for channel estimation in the case of integer delay-Doppler shifts where **Figure 5.9b** depicts the pilot design in case of channel with fractional Doppler shifts.

The total spectral efficiency in OTFS systems depends directly on the prefix configuration, CP size, M, N, and the size of the pilot guard band. To show that, let $l_{\max}$ and $k_{\max}$ be the maximum delay and Doppler spread, respectively, and consider the capacity C for a given instantaneous SNR γ as follows [143]

$$C_{R_{\text{cp}}} = \left(\frac{MN - 8k_{\max}l_{\max}}{MN + L_{\text{cp}}}\right)\log_2\left(1+\gamma\right) \tag{5.3a}$$

$$C_{F_{\text{cp}}} = \left(\frac{MN - 8k_{\max}l_{\max}}{N(M + L_{\text{cp}})}\right)\log_2\left(1+\gamma\right) \tag{5.3b}$$

$$C_{RF_{\text{cp}}} = \left(\frac{MN - 4k_{\max}l_{\max}}{N(M + L_{\text{cp}}) + L_{\text{cp}}}\right)\log_2\left(1+\gamma\right). \tag{5.3c}$$

The capacity of the OTFS system under two channel scenarios, integer and fractional Doppler channels, is shown in **Figure 5.10a** and **Figure 5.10b**, respectively. With parameters set as given in **Table 5.4**, **Figure 5.10a** demonstrates that the proposed FCP pilot

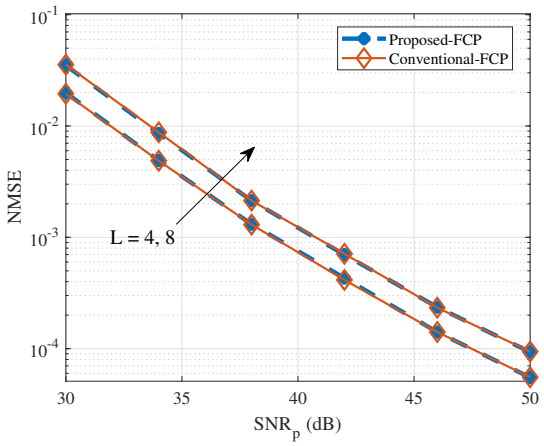


Figure 5.11: Channel NMSE performance for different L taps.

structure improves the capacity of the OTFS system compared to FCP-OTFS as half of the guard in the proposed FCP-OTFS is placed within the CP block. The RCP-OTFS system has the highest capacity due to using only one CP. In the case of fractional Doppler shifts, a long pilot guard covering the entire Doppler dimension is used (i.e., $k_{\max} = N/4$). **Figure 5.10b** compares the capacities of the various OTFS systems and shows that the spectral efficiency of the proposed FCP-OTFS becomes closer to RCP's performance while FCP-OTFS performs the worst.

The impact of the proposed scheme on channel estimation is evaluated by simulating and showing the channel NMSE performance in **Figure 5.11**. The results show that the proposed FCP pilot scheme performs similarly to the conventional scheme [140]. Note that SNR_p in **Figure 5.11** represents the pilot's SNR. In conclusion, the proposed FCP-OTFS achieves similar channel estimation performance as the conventional scheme while utilizing half of the delay-Doppler guard band and ensuring zero ISI between the OTFS subsymbols.

5.4. Fractional Doubly-Dispersive Channel Estimation And Mitigation Framework In OTFS Systems

5.4.1. Cramer-Rao lower bound

We will compare the performance of our proposed algorithm with that of Cramer-Rao lower bound (CRLB), which is a computational technique that uses the Fisher information matrix for maximum performance benchmark. First, CRLB will be derived separately for

the fractional delay and Doppler coefficients ι and κ, respectively. For this, the received delay-Doppler domain signals can be written as [60]

$$Y(l,k) = U(l,k) + W(l,k), \tag{5.62}$$

where $U(l,k)$ represents the received signal without noise effect and will be used for the Fisher information matrix calculation. For the fractional Doppler and fractional delay cases $U(l,k)$ can be respectively given by

$$\begin{aligned} U^{(i,f)}(l,k) = \sum_{i=1}^{L} \sum_{q'=0}^{N-1} h_i \Gamma^{(i)}(l,k) \left(\frac{e^{-j2\pi(-q'-\kappa_i)} - 1}{N e^{-j\frac{2\pi}{N}(-q'-\kappa_i)} - N} \right) \\ X\left([l-l_i]_M, [k-k_i+q']_N \right), \end{aligned} \tag{5.63}$$

and

$$\begin{aligned} U^{(f,i)}(l,k) = \sum_{i=1}^{L} \sum_{q=0}^{M-1} h_i \Gamma^{(i)}(l,k) \left(\frac{e^{j2\pi(-q-\iota_i)} - 1}{M e^{j\frac{2\pi}{M}(-q-\iota_i)} - M} \right) \\ X\left([l-l_i+q]_M, [k-k_i]_N \right). \end{aligned} \tag{5.64}$$

In the case of fractional Doppler channel, we define the $\boldsymbol{\theta} = [\kappa_1, \kappa_2, \ldots \kappa_L]^T$ (or $\boldsymbol{\theta} = [\iota_1, \iota_2, \ldots \iota_L]^T$ for the fractional delay channel) for the derivation of CRLB. The j-th diagonal element of inverse of the Fisher information matrix is j-th element of CRLB which is given as

$$\boldsymbol{\theta}_j^{\mathrm{CRLB}} = [\mathrm{I}^{-1}(\boldsymbol{\theta})]_{jj}, \tag{5.65}$$

where the $L \times L$ matrix $\mathrm{I}(\boldsymbol{\theta})$ represents the Fisher information matrix. The (i,j)-th element of $\mathrm{I}(\boldsymbol{\theta})$ can be found as follows

$$[\boldsymbol{I}(\boldsymbol{\theta})]_{ij} = -\mathbb{E}\left[\frac{\partial^2 \ln p(\boldsymbol{y};\boldsymbol{\theta})}{\partial\theta_i \partial\theta_j} \right], \tag{5.66}$$

where $i = 1, 2, \ldots, L$, $j = 1, 2, \ldots, L$, $\boldsymbol{y} = \mathrm{vec}(\mathrm{Y})$, and the expectation is taken with respect to $p(\boldsymbol{y};\boldsymbol{\theta})$. From (70), the received signal $Y(l,k)$ follows the same distribution as the noise. Assuming the noise to be AWGN the joint probability density function (PDF) of $p(\boldsymbol{y};\boldsymbol{\theta})$ can be expressed as

$$p(\boldsymbol{y};\boldsymbol{\theta}) = \prod_{z=0}^{Z-1} \frac{1}{\sigma\sqrt{2\pi}} e^{-\frac{1}{2}\left(\frac{Y_z - \mu_z}{\sigma}\right)^2}, \tag{5.67}$$

where $\mu_z = U_z$ and Z denotes the total number of received samples used to estimate the channel which is equivalent to the guard symbols. Next, the likelihood function to convert

the product of probability into a summation, and $\ln p(\boldsymbol{y};\boldsymbol{\theta})$ can be represented as

$$\ln p(\boldsymbol{y};\boldsymbol{\theta}) = -\frac{Z}{2}\ln\left(2\pi\sigma^2\right) - \frac{1}{2\sigma^2}\sum_{z=0}^{Z-1}|Y_z - U_z|^2, \tag{5.68}$$

where Y_z and U_z denote the z-th element of vectorized form of Y and U. Hence **(5.80)** can be rewritten as

$$[\boldsymbol{I}(\boldsymbol{\theta})]_{ij} = \frac{1}{2\sigma^2}\sum_{z=0}^{Z-1}\left[-\frac{\partial u_z}{\partial\theta_i}\frac{\partial u_z^*}{\partial\theta_j} - \frac{\partial u_z^*}{\partial\theta_i}\frac{\partial u_z}{\partial\theta_j}\right]. \tag{5.69}$$

To calculate the Fisher information matrix, U must be differentiated with respect to the variables κ and ι to be estimated. The derivative for the Fisher information matrix with respect to κ is given by **(4.144)** and the derivative with respect to ι is given by **(4.145)**.[8]

For the performance analysis of the proposed algorithm in terms of NMSE, CRLB should be normalized separately with respect to fractional delay and Doppler shift as follows

$$\hat{\boldsymbol{\kappa}}_{\text{bound}} = \frac{\sum_{j=1}^{L}\theta_j^{CRLB}}{\|\boldsymbol{\kappa}_{\boldsymbol{\theta}}\|_2^2}, \quad \hat{\boldsymbol{\iota}}_{\text{bound}} = \frac{\sum_{j=1}^{L}\theta_j^{CRLB}}{\|\boldsymbol{\iota}_{\boldsymbol{\theta}}\|_2^2}, \tag{5.72}$$

where $\boldsymbol{\kappa}_{\boldsymbol{\theta}} = [\kappa_1, \kappa_2, \ldots, \kappa_L]^T$ and $\boldsymbol{\iota}_{\boldsymbol{\theta}} = [\iota_1, \iota_2, \ldots, \iota_L]^T$.

5.4.2. Computational complexity analysis

In this section, computational complexity analysis of the proposed methods is examined in terms of number of complex multiplications. The complexity of complex DFT is computed using the Split-Radix algorithm as in [121].

5.4.2.1. Fractional doppler channel estimation

The computational complexity of the fractional Doppler channel estimation framework can be computed directly from **Algorithm 1**. For instance, in *step 2* the delay-Doppler domain symbols are converted back to the time domain with the complexity $O_2^1 = MN\log(N)$ which is valid for rectangular pulse shaping [45]. *Step 6* raises the powers of the received time samples which is of complexity $O_6^1 = \log(MN)$. *Step 7* considers converting the signal to delay-Doppler domain which is of complexity $O_7^1 = MN\log(N)$ and *step 10* computes the mean that is considered to have a complexity of $O_9^1 = 1$ which is calculated L times. Finally, note that *step 6* and *step 7* are computed $\alpha_{max} \times L$ times,

[8] The derived CRLB is relaxed since the non-zero elements are assumed to be known.

a) b)

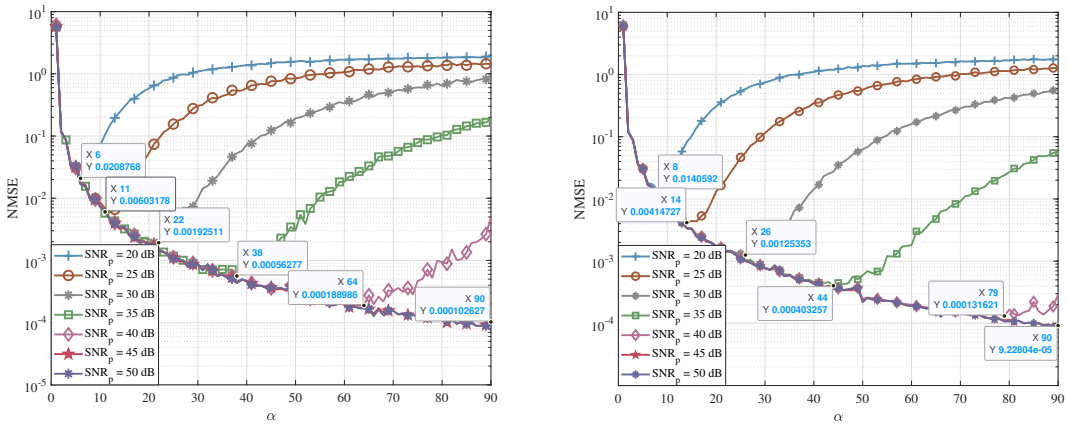


Figure 5.12: NMSE vs α analysis: **a**) fractional Doppler case, **b**) fractional delay case.

therefore, the computational complexity of **Algorithm 1** is found as

$$O^1 = MN\log(N) + \alpha_{max}L(\log(MN) + MN\log(N)) + L. \quad \textbf{(5.73)}$$

5.4.2.2. Fractional delay estimation

Algorithm 2 shares all the steps with **Algorithm 1**. On top of that, in *step 3* the signal is converted to frequency domain with a complexity of $O_3^2 = MN\log(MN)$. *Step 8* converts back the signal to time domain with a complexity of $O_8^2 = MN\log(MN)$. Therefore, the total computational complexity of **Algorithm 2** is as follows

$$O^2 = (\alpha_{\max}L + 1)MN\log(MN^2) + \alpha_{\max}L\log(MN) + L. \quad \textbf{(5.74)}$$

5.4.3. Performance of the proposed channel estimation framework

In this section, we demonstrate the performance of the proposed fractional delay-Doppler channel estimation framework in orthogonal time-frequency space (OTFS) system in terms of estimated channel NMSE, BER, and computational complexity. The delay-Doppler grid size is $M = 32$, $N = 32$, the channel model used is Extended Vehicular A model (EVA) [144], and the fractional delay and Doppler shifts are assumed to be uniformly distributed i.e., $(\kappa,\ \iota) \sim \mathcal{U}(-0.5, 0.5)$.

The NMSE of the estimated fractional Doppler shifts κ and fractional delays ι using the proposed algorithms is compared to the NMSE of the optimal estimator that is given by

a) **b)**

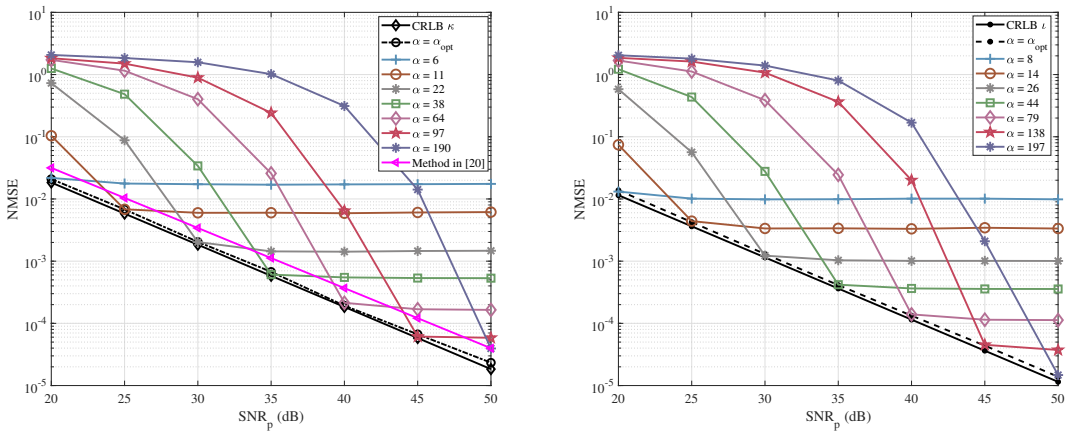


Figure 5.13: NMSE vs SNR_p analysis: **a**) fractional Doppler case, **b**) fractional delay case.

CRLB. The NMSE is calculated as follows

$$\text{NMSE}(\boldsymbol{\eta}) = \frac{1}{L}\sum_{i=1}^{L}\frac{\|\hat{\boldsymbol{\eta}}_i - \boldsymbol{\eta}\|_2^2}{\|\boldsymbol{\eta}\|_2^2}, \tag{5.75}$$

where $\hat{\boldsymbol{\eta}}_i$ is denotes estimated variable of $\boldsymbol{\eta}$ in the i-th path.

Figure 5.12 represents the NMSE vs α for various SNR levels. **Figure 5.12a** shows the effect of changing α in the fractional Doppler case while **Figure 5.12b** represents the fractional delay case. The figures show that as α increases, the normalized error decreases until it reaches a global minimum for an optimal value $\alpha = \alpha_{opt}$. When $\alpha > \alpha_{opt}$, noisy components of the received signal start dominating the higher powers of the signal resulting in an increasing error. Notice that an optimum value of α_{opt} needs to be extracted for each SNR level in both fractional Doppler and delay cases. For instance, for the given simulation parameters, it is found that for $\text{SNR}_p = 40$ dB, the optimal values of alpha are $\alpha_{opt} = 64$ for estimating fractional Doppler shifts as depicted in **Figure 5.12a** and $\alpha_{opt} = 79$ for estimating fractional delay shifts as depicted in **Figure 5.12b**.

Figures **Figure 5.13a-b** represent the NMSE vs SNR for different α values for fractional Doppler and delay cases, respectively. It is shown that choosing a fixed value of α leads to high-error performance even with a high chosen α value. However, with an optimum α_{opt} value at each SNR level, the system performance almost reaches the lower bound error (i.e., CRLB curve) in both fractional Doppler and delay cases. This means that the proposed estimator is indeed an efficient estimator if $\alpha = \alpha_{opt}$. Furthermore, to emphasize

the superiority of the developed estimation framework, the estimation performance of κ is compared to the method in [60] as depicted in **Figure 5.13a**. It is seen that the proposed method outperforms the sparse structured signal recovery estimator in [60].

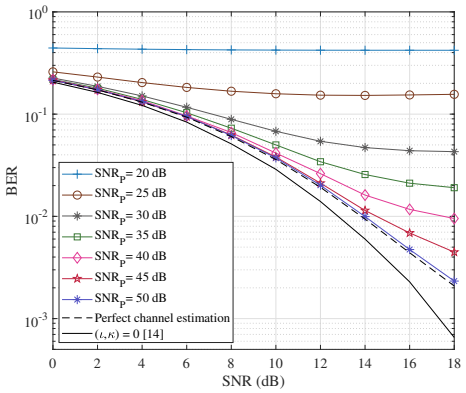


Figure 5.14: BER vs SNR$_p$ analysis.

The BER analysis is made for OTFS with both fractional delay and Doppler shifts, as illustrated in Figures **Figure 5.14**. BER is simulated vs different SNR$_p$ values and then compared with perfect channel estimation and integer channel ($\kappa = \iota = 0$) cases. It is observed that the BER reduces as SNR$_p$ increases, leading to a system with a performance close to the perfect one that provides more accurate channel estimation and better equalization and data detection. Note that choosing SNR$_p$ is a crucial design parameter; for instance, for the given simulation parameters, SNR$_p = [20, 25, 30]$ values should not be used since they result in a very poor BER performance.

Figure 5.15 illustrates the computational complexity of the proposed method for a fixed number of Doppler bins $N = 32$ and with different number of delay bins M compared to the method in [61]. It is shown that the proposed method has a very low computational complexity compared to the off-grid method in [61] where it could achieve almost 100000 times lower complexity at $M = 32$. Moreover, note that the computational complexity of the proposed method is also adjustable based on the required application by selecting different values of $\alpha_{\max}$.

Finally, we demonstrate the feasibility of our proposed framework for jointly estimating fractional delay and Doppler shifts in a real-time experiment. The experiment was conducted using the Keysight Agilent Technologies EXA vector signal analyzer (VSA) N9010A and EXG vector signal generator (VSG) N5172B, a reverberation chamber, and

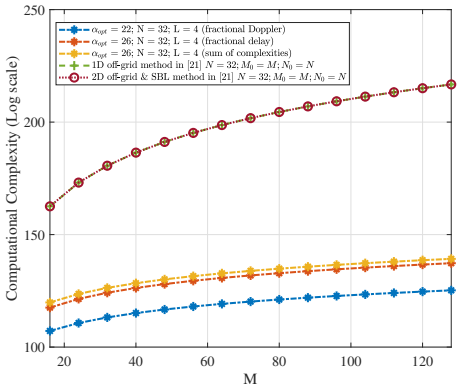


Figure 5.15: Computational complexity analysis.

a fan to generate Doppler. An OTFS frame with parameters $M = 32$, $N = 32$, a bandwidth of 10 MHz, and a central frequency of 2.45 GHz was transmitted, and the received signal was demodulated and extracted from the VSA, as shown in **Figure 5.16**. The proposed algorithm was then tested by iterating through various values of α given that $\alpha_{\max} = 40$. Figures **Figure 5.16a-e** depict the case of estimating the delays when $\alpha = [1, 10, 22, 30, 40]$, where it is seen that as α increases, the 2D sinc pulse shifts in the delay axis. The same thing can be seen for the Doppler case, shown by **Figure 5.16f-j**, where this time as α increases, the 2D sinc pulse shifts in the Doppler axis. Using the results in **Figure 5.16**, Algorithms 1 and 2 can be applied to estimate the fractional delay and Doppler shifts, which are computed to be

$$l_i + \iota_i = 0.225, \qquad k_i + \kappa_i = -0.1. \tag{5.76}$$

These experimental results confirm the effectiveness of our proposed algorithm in estimating fractional channels.

5.5. OTFS-Based ISAC For Super-Resolution Range-Velocity Profile

5.5.1. Cramer-Rao lower bound

To test the performance of our proposed algorithm, a comparison is held with CRLB, which is a lower bound on the variance of any unbiased estimator that uses the Fisher information matrix to show the best achievable performance using an unbiased estimator. The receive delay-Doppler domain signal that is given by as [60].

$$Y(l, k) = U(l, k) + W(l, k), \tag{5.77}$$

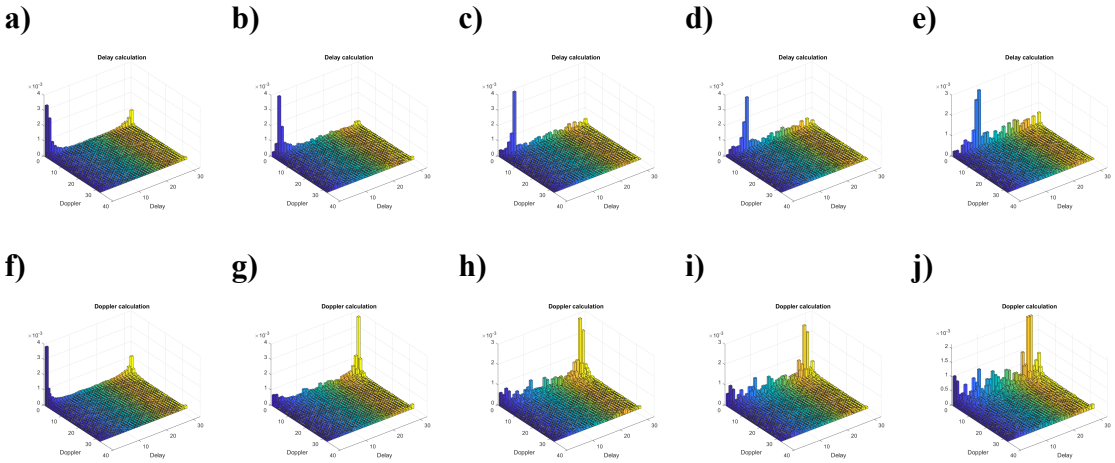


Figure 5.16: The delay-Doppler representation of the received pilot signal acquired using experimental setup for different α values: **a**) delay $\alpha = 1$, **b**) delay $\alpha = 10$, **c**) delay $\alpha = 22$, **d**) delay $\alpha = 31$, **e**) delay $\alpha = 40$, **f**) Doppler $\alpha = 1$, **g**) Doppler $\alpha = 10$, **h**) Doppler $\alpha = 22$, **i**) Doppler $\alpha = 31$, **j**) Doppler $\alpha = 40$.

The Fisher information matrix will be calculated using $U(l,k)$ which represents the received signal without noise effect. For our case where the desired estimated parameters are the range R_i and velocity V_i, the $U(l,k)$ can rewritten based on **(4.178)** and **(4.179)** as given below

$$U(l,k) = \sum_{q'=0}^{N-1}\sum_{q=0}^{M-1} h_i \Gamma^{(i)}(l,k) \left(\frac{e^{-j2\pi(-q'-(\beta V_i - k_i))} - 1}{N e^{-j\frac{2\pi}{N}(-q'-(\beta V_i - k_i))} - N}\right) \left(\frac{e^{j2\pi(-q-(\gamma R_i - l_i))} - 1}{M e^{j\frac{2\pi}{M}(-q-(\gamma R_i - l_i))} - M}\right) X\left([l - l_i + q]_M, [k - k_i + q']_N\right), \tag{5.78}$$

where $\beta = \frac{2f_c NT}{c}$ and $\gamma = \frac{2M\Delta f}{c}$. To derive the CRLB, we define $\boldsymbol{\phi} = [V_1, V_2, \ldots V_L, R_1, R_2, \ldots R_L]^T$, so j-th diagonal element of the Fisher information matrix is found as

$$\boldsymbol{\phi}_j^{\text{CRLB}} = [\mathrm{I}^{-1}(\boldsymbol{\phi})]_{jj}, \tag{5.79}$$

where the elements of the Fisher information matrix $\mathrm{I}(\boldsymbol{\phi})$ are given by

$$[\mathrm{I}(\boldsymbol{\phi})]_{ij} = -\mathbb{E}\left[\frac{\partial^2 \ln p(\boldsymbol{y};\boldsymbol{\phi})}{\partial\phi_i \partial\phi_j}\right], \tag{5.80}$$

where $i = 1, 2, \ldots, L$, $j = 1, 2, \ldots, L$, $\boldsymbol{y} = \mathrm{vec}(\mathrm{Y})$, and the expectation is taken with respect to $p(\boldsymbol{y};\boldsymbol{\phi})$. From (40), the received signal $Y(l,k)$ follows the same distribution as

the noise. Assuming the noise to be AWGN the joint PDF of $p(\boldsymbol{y};\boldsymbol{\phi})$ can be expressed as

$$p(\boldsymbol{y};\boldsymbol{\phi}) = \prod_{z=0}^{Z-1} \frac{1}{\sigma\sqrt{2\pi}} e^{-\frac{1}{2}\left(\frac{Y_z-\mu_z}{\sigma}\right)^2}, \tag{5.81}$$

where $\mu_z = U_z$ and Z denotes the total number of received samples used to estimate the channel which is equivalent to the guard symbols. Next, the likelihood function to convert the product of probability into a summation, and $\ln p(\boldsymbol{y};\boldsymbol{\phi})$ can be represented as

$$\ln p(\boldsymbol{y};\boldsymbol{\phi}) = -\frac{Z}{2}\ln\left(2\pi\sigma^2\right) - \frac{1}{2\sigma^2}\sum_{z=0}^{Z-1}|Y_z - U_z|^2, \tag{5.82}$$

where Y_z and U_z denote the z-th element of vectorized form of Y and U. Hence **(5.80)** can be rewritten as

$$[\mathrm{I}(\boldsymbol{\phi})]_{ij} = \frac{1}{2\sigma^2}\sum_{z=0}^{Z-1}\left[-\frac{\partial u_z}{\partial\phi_i}\frac{\partial u_z^*}{\partial\phi_j} - \frac{\partial u_z^*}{\partial\phi_i}\frac{\partial u_z}{\partial\phi_j}\right]. \tag{5.83}$$

To calculate the Fisher information matrix, the first derivative of U must be obtained with respect to the variables V and R. The derivative for the Fisher information matrix with respect to V is given by (47), and the derivative with respect to R is given by **(4.186)**. For the performance analysis of the proposed algorithm in terms of root mean squared error (RMSE), CRLB bound should be calculated as follows

$$\left(\hat{V},\hat{R}\right)_{\text{bound}} = \sqrt{\sum_{j=1}^{L}\phi_j^{\text{CRLB}}}. \tag{5.49}$$

5.5.2. Computational complexity analysis

In this subsection, we analyze the computational complexity of the proposed algorithm (outlined in **Algorithm 1**) in terms of the number of complex multiplications. Firstly, in *step 2*, the signal conversion from delay-Doppler (DD) domain to the time domain has a complexity order of $O = MN\log(N)$. Then, for each channel tap, the algorithm estimates the delays and Doppler shifts in two loops. In calculating the Doppler shifts, *step 7* involves multiplying the time-domain signal by a bank of phases equal to ϵ_φ, which has a complexity of $O = \epsilon_\varphi MN$. Subsequently, in *step 8*, the signal is converted back to the DD domain with a complexity of $O = \epsilon_\varphi MN\log(N)$. In the other loop, the calculation of the delays requires the same number of complex multiplications as in Doppler shifts with the additional steps of transferring the signal to the frequency domain and back to the time

Table 5.5: Computational complexity comparison

Technique	Complexity
OMP [50]	$\mathcal{O}(L^3 + L^2MN + LM^2N^2)$
SBL [145]	$\mathcal{O}(N_0^2M_0^2NM)$
MP [146]	$\mathcal{O}(NMN_{iter}(24L^2 + 40L\lvert\mathcal{A}\rvert - 4L))$
MRC [147]	$\mathcal{O}(N_{iter}(2L + 1 + 2\log(N)))$ $NM(4L + 2L) + NM(L + 2\log(M) + 3))$
MMSE	$3N^3M^3 + N^2M^2 + NM$
Proposed	$\mathcal{O}\big(MN\log(N) + L(\epsilon_\varphi\,(MN\,(1 + \log(N))))$ $+ \epsilon_\theta\,(MN\,(1 + 2\log(MN) + \log(N)))))\big)$

domain, which both have a total complexity order of $\mathcal{O} = 2\epsilon_\theta MN\log(MN)$. The total computational complexity of the proposed algorithm is given below

$$\begin{aligned} \mathcal{O}_{\text{Total}} =& \mathcal{O}\big(MN\log(N) + L(\epsilon_\varphi\,(MN\,(1 + \log(N))))\\ &+ \epsilon_\theta\,(MN\,(1 + 2\log(MN) + \log(N)))))\big) \end{aligned} \tag{5.50}$$

The computational complexity of the proposed OTFS fractional channel estimation algorithm is compared to other existing techniques in **Table 5.5**. The parameters N_0 and M_0 are greater than or equal to N and M, respectively. N_{iter} and $|\mathcal{A}|$ represent the number of iterations and constellation cardinality, respectively. Compared to the conventional MMSE estimation technique, the proposed algorithm has much lower complexity. As well, it has a reasonable complexity level and estimation performance compared to other iteration techniques, such as the conventional MP and OMP, which assume only integer Doppler scenario. The SBL technique proposed in [145] has the best performance among the techniques in the literature but has much higher computational complexity than our proposed method. Therefore, the proposed algorithm achieves good estimation performance while maintaining significantly lower computational complexity compared to other existing techniques.

5.5.3. Communication and radar performance analysis

Simulations are carried out in this part to validate the performance of the proposed framework design. The radar performance is given in terms of the RMSE of the estimated range and velocity. The communication performance is shown using BER analysis. **Table 5.6** summarizes the OTFS system parameters used for simulation.

Table 5.6: Simulation parameters

Parameters	**Specifications**
DD grid size	$M = 64,\ N = 64$
Pilot location (l_p, k_p)	$(0, 0)$
f_c	77 GHz
Bandwidth B	50 MHz
CP type	Reduced-CP
Signal constellation	4 QAM
Channel model	Extended Vehicular A model (EVA)
Channel taps (L)	4
$(\kappa,\ \iota)$ distribution	$\mathcal{U}(-0.5, 0.5)$

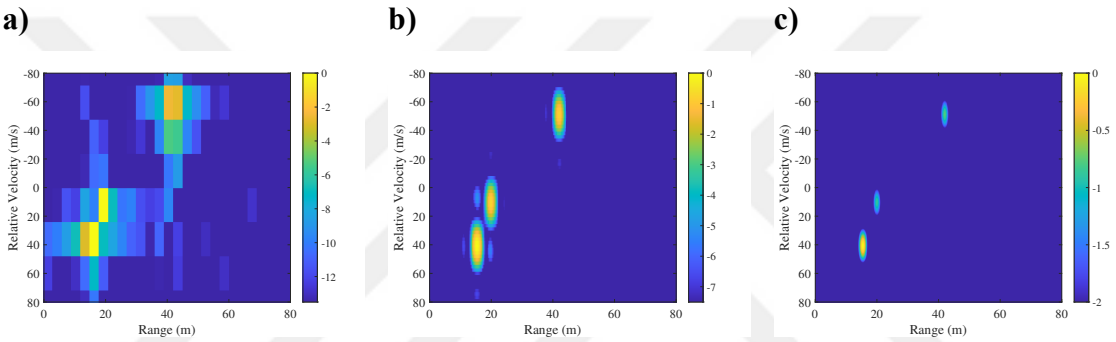


Figure 5.17: Range-velocity map: **a)** $\epsilon_\theta = \epsilon_\varphi = 1$, **b)** $\epsilon_\theta = \epsilon_\varphi = 10$, **c)** $\epsilon_\theta = \epsilon_\varphi = 100$.

The results of the range-velocity map (RVM) generated for three targets having ranges of $[15.5, 20, 42]$ m and velocities of $[40, 10.4, -55]$ m/s are presented in **Figure 5.17**. The RVMs are generated for different values of ϵ, with the worst range-velocity resolution observed for $\epsilon_\theta = \epsilon_\varphi = 1$, as shown in **Figure 5.17a**. As ϵ increases, the range and velocity resolution improve, leading to enhanced detection separability of targets, as shown in **Figure 5.17b-c**. Specifically, for $\epsilon_\theta = \epsilon_\varphi = 100$, as depicted in **Figure 5.17c**, the proposed framework achieves 100 times more accurate estimation results for the targets which are seen as fine dots on the RVM map compared to the results obtained with $\epsilon_\theta = \epsilon_\varphi = 1$.

The RMSE is calculated as follows

$$\text{RMSE}(\boldsymbol{\eta}) = \frac{1}{P}\sum_{i=1}^{P}\sqrt{\|\hat{\boldsymbol{\eta}}_i - \boldsymbol{\eta}\|_2^2}. \tag{5.51}$$

Figures **Figure 5.18a-b** depict the RMSE performance of our proposed OTFS-based sensing algorithm for range and velocity estimation, respectively, as a function of the pilot's SNR. The results show that our proposed algorithm achieves finer estimation of range

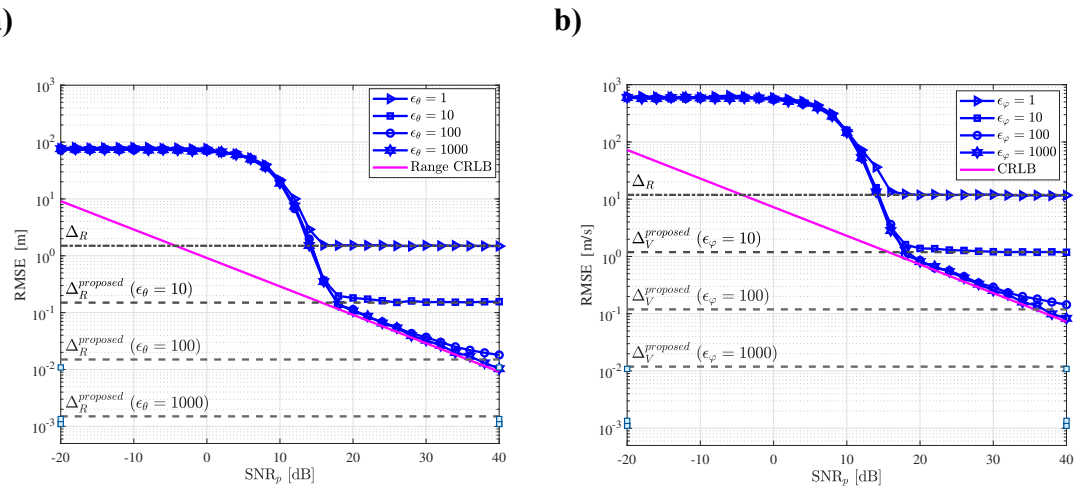


Figure 5.18: The RMSE performance of the estimated range and velocity vs SNR$_p$ ($N = M = 64$, $f_c = 77$ GHz , $B = 50$ MHz): **a**) range, **b**) velocity.

and velocity parameters beyond the conventional range-velocity resolution achievable by using the bandwidth, time-duration, and central frequency parameters given in **Table 5.6**. The resolution achieved depends on the step size ϵ, where larger ϵ leads to better RMSE performance. Furthermore, we observe that for high ϵ values (i.e., $\epsilon_\varphi = \epsilon_\theta = 1000$) and high SNR$_p$ (above 20 dB), the proposed framework achieves promising results almost near the CRLB, highlighting the high accuracy of our proposed method.

Figure 5.19 depicts a comparison of our proposed technique with frequency modulated continuous wave (FMCW) and [148] in terms of range and velocity estimation versus SNR$_{radar}$ which is the SNR at the nodes intended for sensing only. In **Figure 5.19a**, we observe that for small values of ϵ_θ ($\epsilon_\theta = 10$), the proposed framework requires slightly higher SNR to start performing for range estimation. However, it outperforms the previous works [76] and [148] in terms of range estimation performance for high values of ϵ_θ. Our algorithm can achieve centimeter-level resolution for the same SNR level where [76] and [148] can only achieve meter-level resolution, as they are both limited by conventional range and velocity resolutions. In **Figure 5.19b**, we also present a comparison of velocity estimation performance, and we observe that our proposed framework achieves a resolution of centimeter's per second for the same resources, whereas [76] and [148] only converge to a resolution of range ten's of meters per second. This highlights the superior performance of our proposed technique in both range and velocity estimation compared to existing methods.

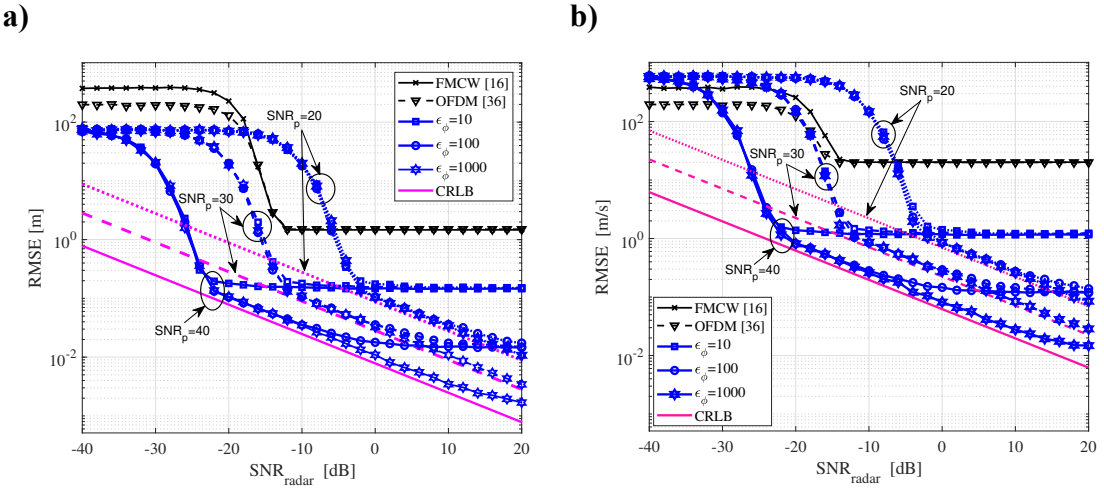


Figure 5.19: The RMSE performance of the estimated range and velocity vs SNR$radar$ ($N = M = 64$, $f_c = 77$ GHz , $B = 50$ MHz): **a**) range, **b**) velocity.

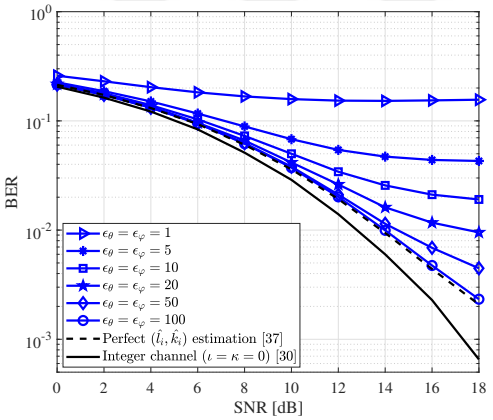


Figure 5.20: The BER performance of the proposed ISAC scheme.

In conclusion, the results indicate that our proposed framework outperforms existing methods in terms of both range and velocity estimation. The significant improvement in resolution achieved by our proposed technique can allow a better object detection and tracking, which has significant implications for various applications in wireless communication.

In this subsection, we analyze the BER of OTFS with fractional delay and Doppler shift estimation as depicted in **Figure 5.20**. The proposed method estimates only the fractional delays and Doppler shifts, while the channel complex gains are estimated according to the approach proposed in [149]. The simulated BER is compared to the perfect channel estimation [149] and integer channel ($\kappa = \iota = 0$) [134] cases for various SNR values (note that these SNR values denote the communication SNR value). It is observed that the BER decreases as the SNR increases. **Figure 5.20** also shows that the BER performance is

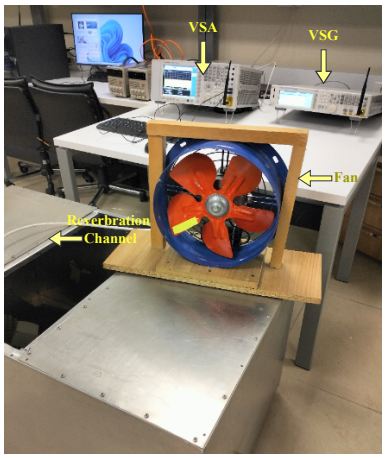


Figure 5.21: The experiment setup.

a function of the step size ϵ, where the larger the better the BER becomes, approaching the performance of the perfect channel estimation at $\epsilon_\varphi = \epsilon_\theta = 100$. This is due to the achievable accurate channel estimation at large ϵ value that leads to a better equalization, and thus improved data detection.

5.5.4. Experimental results

In this part, we demonstrate the feasibility of our proposed framework for jointly estimating high-resolution range-velocity profile in a real-time experiment. The experiment was conducted using the Keysight Agilent Technologies EXA VSA N9010A and EXG VSG N5172B, a reverberation chamber, and a fan to simulate Doppler located at $R_{\text{fan}} = 0.7$ m with $V_{\text{fan}} = 20.94$ m/s (200 rpm), as illustrated in **Figure 5.21**. An OTFS frame with parameters $M = 64$, $N = 64$, a bandwidth of 10 MHz, and a central frequency of 2.45 GHz was transmitted, and the received signal was demodulated and extracted from the VSG, as shown in **Figure 5.23a**. In the proposed algorithm, the only design parameter is ϵ. So, **Figure 5.22** actually helps us to determine ϵ based on three criteria/constrains, namely, pilot power (SNR_p), RMSE performance, and the computational complexity. In our experiment, the algorithm was then tested by iterating through various values of θ and φ given that $\epsilon_\varphi = \epsilon_\theta = 20$ which gives good trad-off between the error performance and the complexity. **Figure 5.23b** depicts the case when $\theta = 0$ and $\varphi = 0.15$, where the fractional Doppler (i.e., 2D pulse sidelobes in Doppler axis) was completely removed, and the Doppler shift becomes integer. The algorithm continued to iterate until the delay (i.e., 2D pulse sidelobes in delay axis) was almost removed, as seen in **Figure 5.23e**. Note that the

a) **b)**

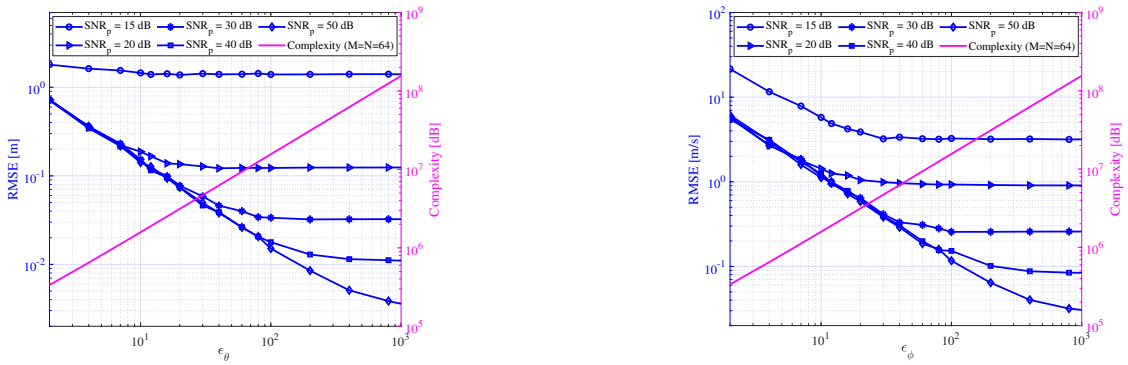


Figure 5.22: The relationship between ϵ and performance (RMSE), complexity, and SNR_p: **a**) range, **b**) velocity.

slight degradation in delay estimation is due to equipment limitations.

Using the results in **Figure 5.23**, the fractional delay and Doppler shifts are computed respectively as

$$l_i + \iota_i = 0.05, \tag{5.52}$$

and

$$k_i + \kappa_i = 0.15. \tag{5.53}$$

Consequently, we find

$$\hat{R}_{\text{fan}} = \frac{0.05 \cdot 3 \cdot 10^8}{2 \cdot 10 \cdot 10^6} = 0.75 \text{ m}, \tag{5.54}$$

and

$$\hat{V}_{\text{fan}} = \frac{0.15 \cdot 3 \cdot 10^8}{2 \cdot 2.45 \cdot 10^9 \cdot 64 \cdot \frac{64}{10 \cdot 10^6}} = 22.42 \text{ m/s}. \tag{5.55}$$

These experimental results confirms the effectiveness of our proposed algorithm in estimating high-resolution range-velocity profile in narrow band short duration systems.

5.6. OTFS-FMCW Waveform Design For Low Complexity Joint Sensing And Communication

In this section, we evaluate the computational complexity, the sensing, and the communication performance of the proposed OTFS-Chirp waveform. For sensing, the RMSE of the estimated radar parameters (range and velocity) is evaluated and compared with FMCW's performance. For communication, the BER and the spectral efficiency of the proposed

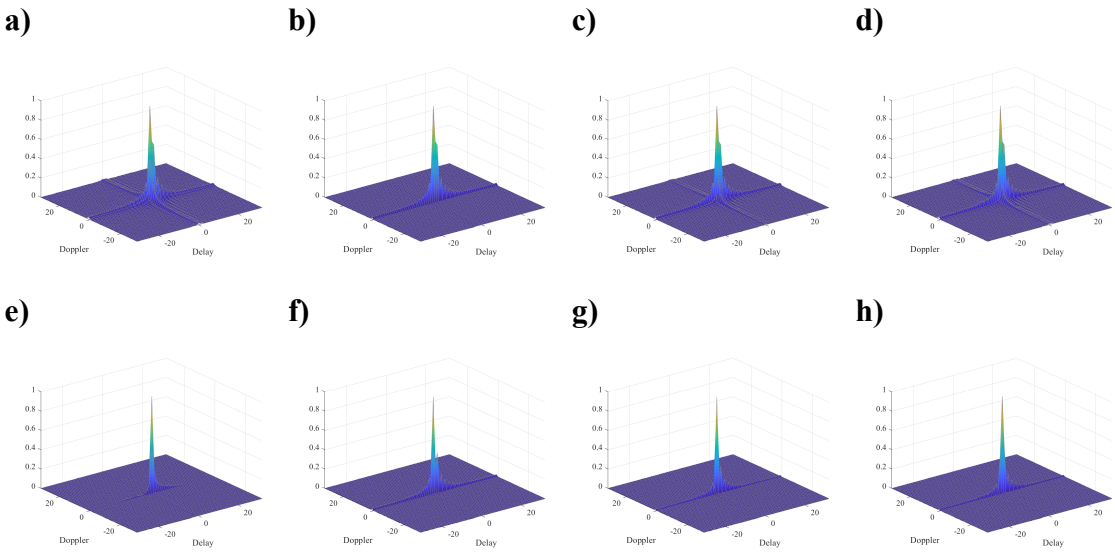


Figure 5.23: Experimental results for $\epsilon_\theta = \epsilon_\varphi = 20$: **a**) $\theta = 0,\ \varphi = 0$, **b**) $\theta = 0,\ \varphi = 0.15$, **c**) $\theta = 0,\ \varphi = 0.35$, **d**) $\theta = 0,\ \varphi = 0.6$, **e**) $\theta = 0.05,\ \varphi = 0.15$, **f**) $\theta = 0.15,\ \varphi = 0.15$, **g**) $\theta = 0.3,\ \varphi = 0.15$, **h**) $\theta = 0.8,\ \varphi = 0.15$.

OTFS-Chirp waveform are evaluated and compared to OTFS, OFDM, and FMCW. Unless stated otherwise, the key system's simulation parameters are given in **Table 5.7**.

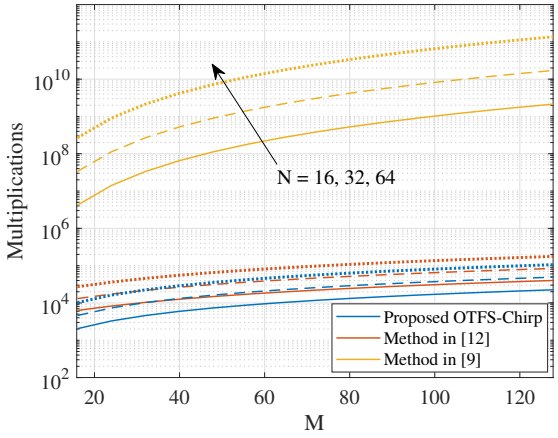


Figure 5.24: Complexity comparison between different sensing algorithms.

5.6.1. Computational complexity analysis

As explained in **Subsection 4.6.4.1**, the only computation needed comes from performing the 2D-fast Fourier transform (FFT) of size $M \times N$. Thus, the radar complexity of the proposed scheme is in the order of $O\{MN\log(MN)\}$. **Figure 5.24** summarizes and compares the sensing computational complexity of the proposed OTFS-Chirp waveform with the existing methods in terms of multiplications. Note that not only the computational

Table 5.7: Simulation parameters

Description	Parameters	Value
Carrier frequency	f_c	77 GHz
Bandwidth	B	200 MHz
Subcarrier spacing	Δf	B/M MHz
No. of sub-carriers per symbol	M	32
No. of OFDM symbols	N	32
No. of OTFS symbols	N_{OTFS}	100
No. of chirps per OTFS symbol	N_c	2
Range resolution	Δr	0.3747 m
Velocity resolution	Δv	1.901 m/s
Range of targets	r_r	$\sim \mathcal{U}(0, 100)$ m
Velocity of targets	v_r	$\sim \mathcal{U}(-80, +80)$ m/s
Signal-to-noise ratio	SNR	15 dB

complexity is low in the proposed OTFS-Chirp waveform but also the implementation complexity which allows the proposed waveform to be implemented in existing IoT devices for sensing due to Chirp signal sampling properties. For instance, if the RF signal spans a large bandwidth of few GHz, the ADC would sample a signal of only few MHz to get the sensing information, which is the case for IoT devices that have low-sampling frequency ADCs.

5.6.2. Sensing performance

Figure 5.25 illustrates the range-velocity plot for a JSAC scenario considering random moving targets with parameters given in **Table 5.7**. 2D-FFT is applied to obtain beat frequency $f_b = \frac{2r_r\Delta f}{cT} + \nu_r$ coupled with Doppler frequency ν_r . This operation is also known as the range transform which allows the estimation of Doppler shift corresponding to a unique range. The range-velocity map shown in **Figure 5.25** expresses three peaks around the real range-velocity values of the radar targets within a specific resolution as given in (**4.226)**.

Figure 5.25a depicts the range-velocity map when a single FMCW in case of a single UT is transmitted for JSAC. As seen in the figure, 4 targets with different range and velocities are detected, specifically, at $(r, v) = [(5, -30),\ (20, 40),\ (55, 10),\ (80, 15)]$. On the other hand, **Figure 5.25b-d** show the range-velocity map of three different users in multi-UT JSAC mode, where the radar receiver applies different correlators (i.e., ψ_i) in parallel to

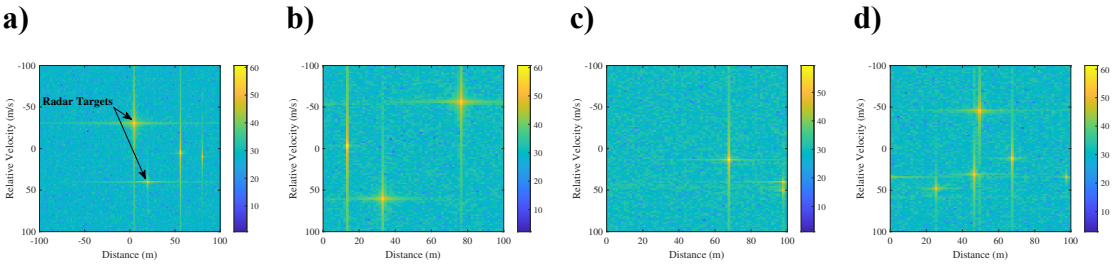


Figure 5.25: The range-velocity plot from the received: **a**) single UT signal x_c, **b**) multi-UT signal ψ_0, **c**) multi-UT signal ψ_1, **d**) multi-UT signal ψ_2.

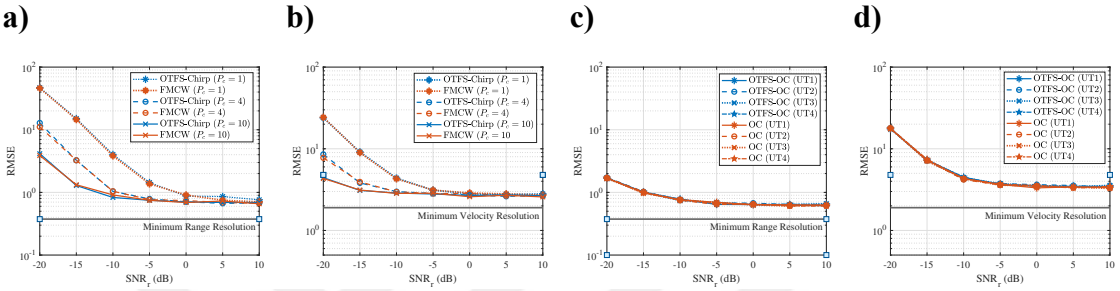


Figure 5.26: The RMSE of the target range and velocity estimation vs SNR$_r$: **a**) range (single UT), **b**) velocity (single UT), **c**) range (multi UT), **d**) velocity (multi UT).

get the sensing information of each UT separately. Accordingly, it is observed that the first UT sees three objects, the second UT observes two objects, and the third UT sees five objects, as shown in **Figure 5.25b**, **Figure 5.25c**, and **Figure 5.25d**, respectively.

Figure 5.26 shows the range and velocity estimation in terms of RMSE, where the performance of the proposed OTFS-Chirp is compared with the RMSE performance of FMCW. Three targets are considered to be scattered within the environment, and their ranges and velocities are assumed to follow a uniform distribution, as indicated in **Table 5.7**. **Figure 5.26a-d** show that the proposed JASC waveform achieves the same sensing performance as FMCW for different transmit powers and for both single and multi-UT sensing. This confirms the superiority of the proposed sensing scheme. It is also shown that the larger the chirp power P_c is, the better the RMSE performance becomes, especially at the low radar SNR regime (i.e., SNR$_r$ < 0 dB). The RMSE performance of both range and velocity converges to be the same minimum error at high radar SNR values due to the range and velocity resolution limitations. Note that the error does not converge exactly to the minimum resolution because the RMSE is computed for multiple targets instead one target.

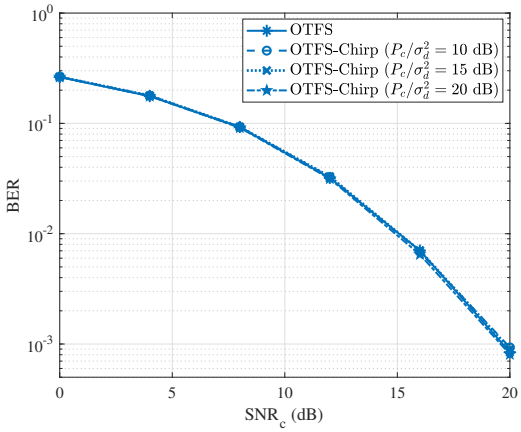


Figure 5.27: BER vs SNR$_c$ analysis.

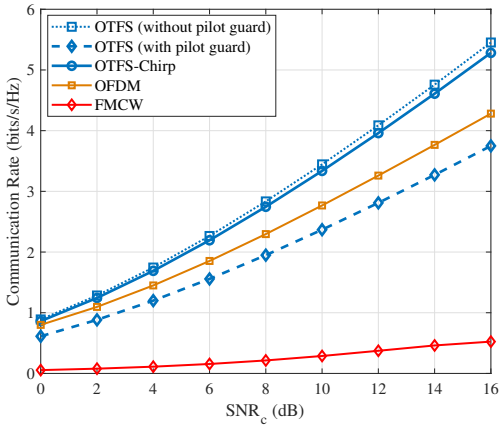


Figure 5.28: Communication rate vs SNR$_c$ analysis.

5.6.3. Communication performance

Figure 5.27 shows the BER performances of the OTFS waveform for conventional and proposed design for different chirp powers ($P_c/\sigma_d^2 \in (0, 3, 10)$ higher than that of the data symbols, where σ_d^2 is the data variance). Perfect channel estimation for both designs is considered for the evaluation benchmark. It is seen that for different chirp powers the same BER performance for both conventional OTFS and the proposed design is obtained. This is due to the orthogonal coexistence between the chirp and the OTFS subcarriers in delay-Doppler domain as explained in **Subsection 4.6.2**. Finally, we compare the communication rates at the receiver for OFDM, OTFS, and, FMCW which respectively given

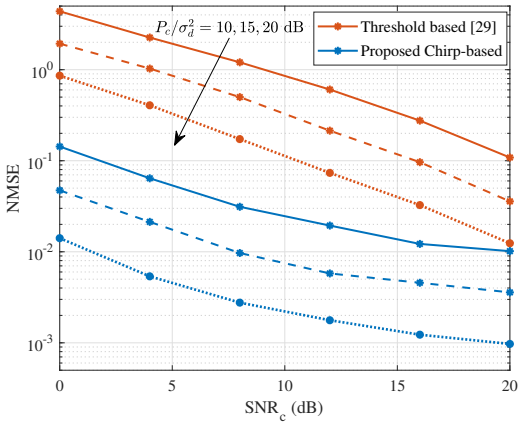


Figure 5.29: Channel NMSE performance of the proposed chirp-based estimation vs embedded pilot threshold based channel estimation [29].

as [150], [151]

$$C_{\text{OFDM}} = \left(\frac{T}{T+T_{\text{cp}}}\right)\log_2\left(1+\gamma\right), \tag{5.56a}$$

$$C_{\text{OTFS}} = \frac{1}{NM}\log_2\det\left(\boldsymbol{I}+\gamma\Psi\Psi^H\right), \tag{5.56b}$$

$$C_{\text{FMCW}} = \frac{2^{\gamma}(SF-\gamma)}{2^{SF}}, \tag{5.56c}$$

where γ denotes the communication SNR$_c$ and SF is a spreading factor ranging from 7 to 12. **Figure 5.28** depicts the communication rate in [bits/s/Hz] of the proposed OTFS-Chirp waveform compared to OTFS with and without guard, OFDM, and FMCW. It is realized that the proposed waveform performs almost similarly to OTFS without guard while outperforming OTFS with guard, OFDM, and FMCW. Note that the rate of FMCW is very poor, emphasizing the motivation and the need for the proposed design in various applications.

5.6.4. Channel estimation

Figure 5.29 depicts the performance comparison between our proposed chirp-based channel estimation method and the conventional embedded pilot approach using the NMSE metric. The NMSE is computed using

$$\text{NMSE}_h = \frac{\sum_r \left|\hat{h}_r - h_r\right|^2}{\sum_r |h_r|^2}, \tag{5.57}$$

where $\hat{h}_r$ and h_r denote the estimated and true channel coefficients, respectively.

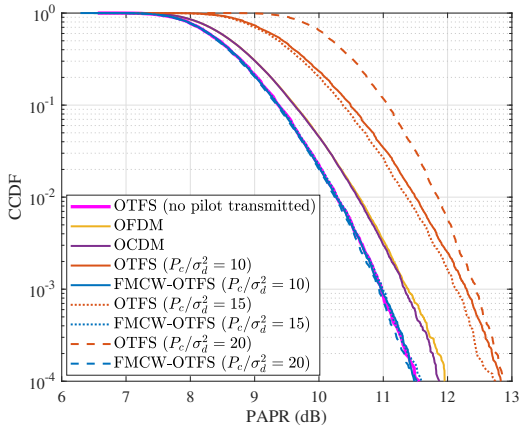


Figure 5.30: Comparison of the CCDF of the PAPR of the transmitted signal in different systems.

It is assumed that the pilot power is $P_c/\sigma_d^2 = 10$, 15, and 20 dB higher than that of the data symbols. To evaluate the performance of our method, we compared its NMSE performance to that of a conventional channel estimation approach with a guard space [29], using the latter as a reference. The proposed chirp-based channel estimation method demonstrated superior performance, despite the absence of interference guard the pilot and data symbols compared to the conventional approach. This can be attributed to the ability of our method to filter out data interference in the chirp/Fresnel domain at the receiver side, which leads to better channel estimation performance. Furthermore, spreading the pilot power over multiple symbols provides increased robustness against noise effects, which further enhances the accuracy of our channel estimation method.

The discrete time representation of the transmitted OTFS signal can be expressed using inverse discrete Zak transform (IDZT), where it can be seen that the time domain samples are nothing but the M times, N-point IDFT values of the symbols in the time domain. Assuming that the delay-Doppler symbols are identically distributed, this property gives OTFS an advantage over OFDM and OCDM systems that use $M \times N$-point IDFT for signal generation, resulting in lower PAPR. However, in situations where a high-power pilot is surrounded by guards, the distribution of the symbols can be changed, leading to higher PAPR as depicted by the orange curves in **Figure 5.30**. On the other hand, spreading the pilot over more than a symbol, as in the proposed case, mitigates this effect and preserve the distribution of the symbols in the delay Doppler domain. As shown in **Figure 5.30**, the proposed approach results in similar performance to OTFS without pilot guards.

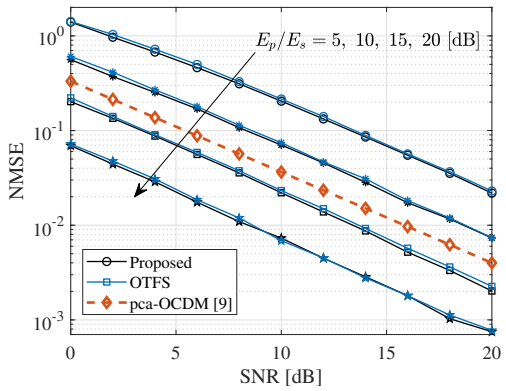


Figure 5.31: Channel NMSE performance for different E_p/E_s values.

5.7. Delay-Doppler-Based Channel Estimation Method In Doubly-Dispersive OCDM Systems

In this section, we conduct an evaluation of various aspects, including the computational complexity, the NMSE of the estimated doubly-dispersive channel, and the BER of the proposed OCDM system. Quadrature phase shift keying (QPSK) modulation is used in the simulations, employing a frame size of $N = 1024$ and a delay-Doppler grid size of $M_d \times N_d = 32 \times 32$. For modeling the channel, we adopt the extended vehicular A model (EVA) [140], wherein the maximum delay-Doppler spread is $l_{\max} = k_{\max} = M_d/4 = 8$. Then, the number of pilots utilized in our scheme is $N_p = 8$.

In this thesis, we adopt the number of complex multiplications as a metric for assessing computational complexity. In the proposed method, the DFT can be efficiently implemented using the split-radix FFT algorithm, which requires approximately $\frac{N}{3}\log_2(N)$ complex multiplications for an N-point DFT when N is a power of 2 [152]. As described in **Subsection 4.7.2**, the computational operations involved in our proposed method primarily revolve around converting the received signal to the time domain. This conversion requires performing the Fresnel transform, which consists of an N-point FFT and $2N$ element-wise multiplications. Subsequently, the time domain signal is transformed to the delay-Doppler domain using an N_d-point FFT. Note that step 3 and 4, in Algorithm I, have negligible computational complexity; therefore, they can be ignored. Based on these considerations, the total computational complexity of our proposed scheme can be expressed as $O(\frac{N}{3}\log_2(N) + 2N + \frac{N_d}{3}\log_2(N_d))$. It is important to note that our proposed estimation scheme exhibits low computational complexity, particularly when compared

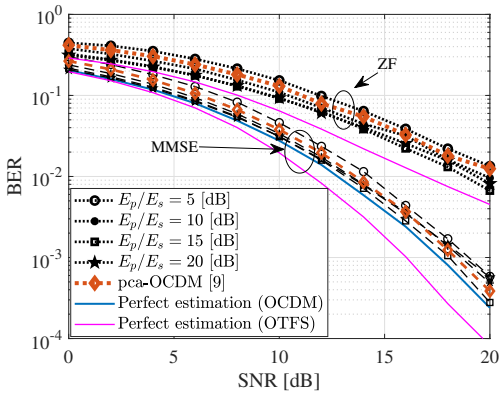


Figure 5.32: The BER performance for different E_p/E_s values.

to the PCA-OCDM method. The PCA-OCDM method employs the MMSE estimator, which has a significantly higher computational complexity proportional to $O(N^3)$.

The NMSE performance of the proposed channel estimation technique is assessed and compared to the PCA-OCDM scheme, as illustrated in **Figure 5.31**. The results demonstrate that the performance of our estimator improves with increasing pilot power E_p/E_s, where SNR in **Figure 5.31** represents the SNR of the data. Notably, our proposed scheme exhibits superior performance compared to the PCA-OCDM method presented in [107] when E_p/E_s almost exceeds 13 dB. It is worth mentioning that our proposed channel estimation scheme offers greater flexibility by allowing the utilization of any channel estimation scheme developed for the delay-Doppler domain depending on the users/transceivers capabilities and requirements, while achieving the same performance as OTFS channel estimation.

The results of BER are illustrated in **Figure 5.32**, showcasing the implementation of zero-forcing (ZF) and MMSE detectors for symbol detection. The results indicate that when $E_p/E_s > 13$ dB, the proposed method outperforms the PCA-OCDM technique in [107]. This can be attributed to the higher accuracy of the estimated channel in the proposed method. It is also seen that OTFS performs better than the OCDM under perfect channel estimation. Also, note that the MMSE detector exhibits superior performance compared to the ZF due to its utilization of noise statistics in the detection process.

CHAPTER 6

6. CHALLENGES AND RESEARCH DIRECTIONS

Since the proposed PHY layer framework contains various building blocks with multiple options, it gives rise to challenges such as:

- Waveform options - While the aforementioned framework is general and forward-looking, the standardization would require consensus of the community regarding which options are to be defined (at least in the initial releases of 6G) to ensure compatibility between devices. Moreover, the different waveforms have their own challenges that might require mitigation. An example of this is the fractional delay/Doppler shift phenomena faced in OTFS systems. The severity or impact of such issues also needs to be considered before deciding the practical option(s).

- Overhead - The number of waveform options and their constituent parameters, such as spreading and filtering, directly influence signaling overhead. This issue becomes critical for low-latency applications involving small or sporadic data transmissions. Hence, it is crucial to develop a mechanism that retains waveform parameters for such applications, minimizing the need for repeated signaling.

- Implementation - A critical issue in terms of realizing the proposed PHY layer framework is its cost and/or complexity in terms of hardware implementation. For instance, while all the options in **Figure 2.3** share the same pulse shape, the spreading and windowing/filtering options vary greatly. This means that a device which were to use different waveforms would require additional hardware compared to the existing one. While this is feasible for high-end network nodes such as base stations, it might be challenging to provide the same flexibility at higher frequencies such as terahertz (THz) [153] or in user devices, considering their smaller form

factors and power/complexity constraints.

- Key performance indicators (KPIs) - Even though the discussion of 6G has been ongoing for a while, and International Telecommunication Union (ITU)'s study group has highlighted requirements related to sustainability, connectivity, security and privacy, the specific KPIs for them are still lacking [154] and need to be defined for network optimization. Moreover, the weightage of different requirements also needs to be evaluated. For instance, as [155] states, a slight reduction in spectral efficiency can lead to significant gains in energy efficiency. Therefore, if the latter was to be more critical for a given scenario, it would have to be assigned more weight in network evaluation.

- Multiple accessing and MIMO - Throughout the different standards, data has been put directly on the PHY TF resource grid. However, in the proposed framework, an additional flexibility of the data lattice has been provided which is not limited to the TF domain. However, defining the rules (i.e. precoding represented by $f(.)$ in (**2.22)**) of multiple accessing, particularly when different users opt for different waveforms, becomes critical. Moreover, MIMO capability is imperative for any future network to provide improved reliability and capacity. While OFDM's orthogonality forms great synergy with MIMO, the same needs to be explored in practical systems for the new candidate waveforms.

CHAPTER 7

7. CONCLUSION AND FUTURE WORK

The plethora of new use cases, applications, and their associated requirements envisioned for 6G necessitate a new PHY layer design. However, as a community we need to be pragmatic in our approach considering the resistance of the industry (particularly operators) against something designed from scratch due to the potential costs it would incur. Consequently, this thesis presents a simultaneously backward-compatible and forward-looking PHY framework for 6G. This framework indicates that the different waveforms being proposed share various slices/blocks. While most of the academic works try to emphasize their individuality, realizing their mutual relationships might open new avenues towards leveraging their respective benefits in a more profound manner. In light of this, we believe that the use of OFDM as a (rectangular) pulse shape with appropriate precoding for different applications presents the best way forward for next-generation wireless systems. Based on that, multiple candidate waveforms for 6G are investigated, including OFDM, CCP-OFDM, OTFS, FMCW, and OCDM. Each waveform serves a specific purpose, addressing distinct requirements within the context of 6G communication systems. Throughout this research, the characteristics and capabilities of these waveforms are examined and their relationships are explored for potential applications, such as channel estimation and sensing and communication. The following summary highlights the key contributions and findings for each section:

In **Section 4.1**, a novel security algorithms for providing data and pilot security is proposed. Unlike conventional security schemes which use the full channel, the proposed algorithms decompose the channel into its minimum-phase and all-pass components and exploit only the all-pass part. The latter provides enough randomness to secure the communication without causing any power issues such as high PAPR value at the transmitter

due to its unit amplitude property. Particularly, the all-pass component and its conjugate are used to secure the pilots and the data, respectively. For data security, we have considered two scenarios of correlated and uncorrelated eavesdropping channels and evaluated the BER gap. Our results reveal that using one component of the channel provides better security than using the total effective channel in both scenarios. Moreover, the results also ensure that the proposed algorithm provides effective security with minimal degradation in the legitimate user's performance compared to conventional algorithms. The results show that the proposed algorithm is capable of providing significant degradation in the estimated channel quality at the eavesdropper. This will ensure not only securing the channel state information (CSI) but also securing radio environment mapping information. Additionally, the proposed algorithm can enable flexibility in terms of providing security to data, pilot, or both depending upon the application requirements.

In **Section 4.2**, a new transceiver design for CCP-OFDM system is proposed, where the channel estimation is feasible with minimum computational complexity in the frequency domain unlike the conventional schemes where complex time estimation must be used. This is achieved by deploying two block-DFT processes at the transmitter and receiver to ensure the recovery of the pilots without any interference from data. Simulation results have validated the effectiveness of the proposed scheme, which is demonstrated to be reliable and less complex than the MMSE and ML estimators. As a future work, joint frequency offset and channel estimation will be investigated for the proposed scheme.

In **Section 4.3**, it is shown that appending a FCP to the $M \times N$ OTFS frame is equivalent to extending the delay-Doppler grid to $(M + L_{\text{cp}}) \times N$ by repeating the last L_{cp} rows of the data. Accordingly, a novel mixed prefix structure has been proposed where jointly reduced and full-CP structures are appended to the OTFS frame. While the full-CP ensures zero-ISI between the OTFS subsymbols, the added reduced-CP guarantees that the CP blocks are not discarded and that the information carried by them is being extracted along with the data frame at the receiver side, unlike the CP blocks in OFDM systems. Then, by exploiting the proposed FCP-OTFS structure, two possible use cases were presented where the first one is a simple combining scheme that uses repeated data in the CP block to enhance reliability, and the latter introduces a spectrally efficient pilot allocation scheme for channel estimation. In our future work, we will consider new applications of the proposed FCP-OTFS under the effect of both fractional delay and Doppler.

OTFS has garnered increasing attention over recent years due to its benefits for mobile environments. However, most academic works pertaining to OTFS assume integer delays and Doppler shifts. This is only possible in the case of extremely large bandwidths and frame durations, which is not realistic in practical systems. In most scenarios, the system will suffer from fractional delay and Doppler shifts, leading to IDI and IDeI. This necessitates a framework for the estimation of fractional delay and Doppler channels. In **Section 4.4**, we have proposed a framework to estimate OTFS channels with fractional delays and Doppler shifts, allowing flexible OTFS frame design to fulfill various applications and user requirements. A pulsone, which holds its shape under the operations of time delay and Doppler shift as well as being self-dual between time and frequency, is adopted for the estimation by raising the received pilot pulsone to higher powers in both time and frequency domains to estimate fractional Doppler and delay shifts, respectively. In order to assess the estimation performance of the proposed technique, the CRLB has been developed. It has been demonstrated that the proposed framework performs optimally near CRLB.

Section 4.5 proposes a ISAC narrowband OTFS system that can achieve high-resolution range-velocity profile based on DD impulse sensing. A single OTFS carrier is exploited as a pilot to estimate both accurate range and velocity without the need to use wideband long duration signals. This is achieved by exploiting the features of the OTFS carrier, which are the self-duality property of its Fourier transform and its ability to hold shape under the operations of time delays and Doppler shifts. It is shown that if an OTFS carrier is used for radar and if the targets are sufficiently separated from each other, then the exact range and velocity can be estimated beyond the conventional resolution constraints. As a future direction, the proposed approach can be extended to estimate the range, velocity, and angle of the targets by deploying MIMO system which is crucial for radio environment mapping application.

Section 4.6 provides a novel JSAC waveform called OTFS-Chirp to simultaneously enable communication and sensing. The proposed approach uses OTFS transmission to provide high data rates in a mobile environment while achieving accurate sensing capability using chirp/FMCW signaling with low complexity. This is achieved by exploiting the sparse nature of chirp signals in the delay-Doppler domain. Furthermore, it is shown that multiple sensing users can be multiplexed in the same time-frequency resources without

adding any complexity for the sensing transceivers that are only required to perform sampling at low frequencies (beat frequency) followed by 2D-FFT operation. Moreover, the proposed waveform/framework paves its way to improve the coexistence between communication and sensing for the 6G networks by utilizing the inherent property of OTFS signaling being a precoded OFDM and improving that the chirp signal is essentially a precoded OTFS. In our future work, we will study the coexistence between OFDM, OTFS, and chirp waveforms to develop a generalized flexible waveform that serves multiple user requirements other than communication and sensing.

Section 4.7 presents a novel embedded pilot-aided OCDM channel estimation scheme. In the Fresnel domain, the arrangement of pilot, guard, and data symbols is specifically designed to mitigate interference between pilot and data symbols. The pilots are designed to exhibit sparsity in the delay-Doppler domain by leveraging the inherent characteristics of OCDM signaling as a precoded OTFS. Then, this thesis presents a novel approach to accurately estimate doubly-dispersive channels in the delay-Doppler domain, while ensuring minimal computational cost.

BIBLIOGRAPHY

[1] Z. Zhang *et al.*, "6G wireless networks: Vision, requirements, architecture, and key technologies," *IEEE Vehicular Technology Magazine*, vol. 14, no. 3, pp. 28–41, 2019.

[2] N. C. Luong, X. Lu, D. T. Hoang, D. Niyato, and D. I. Kim, "Radio resource management in joint radar and communication: A comprehensive survey," *IEEE Communications Surveys & Tutorials*, vol. 23, no. 2, pp. 780–814, 2021.

[3] O. Kodheli *et al.*, "Satellite communications in the new space era: A survey and future challenges," *IEEE Communications Surveys & Tutorials*, vol. 23, no. 1, pp. 70–109, 2020.

[4] A. Yazar, S. Dogan-Tusha, and H. Arslan, "6G vision: An ultra-flexible perspective," *ITU Journal on Future and Evolving Technologies*, vol. 1, no. 1, pp. 121–140, 2020.

[5] A. B. Kihero, M. S. J. Solaija, and H. Arslan, "Inter-numerology interference for beyond 5G," *IEEE Access*, vol. 7, pp. 146 512–146 523, 2019.

[6] M. Dohler, R. W. Heath, A. Lozano, C. B. Papadias, and R. A. Valenzuela, "Is the PHY layer dead?" *IEEE Communications Magazine*, vol. 49, no. 4, pp. 159–165, 2011.

[7] Z. E. Ankarali, B. Peköz, and H. Arslan, "Flexible radio access beyond 5G: A future projection on waveform, numerology, and frame design principles," *IEEE Access*, vol. 5, pp. 18 295–18 309, 2017.

[8] Y. Zhou *et al.*, "Overview and performance analysis of various waveforms in high mobility scenarios," *arXiv preprint arXiv:2302.14224*, 2023.

[9] NGMN Alliance, "6G requirements and design considerations," *White Paper*, Feb. 2023.

[10] F. Hlawatsch and G. Matz, *Wireless communications over rapidly time-varying channels*. Academic press, 2011.

[11] R. Hadani, S. Rakib, M. Tsatsanis, A. Monk, A. J. Goldsmith, A. F. Molisch, and R. Calderbank, "Orthogonal time frequency space modulation," in *2017 IEEE Wireless Communications and Networking Conference (WCNC)*. IEEE, 2017, pp. 1–6.

[12] S. E. Zegrar and H. Arslan, "Effect of Prefix/Suffix Configurations on OTFS Systems with Rectangular Waveforms," *arXiv preprint arXiv:2205.14872*, 2022.

[13] M. Mert Şahin and H. Arslan, "Multi-functional coexistence of radar-sensing and communication waveforms," in *IEEE 92nd Vehicular Technology Conference (VTC2020-Fall)*, 2020, pp. 1–5.

[14] X. Ouyang and J. Zhao, "Orthogonal chirp division multiplexing," *IEEE Transactions on Communications*, vol. 64, no. 9, pp. 3946–3957, 2016.

[15] M. Chafii, L. Bariah, S. Muhaidat, and M. Debbah, "Twelve scientific challenges for 6G: Rethinking the foundations of communications theory," *IEEE Communications Surveys & Tutorials*, vol. 25, no. 2, pp. 868–904, 2023.

[16] Z. Wei, W. Yuan, S. Li, J. Yuan, and D. W. K. Ng, "Transmitter and receiver window designs for orthogonal time-frequency space modulation," *IEEE Transactions on Communications*, vol. 69, no. 4, pp. 2207–2223, 2021.

[17] X. Zhang and E. W. Knightly, "CSIsnoop: Inferring channel state information in multi-user MIMO WLANs," *IEEE/ACM Transactions on Networking*, vol. 27, no. 1, pp. 231–244, 2018.

[18] A. Mukherjee, S. A. A. Fakoorian, J. Huang, and A. L. Swindlehurst, "Principles of Physical Layer Security in Multiuser Wireless Networks: A Survey," *IEEE Communications Surveys Tutorials*, vol. 16, no. 3, pp. 1550–1573, 2014.

[19] M. Soltani, T. Baykaş, and H. Arslan, "Achieving secure communication through pilot manipulation," in *IEEE 26th Annual International Symposium on Personal, Indoor, and Mobile Radio Communications (PIMRC)*, 2015, pp. 527–531.

[20] T.-Y. Liu, S.-C. Lin, and Y.-W. P. Hong, "On the Role of Artificial Noise in Training and Data Transmission for Secret Communications," *IEEE Transactions on Information Forensics and Security*, vol. 12, no. 3, pp. 516–531, 2017.

[21] T.-H. Chang, Y.-W. P. Hong, and C.-Y. Chi, "Training signal design for discriminatory channel estimation," in *IEEE Global Communications Conference (GLOBECOM)*, 2009, pp. 1–6.

[22] Q. Zhu, S. Wu, and Y. Hua, "Optimal pilots for anti-eavesdropping channel estimation," *IEEE Transactions on Signal Processing*, vol. 68, pp. 2629–2644, 2020.

[23] Y.-N. Du, S. Han, S. Xu, and C. Li, "Improving secrecy under high correlation via discriminatory channel estimation," in *IEEE International Conference on Communications (ICC)*, 2018, pp. 1–6.

[24] A. Albehadili, K. A. Al Shamaileh, A. Y. Javaid, and V. K. Devabhakuni, "Link-Signature-Based Discriminatory Channel Estimation (LS-DCE) for Physical Layer Security in Stationary and Mobile OFDM Transceivers," *IEEE Transactions on Vehicular Technology*, vol. 69, no. 8, pp. 8119–8131, 2020.

[25] M. Simsek *et al.*, "On the flexibility and autonomy of 5G wireless networks," *IEEE Access*, vol. 5, pp. 22 823–22 835, 2017.

[26] A. Yazar *et al.*, "6G vision: An ultra-flexible perspective," *ITU J. Future and Evolving Technologies*, vol. 1, no. 1, pp. 121–140, 2020.

[27] J.-Y. Chouinard *et al.*, "MSE-OFDM: A new OFDM transmission technique with improved system performance," in *Proc.(ICASSP'05). IEEE Int. Conf. Acoust., Speech, and Signal Process., 2005.*, vol. 3. IEEE, 2005, pp. iii–865.

[28] X. Wang *et al.*, "On the comparison between conventional OFDM and MSE-OFDM systems," in *GLOBECOM'03. IEEE Global Telecommun. Conf. (IEEE Cat. No. 03CH37489)*, vol. 1. IEEE, 2003, pp. 35–39.

[29] A. B. Kihero *et al.*, "Inter-numerology interference for beyond 5G," *IEEE Access*, vol. 7, pp. 146 512–146 523, 2019.

[30] Y. Varun *et al.*, "Inter-numerology interference reduction based on precoding for multi-numerology OFDM systems," in *2020 IEEE 3rd 5G World Forum (5GWF)*. IEEE, 2020, pp. 542–546.

[31] X. Wang *et al.*, “On the design and performance analysis of multisymbol encapsulated OFDM systems,” *IEEE Trans. Veh. Technol.*, vol. 55, no. 3, pp. 990–1002, 2006.

[32] X. Wang *et al.*, “System design and implementation of multiple-symbol encapsulated OFDM,” in *2005 IEEE 61st Veh. Technol. Conf.*, vol. 2. IEEE, 2005, pp. 1043–1047.

[33] B. Tian *et al.*, “A channel estimation algorithm in MSE-OFDM systems,” in *2006 8th Int. Conf. Signal Process.*, vol. 3. IEEE, 2006.

[34] J.-Y. Chouinard *et al.*, “MSE-OFDM: A new OFDM transmission technique with improved system performance,” in *Proc.(ICASSP’05). IEEE Int. Conf. Acoust., Speech, and Signal Process., 2005.*, vol. 3. IEEE, 2005, pp. iii–865.

[35] J. K. Francis, R. Mary Augustine, and A. Chockalingam, “Diversity and PAPR enhancement in OTFS using indexing,” in *2021 IEEE 93rd Vehicular Technology Conference (VTC2021-Spring)*, 2021, pp. 1–6.

[36] P. Raviteja, E. Viterbo, and Y. Hong, “OTFS performance on static multipath channels,” *IEEE Wireless Communications Letters*, vol. 8, no. 3, pp. 745–748, 2019.

[37] S. E. Zegrar, S. Rafique, and H. Arslan, “OTFS-FMCW waveform design for low complexity joint sensing and communication,” in *2022 IEEE 33rd Annual International Symposium on Personal, Indoor and Mobile Radio Communications (PIMRC)*, 2022, pp. 988–993.

[38] W. Shen, L. Dai, J. An, P. Fan, and R. W. Heath, “Channel estimation for orthogonal time frequency space (OTFS) massive MIMO,” *IEEE Transactions on Signal Processing*, vol. 67, no. 16, pp. 4204–4217, 2019.

[39] Z. Yuan, F. Liu, W. Yuan, Q. Guo, Z. Wang, and J. Yuan, “Iterative detection for orthogonal time frequency space modulation with unitary approximate message passing,” *IEEE Trans. wireless Commun.*, 2021.

[40] S. Li, W. Yuan, Z. Wei, R. Schober, and G. Caire, “Orthogonal time frequency space modulation – part II: Transceiver designs,” *IEEE Communications Letters*, pp. 1–1, 2022.

[41] P. Du and Y. Zhang, “Joint precoding and equalization design for reduced-CP OTFS based on the compact input-output model,” *Physical Communication*, p. 101748, 2022.

[42] S. E. Zegrar and H. Arslan, “Common CP-OFDM transceiver design for low-complexity frequency domain equalization,” *IEEE Wireless Communications Letters*, vol. 11, no. 7, pp. 1349–1353, 2022.

[43] R. Hadani *et al.*, “Orthogonal time frequency space modulation,” in *IEEE Wireless Communications and Networking Conference (WCNC)*, 2017, pp. 1–6.

[44] R. Hadani *et al.*, “Orthogonal time frequency space (OTFS) modulation for millimeter- wave communications systems,” in *IEEE MTT-S Int. Microw. Symp. (IMS)*, 2017, pp. 681–683.

[45] Y. Liu, S. Zhang, F. Gao, J. Ma, and X. Wang, “Uplink-aided high mobility downlink channel estimation over massive MIMO-OTFS system,” *IEEE J. Sel. Areas Commun.*, vol. 38, no. 9, pp. 1994–2009, 2020.

[46] W. Yuan, S. Li, Z. Wei, J. Yuan, and D. W. K. Ng, “Data-aided channel estimation for OTFS systems with a superimposed pilot and data transmission scheme,” *IEEE Wireless Commun. Lett.*, vol. 10, no. 9, pp. 1954–1958, 2021.

[47] O. K. Rasheed, G. D. Surabhi, and A. Chockalingam, “Sparse delay-doppler channel estimation in rapidly time-varying channels for multiuser OTFS on the uplink,” in *IEEE 91st Veh. Technol. Conf. (VTC2020-Spring)*, 2020, pp. 1–5.

[48] M. Zhang, F. Wang, X. Yuan, and L. Chen, “2D structured turbo compressed sensing for channel estimation in OTFS systems,” in *IEEE Int. Conf. Commun. Syst. (ICCS)*, 2018, pp. 45–49.

[49] L. Zhao, W.-J. Gao, and W. Guo, “Sparse bayesian learning of delay-doppler channel for OTFS system,” *IEEE Commun. Lett.*, vol. 24, no. 12, pp. 2766–2769, 2020.

[50] P. Raviteja, K. T. Phan, Y. Hong, and E. Viterbo, “Interference cancellation and iterative detection for orthogonal time frequency space modulation,” *IEEE Trans. Wireless Commun.*, vol. 17, no. 10, pp. 6501–6515, 2018.

[51] P. Raviteja, K. T. Phan, Y. Hong, and E. Viterbo, “Embedded delay-Doppler channel estimation for orthogonal time fre- quency space modulation,” in *IEEE 88th Veh. Technol. Conf. (VTC-Fall)*, 2018, pp. 1–5.

[52] P. Raviteja, K. T. Phan, and Y. Hong, “Embedded pilot-aided channel estimation for OTFS in delay–Doppler channels,” *IEEE Trans. Veh. Technol.*, vol. 68, no. 5, pp. 4906–4917, 2019.

[53] S. S. Das, V. Rangamgari, S. Tiwari, and S. C. Mondal, “Time domain channel estimation and equalization of CP-OTFS under multiple fractional dopplers and residual synchronization errors,” *IEEE Access*, vol. 9, pp. 10 561–10 576, 2021.

[54] D. Shi *et al.*, “Deterministic pilot design and channel estimation for downlink massive MIMO-OTFS systems in presence of the fractional Doppler,” *IEEE Trans. Wireless Commun.*, vol. 20, no. 11, pp. 7151–7165, 2021.

[55] N. Hashimoto, N. Osawa, K. Yamazaki, and S. Ibi, “Channel estimation and equalization for CP-OFDM-based OTFS in fractional doppler channels,” in *IEEE Int. Conf. Commun. Workshops (ICC Workshops)*, 2021, pp. 1–7.

[56] H. B. Mishra, P. Singh, A. K. Prasad, and R. Budhiraja, “OTFS channel estimation and data detection designs with superimposed pilots,” *IEEE Trans. Wireless Commun.*, vol. 21, no. 4, pp. 2258–2274, 2022.

[57] F. Liu, Z. Yuan, Q. Guo, Z. Wang, and P. Sun, “Message passing-based structured sparse signal recovery for estimation of OTFS channels with fractional doppler shifts,” *IEEE Trans. Wireless Commun.*, vol. 20, no. 12, pp. 7773–7785, 2021.

[58] Z. Wei, W. Yuan, S. Li, J. Yuan, and D. W. K. Ng, “Off-grid channel estimation with sparse Bayesian learning for OTFS systems,” *IEEE Trans. Wireless Commun.*, pp. 1–1, 2022.

[59] S. M. Patole, M. Torlak, D. Wang, and M. Ali, “Automotive radars: A review of signal processing techniques,” *IEEE Signal Processing Magazine*, vol. 34, no. 2, pp. 22–35, 2017.

[60] C. Waldschmidt, J. Hasch, and W. Menzel, "Automotive radar — from first efforts to future systems," *IEEE Journal of Microwaves*, vol. 1, no. 1, pp. 135–148, 2021.

[61] D. Ma, N. Shlezinger, T. Huang, Y. Liu, and Y. C. Eldar, "Automotive dual-function radar communications systems: an overview," in *2020 IEEE 11th Sensor Array and Multichannel Signal Processing Workshop (SAM)*. IEEE, 2020, pp. 1–5.

[62] J. R. Klauder, A. Price, S. Darlington, and W. J. Albersheim, "The theory and design of chirp radars," *Bell System Technical Journal*, vol. 39, no. 4, pp. 745–808, 1960.

[63] F. Uysal, "Phase-coded FMCW automotive radar: System design and interference mitigation," *IEEE Transactions on Vehicular Technology*, vol. 69, no. 1, pp. 270–281, 2020.

[64] U. Chipengo, A. Sligar, and S. Carpenter, "High fidelity physics simulation of 128 channel MIMO sensor for 77GHz automotive radar," *IEEE Access*, vol. 8, pp. 160 643–160 652, 2020.

[65] A. Mushtaq, W. Winkler, and D. Kissinger, "A 79-GHz scalable FMCW MIMO automotive radar transceiver architecture with injection-locked synchronization," in *IEEE MTT-S International Microwave Symposium (IMS)*, 2019, pp. 690–693.

[66] C. D. Ozkaptan, E. Ekici, O. Altintas, and C.-H. Wang, "OFDM pilot-based radar for joint vehicular communication and radar systems," in *Vehicular Networking Conference (VNC)*. IEEE, 2018, pp. 1–8.

[67] C.-H. Wang, O. Altintas, C. D. Ozkaptan, and E. Ekici, "Multi-range joint automotive radar and communication using pilot-based OFDM radar," in *Vehicular Networking Conference (VNC)*. IEEE, 2020, pp. 1–4.

[68] L. Pucci, E. Paolini, and A. Giorgetti, "System-level analysis of joint sensing and communication based on 5g new radio," *IEEE Journal on Selected Areas in Communications*, vol. 40, no. 7, pp. 2043–2055, 2022.

[69] Z. Wei *et al.*, "Orthogonal time-frequency space modulation: A promising next-generation waveform," *IEEE wireless communications*, vol. 28, no. 4, pp. 136–144, 2021.

[70] W. Yuan *et al.*, "New delay Doppler communication paradigm in 6G era: A survey of orthogonal time frequency space (OTFS)," *China Communications*, vol. 20, no. 6, pp. 1–25, 2023.

[71] R. Hadani and A. Monk, "OTFS a new generation of modulation addressing the challenges of 5G," *arXiv preprint arXiv:1802.02623*, 2018.

[72] F. Liu *et al.*, "Integrated sensing and communications: Toward dual-functional wireless networks for 6g and beyond," *IEEE Journal on Selected Areas in Communications*, vol. 40, no. 6, pp. 1728–1767, 2022.

[73] S. E. Zegrar, S. Rafique, and H. Arslan, "OTFS-FMCW waveform design for low complexity joint sensing and communication," in *IEEE 33rd Annual International Symposium on Personal, Indoor and Mobile Radio Communications (PIMRC)*, 2022, pp. 988–993.

[74] L. Gaudio, M. Kobayashi, G. Caire, and G. Colavolpe, “On the effectiveness of OTFS for joint radar parameter estimation and communication,” *IEEE Transactions on Wireless Communications*, vol. 19, no. 9, pp. 5951–5965, 2020.

[75] S. K. Dehkordi, L. Gaudio, M. Kobayashi, G. Colavolpe, and G. Caire, “Beamspace MIMO radar with OTFS modulation for integrated sensing and communications,” in *International Conference on Communications Workshops (ICC Workshops)*. IEEE, 2022, pp. 509–514.

[76] C. Liu, S. Liu, Z. Mao, Y. Huang, and H. Wang, “Low-complexity parameter learning for OTFS modulation based automotive radar,” in *International Conference on Acoustics, Speech and Signal Processing (ICASSP)*. IEEE, 2021, pp. 8208–8212.

[77] W. Yuan, Z. Wei, S. Li, J. Yuan, and D. W. K. Ng, “Integrated sensing and communication-assisted orthogonal time frequency space transmission for vehicular networks,” *IEEE Journal of Selected Topics in Signal Processing*, vol. 15, no. 6, pp. 1515–1528, 2021.

[78] S. Li *et al.*, “A novel ISAC transmission framework based on spatially-spread orthogonal time frequency space modulation,” *IEEE Journal on Selected Areas in Communications*, vol. 40, no. 6, pp. 1854–1872, 2022.

[79] S. D. Liyanaarachchi, T. Riihonen, C. B. Barneto, and M. Valkama, “Optimized waveforms for 5G–6G communication with sensing: Theory, simulations and experiments,” *IEEE Transactions on Wireless Communications*, vol. 20, no. 12, pp. 8301–8315, 2021.

[80] J. A. Zhang *et al.*, “Enabling joint communication and radar sensing in mobile networks—a survey,” *IEEE Communications Surveys & Tutorials*, vol. 24, no. 1, pp. 306–345, 2022.

[81] N. C. Luong, X. Lu, D. T. Hoang, D. Niyato, and D. I. Kim, “Radio resource management in joint radar and communication: A comprehensive survey,” *IEEE Communications Surveys & Tutorials*, vol. 23, no. 2, pp. 780–814, 2021.

[82] T. T. Nguyen, K. Elbassioni, N. C. Luong, D. Niyato, and D. I. Kim, “Access management in joint sensing and communication systems: Efficiency versus fairness,” *IEEE Transactions on Vehicular Technology*, vol. 71, no. 5, pp. 5128–5142, 2022.

[83] D. Ma, N. Shlezinger, T. Huang, Y. Liu, and Y. C. Eldar, “Joint radar-communication strategies for autonomous vehicles: Combining two key automotive technologies,” *IEEE Signal Processing Magazine*, vol. 37, no. 4, pp. 85–97, 2020.

[84] L. Zheng, M. Lops, Y. C. Eldar, and X. Wang, “Radar and communication coexistence: An overview: A review of recent methods,” *IEEE Signal Processing Magazine*, vol. 36, no. 5, pp. 85–99, 2019.

[85] W. Yuan, S. Li, Z. Wei, J. Yuan, and D. W. K. Ng, “Bypassing channel estimation for otfs transmission: An integrated sensing and communication solution,” in *2021 IEEE Wireless Communications and Networking Conference Workshops (WCNCW)*. IEEE, 2021, pp. 1–5.

[86] L. Gaudio, M. Kobayashi, G. Caire, and G. Colavolpe, “On the effectiveness of OTFS for joint radar parameter estimation and communication,” *IEEE Transactions on Wireless Communications*, vol. 19, no. 9, pp. 5951–5965, 2020.

[87] H. Zhang, T. Zhang, and Y. Shen, “Modulation symbol cancellation for OTFS-based joint radar and communication,” in *IEEE International Conference on Communications Workshops (ICC Workshops)*, 2021, pp. 1–6.

[88] P. Raviteja, K. T. Phan, Y. Hong, and E. Viterbo, “Orthogonal time frequency space (OTFS) modulation based radar system,” in *IEEE Radar Conference (RadarConf)*, 2019, pp. 1–6.

[89] S. K. Dehkordi, L. Gaudio, M. Kobayashi, G. Caire, and G. Colavolpe, “Beam-space MIMO radar for joint communication and sensing with OTFS modulation,” *IEEE Transactions on Wireless Communications*, 2023.

[90] K. Wu, J. A. Zhang, X. Huang, and Y. J. Guo, “OTFS-based joint communication and sensing for future industrial IoT,” *IEEE Internet of Things Journal*, pp. 1–1, 2021.

[91] Z. Feng, Z. Fang, Z. Wei, X. Chen, Z. Quan, and D. Ji, “Joint radar and communication: A survey,” *China Communications*, vol. 17, no. 1, pp. 1–27, 2020.

[92] S. Darlington, “Demodulation of wideband, low-power FM signals,” *Bell System Technical Journal*, vol. 43, no. 1, pp. 339–374, 1964.

[93] W. Hirt and S. Pasupathy, “Continuous phase chirp (CPC) signals for binary data communication-part I: Coherent detection,” *IEEE Transactions on Communications*, vol. 29, no. 6, pp. 836–847, 1981.

[94] C.-H. Wang and O. Altintas, “Demo: A joint radar and communication system based on commercially available FMCW radar,” in *IEEE Vehicular Networking Conference (VNC)*, 2018, pp. 1–2.

[95] D. Gaglione, C. Clemente, C. V. Ilioudis, A. R. Persico, I. K. Proudler, and J. J. Soraghan, “Fractional Fourier based waveform for a joint radar-communication system,” in *IEEE Radar Conference (RadarConf)*, 2016, pp. 1–6.

[96] X. Ouyang and J. Zhao, “Orthogonal chirp division multiplexing,” *IEEE Trans. Commun.*, vol. 64, no. 9, pp. 3946–3957, 2016.

[97] M. S. Omar and X. Ma, “Performance analysis of OCDM for wireless communications,” *IEEE Trans. Wireless Commun.*, vol. 20, no. 7, pp. 4032–4043, 2021.

[98] M. S. Omar and X. Ma, “The effects of narrowband interference on OCDM,” in *IEEE 21st Int. Workshop on Signal Process. Advances in Wireless Commun. (SPAWC)*, 2020,
pp. 1–5.

[99] X. Lv *et al.*, “A joint radar-communication system based on OCDM-OFDM scheme,” in *Int. Conf. Microw. and Millimeter Wave Technol. (ICMMT)*, 2018, pp. 1–3.

[100] X. Wang *et al.*, “On low-complexity MMSE channel estimation for OCDM systems,” *IEEE Wireless Commun. Lett.*, vol. 10, no. 8, pp. 1697–1701, 2021.

[101] M. S. Omar and X. Ma, “Pilot symbol aided channel estimation for OCDM

transmissions," *IEEE Commun. Lett.*, vol. 26, no. 1, pp. 163–166, 2021.

[102] L. G. de Oliveira *et al.*, "Discrete-Fresnel domain channel estimation in OCDM-based radar systems," *IEEE Trans. Microw. Theory and Techn.*, 2022.

[103] R. Zhang *et al.*, "Channel estimation for OCDM transmissions with carrier frequency offset," *IEEE Wireless Commun. Lett.*, vol. 11, no. 3, pp. 483–487, 2021.

[104] Y. Wang *et al.*, "Pilot chirp assisted OCDM communications over time-varying channels," *IEEE Wireless Commun. Lett.*, vol. 12, no. 9, pp. 1578–1582, 2023.

[105] L. Dai, Z. Wang, and Z. Yang, "Spectrally efficient time-frequency training OFDM for mobile large-scale MIMO systems," *IEEE Journal on Selected Areas in Communications*, vol. 31, no. 2, pp. 251–263, 2013.

[106] Y. Liu, Z. Tan, H. Hu, L. J. Cimini, and G. Y. Li, "Channel estimation for OFDM," *IEEE Communications Surveys & Tutorials*, vol. 16, no. 4, pp. 1891–1908, 2014.

[107] A. Van Zelst and T. C. Schenk, "Implementation of a MIMO OFDM-based wireless LAN system," *IEEE Transactions on Signal Processing*, vol. 52, no. 2, pp. 483–494, 2004.

[108] D. Mi, M. Dianati, L. Zhang, S. Muhaidat, and R. Tafazolli, "Massive MIMO performance with imperfect channel reciprocity and channel estimation error," *IEEE Transactions on Communications*, vol. 65, no. 9, pp. 3734–3749, 2017.

[109] H. M. Furqan, M. S. J. Solaija, H. Türkmen, and H. Arslan, "Wireless Communication, Sensing, and REM: A Security Perspective," *IEEE Open Journal of the Communications Society*, vol. 2, pp. 287–321, 2021.

[110] A. V. Oppenheim, *Discrete-time signal processing*. Pearson Education India, 1999.

[111] Y. Zou, J. Zhu, X. Wang, and L. Hanzo, "A Survey on Wireless Security: Technical Challenges, Recent Advances, and Future Trends," *Proceedings of the IEEE*, vol. 104, no. 9, pp. 1727–1765, 2016.

[112] S. Goel and R. Negi, "Guaranteeing Secrecy using Artificial Noise," *IEEE Transactions on Wireless Communications*, vol. 7, no. 6, pp. 2180–2189, 2008.

[113] D. Hu, L. Yang, Y. Shi, and L. He, "Optimal pilot sequence design for channel estimation in MIMO OFDM systems," *IEEE Communications Letters*, vol. 10, no. 1, pp. 1–3, 2006.

[114] Y. S. Cho, J. Kim, W. Y. Yang, and C. G. Kang, *MIMO-OFDM wireless communications with MATLAB*. John Wiley & Sons, 2010.

[115] K. P. Bagadi and S. Das, "MIMO-OFDM channel estimation using pilot carries," *International Journal of computer applications*, vol. 2, no. 3, pp. 81–88, 2010.

[116] N. S. Ferdinand, D. B. da Costa, A. L. de Almeida, and M. Latva-aho, "Physical layer secrecy performance of TAS wiretap channels with correlated main and eavesdropper channels," *IEEE Wireless Communications Letters*, vol. 3, no. 1, pp. 86–89, 2013.

[117] V. Pan, "Sequential and parallel complexity of approximate evaluation of polynomial zeros," *Computers & Mathematics with Applications*, vol. 14, no. 8, pp.

591–622, 1987.

[118] M. K. Ozdemir and H. Arslan, “Channel estimation for wireless OFDM systems,” *IEEE Commun. Surveys Tuts.*, vol. 9, no. 2, pp. 18–48, 2007.

[119] P. Duhamel, “Implementation of“ Split-radix” FFT algorithms for complex, real, and real-symmetric data,” *IEEE Trans. Acoust., Speech, and Signal Process.*, vol. 34, no. 2, pp. 285–295, 1986.

[120] M. N. I. Khan and M. J. Alam, “Noise reduction algorithm for LS channel estimation in OFDM system,” in *2012 15th Int. Conf. Computer and Information Technol. (ICCIT)*. IEEE, 2012, pp. 310–315.

[121] S. Ramavath and R. S. Kshetrimayum, “Analytical calculations of CCDF for some common PAPR reduction techniques in OFDM systems,” in *2012 Int. Conf. Commun., Devices and Intelligent Systems (CODIS)*. IEEE, 2012, pp. 393–396.

[122] P. Raviteja, Y. Hong, E. Viterbo, and E. Biglieri, “Practical pulse-shaping waveforms for reduced-cyclic-prefix OTFS,” *IEEE Transactions on Vehicular Technology*, vol. 68, no. 1, pp. 957–961, 2018.

[123] N. Hashimoto, N. Osawa, K. Yamazaki, and S. Ibi, “Channel estimation and equalization for CP-OFDM-based OTFS in fractional doppler channels,” in *2021 IEEE International Conference on Communications Workshops (ICC Workshops)*, 2021, pp. 1–7.

[124] A. Farhang, A. RezazadehReyhani, L. E. Doyle, and B. Farhang-Boroujeny, “Low complexity modem structure for OFDM-based orthogonal time frequency space modulation,” *IEEE Wireless Communications Letters*, vol. 7, no. 3, pp. 344–347, 2017.

[125] G. D. Surabhi, R. M. Augustine, and A. Chockalingam, “On the diversity of uncoded OTFS modulation in doubly-dispersive channels,” *IEEE Trans. Wireless Commun.*, vol. 18, no. 6, pp. 3049–3063, 2019.

[126] A. V. Oppenheim, *Discrete-time signal processing*. Pearson Education India, 1999.

[127] Z. Wei, W. Yuan, S. Li, J. Yuan, and D. W. K. Ng, “Performance analysis and window design for channel estimation of OTFS modulation,” in *IEEE Int. Conf. Commun.*, 2021, pp. 1–7.

[128] F. Lampel, A. Avarado, and F. M. Willems, “On OTFS using the discrete Zak transform,” in *IEEE International Conference on Communications Workshops (ICC Workshops)*, 2022, pp. 729–734.

[129] Z. Yuan, F. Liu, W. Yuan, Q. Guo, Z. Wang, and J. Yuan, “Iterative detection for orthogonal time frequency space modulation with unitary approximate message passing,” *IEEE Transactions on Wireless Communications*, vol. 21, no. 2, pp. 714–725, 2022.

[130] S. K. Mohammed, R. Hadani, A. Chockalingam, and R. Calderbank, “OTFS—a mathematical foundation for communication and radar sensing in the delay-Doppler domain,” *IEEE BITS the Information Theory Magazine*, vol. 2, no. 2, pp. 36–55, 2022.

[131] S. Li, W. Yuan, Z. Wei, J. Yuan, B. Bai, and G. Caire, "On the pulse shaping for delay-Doppler communications," *arXiv preprint arXiv:2306.08704*, 2023.

[132] G. D. Surabhi and A. Chockalingam, "Low-complexity linear equalization for otfs modulation," *IEEE Communications Letters*, vol. 24, no. 2, pp. 330–334, 2020.

[133] V. Khammammetti and S. K. Mohammed, "OTFS-based multiple-access in high doppler and delay spread wireless channels," *IEEE Wireless Communications Letters*, vol. 8, no. 2, pp. 528–531, 2019.

[134] H. Arslan, *Wireless communication signals: A laboratory-based approach*. John Wiley & Sons, 2021.

[135] J. Hasch, E. Topak, R. Schnabel, T. Zwick, R. Weigel, and C. Waldschmidt, "Millimeter-wave technology for automotive radar sensors in the 77 GHz frequency band," *IEEE Transactions on Microwave Theory and Techniques*, vol. 60, no. 3, pp. 845–860, 2012.

[136] P. Raviteja, K. T. Phan, and Y. Hong, "Embedded pilot-aided channel estimation for OTFS in delay–doppler channels," *IEEE Transactions on Vehicular Technology*, vol. 68, no. 5, pp. 4906–4917, 2019.

[137] S. M. Kay, *Fundamentals of statistical signal processing: estimation theory*. Prentice-Hall, Inc., 1993.

[138] P. Raviteja, K. T. Phan, and Y. Hong, "Embedded pilot-aided channel estimation for otfs in delay–doppler channels," *IEEE Trans. Veh. Technol.*, vol. 68, no. 5, pp. 4906–4917, 2019.

[139] J. M. Hamamreh, E. Basar, and H. Arslan, "OFDM-Subcarrier Index Selection for Enhancing Security and Reliability of 5G URLLC Services," *IEEE Access*, vol. 5, pp. 25 863–25 875, 2017.

[140] H. Qin *et al.*, "Power allocation and time-domain artificial noise design for wiretap OFDM with discrete inputs," *IEEE Transactions on Wireless Communications*, vol. 12, no. 6, pp. 2717–2729, 2013.

[141] H. M. Furqan, J. M. Hamamreh, and H. Arslan, "Enhancing physical layer security of OFDM systems using channel shortening," in *IEEE 28th Annual International Symposium on Personal, Indoor, and Mobile Radio Communications (PIMRC)*, 2017, pp. 1–5.

[142] 3GPP, "Evolved universal terrestrial radio access (E-UTRA); base station (BS) radio transmission and reception," 3rd Generation Partnership Project (3GPP), Technical Specification (TS) 36.104, 01 2016, version 13.2.0.

[143] R. Liu, Y. Huang, D. He, Y. Xu, and W. Zhang, "Optimizing channel estimation overhead for OTFS with prior channel statistics," in *2021 IEEE Wireless Communications and Networking Conference (WCNC)*, 2021, pp. 1–6.

[144] 3GPP, "Evolved universal terrestrial radio access (E-UTRA); base station (BS) radio transmission and reception," 3rd Generation Partnership Project (3GPP), Technical Specification (TS) 36.104, 01 2016, version 13.2.0.

[145] Q. Wang, Y. Liang, Z. Zhang, and P. Fan, "2D Off-grid Decomposition and SBL Combination for OTFS Channel Estimation," *IEEE Transactions on Wireless Communications*, 2022.

[146] H. Zhang and T. Zhang, "A low-complexity message passing detector for OTFS modulation with probability clipping," *IEEE Wireless Communications Letters*, vol. 10, no. 6, pp. 1271–1275, 2021.

[147] T. Thaj and E. Viterbo, "Low complexity iterative rake decision feedback equalizer for zero-padded OTFS systems," *IEEE Transactions on Vehicular Technology*, vol. 69, no. 12, pp. 15 606–15 622, 2020.

[148] L. Pucci, E. Paolini, and A. Giorgetti, "System-level analysis of joint sensing and communication based on 5G new radio," *IEEE Journal on Selected Areas in Communications*, vol. 40, no. 7, pp. 2043–2055, 2022.

[149] F. Liu, Z. Yuan, Q. Guo, Z. Wang, and P. Sun, "Message passing-based structured sparse signal recovery for estimation of OTFS channels with fractional doppler shifts," *IEEE Transactions on Wireless Communications*, vol. 20, no. 12, pp. 7773–7785, 2021.

[150] L. Gaudio, M. Kobayashi, B. Bissinger, and G. Caire, "Performance analysis of joint radar and communication using OFDM and OTFS," in *IEEE International Conference on Communications Workshops (ICC Workshops)*, 2019, pp. 1–6.

[151] Q. Yu, H. Wang, Z. Lu, and S. An, "Group-Based CSS modulation: A novel enhancement to LoRa physical layer," *IEEE Wireless Communications Letters*, vol. 11, no. 3, pp. 660–664, 2022.

[152] J. G. Proakis *et al.*, "Signal analysis with higher order spectra, advanced digital signal processing," 1992.

[153] I. F. Akyildiz, C. Han, Z. Hu, S. Nie, and J. M. Jornet, "Terahertz band communication: An old problem revisited and research directions for the next decade," *IEEE Transactions on Communications*, vol. 70, no. 6, pp. 4250–4285, 2022.

[154] C. Castro, *ITU: 6G Standardisation Ready 'No Later Than 2030'*, accessed July 1, 2023. [Online]. Available: https://www.6gworld.com/exclusives/itu-6g-standardisation-ready-no-later-than-2030/

[155] G. P. Fettweis and H. Boche, "6G: the personal tactile internet and open questions for information theory," *IEEE BITS the Information Theory Magazine*, vol. 1, no. 1, pp. 71–82, 2021.

[156] D. W. Bliss, K. W. Forsythe, and A. M. Chan, "MIMO wireless communication," MASSACHUSETTS INST OF TECH LEXINGTON LEXINGTON United States, Tech. Rep., 2005.

[157] M.-X. Chang and Y. T. Su, "Performance analysis of equalized OFDM systems in Rayleigh fading," *IEEE Transactions on Wireless Communications*, vol. 1, no. 4, pp. 721–732, 2002.

APPENDIX A

Appendix A1 BER derivation

The received data at k_d subcarriers is expressed by

$$\underline{\mathrm{Y}}_{ab}(k) = \mathrm{H}_{ab}(k)\mathrm{Q}_D(k)\underline{\mathrm{D}}(k) + \underline{\mathrm{W}}_{ab}(k)\ k \in k_d. \tag{A1.1}$$

Therefore, by enforcing the constraint $\mathrm{E}[\mathrm{Tr}(\underline{\mathrm{D}}(k)\underline{\mathrm{D}}^H(k))] = 1$, the signal-to-noise ratio (SNR) of the received signal at the k-th subcarrier is given by [156]

$$\gamma_{ab} \triangleq \frac{\mathrm{E}\left[\mathrm{Tr}\left(\mathrm{H}_{ab}(k)\mathrm{Q}_D(k)\,(\mathrm{H}_{ab}(k)\mathrm{Q}_D(k))^H\right)\right]}{M_a N_b M\,\mathrm{E}\left[\mathrm{Tr}(\underline{\mathrm{W}}(k)\underline{\mathrm{W}}^H(k))\right]}, \tag{A1.2}$$

where M denotes the number of bits represented by each symbol. As demonstrated in Subsection 4.1.2.1, the minimum-phase component shares the same power with the overall channel response itself $|\mathrm{H}_{ab}(k)\mathrm{Q}_D(k)|^2 = |\mathrm{H}_{ab}(k)|^2$. Thus, the SNR can be written as

$$\begin{aligned}\gamma_{ab} &\triangleq \frac{\mathrm{E}\left[\mathrm{Tr}\left(\mathrm{H}_{ab}(k)\,(\mathrm{H}_{ab}(k))^H\right)\right]}{M_a N_b M\,\mathrm{E}\left[\mathrm{Tr}(\underline{\mathrm{W}}(k)\underline{\mathrm{W}}^H(k))\right]} \\ &= \frac{\mathrm{E}\left[\sum_{n=1}^{N_b}|H_{ab}^{(n)}(k)|^2\right]}{M_a N_b M\cdot\mathrm{E}\left[\sum_{n=1}^{N_b}|W^{(n)}(k)|^2\right]}.\end{aligned} \tag{A1.3}$$

Using linearity property and assuming that noise samples are i.i.d, (**A1.3)** becomes

$$\begin{aligned}&= \frac{1}{N_b}\sum_{n=1}^{N_b}\frac{\mathrm{E}\left[|H_{ab}^{(n)}(k)|^2\right]}{M_a M\sigma^2} \\ &= \frac{1}{N_b}\sum_{n=1}^{N_b}\gamma_{ab}^{(n)}.\end{aligned} \tag{A1.4}$$

We conclude from (**A1.4)** that the bit error rate (BER) can be computed by averaging the error at each receive antenna. The average bit error probability (BEP) $P_{ab}^{(n)}(e)$ then is given as function of $\gamma_{ab}^{(n)}$ and the correlation coefficients ρ_{ab}^1 and ρ_{ab}^2 between the actual and the

estimated channel responses [157] by

$$P_{ab}^{(n)}(e) = \frac{1}{2}\left[1 - \frac{1}{2}\frac{\frac{(\rho_{ab}^{1}+\rho_{ab}^{2})}{\sqrt{2}}}{\sqrt{1+\frac{1}{2\gamma_{ab}^{(n)}}-\frac{(\rho_{ab}^{1}-\rho_{ab}^{2})^{2}}{2}}} - \frac{1}{2}\frac{\frac{(\rho_{ab}^{1}-\rho_{ab}^{2})}{\sqrt{2}}}{\sqrt{1+\frac{1}{2\gamma_{ab}^{(n)}}-\frac{(\rho_{ab}^{1}+\rho_{ab}^{2})^{2}}{2}}}\right]. \tag{A1.5}$$

The total BER is then given by

$$P_{ab}(e) = \frac{1}{N_b}\sum_{n=1}^{N_b} P_{ab}^{(n)}. \tag{A1.6}$$

Note that similar step can be followed to compute the BER at Eve.

Appendix A2 Proof of (**4.26**)

Assuming the system model in (**4.25**)

$$\underline{\mathrm{H}}_{ae} = \hat{\rho}_{ae}\underline{\mathrm{H}}_{ab} + \sqrt{1-\hat{\rho}_{ae}^{2}}\,\underline{\mathrm{H}}_{e}. \tag{A2.7}$$

Let the correlation function of the legitimate channel gain with the eavesdropping channel be given as

$$\begin{aligned}\rho_{ae} &= \frac{\mathrm{Cov}(\underline{\mathrm{H}}_{ab}^{H}, \underline{\mathrm{H}}_{ae})}{\sqrt{\mathrm{var}(\underline{\mathrm{H}}_{ab}^{H})\,\mathrm{var}(\underline{\mathrm{H}}_{ae})}} \\ &= \frac{\mathrm{E}[\underline{\mathrm{H}}_{ab}H_{ae}^{H}] - \mathrm{E}[\underline{\mathrm{H}}_{ab}]\,\mathrm{E}[\underline{\mathrm{H}}_{ae}^{H}]}{\sigma_a\sigma_e}.\end{aligned} \tag{A2.8}$$

We know that $\mathrm{E}[\underline{\mathrm{H}}_{ab}] = \mathrm{E}[\underline{\mathrm{H}}_{ae}] = 0$. Additionally $\underline{\mathrm{H}}_{ae}$ is given by (**4.25**), then

$$\begin{aligned}\rho_{ae} &= \frac{\mathrm{E}[\underline{\mathrm{H}}_{ab}^{H}\cdot(\hat{\rho}_{ae}\underline{\mathrm{H}}_{ab} + \sqrt{1-\hat{\rho}_{ae}^{2}}\,\underline{\mathrm{H}}_{e})]}{\sigma_a\sigma_e} \\ &= \frac{\hat{\rho}_{ae}\,\mathrm{E}[|\underline{\mathrm{H}}_{ab}|^{2}] + \sqrt{1-\hat{\rho}_{ae}^{2}}\,(\mathrm{E}[\underline{\mathrm{H}}_{ab}^{H}]\,\mathrm{E}[\underline{\mathrm{H}}_{e}])}{\sigma_a\sigma_e} \\ &= \frac{\hat{\rho}_{ae}\,\mathrm{E}[|\underline{\mathrm{H}}_{ab}|^{2}]}{\sigma_a\sigma_e}.\end{aligned} \tag{A2.9}$$

Note that $\sigma_a^2 = \mathrm{var}(\underline{\mathrm{H}}_{ab}) = \mathrm{E}[|\underline{\mathrm{H}}_{ab}|^2] - \left(\mathrm{E}[\underline{\mathrm{H}}_{ab}]\right)^2 = \mathrm{E}[|\underline{\mathrm{H}}_{ab}|^2]$, and $\sigma_e^2 = \mathrm{var}(\hat{\rho}_{ae}\underline{\mathrm{H}}_{ab} + \sqrt{1-\hat{\rho}_{ae}^2}\underline{\mathrm{H}}_e) = \hat{\rho}_{ae}^2\sigma_a^2 + (1-\hat{\rho}_{ae}^2)\sigma_a^2 = \sigma_a^2$. Therefore, we find

$$\rho_{ae} = \frac{\hat{\rho}_{ae}\sigma_a^2}{\sigma_a\sigma_a} = \hat{\rho}_{ae}. \tag{A2.10}$$

Thus, we prove that in the channel model given by (**4.25**), $\hat{\rho}_{ae}$ corresponds to the channel correlation between Bob and Eve.

Appendix A3 Proof of (**4.30**)

To identify the expression of Γ and instead of using complex probability distributions analysis, we exploit the four constraints given in (**5.56**). For instance, from (**5.56a**), we know that Γ is proportional to $\sqrt{1-\rho_{ae}^2}$. And if a linear relationship is assumed, we find

$$\Gamma = \alpha + \beta\sqrt{1-\rho_{ae}^2}, \tag{A3.11}$$

where α and β are the linear model's parameters to be defined, and by solving the equation in (**5.56c**), i.e., $\rho_{ae}(\Gamma = 1) = 1$, we find the value of the slope as $\alpha = 1$.
Also, by using (**5.56b**) and (**5.3c**) we find the following

$$0 \le \sqrt{1-\rho_{ae}^2} \le \beta. \tag{A3.12}$$

And since $0 \le \sqrt{1-\rho_{ae}^2} \le 1$, we conclude that $\beta = 1$, therefore

$$\Gamma = 1 + \sqrt{1-\rho_{ae}^2}. \tag{A3.13}$$

This model for Γ agrees very well with the simulation results as shown in Fig. **4.5.**

Appendix A4 Proof of (**4.28)**

The correlation function of the legitimate minimum-phase channel component gain with the eavesdropping channel be given as

$$\begin{aligned}\rho_{ae}^{\min} &= \frac{\mathrm{Cov}(\underline{\mathrm{H}}_{ab}^{\min H}, \underline{\mathrm{H}}_{ae}^{\min})}{\sqrt{\mathrm{var}(\underline{\mathrm{H}}_{ab}^{\min H})\,\mathrm{var}(\underline{\mathrm{H}}_{ae}^{\min})}} \\ &= \frac{\mathrm{E}[\underline{\mathrm{H}}_{ab}^{\min H}\cdot\underline{\mathrm{H}}_{ae}^{\min}] - \mathrm{E}[\underline{\mathrm{H}}_{ab}^{\min H}]\,\mathrm{E}[\underline{\mathrm{H}}_{ae}^{\min}]}{\sqrt{\left(\mathrm{E}[|\underline{\mathrm{H}}_{ab}^{\min}|^2] - \left(\mathrm{E}[\underline{\mathrm{H}}_{ab}^{\min}]\right)^2\right)\left(\mathrm{E}[|\underline{\mathrm{H}}_{ae}^{\min}|^2] - \left(\mathrm{E}[\underline{\mathrm{H}}_{ae}^{\min}]\right)^2\right)}}.\end{aligned} \tag{A4.14}$$

Note that $\mathrm{E}[\underline{\mathrm{H}}_{ab}^{\min}] = \mathrm{E}[\underline{\mathrm{H}}_{ae}^{\min}] = 0$, $\mathrm{E}[|\underline{\mathrm{H}}_{ae}^{\min}|^2] = \mathrm{E}[|\underline{\mathrm{H}}_{ae}|^2] = \sigma_e^2$, and $\mathrm{E}[|\underline{\mathrm{H}}_{ab}^{\min}|^2] = \mathrm{E}[|\underline{\mathrm{H}}_{ab}|^2] = \sigma_a^2$. Please refer to Appendix A.5.

Thus, we find

$$\begin{aligned}\rho_{ae}^{\min} &= \frac{\mathrm{E}[\underline{\mathrm{H}}_{ab}^{\min H}\underline{\mathrm{H}}_{ae}^{\min}]}{\sigma_a\sigma_e} \\ &= \frac{\mathrm{E}\left[\underline{\mathrm{H}}_{ab}^{\min H}\cdot\left(\frac{\rho_{ae}}{1+\sqrt{1-\rho_{ae}^2}}\underline{\mathrm{H}}_{ab}^{\min} + \sqrt{1-\left(\frac{\rho_{ae}}{\Gamma}\right)^2}\underline{\mathrm{H}}_{e}^{\min}\right)\right]}{\sigma_a\sigma_e} \\ &= \frac{\frac{\rho_{ae}}{1+\sqrt{1-\rho_{ae}^2}}\mathrm{E}[|\underline{\mathrm{H}}_{ab}^{\min}|^2] + \sqrt{1-\left(\frac{\rho_{ae}}{\Gamma}\right)^2}\left(\mathrm{E}[\underline{\mathrm{H}}_{ab}^{\min H}]\,\mathrm{E}[\underline{\mathrm{H}}_{e}^{\min}]\right)}{\sigma_a\sigma_e} \\ &= \frac{\frac{\rho_{ae}}{1+\sqrt{1-\rho_{ae}^2}}\sigma_a^2}{\sigma_a\sigma_e}.\end{aligned} \tag{A4.15}$$

Finally, the correlation is found as

$$\rho_{ae}^{\min} = \frac{\rho_{ae}}{1+\sqrt{1-\rho_{ae}^2}} < \rho_{ae}. \tag{A4.16}$$

Appendix A5 Proof of $\mathrm{E}[\underline{\mathrm{H}}_{ab}^{\min}] = \mathrm{E}[\underline{\mathrm{H}}_{ae}^{\min}] = 0$.

As explained in Subsection 4.1.2.1, any FIR causal channel $\underline{\mathrm{H}}_{ab}$ can be decomposed as follows: $\underline{\mathrm{H}}_{ab} = \underline{\mathrm{H}}_{ab}^{\min}\cdot\underline{\mathrm{H}}_{ab}^{\mathrm{ap}}$, where $\underline{\mathrm{H}}_{ab}^{\mathrm{ap}} = e^{jU}$ and $U \sim \mathcal{U}(0, 2\pi)$. Thus, $\underline{\mathrm{H}}_{ab}^{\mathrm{ap}}$ has the following probability density function (PDF): $f_X(x) = \frac{1}{j2\pi x}$.

With reference to the main problem, the expectation of $\underline{\mathrm{H}}_{ab}$ is given as

$$\mathrm{E}[\underline{\mathrm{H}}_{ab}] = \mathrm{E}[\underline{\mathrm{H}}_{ab}^{\min H} \cdot \underline{\mathrm{H}}_{ab}^{\mathrm{ap}}] = 0. \quad \textbf{(A5.17)}$$

Since the minimum-phase and all-pass components are independent, we find

$$\mathrm{E}[\underline{\mathrm{H}}_{ab}] = \mathrm{E}[\underline{\mathrm{H}}_{ab}^{\min}]\,\mathrm{E}[\underline{\mathrm{H}}_{ab}^{\mathrm{ap}}] = 0. \quad \textbf{(A5.18)}$$

As shown in **(A5.18)**, whether $\mathrm{E}[\underline{\mathrm{H}}_{ab}^{\min}] = 0$ or $\mathrm{E}[\underline{\mathrm{H}}_{ab}^{\mathrm{ap}}] = 0$. However, $\mathrm{E}[\underline{\mathrm{H}}_{ab}^{\mathrm{ap}}] = \int_{-\infty}^{+\infty} \frac{x}{j2\pi x} dx \neq 0$. Therefore

$$\mathrm{E}[\underline{\mathrm{H}}_{ab}^{\min}] = 0. \quad \textbf{(A5.19)}$$

CURRICULUM VITAE

Name Surname : Salah Eddine Zegrar

EDUCATION:

B.Sc. : 2019, Gebze Technical University, Engineering, Electronics Engineering, Kocaeli, Turkey.

PROFESSIONAL EXPERIENCE AND REWARDS:

- 2023, First prize in RadyoFest contest which took place in Medipol university, where I have implemented two ISAC systems to monitor the respiration rate of humans using RF signals, and the second to get the radar information in V2X networks.
- 2021, Contributed to WiFi-7 standardization activities as a **VOTER** member of the IEEE 802.11be task group.
- 2019, One of the best international students in Turkey, awarded by the president of Turkey: **Recep Tayyip Erdoğan**.
- 2019, Degree of high honor (Major in Electronics Engineering), first class (CGPA: 3.88).
- 2019, Degree of high honor (Minor in Physics), first class (CGPA: 3.72).
- 2014, Fully funded undergraduate scholarship issued by the presidency for Turks abroad and related communities.

PUBLICATIONS, PRESENTATIONS, AND PATENTS ON THE THESIS:

- Zegrar, S.E., Sacid, A.S. and Arslan, H., 2024. Fractional Delay & Fractional Doppler Estimation and Mitigation Framework in OTFS Systems. IEEE Transactions on Vehicular Technology.
- Zegrar, S.E., Hamza, H. and Arslan, H., 2024. OTFS-Based ISAC for Super-Resolution Range-Velocity Profile. IEEE Transactions on Communications.
- Zegrar, S.E., Ayoub, A.B. and Arslan, H., 2024. A Novel OTFS-Chirp Waveform for Low-Complexity Multi-User Joint Sensing and Communication. IEEE Transactions on Communications.
- Zegrar, S.E. and Arslan, H., 2024. A Novel Delay-Doppler-Based Channel Estimation Method in Doubly-Dispersive OCDM Systems. IEEE Wireless Communications Letters.

- Zegrar, S.E. and Arslan, H., 2023. A Novel Cyclic Prefix Configuration for Enhanced Reliability and Spectral Efficiency in OTFS Systems. IEEE Wireless Communications Letters.
- Zegrar, S.E., Rafique, S. and Arslan, H., 2022, September. OTFS-FMCW waveform design for low complexity joint sensing and communication. In 2022 IEEE 33rd Annual International Symposium on Personal, Indoor and Mobile Radio Communications (PIMRC) (pp. 988-993). IEEE.
- Zegrar, S.E. and Arslan, H., 2022. Common CP-OFDM transceiver design for low-complexity frequency domain equalization. IEEE Wireless Communications Letters, 11(7), pp.1349-1353.
- Zegrar, S.E., Furqan, H.M. and Arslan, H., 2022. Flexible physical layer security for joint data and pilots in future wireless networks. IEEE Transactions on Communications, 70(4), pp.2635-2647.
- Zegrar, S.E., Afeef, L. and Arslan, H., 2021, September. Reconfigurable intelligent surface (RIS): Eigenvalue decomposition-based separate channel estimation. In 2021 IEEE 32nd Annual International Symposium on Personal, Indoor and Mobile Radio Communications (PIMRC) (pp. 1-6). IEEE.
- Zegrar, S.E., Duranay, A.E. and Arslan, H., 2020. Precoding based cross-tier interference mitigation in centralized-RAN. IEEE Wireless Communications Letters, 10(1), pp.21-25.
- Zegrar, S.E. and Arslan, H., "OFDM-based joint radar and communication," *Turkish Patent Application* 2021/019525
- Zegrar, S.E. and Arslan, H., "İkili Dağıtıcı Kablosuz Kanallarda Gecikme-Doppler'e Dayanıklı OFDM," *Turkish Patent Application* 2021/019519
- Zegrar, S.E. and Arslan, H., "Ortak Haberleşme Algılama Ve Kanal Tahminine Yönelik Ortak Cıvıltı-OTFS Dalga Boyu Tasarımı," *Turkish Patent Application* 2021/019515
- Zegrar, S.E., Furqan, H.M. and Arslan, H., "Gelecekteki Kablosuz Ağlara Yönelik Kanal Ayrıştırma Tabanlı Uyarlamalı Fiziksel Katman Güvenliği," *Turkish Patent Application* 2021/019512
- Zegrar, S.E., Furqan, H.M. and Arslan, H., "Ygelecekteki Kablosuz Ağlara Yönelik Kanal Ayrıştırma Tabanlı Esnek Fiziksel Katman Güvenliğ," *Turkish Patent Application* 2021/019503
- Zegrar, S.E. and Arslan, H., "OFDM Sistemlerinde Kanalın Frekans Seçicilik Şiddetine Bakılmaksızın Pilot Destekli Kanal Tahmini İçin Bir Yöntem," *Turkish Patent Application* 2021/017199.
- Zegrar, S.E., A.E. and Arslan, H., "Çok-Katmanlı Merkezi Radyo İletişim Şebekelerinde Kullanıcı Üstünlüğüne Dayalı Girişim Azaltma Yöntemi," *Turkish Patent Application* 2020/19334.
- Zegrar, S.E., Afeef, L. and Arslan, H., "Yapılandırılabilir Yüzeyler İçin Kanal Kestirimi," *Turkish Patent Application* 2020/16930

OTHER PUBLICATIONS, PRESENTATIONS, AND PATENTS:

- Hamza, H., Zegrar, S.E. and Arslan, H., 2024. Novel OCDM Transceiver Design for Doubly-dispersive Channels. IEEE Transactions on Vehicular Technology.
- Solaija, M.S.J., Zegrar, S.E. and Arslan, H., 2024. Is OFDM the way forward for 6G PHY? IEEE Vehicular Technology Magazine.
- Abdelali, A., Zegrar, S.E. and Arslan, H., 2024. A Novel Delay-Doppler-Based Channel Estimation Method in Doubly-Dispersive OCDM Systems. IEEE Wireless Communications Letters.
- Solaija, M.S.J., Zegrar, S.E. and Arslan, H., 2023. Delay-Doppler Based Key Generation Using OTFS. IEEE Wireless Communications Letters.
- Abushattal, A., Zegrar, S.E., Yazgan, A. and Arslan, H., 2022. A Comprehensive Experimental Emulation for OTFS Waveform RF-Impairments. Sensors, 23(1), p.38.
- Janjua. M. B, Zegrar, S.E., and Arslan, H.,"Statik Ve Mobil Geri Saçılım Cihazlarına Yönelik Dikey Zaman Frekans Alanı (OTFS) Dalga Formu Kullanılarak Geri Saçılım İletişiminde Çoklama," *Turkish Patent Application* 2021/019866

WAVEFROM DESIGN FOR 5G AND BEYOND WIRELESS WIRELESS NETWORKS

ORIGINALITY REPORT

13%	8%	11%	1%
SIMILARITY INDEX	INTERNET SOURCES	PUBLICATIONS	STUDENT PAPERS

PRIMARY SOURCES

1	www.funasa.gov.br Internet Source	1%
2	ebin.pub Internet Source	1%
3	physionet.org Internet Source	1%
4	unsworks.unsw.edu.au Internet Source	1%
5	Abdelrahman Abushattal, Salah Eddine Zegrar, Ayhan Yazgan, Hüseyin Arslan. "A Comprehensive Experimental Emulation for OTFS Waveform RF-Impairments", Sensors, 2022 Publication	<1%
6	www.laughingpanda.org Internet Source	<1%
7	acikbilim.yok.gov.tr Internet Source	<1%